Computational study of supported or bacterial lipid membranes

Mariia Savenko

THÈSE DE DOCTORAT DE L'ÉTABLISSEMENT UNIVERSITÉ BOURGOGNE FRANCHE-COMTÉ PREPARÉE À L'UNIVERSITÉ DE FRANCHE-COMTÉ

École doctorale n°554

ÉCOLE DOCTORALE ENVIRONNEMENTS – SANTÉ

Doctorat de physique

Par

Madame Savenko Mariia

Études numériques de membranes lipidiques supportées ou bactériennes

Thèse présentée et soutenue à Besançon, le 29/09/2023

Composition du Jury :

Madame Baud Stéphanie	Professeure	Université de Reims Champagne-Ardenne	Rapporteuse
Monsieur D'Amelio Nicola	Professeur	Université de Picardie Jules Verne	Rapporteur
Madame Duboué-Dijon Élise	Chargée de recherche	CNRS	Membre du jury
Monsieur Trouillas Patrick	Professeur	Université de Limoges	Membre du jury
Monsieur Ramseyer Christophe	Professeur	Université de Franche-Comté	Directeur de thèse

Acknowledgments

I would like to start this section by thanking the members of my doctoral committee for the defense who accepted to get involved in my work. It is thriving and emulating to receive the insight from experienced researchers on the work I dedicated my whole time for the past years. I am looking forward to keep discussing MD and other simulations applied to biological problems with you.

I want to express my sincere gratitude to Christophe, who has guided me through the PhD. I also would like to thank all my colleagues from Chrono-environnement laboratory who welcomed me for these past years. I especially want to thank the PhD candidates from K3-K4 for all the exchanges we had.

I want to thank my family, pets, and friends for extensive moral support. I especially want to underline my gratitude to my husband, who helped me not only morally, but also with the extensive knowledge in the domain to teach me and made me go through many challenges of my thesis.

Finally, I want to express my deep gratitude to the Army of Ukraine and countless volunteers. Thanks to them I always have a home to return.

Table of Contents

Table of Figures

Index of Tables

Résumé de thèse

La problématique d'antibiorésistance affecte grandement notre société à l'heure actuelle, et les prédictions des instances internationales comme l'organisation mondiale de la santé laissent présager des conséquences drastiques pour les sociétés, autant sur le plan sanitaire que socio-économique. De sorte à endiguer ce phénomène, plusieurs directions sont envisagées, dont le développement de thérapies innovantes. L'utilisation de molécules ciblant la matrice lipidique des membranes bactériennes est une des pistes actuellement explorées. Les bactéries à Gram négatif présentent un véritable challenge, du fait de la présence de la membrane externe, dont le feuillet extérieur est principalement composé de lipopolysaccharides (LPS), et qui constitue une barrière difficile à passer pour la plupart des molécules. La famille des polymyxines, dont la colistine fait partie, sont des lipopeptides qui ciblent ces LPS et induisent la disruption de la membrane externe. Les polymyxines sont actuellement utilisées en dernier recours, d'une part du fait de leur importante toxicité, mais aussi de sorte à endiguer l'apparition de souches résistantes. Cependant, ces dernières décennies, de plus en plus de souches résistantes aux polymyxines ont été identifiées à l'occasion des veilles sanitaires présentes au niveau national. Ainsi, il est d'une grande importance d'étudier les mécanismes d'action des polymyxines au niveau des LPS de sorte à proposer des stratégies permettant d'outrepasser les mécanismes de résistance observés. Dans le même temps, plusieurs peptides antimicrobiens ont montré expérimentalement leur potentiel à induire une disruption partielle ou totale de la membrane externe sans pour autant qu'un mécanisme d'action au niveau de la matrice lipidique de la membrane externe ne soit détaillé. Une bonne compréhension du mécanisme des polymyxines pourrait permettre d'identifier un mécanisme commun à ces peptides. Dans un second temps, le lien entre expérimentation et simulation est d'une importance capitale. Une grande partie des expériences d'interaction médicament-membrane utilise des systèmes lipidiques déposés. Il est important de mieux comprendre les interactions membrane-surface, de sorte à pouvoir établir un lien plus direct entre simulation et expérience et afin de prédire quels couples membrane-substrat permettent d'obtenir à la fois un système déposé stable qui permette

d'accéder à une grande définition et dans le même temps de conserver les propriétés biologiques des systèmes déposés.

I. Les propriétés de membranes déposées répondent de manière continues à l'hydrophilicité du substrat

Afin de mieux comprendre l'influence de l'hydrophilicité d'un substrat sur la structure d'un système lipidique déposé, en particulier une bicouche lipidique supportée, nous avons sélectionné plusieurs substrats dont le degré d'hydrophilicité varie sur une large plage. En particulier, nous avons sélectionné une surface de graphène (GR), un groupe de surface d'oxyde de graphène (GO) pour lesquelles nous faisions varier le degré d'oxydation de la surface, et une surface de silice. Ce choix a aussi été guidé de sorte à sélectionner des substrats fréquemment utilisés pour des applications biotechnologiques. Ce travail a fait l'objet d'une publication [1].

Nous avons montré que ces différents substrats modifient drastiquement les propriétés de la bicouche supportée. En premier lieu, nous pouvons relier ces modifications structurelles à la distance substrat-membrane. Le tableau 1 recense les distances obtenues entre substrat et membrane. Il est à noter que deux modèles de membranes ont été modélisés. D'une part une membrane semi-périodique, ci-après dénommée bicelle et, d'autre part, une membrane infiniment périodique selon les axes X et Y. Par convention, l'axe Z est assimilé à la normale des modèles de membranes.

Les distances substrat-membrane sont de l'ordre de 4 à 6 Å ce qui pourrait correspondre à un état de contact proche comme caractérisé par Vishnyakov *et al. [2]*, ce qui peut être corroboré par la mesure de l'épaisseur de la couche d'eau intersticielle qui ne dépasse pas les 4 Å.

Table 1: Distance entre le centre de géométrie du substrat et celui des phosphates du feuillet lipidique le plus proche de la surface.

Système	Surface (degré d'oxydation, ratio epoxy:hydroxy)	Distance (Å)	Erreur (Å)
S2 (bicelle)	GO (5%; 1:1), humide	5.4	0.4
S4 (bicelle)	GO (17%; 1:1), humide	4.2	0.1
S5 (bicouche)	GO (17%; 1:1), humide	5	0.2
S9 (bicelle)	Silice, humide	5.8	0.4

L'équilibration des membranes dans un état de contact proche induit un effet direct sur l'épaisseur des modèles membranaires. Ainsi, l'épaisseur relative à une bicouche simulée en l'absence de substrat est de 93 % dans le cas de la silice, de 84 % dans le cas de l'oxyde de graphène avec un degré d'oxydation de 17 %, et de 72 % pour un degré d'oxydation de 5 %. Regan *et al.* [3] ont montré que l'épaisseur d'une bicouche de DOPC déposée sur une lame de verre traitée de différentes manières est réduite par rapport à l'épaisseur d'une couche n'interagissant pas directement avec le substrat. Les épaisseurs relatives variaient alors entre 89 to 92.7%.

La conséquence directe de cette observation est que le nombre de molécules d'eau à l'interface augmente au fur et à mesure que l'hydrophilicité de la surface augmente. Dans le cas des systèmes de pur graphène et de GO, l'hydrophilicité peut être caractérisée par la variation du degré d'oxydation (OL) de la surface. Nous observons qu'aucune molécule d'eau n'est présente à l'interface dans le cas de la monocouche déposée sur la surface de graphène (S1), seules 2.5 molécules d'eau par lipide sont présentes pour la bicelle avec 5 % OL (S2), 13 molécules d'eau par lipide pour GO 17 % OL (S4), et 14 molécules d'eau par lipide dans le cas de la silice.

En outre, les interactions substrat-membrane influence la bicouche lipidique de manière asymétrique. L'étude de la distribution des orientations du vecteur P-N relativement à la normale de la membrane, respectivement pour chaque feuillet membranaire, montre des comportements notablement différents (Figure 1). La distribution du feuillet supérieur est large et est une signature de la mobilité des têtes lipidiques. Au contraire, dans le cas du feuillet inférieur, à l'exception des systèmes déposés sur la silice, la distribution est centrée autour de 90° montrant l'influence majeure du substrat sur cette monocouche. Dans le cas de la silice, il est notable que les groupes cholines sont majoritairement plus proches de la surface que les groupes phosphates.

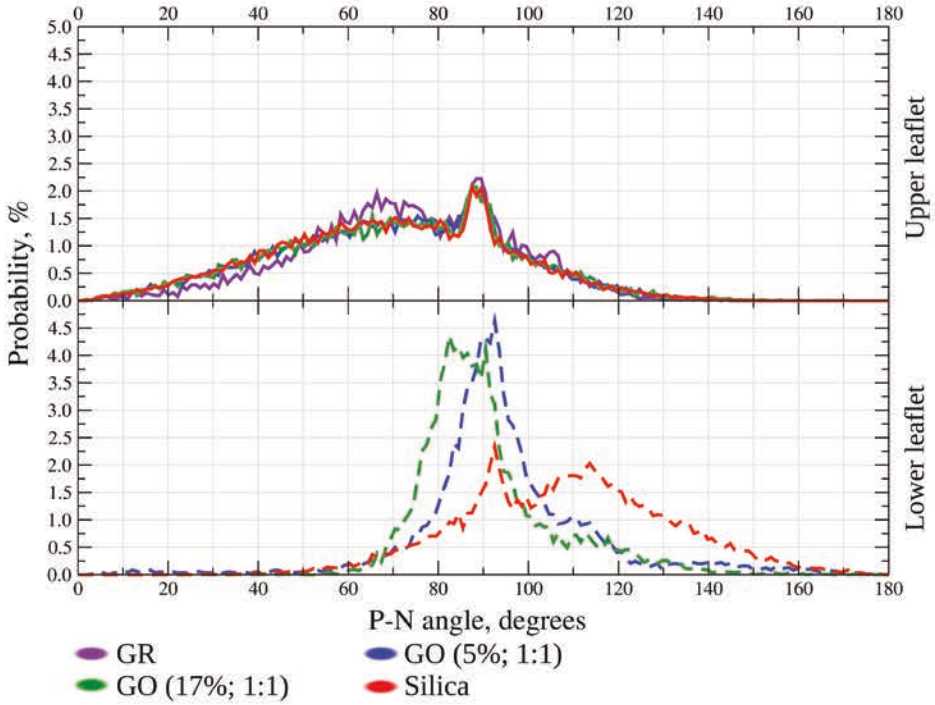

Figure 1: Distribution des angles P-N par rapport à la normale à la membrane pour chaque monocouche lipidique pour les bicelles déposées.

La Figure 2 résume bien les conclusions de l'étude, en montrant des images issues des simulations des couches d'atomes de la membrane à proximité direct avec le substrat, et ce pour différents substrats d'hydrophilicité croissante. Il est clair que la transition entre une structure prenant la forme d'une monocouche auto-assemblée (SAM) et celle d'une bicouche lipidique supportée (SBL) est continue pour des systèmes dans un état de contact proche. En effet, une proportion graduellement plus importante de chaînes aliphatiques se retrouve en contact direct avec le substrat plus le substrat choisi est hydrophobique.

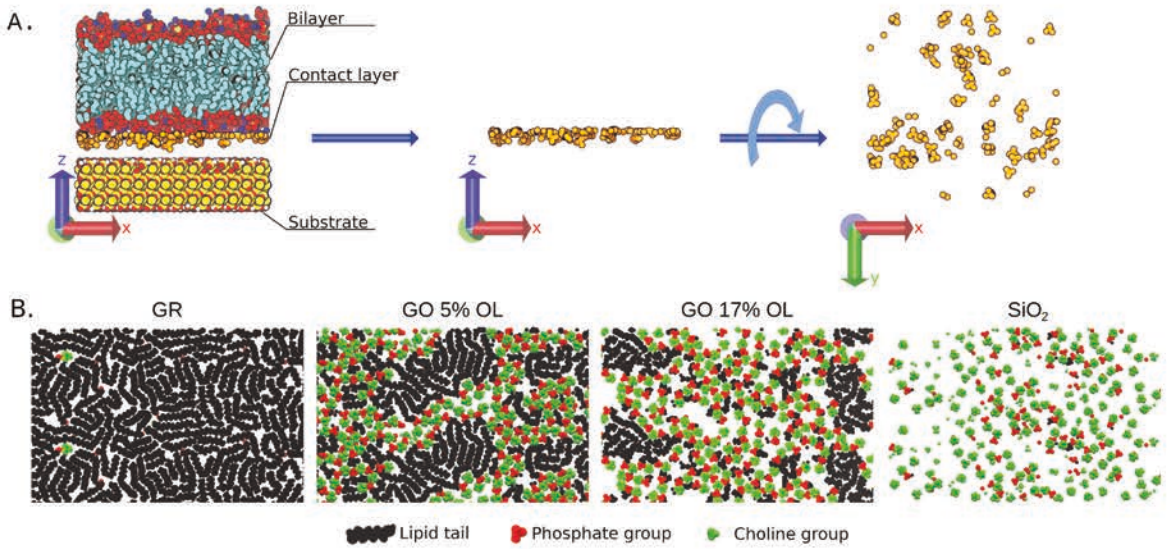

Figure 2: A. Représentation schématique du sous-groupe d'atomes sélectionné qui sont représentés en B (ci-dessous). B. montre des images provenant des simulations, dans le plan XY pour différents systèmes simulés avec la bicelle déposée. Les images montrent une vue en coupe de la bicelle sélectionnant les atomes à une distance inférieure à 6 Å du substrat.

II. Prédiction de l'énergie libre de déposition d'une membrane lipidique supportée

De sorte à vérifier et quantifier les observations mentionées dans la section précédente [1] et celles publiées par Vishnyakov et co-auteurs [2], nous avons cherché à établir un protocol pour la mesure du profil d'énergie libre de dépôt d'une membrane lipidique sur une surface. Il ne semble pas y avoir de travaux proposant une telle approche quantitative à l'heure actuelle, et celle-ci permettrait de 1. vérifier si les états de contact proche et lointain décrit dans la littérature existent, 2. comprendre comment ces états dépendent de l'énergie de surface et dans quelle mesure la composition lipidique de la membrane influe ce profil d'énergie libre, 3. prédire et caractériser l'influence d'un substrat sur un système lipidique, ce qui permettrait de guider le choix du substrat de sorte à conserver les fonctions biologiques de la membrane étudiée.

De sorte à étudier les interactions membrane-substrat, deux propriétés sont à noter. Tout d'abord, l'aire par lipide peut varier, en particulier pour des faibles distances entre membrane et substrat [1], [4]. Ensuite, l'eau à l'interface doit pouvoir être redistribuée vers le reste du solvant par un design approprié du système. En effet, il est évident qu'une relaxation de la quantité d'eau à l'interface lors du processus d'adsorption ne peut être modélisé par perméation passive au travers de la membrane, car ce processus est extrêmement défavorable du fait des chaînes d'acide gras présentes au sein de la membrane.

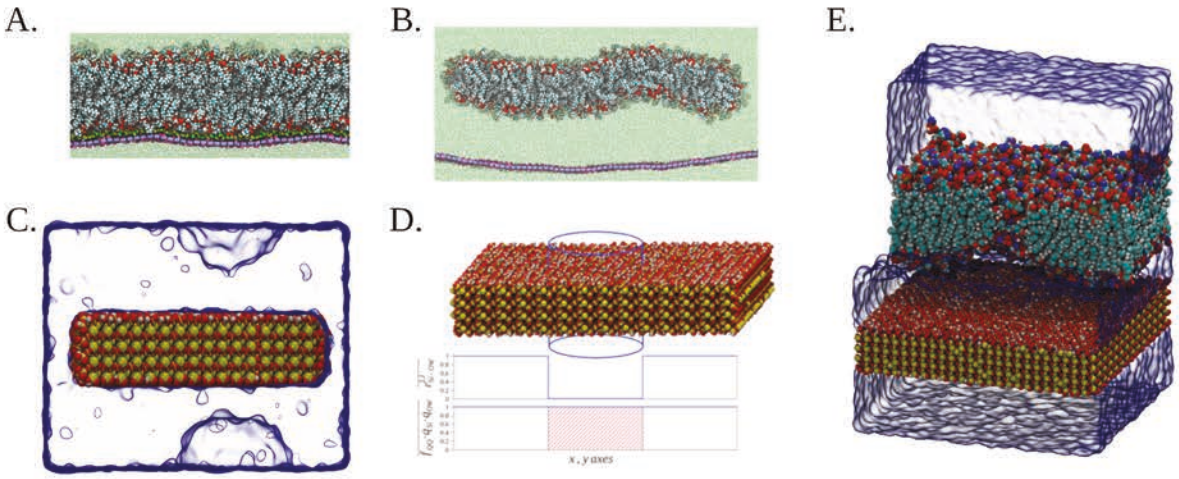

Figure 3: Représentation schématique de différents designs considérés pour étudier le phénomène de dépôt d'un système lipidique sur un substrat. A. membrane périodique sur une surface périodique en l'absence de pore au niveau de la membrane et du substrat, B. membrane semi-périodique (bicelle) sur une surface périodique en l'absence de pore au niveau de la membrane et du substrat, C. membrane périodique sur une surface semi-périodique en l'absence de pore au niveau de la membrane et du substrat, D. membrane périodique sur une surface périodique en présence d'un pore au niveau du substrat uniquement, E. membrane périodique sur une surface périodique en présence d'un pore au niveau de la membrane uniquement.

Plusieurs stratégies permettent de répondre à certaines de ces contraintes lors du design du système :

1. le dépôt d'une bicouche périodique (Figure 3 A.) sur une surface périodique constitue le système supposément le plus simple à créer dans l'optique de simulations par dynamique moléculaire. Cependant, ce système ne permet pas à l'eau présente à l'interface de se redistribuer librement au cours du processus d'équilibration. Qui plus est, l'utilisation d'une surface périodique implique que l'aire par lipide de la membrane est fixe tout au long de la simulation.

2. le dépôt d'une bicelle (Figure 3 B.), c'est-à-dire d'une bicouche lipidique semi-périodique sur une surface périodique, permet à la fois à la membrane d'adapter son aire par lipide, mais aussi à l'eau à l'interface d'être redistribuée rapidement au cours du processus d'adsorption. C'est l'approche principale utilisée lors de l'étude présentée à la section précédente. Cependant, plusieurs désavantages sont présent. Tout d'abord, le design n'optimise pas la taille du système. En effet, les coiffes lipidiques qui forme le bord de la membrane le long de sa dimension non-périodique interagissent potentiellement différemment de la zone éloignée de ces coiffes. Ainsi,

pour obtenir des analyzes aussi peu biaisées que possible par ces conditions aux bords spéficiques, la taille de la membrane est conséquente le long de la dimension non-périodique, entraînant un coût de calcul plus important. La conséquence indirecte de la géométrie de ce système est qu'il est davantage susceptible d'adopter des rayons de courbure faibles. Ainsi, le processus d'adsorption complet risque de ne pas être synchrone entre toutes les parties de la membrane. En plus d'impliquer des analyzes plus complexes du fait des courbures locales, ce comportement peut créer des poches d'eau qui ont du mal à se dissiper naturellement.

3. le dépôt d'une bicouche périodique sur une surface semi-périodique (Figure 3 C.) est une alternative à priori avantageuse à la solution précédente. En effet, si le système est couplée en pression de manière anisotropique, la taille de la boîte de simulation peut varier le long de la coordonnée selon laquelle le substrat est de dimension finie. Qui plus est, les conditions aux bords étant localisées dans le cas d'un substrat (contrairement à celui d'une bicelle), la taille du système reste contenue, ce qui n'affecte pas le temps de calcul. En outre, cette semi-periodicité joue le même rôle que dans le cas de la bicelle et permet à l'eau intersticielle d'être efficacement redistribuée. Cependant, de sorte à ne pas perturber la membrane et influer sur le processus d'adsorption, la taille de l'interstice (distance entre les bords du substrats) doit être contenu. Les multiples essais réalisés montrent que les interactions entre les bords du substrats sont extrêmement défavorables et ne permettent pas une equilibration du système. Ainsi, ce design ne pourrait être utilisée qu'en modifiant drastiquement la topologie du substrat de sorte à annuler les selfs interactions entre les bords de la surface. Cette opération étant complexe et difficile à justifier, il est préférable d'opter pour une solution alternative.

4. le dépôt d'une bicouche périodique sur une surface périodique présentant un pore (Figure 3 D.) est une alternative que nous avons considéré. Il existe peu de designs qui permettraient à la membrane de pouvoir ajuster son aire par lipide au cour du processus de dépôt. Soit la membrane est de taille inférieure à celle du substrat, au moins selon une dimension (cas 2), soit le substrat est de taille inférieure à la membrane, au moins selon une dimension (cas 3). Comme l'implémentation de ces designs ne permettait pas d'obtenir un système fonctionnel, au moment où ce travail

a été mené, il a été décidé de se focaliser sur un design permettant de faciliter la redistribution de l'eau interfacielle lors du processus d'adsorption. Une implémentation de ce design a été proposée par Roark e*t al.* [5]. De sorte à conserver des interactions aussi réalistes que possible entre membrane et substrat, nous avons décidé de ne pas appliquer de contraintes sur les atomes du substrat et de conserver les interactions intra-moléculaires. La création d'un pore physique est par conséquent un challenge important car cela implique d'obtenir une surface réaliste pour une portion de silica courbe. Pour éviter cette complexité, nous avons décidé de créer un pore virtuel où les interactions substrat-eau sont annulées. Malheureusement, s'il est bien possible d'annuler les interactions de type van der Waals pour une partie d'une molécule dans les différentes versions de Gromacs [6] alors utilisées, il n'est pas possible de faire cela pour les interactions électrostatiques. Ces interactions encore présentes ne permettent pas d'obtenir un système stable.

5. le dépôt d'une bicouche périodique présentant un pore sur une surface périodique (Figure 3 E.) a enfin été considéré. Bien que cette stratégie ne soit pas parfaite, elle a déjà été utilisée avec succès lors de plusieurs travaux [2], [7]–[9] et permet d'avoir un premier point de vue sur le processus de dépôt de système lipidique. De manière analogue au système précédent (4), ce design ne permet pas à la membrane d'adapter son aire par lipide, mais favorise bien la redistribution des molécules d'eau interfacielles. Comme l'implémentation de la variable collective utilisée pour le calcul du profil d'énergie libre de dépôt de la membrane utilise le plug-in Plumed [10], nous avons implémenté le potentiel appliqué sur la membrane pour stabiliser un pore avec ce même plug-in. Nous avons systématiquement testé plusieurs paramètres, en particulier plusieurs diamètre, de sorte à obtenir un pore aussi petit que possible de sorte à biaiser aussi peu que possible les interactions membrane-substrat tout en favorisant autant que possible un flux important de molécules d'eau pour permettre une relaxation rapide du système lors du processus de dépôt.

De sorte à calculer le profil d'énergie libre de dépôt d'une membrane sur un substrat, il nous faut définir une variable collective (CV) appropriée. La première hypothèse que nous avons formulé est basée sur les conclusions de l'étude précédente. En effet, le dépôt d'une membrane est intrinsèquement lié au nombre de molécules d'eau par lipide (en ne comptant

que les lipides du feuillet inférieur de la bicouche lipidique) présentes à l'interface substrat membrane. Pour implémenter ce type de CV complexe, Plumed [10] est le plug-in le plus complet à notre connaissance. Il se trouve que l'implémentation de ce CV ne semble pas possible au moment où nous avons réalisé cette étude, en utilisant ce plug-in. Ce CV est intrinsèquement relié à la distance entre la membrane et le substrat, aussi, nous avons décidé d'établir une mesure de cette distance comme une alternative au CV précédent. Bien que cette option ne soit potentiellement pas optimale, elle permet de créer un CV relativement simple pour décrire ce processus complexe. En effet, la distance membrane-substrat sera sans doute affectée différemment dans le cas où le nombre de molécules d'eau par lipide est faible, car les molécules restantes seront principalement celles participant à la solvatation des têtes lipidiques ou interagissant directement avec les groupes à la surface du substrat. La Figure 4 est une représentation schémtique du choix réalisé pour l'implémentation du CV. Si la distance mesurée est directement celle entre la monocouche inférieure et le substrat, la procédure de *steered molecular dynamics* (SMD) aura rapidement tendance à étirer la membrane, qui risque de se retrouver drastiquement hors équilibre. Le choix a donc été fait de définir le CV comme la mesure de la plus grande distance entre les phosphores du feuillet supérieur de la membrane et la surface du substrat. Il est clair que ce CV risque d'induire un hystéresis dans le cas du calcul d'un profil inverse (procédure de SMD depuis une membrane déposée vers une membrane libre flottante). Néanmoins, cela sera principalement dû au fait que la procédure inverse induit une élongation de la membrane. Ainsi, le profil de dépôt devrait être une bonne approximation du profil d'énergie libre réel et devrait permettre, en tout cas, d'identifier la présence de minima locaux.

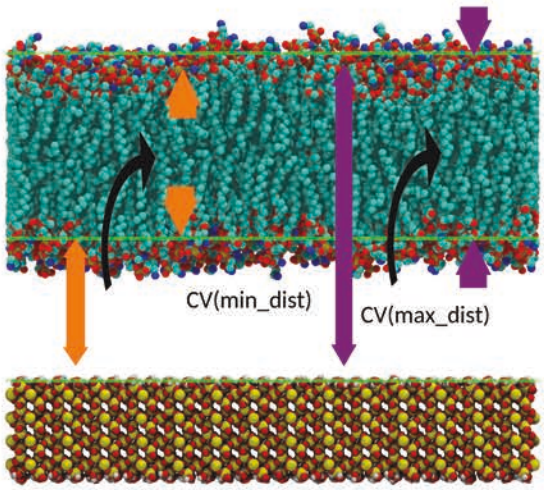

Figure 4: Représentation schématique du CV choisi. Le choix a été fait d'étudier le processus de dépôt de la membrane. La distance représentée par la double flèche orange pourrait induire une élongation de la membrane plaçant le système hors équilibre. Le choix a donc été fait d'utiliser la mesure représentée en violet de sorte à limiter cet effet lors de la procédure de SMD.

Afin de vérifier la faisabilité du calcul d'énergie libre, nous avons cherché à caractériser le temps caractéristique de relaxation du système vers l'équilibre. Nous avons caractérisé cet équilibre par une variation nulle du nombre de molécules d'eau présentes à l'interface. La Figure 5 montre l'évolution de ce nombre de molécules à l'interface dans le temps suite à une procédure de SMD. Il est clair que le processus suit globalement exponentielle décroissante, ce qui nous permet de caractériser le temps caractéristique permettant d'atteindre un équilibre. Nous avons ainsi pu déterminer que le système devrait être à l'équilibre pour des simulations de l'ordre de 200-400 ns par fenêtre d'*umbrella sampling* (US). Cependant, malgré des temps de simulations de cet ordre de grandeur, le profil d'énergie libre ne semble pas converger comme le montre la Figure 8.

Malgré les différentes difficultés rencontrées lors de cette études, plusieurs fortes conclusions sont à souligner. Tout d'abord, il est possible de simplifier davantage le design du système en ne prenant pas en compte les interactions liées du substrat. Cette étape, que nous menons actuellement, nous permet d'implémenter une version du système (4) où le susbtrat est restraint. Cela nous permet d'obtenir, pour des raisons techniques liées à l'utilisation de Gromacs, des performances bien supérieures (x20), qui rendent l'obtention d'un profil d'énergie libre de dépôt accessible en dynamique moléculaire. Ensuite, il semble clair que l'utilisation d'un pore au niveau de la membrane est risqué du point de vue des simulations, entraînant la membrane dans un état très éloigné de l'équilibre et rendant la convergence du profil d'énergie libre compromise.

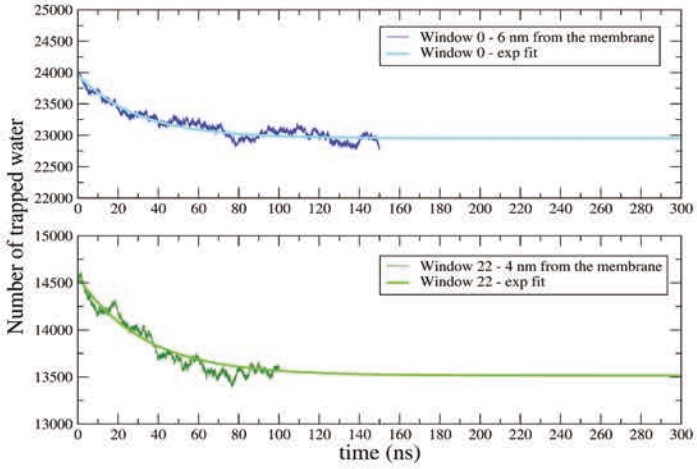

Figure 5: Evolution of the number of trapped water molecules at the interface between the membrane and the substrate with the simulation time for two positions of the center of the biasing potential following a SMD procedure

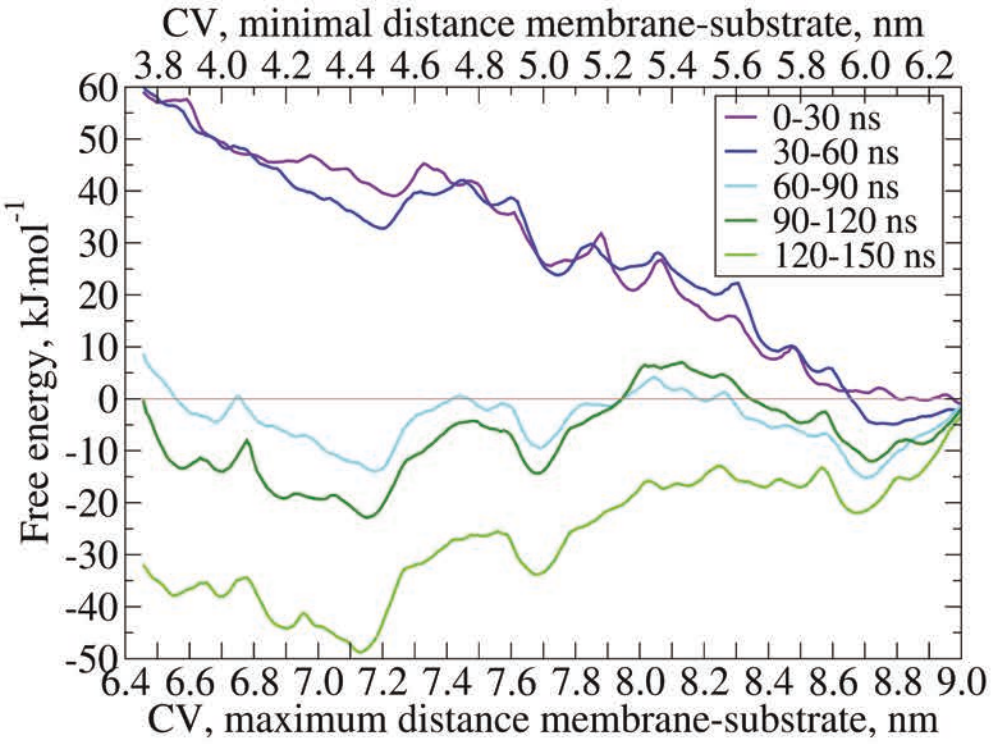

Figure 6: Étude de la convergence du profil d'énergie libre sur les 150 dernières nanosecondes de simulation par fenêtre de simulation pour une procédure d'US. La figure montre clairement qu'aucune convergence n'a été atteinte. Des calculs supplémentaires pour une petites portion du profil correspondant à une vingtaine de fenêtres a été réalisée pour des temps de simulation par fenêtre de 350 ns. Ces calculs ne montrent pas de convergence du profil d'énergie libre.

III. Mécanismes d'action d'antibiotique au niveau de la membrane externe de bactéries à Gram négatif

La membrane externe (OM) de bactéries à Gram négatif est connue pour son imperméabilité et sa rigidité en comparaison de celle de la membrane interne [11]–[13]. Il a été prouvé que la présence de cations divalents, calcium et magnésium, est essentielle pour le maintien de la stabilité de la membrane externe [14], [15]. Ces ions sont principalement localisés à proximité des groupes phosphates des LPS et sont connus pour former un pont entre les LPS, ce qui est un élément majeur stabilisant les LPS entre eux ; en su des multiples liaisons hydrogènes présentes entre les lipides [16]–[19]. Par conséquent, l'OM est particulièrement sensible à la concentration en ions divalents. Une plus faible concentration aurait tendance à accroître sa fluidité, ce qui pourrait ainsi permettre d'accroître sa perméabilité à diverses molécules d'intérêt biologique, en particulier à des antibiotiques. Inversement, une plus grande concentration en ions divalents peut avoir pour effet de « geler » la membrane, ce qui peut avoir pour conséquence de perturber localement la membrane. Expérimentalement, il a été montré qu'une fois dans cet état, l'OM était susceptible de permettre à de larges protéines ou à de l'ADN de perméer [11].

Différentes molécules, dont l'acide éthylènediaminetétraacétique (EDTA) et les peptides antimicrobiens cationiques (AMP) ou antibiotiques peptidiques, perméabiliseraient l'OM en agissant sur ces ions divalents [20]. En particulier, deux polymyxines, les polymyxines B et E (colistine), qui sont des lipopeptides, sont actuellement utilisées comme antibiotiques de dernier recours contre les bactéries à Gram négatif. Leur mode d'action est encore sujet à discussion [21], [22], cependant leur efficacité est semble être liée à leurs interactions avec les ions divalents présents dans les régions core et lipide A des LPS. Il a été émis l'hypothèse que les polymyxines peuvent affaiblir les interactions LPS-LPS en supprimant le pont formé par les cations divalents conduisant soit à la perturbation de l'OM (complète ou partielle), soit à sa perméabilisation [15]. Il a été démontré que la présence de polymyxine B1 (PMB1) augmentait la teneur en eau dans la région des sucres de l'OM, ce qui pourrait être une conséquence de la diminution des interactions LPS-LPS [15]. Jiang *et al.* [23] ont montré que la présence de PMB1 affecte la densité des ions dans le noyau interne et externe du LPS.

Si le mode d'action de la colistine a été largement étudiée, et que de nombreuses études *in silico* ont été menées [24], il n'existe, à notre connaissance, aucune observation quantitative de ses effets avec des ions divalents à une résolution moléculaire. Dans cette partie, nous proposons d'abord une nouvelle variable collective qui n'affecte que les ions divalents au voisinage d'un peptide adsorbé, afin de quantifier la facilitation de leur déplacement provoquée par ce peptide. Pour cela, nous calculons le profil d'énergie libre permettant de créer un défaut local d'ions divalents, et ce pour deux systèmes : l'un contenant de la colistine et l'autre en l'absence de colistine.

Pour ce faire, nous utilisons un modèle gros grain des LPS (RAMP) implémenté pour le champ de force Martini [25] qui se base sur un LPS muté présentant le noyau entier (*i.e.* les parties interne et externe du noyau) mais pas d'antigènes O. Ce modèle est beaucoup plus réaliste que l'utilisation d'un modèle dit « deep rough » du LPS (le modèle REMP par exemple) ou de l'usage du seul lipide A, car il est connu que de telles mutations du LPS in vitro ont des conséquences drastiques sur la perméabilité membranaire [11]. De plus la membrane modèle que nous utilisons est celle d'une bicouche asymétrique où le feuillet interne est composé de POPE, et non d'une membrane LPS symétrique qui ne correspondrait pas non plus à la réalité. Cette première partie permet de quantifier la teneur en ions divalents au voisinage de la colistine, ce qui serait difficile sans des méthodes d'échantillonnage améliorées, du fait de la rigidité de la membrane et de la présence de nombreux groupements chargés qui conduisent *in fine* à la présence de nombreux potentiels états métastables.

Nous avons proposé une variable collective permettant de suivre la création d'une inhomogénéité locale de la distribution en ions divalent au sein de la membrane. Cette variable collective défini un cylindre transversal à la membrane et centré dans la boîte de simulation. La variable collective est définie comme le nombre d'ions divalents (calcium) présent dans ce cylindre. Les profils d'énergie libre calculés à partir de cette observable (Figure 7) montrent d'une part que la présence que de colistine adsorbée sur les modèles gros grains a tendance à limiter la propension à ces ions de créer une inhomogénéité.

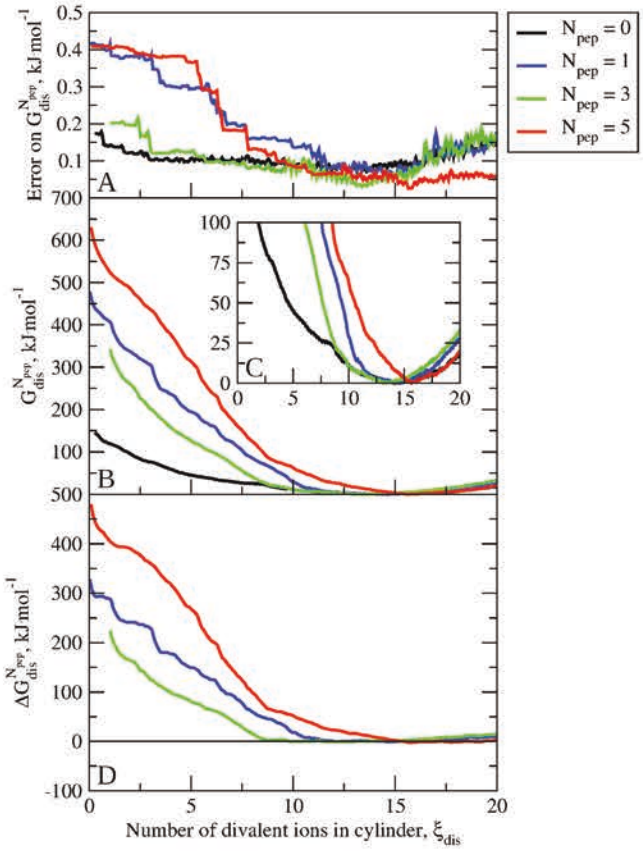

Figure 7: Résultats des calculs d'énergie libre montrant en A. l'incertitude sur l'énergie libre, en B. les profils d'énergie libre pour différentes concentration en colistine, et en C. la différence d'énergie libre entre les profils liés aux systèmes contenant de la colistine et celui lié au système sans peptide.

En outre, l'analyse des simulations réalisée en utilisant le champs de force Martini montrent que la création d'une inhomogénéité contribue à changer drastiquement les propriétés membranaires. En particulier, ce qui semble être une transition de phase a été observé. En outre, la présence de colistine a tendance à amplifier cette observation.

Finalement, nous avons aussi modélisé la membrane externe en utilisant un champs de force tout atome, CHARMM36. Nous avons ainsi étudié deux aspects conjointement. Le premier est l'influence de deux paramétrisations des groupes phosphates correspondant à deux états de protonation. Suite à cette analyse, il semble que le champ de force Martini reproduise des résultats proches de ceux associés à une charge nette de -2 pour les groupements phosphates, qui a été critiquée du fait qu'elle correspondrait à un état de protonation dans un milieu plus acide que les milieux naturellement rencontrés par les bactéries. Cependant, le débat au sujet de l'état de protonation des groupes phosphates des LPS n'est pas encore clôt, aussi il convient de prendre des précautions sur les conclusions à donner. Enfin, la seconde partie de

cette étude second aspect concerne la modélisation de deux modèles liés à des mutations associés à des mécanismes de résistance, en particulier aux polymyxines.

Introduction

Lipid membranes play a fundamental role in life of all alive organisms: it protects cell content, helps maintaining homeostasis of the cell, and its semipermeability is used for addressing drugs intracellularly and to study communication between the cells. That is why lipid membranes are involved in such a wide variety of research areas, continuously through the past century. Not only membranes drastically vary in lipid content, but biological membranes are also complex in their shapes and dynamics. The three taxonomic domains – namely the Archaea, the Bacteria, and the Eucarya – have distinctive biological membrane structures and compositions.

Since the emergence of antibiotic resistance through many species of bacteria, the need of developing new types of antibiotics arose. As the structure of cell membranes are highly conservative, it can be advantageously used as a target for new therapeutics. However, the striking differences between the cell envelopes of Gram positive and Gram negative bacteria leads to the development of specialized drugs. Indeed, the thick layer of peptidoglycans above the cell membrane in Gram positive bacteria and the stiff outer membrane exposing a leaflet of lipopolysaccharides in Gram negative bacteria are two different challenges to face. In this work we are focusing on Gram negative bacteria, as they present a real challenge for modern antibiotics due to their outer membrane (OM).

To study the interactions between membranes and any molecules of biological interest experimentally, it is customary to use model membranes, which allow to exert more controls on the range of observables affecting the measures. Model membranes allow to control such lipid structure and composition, lipid phase state, membrane curvature, presence or absence of proteins, and the exposition to any drug or environment. To make model membranes more stable and less mobile, which is necessary for experiments such as atomic force microscopy (AFM), X-ray reflectometry or neutron scattering, there is a need for immobilization of the lipid structures, leading to a wide category of model membranes – namely supported lipid membranes (SLBs) and self-assembled monolayers (SAMs).

While using SLBs, it is important to take into consideration the type of substrate for the deposition which is known to have influence on various membrane properties, including the lateral diffusion, rate of flip-flopping, the thickness of the bilayer, the symmetry/asymmetry between monolayers, *etc.* It is crucial, while using such methods, to ensure that the SLB or SAM preserves the biological functions of the real biological membrane – especially if this membrane is interacting with other components such as proteins or drugs. Hence, there is a need to obtain a better understanding, at the molecular level, of the interactions between substrates and membranes, in order to predict which system would be optimal for measurements, *i.e.* which pair substrate-membrane would lead at the same time to a stable membrane and to a minimum effect on its functions. Through this work, we made use of molecular dynamics (MD) simulations, both at the all-atom (AA) and coarse-grained (CG) level, to address such questions.

SLBs are used to study a wide range of properties, including membrane structural, physical and chemical properties, interactions with proteins, or translocation or pore formation of potential drugs through the membrane. In this work we address the influence of substrate hydrophilicity / hydrophobicity on the bilayer structural properties, such as its general shape and thickness, and the collective effects on the lipids. We address the electrostatic origin of these interactions between the substrate and the SLB. One element which greatly contributes in the preservation of the SLBs biological functions is the presence of interfacial water between the substrate and the lower leaflet of the deposited structure. We made an extensive literature analysis and subsequently studied the influence of the interfacial water thickness on membrane properties. In order to address a wide variety of substrates, we made the use of the variety of oxidation levels on graphene oxide (GO) substrates. By tuning the oxidation level of the GO we were able to tune the hydrophilicity of the substrate. To compare our results with the many experimental results, we also included silica in the set of studied substrates. In our study we used a simplified bilayer model, containing DOPC lipids only. Such bilayer with all its simplicity allows to focus on structural properties only without taking into consideration all complexities of membrane asymmetry. However, as a first model, we wanted to use a simple zwitterionic phospholipid as the inner leaflet of bacterial membranes is mainly composed of such lipids. In the perspective, it is really important to model correctly an envelope of Gram negative bacteria with both outer and inner membrane (IM) to study their interactions with potential antimicrobials in their deposited state.

At the date of the work, there was no consensus on the thickness of the interfacial water layer. This layer is of major importance as it contributes to the screening of the substrate interactions. It is thus one of the process which controls the balance between the stability of the membrane, and its structural integrity. The literature shows two contrasting measurements which we will refer to as close-contact and far-contact states in this work. To address the question about the existence of the both states and on the properties which drive a SLB to stabilize preferentially in one or another, we studied free energy of the deposition of lipid membrane. To do so, we implemented unique methodologies both at the all-atom and coarse-grained scales.

It is widely accepted that with a correct choice for both the deposition method and the substrate type, the lipid membrane properties – especially for the outer monolayer – are close to free floating lipid membranes. To simplify the MD set-up, we used simple solvated bilayers as models for studying OM-drug interactions. In the present time, the only class on antibiotics available on the market, which targets particularly the OM of Gram negative bacteria are polymyxins. These cyclic lipopeptides are widely used nowadays as last resort antibiotics due to their high toxicity and to avoid growth of resistance rate. At the same time, their precise pathway is still actively studied as many factors are still unknown.

As both IM and OM – and especially their lipid content – can be a target of choice for innovative antibiotics including for instance antimicrobial peptides (AMPs), we want to study the interactions of some polymyxins with the OM to understand if some mechanisms are transposable to other drugs. Indeed, as we mentioned above, crossing the OM is one of the main challenges for drugs targeting Gram negative bacteria. Hence, designing AMPs which lower the permeability barrier of the OM of such bacteria could greatly contribute to their efficiency. One of the most accepted mechanisms of polymyxins is to interacts with divalent ions in the core and lipid A regions of the LPS of the OM. In this work we studied influence of colistin (polymyxin E) on calcium ions displacement. One of the high concern in the present days is the raise of observed resistant strains to last-resort antibiotics. Polymyxins are no exception to this raise and several mutations of the LPS are attributed to the resistance mechanisms. We modeled two membranes which are associated with decreased polymyxins sensitivity. To underline the importance of calcium ions and their

parametrization, we studied this topic with means of both AA and CG MD, since they use different phosphates (binding place of calcium ions in LPS) charges assignments.

Sections Lipid membranes, Supported lipid structures, Antibacterial drugs, Molecular dynamics form the first part of this manuscript. They draw the link between the biological systems and the models that are used in the present work, and detail the numerical methods which are applied to simulate these systems. The second part of this manuscript details the results of the work. Section Influence of substrate hydrophilicity on structural properties of deposited lipid structures details the work related to the reshaping and changes of properties of SAMs and SLB depending on the type of substrate and its associated surface energy. Section Free energy of deposition of lipid membranes on solid substrates introduces new methodologies to compute the free energy of adsorption of SLBs. Section Antimicrobial drugs facing the outer membrane of Gram negative bacteria addresses the pathway of colistin in the OM of Gram negative bacteria and draws directions to transfer these mechanisms to AMPs. Finally, section Conclusions and Perspective gives general conclusions on the present work and opens towards the development of AMPs capable to interact with both the OM and the IM of Gram negative bacteria so that, on the one hand, the availability of those peptides will be high on the IM, and, on the second hand, that they would efficiently rupture the IM, *e.g.* by means of pore formation.

Part I – context, theory, and methods

Lipid membranes

The major cornerstone in the understanding of lipid membrane structures comes from the fluid mosaic model, which was proposed by Singer and Nicolson [26] in 1972. However, with all the importance of this model, this was not the first study of the structure of cell membranes through the centuries. For example, osmotic studies on the red blood cells (RBC) by William Hewson in 1773 with help of microscopy were able to show osmotic swelling and hemolysis in presence of an excess of water in the environment around the erythrocytes [27]. These experiments with water, serum and saline solutions implied that RBC are permeable not only to water, but also to the hemoglobin molecules, which defined them as vesicles with liquid content, where cell membrane had different structure from the intracellular content. However, membranes were falsely attributed the property of defining the cell shape [27]. Almost 70 years later C.H. Schultz was able to visualize the plasma membrane with iodine and was able to estimate its thickness – about 220 Å [28]. This brought Charles Ernest Overtone to his major work on membranes permeability in 1899, as, until that time, cell membranes were considered permeable only to water molecules[1] [28]. He introduced what is now known as the Overton biomembrane model which introduced the hypothese that cell membranes are made of lipids. He stated that the lipid from cell membranes could be similar to phospholipids or esters. It is interesting to mention that the leading theory of membrane content at the time was protein-based, due to the suggestions that cell membrane and vacuolar membranes could fuse thanks to their common properties (Pfeffer 1891) and due to the study of Ramsden in 1904 where he demonstrated spontaneous formation of solid films on the air-protein solution interface [29]. The direct proof that biological membranes are made primarily out of lipids came in 1925, when the study by E. Gorter and F. Grendel was published [30]. In their work, they extracted the lipid content from a sample with a known number of RBC. They spread the lipids as a monolayer using a monolayer trough to measure the total surface area of that lipid content. Taking into account

[1] Those conclusions came from the experiments lead by Nageli and Cramer which showed that anthocyan did not diffuse through plant cells and from the work by de Vries which did not show the permeation of the sucrose of beet roots though cell membranes [29]

the disc shape of RBCs, and knowing the number of cells in the initial sample, they found that each cell was made of 2 lipid monolayers. Hence, they proposed the first model of the lipid matrix of cell membranes under the form of a lipid bilayer.

The Danielli-Davson model (1935) [31] introduced the presence of proteins adsorbed on the lipid bilayers, hence answering some of the concerns regarding the biological functions of a membrane made out only of lipids. However, at the moment of this work, only globular proteins were known, so in this model proteins are only attached to the lipid surface.

In the light of those improvement, it is easier to get why the fluid mosaic model changed so much. Singer and Nicolson proposed with this model that proteins were incorporated into membranes inhomogeneously, and more importantly, that the membrane was considered changing, fluid and dynamic, with free lateral diffusion of lipids and proteins.

The emergence of the concept of lipid domains in 1982 [32] drove to focus on lipid-lipid interactions, leading to the discovery of the affinity of sphingomyelin (SM) for cholesterol. These discoveries were later driving to the hypothesis of the so-called lipid rafts which was made by Simons in 1997 [33]. Lipid rafts are hypothetical SM-rich and cholesterol-rich microdomains which flow in lipid matrix [34].

The present work focuses on the interactions between models of the lipid matrix of biological membranes of bacteria with antimicrobial peptides. To give a better insight in the properties of such membranes, we describe briefly their general constituents – the lipids, in a first section of the present chapter, and, in a second section, we expose the current knowledge of the composition of bacterial membranes.

IV. General properties

Despite having no covalent bonds holding lipids together, membrane form very stable structures, thanks to the amphiphilic properties of the lipids. Hence, bilayers form spontaneously in aqueous environment thanks to the hydrophobicity of the hydrocarbons of lipid tails. This hydrophobicity comes from the fact that no hydrogen bonds can be formed between water and lipid tails. In the meantime, the lipid head groups interact favorably with water thanks to their polar nature as well as with one another – which increases membrane stability. In addition to the hydrophobic effect, lipid tails avoid the water cage which restricts their motion to increase their entropy. The van der Waals interactions – which is a

result of induced dipoles that form between very close molecular surfaces as in the case of densely packed acyl chains – also plays a preponderant role in maintaining the lipid bilayer structure [28]. Figure 8 shows a schematic representation of some of the main contributing interactions which result in the spontaneous formation of stable lipid structures in an aqueous environment.

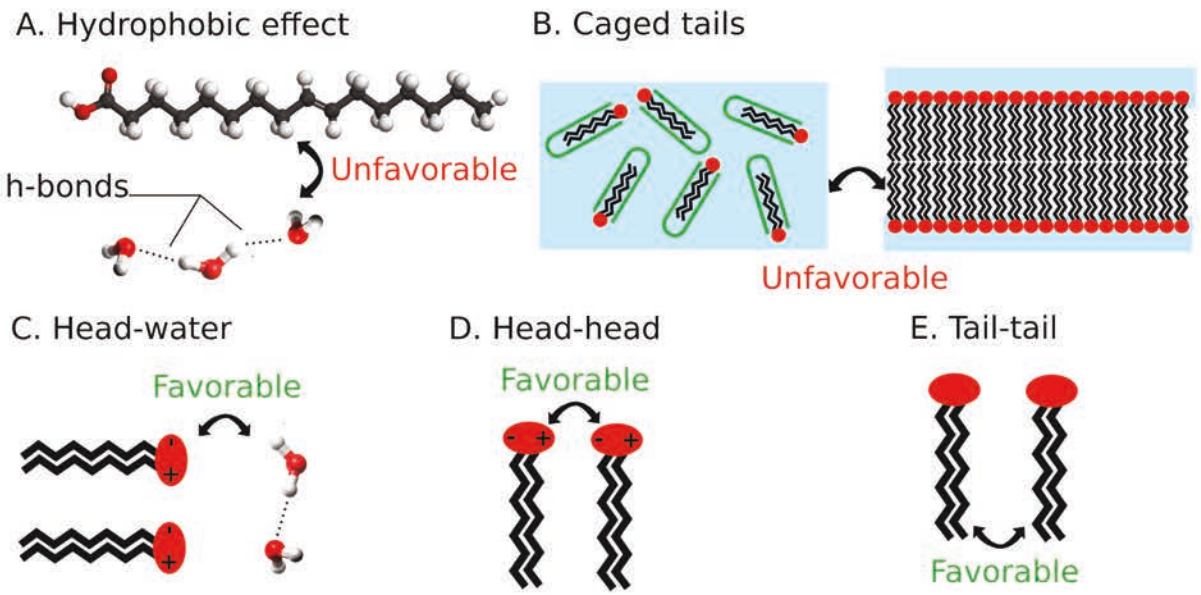

Figure 8: Schematic representation of some of the main contributions of the interactions in between lipids and between lipids and water which are at the origin of the spontaneous formation of stable lipid structures such as lipid membranes, micelles, or vesicles.

Lipids can be classified in several ways depending on their chemical structures, as an example Fahy *et al.* [35] defines eight major categories which each have numerous subclasses[2]:

1. Fatty acids
2. Glycerophospholipids
3. Glycerolipids
4. Sphingolipids
5. Sterol lipids
6. Phenol lipids

[2] For instance, the glycerophospholipids have 21 proposed categories, which describe the variety of head groups

7. Saccharolipids

8. Polyketides

In the present work, we focus on glycerophospholipids (commonly referred to as phospholipids), as they are the major class of animal membrane polar lipids. Four major phospholipids predominate in the plasma membrane of many mammalian cells: phosphatidylcholine, phosphatidylethanolamine, phosphatidylserine, and sphingomyelin [36]. They are composed of one glycerol, one phosphate, two fatty acids, and an alcohol [Stillwell]. It is common that one tail has one or more cis-double bonds while other tail is fully saturated. Differences in the length and saturation of the fatty acid tails influence the ability of phospholipid molecules to pack against one another [36].

i. Phase transition

The fluidity of lipid bilayer depends on both composition and temperature. The phase transition from a liquid phase to a liquid crystalline phase markedly affects lipid properties, including their diffusion coefficient and the order of their tails. It is noteworthy that the transition temperature between those phases is very different from on lipid to another and is mainly affected by three factors: the acyl chain length, the degree of unsaturation of these tails, and the precise composition of the lipid membrane.

Along with changes of temperature or other sources of energy added to the system, *trans*-configuration of C-C bond denoted as A in Figure 9 is transitioning to *gauche* one (B in Figure 9), while crossing a transition state referred to as *eclipsed* state (C in Figure 9). This reshaping of lipid tail structure is referred as *gauche* kink and it results in melting. This way lipid membrane goes from the gel phase to liquid phase. As a result, area per lipid increases and membrane becomes more fluid and permeable [28].

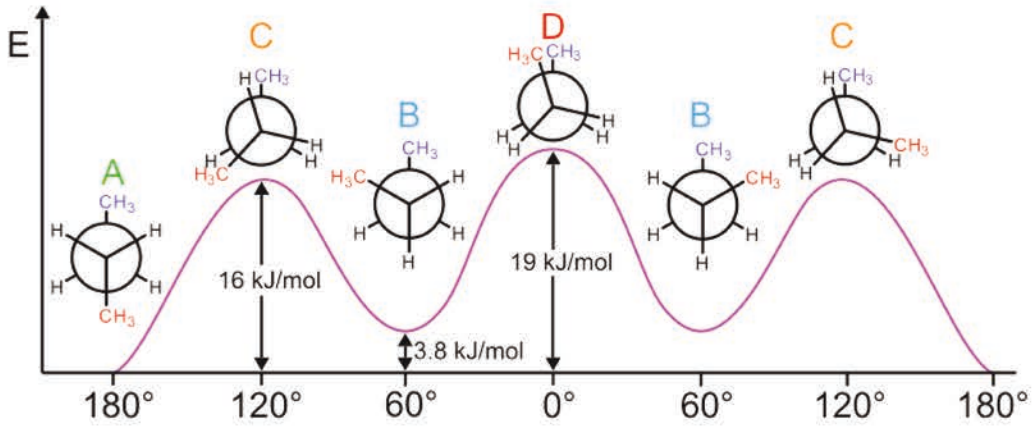

Figure 9. Relative conformation energy diagram of butane as a function of dihedral angle. A: antiperiplanar, anti or trans. B: synclinal or gauche. C: anticlinal or eclipsed. D: synperiplanar or cis .

ii. Membrane asymmetry

Another important feature of biological membrane is their asymmetry on various levels: protein, carbohydrate and lipid ones.

One of the examples of protein asymmetry was shown by Fernandez-Moran, who showed with EM imaging that ATPases in a mitochondrial elementary particle (EP) face only inward for the mitochondrial inner membrane and the bacterial plasma membrane, and outward for the thylakoid while no ATPase was found to face in both directions simultaneously [37].

Sugar asymmetry where carbohydrates are 100% asymmetrically distributed across the membrane with sugars always facing the outside was proven many times with lectin-based imaging studies [38].

At the same time, lipid content is also not evenly distributed, for instance, in the human red blood cell membrane, almost all of the lipid molecules that have choline in their head group are in the outer monolayer and terminal primary amino group containing lipids – such as phosphatidylserines – are in the inner one [39]. Such and many others examples of asymmetry come from the fact that many cytosolic proteins have specific binding sites in peculiar head groups, moreover plasma membrane asymmetry allows animals to distinguish dead cells from alive ones: the phosphatidylserine exposed on the cell surface serves as a signal to induce neighboring cells to phagocytose the dead cell and digest it [36], [40].

iii. Lipid diffusion

Lipid membranes have two characteristic types of lipid diffusion: lateral and trans-membrane (flip-flop) ones. Since the Frye-Edidin experiment in 1970, which concluded that "the cell surface of heterokaryons is not a rigid structure, but is 'fluid' enough to allow free 'diffusion' of surface antigens" [41], fluorescence recovery, single particle tracking and other studies were performed to study in details diffusion rates. Phospholipid diffusion was shown to be mainly independent of the head group, but impacted by membrane phase and presence of cholesterol [28].

Flip-flop, on the other hand, is a much more complex process, as thermodynamically unfavorable events must occur: tails should be exposed to water and polar head groups must be exposed to the hydrophobic membrane interior, but occurring rate can be increased by transmembrane protein incorporation [42]. With all mentioned above, it was clear that spontaneous flip-floping is not enough to create membrane asymmetry as we know it, so M. Bretscher in 1972 [43] suggested existence of flippases – lipid translocator proteins. Now this term is used only for those moving lipids into inner leaflet and floppases refer to the opposite process. Moreover, the class of scramblases was distinguished for proteins which move lipids bi-directionally across the membrane without use of ATP [28].

Altogether, these two aforementioned motion types (flip-flop and lateral diffusion), along with rotational movement around the longitudinal axis of the molecule describe the membrane fluidity. Various environmental factors, such as pressure, temperature, pH and ionic strength influence membrane viscosity thus changing fluidity [28].

V. Bacterial envelope

Unlike cells of higher organisms, bacteria face an unpredictable, dilute and often hostile environment and, in order to survive, have evolved a sophisticated and complex cell envelope, *i.e.* with the membrane(s) and the related structures that surround and protect the cytoplasm [44]. Such important properties as the cell shape, rigidity, or resistance are given to bacteria by their envelope, which is crucially important for growth, division, and horizontal genes transfer [45]. The essential nature of the cell envelope makes it vulnerable to small molecules that bacteria deploy when competing for resources, which is the

foundation of antibiotic therapy. The cell envelope remains a popular target in the search for novel therapeutics to combat the rise in multi-drug resistance [45].

In general, the bacterial cell envelope comes in two types: that of Gram negative bacteria which have inner and outer membranes separated by the periplasm which contains a thin cell wall of peptidoglycans, and that of Gram-positive bacteria which have only a cytoplasmic membrane surrounded by a much thicker peptidoglycan layer (Figure 10) [45].

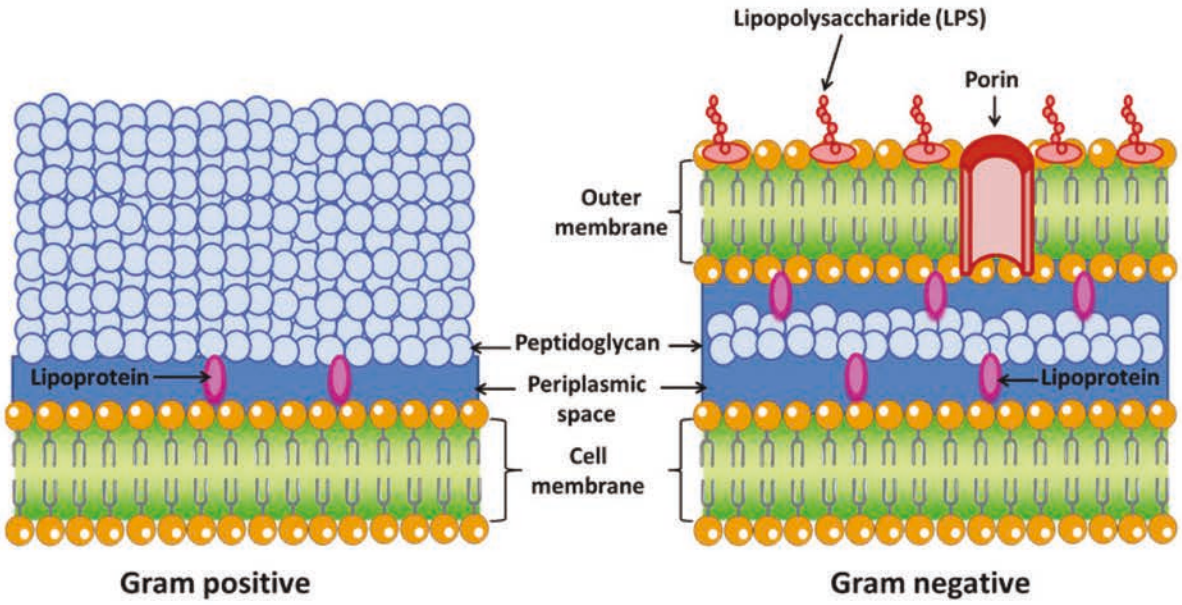

Figure 10. Differences between Gram negative and Gram-positive bacteria [Bacteria-Assisted Transport of Nanomaterials to Improve Drug Delivery in Cancer Therapy - Scientific Figure on ResearchGate. Available from: https://www.researchgate.net/figure/Differences-between-Gram-negative-and-Gram-positive-bacteria_fig2_357901900 [accessed 4 Jun, 2023].

This separation is coming from the Gram stain or Gram's method, one of the most used staining procedures in microbiology and bacteriology in particular. Created initially as a way to stain bacteria differently from the studied tissue by using Crystal Violet (Gentian Violet) as the primary stain, an iodine solution as a mordant followed by treatment with ethanol as a decolorizer, this procedure leaves the nuclei of eukaryotic cells unstained, while bacteria are colored blue/violet (Figure 11).

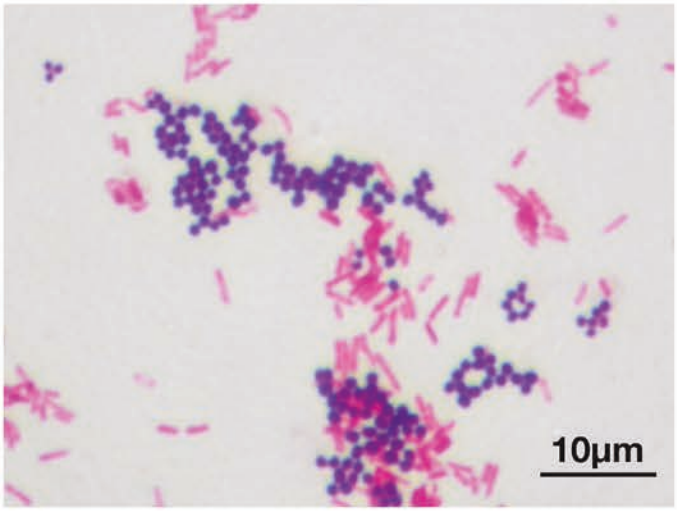

Figure 11. Microscopic image of a Gram stain of mixed Gram-positive cocci (Staphylococcus aureus ATCC 25923, purple) and Gram negative bacilli (Escherichia coli ATCC 11775, red). [Source: https://commons.wikimedia.org/wiki/File:Gram_stain_01.jpg]]

Only later Gram found that some bacteria (he showed it on Typhoid bacilli) were decolorized. Now the species which undergo decolorization are called Gram negative, while those stained blue/violet are called Gram-positive. Most animal and plant cells stain Gram negative, while certain yeasts, bacteria and molds have the ability to retain the primary dye. It should be noted that some bacteria show a mix of pink and violet cells called a Gram-variable pattern, which can come from the sensitivity of cell walls while cell division, a decrease of peptidoglycan layer thickness during growth, or an aging culture. *Acinetobacter spp.* often appear Gram-positive, even though, structurally, their cell wall is Gram negative, and *Mycobacterium spp.* are not stainable with these dyes, even if these bacteria are considered Gram-positive. However, even with all those weaknesses Gram's method remains the initial diagnostic test to evaluate infections and to find the appropriate antibiotics to use thanks to its rapidity and low cost [46], [47].

As far as membranes play an important role in protecting the intracellular biological material, hosting transport proteins and other important functions, it is critically important to know their composition and physical properties. Our understanding of the structure and function of biological membranes has been guided by the classical fluid mosaic model of Singer and Nicolson [26]. As mentioned above, the cell membrane was defined as a two-dimensional liquid in which lipids and embedded proteins are free to diffuse laterally, thus resulting in a largely homogeneous structure [48]. Membranes are formed mostly by

glycerophospholipids (GPL), such as phosphatidylethanolamine (PE), phosphatidylglycerol (PG), cardiolipin (CL), lysyl-phosphatidylglycerol (LPG), phosphatidylinositol (PI), phosphatidic acid (PA) and phosphatidylserine (PS), but also bacteria-synthesized lipids without phosphate group in their head group, such as ornithine lipids (OLs), sulfolipids, or hopanoids (HOPs). Not only bacteria have a general membrane composition differing drastically to eukaryotes, but they are also characterized by an incredible flexibility relatively to this composition.

Indeed, bacteria could change the composition of their membranes to adapt to the environment. These changes could be triggered by a variety of variables including the level of nutrients, the pH, the oxygen level, the temperature, the accumulation of metabolites inside the cell, the pressure, *etc*. The membrane lipid modifications occurring can be divided in two types:

1. Existing lipids can be modified to obtain a membrane with different properties; for example, the anionic lipid PG can be changed into the cationic lipid LPG by the simple transfer of one lysyl group. This modification of preexisting membrane lipids has the advantage that it allows a quick response to changes in environmental conditions.

2. Existing lipids are degraded and lipids are synthesized *de novo* replacing the old lipids.

All above-mentioned factors show the importance of the knowledge of the composition of bacterial membranes. For many years *E. coli* was the main model organism for bacteria but the need to access to a more precise view of the bacterial lipodome has arisen.

Through all species of bacteria, the so-called ESKAPE group especially distinguishes. This group is named after highly pathogenic bacteria which show increasing multi-drug resistance and includes the following species: *Enterococcus faecium, Staphylococcus aureus, Klebsiella pneumoniae, Acinetobacter baumannii, Pseudomonas aeruginosa, and Enterobacter* spp. It is a nonhomogeneous group which embeds both Gram-positive and Gram negative species. In order to model their cell envelopes to design new therapeutic strategies, one shall know their membranes composition.

Table 2. An overview of the lipid content of ESKAPE bacteria and their envelope based on the literature

Species	Phospholipid composition	Fatty acids	Literature source
Enterococcus faecium	CL 44.5%; PG 23%; LPG 32.33%	1: C18:1 81.72%; CPA-C19:0 9.24%; C16:0 8.22%	1: [49]
Staphylococcus aureus	1: Newman strain: CL 22.5%; PG 43.1%; LPG 30.1% 2: S. aureus 209 P at stationary phase: PG 65.9%; CL 13.7%; LPG 10%	3: C aneiso-15:0 around 45%; C aneiso-17:0 around 20%; C iso-15:0, C iso-17:0, C 18:0, C aniso-19:0 each around 5% 4: for CL 14:0 22.2%, 15:0 24.6%, 17:0 15.6%, 16:0 12.1%, 22:0 12.3%; for PG 15:0 51%, 17:0 23.2%, 19:0 13.9%; for LPG 15:0 37%, 17:0 25%, 19:0 13.5%.	1: [50] 2:[51] 3: [52] 4: [51]
Klebsiella pneumoniae	1: Cl 6%, PG 5%, PE 82%.	2: C16:0 41.9%, C17:0 Δ9 24.53%, C19:0 Δ9 13.34%, C14:0 12.42%	1: [53] 2: [54]
Acinetobacter baumannii	1: CL around 45-50%, PE around 20%, LCL around 15%, PG around 10%	2: Main fatty acids are C16:0 and C18:1; C16:1 and C18:0 are also present plus minor amounts of C17:0, C17:1, C15:0, C14:0 and C12:0 in order of abundance	1: [55] 2: [56]
Pseudomonas aeruginosa	1: PE 70.8%, PG 11.8%, BMP 8.4% 2: PE 77%, PG 20%, CL 3% 3: PE 71.6%, PG 11.8%, PC 7.9%, PA 2.4%, LPC 3.9%	4: 16:0 35%, 19 ∇ 30%, 18:1 15% 5: C 16:0 45%, C18:1 34.2%, C 16:1 6.3%, C 19:0cyc(11,12) 6.3%	1: [57] 2: [58] 3: [59] 4: [57] 5: [60]
Enterobacter spp.	PE 74%, PG 21%, CL 3%		5: [53]

The analysis of the literature (Table 2) shows that, at the moment, even for so important bacterial species as the ESKAPE pathogens, there is not enough information to draw a precise picture of the bacterial envelope. The values reported do not distinguish the different membranes of the cell envelope, the distribution of fatty acid is not related to the precise lipid strains or even species, and seldom studies characterize the lipidomics extensively. Also, there are almost no lipidomics studies which report well and precisely the characteristics of the head groups and fatty acids at the same time with the same conditions and for the same strain, to make it be possible to combine those data together.

i. Gram negative envelope

For Gram negative bacteria there are three principal layers in the envelope for which chemical composition and physical nature differ very markedly: the outer membrane (OM), the peptidoglycan cell wall, and the cytoplasmic or inner membrane (IM) [44]. The cytoplasmic membrane is an important interface for the cell envelope because the structural components of the cell wall are synthesized and assembled there [61]. Bacteria lack intracellular organelles, and consequently, the membrane-associated functions of all of the eukaryotic organelles are performed in the IM. Many of the membrane proteins that function in energy production, lipid biosynthesis, protein secretion, and transport are conserved in bacteria, but their cellular location is different. In Gram negative bacteria, these proteins are located in the IM [44]. The inner membrane was long believed to be a typical symmetric GPL bilayer [62], where phospholipids maintain the barriers' permeability for hydrophilic molecules and support the functions of the IM proteins [63]. However, Bogdanov *et al*. [64] show – for a variety of cells of different shapes – that PE and CL are distributed asymmetrically in the IM, moreover, the control over PE asymmetry is crucial for bilayer properties.

Inner and outer membranes are separated by the periplasm – an aqueous cellular compartment densely packed with proteins. Periplasm and cytoplasm are structurally strongly different. The periplasm is more viscous and contains degradative enzymes like RNAse or alkaline phosphatase[3]. The periplasm also embeds transport proteins, including the transporting sugars, amino acids, and other compounds, which play an important role in the envelope biogenesis. The structure of the periplasm is still a subject of discussion, and the size of the compartment and the uniformity of this size throughout the cell is still uncertain. But not only proteins and enzymes of the periplasm are important, and one of the targets for antibiotics[4] is the peptidoglycan cell wall. Even if for Gram negative bacteria this wall is not so thick as for Gram-positive ones, it remains an important structure which keeps the shape and structure of the cell. Damages to peptidoglycans can cause cell lysis due to turgor pressure of the cytoplasm. The peptidoglycans do not flow freely in the periplasm, but are attached to the outer membrane by the so-called lipoprotein Lpp [1,7].

[3] That is why some call the periplasm a precursor of lysosomes of eukaryotic cells [65]

[4] The beta-lactams for example

The outer membrane is a unique feature of Gram negative bacteria which presents a transversal asymmetry. The outer leaflet contains lipopolysaccharides (LPS), which are absent in Gram-positive bacteria. LPS are well studied due to their high importance for bacteria and are responsible for the endotoxic shock and cause response from animal immune system. This is why they were first called “endotoxins” by the German bacteriologist R. F. J. Pfeiffer. The OM is a first line of protection for bacteria from the environment, and it is one of the reasons why Gram negative bacteria are often more resistant to antibiotics than Gram-positive ones. The OM is so strongly impermeable, that even lipophilic molecules cannot enter due to strong efflux – leaving its permeability two orders of magnitude lower than for phospholipid bilayers [11]. Three main parts can be distinguished, namely 1. the lipid A, 2. the core saccharide, and 3. the O-antigene polysaccharide. All these parts play important roles. The O-antigen is crucial for the bacterial adhesion, for binding proteins of immune system and bacteriophages. The core saccharide, which has two domains (inner and outer cores), embeds 3-deoxy-D-manno-oct-2-ulosonic acid (KDO) in the inner core which is essential for bacterial growth. In fact, the development of inhibitors of biosynthesis of KDO represents one of the directions for developing new antibiotics. Generally, the core helps keeping the asymmetry of the OM, which was shown on deep-rough mutants which lack the outer core and where the asymmetry was disturbed. Those mutants have patches of phospholipid bilayers in their cell membranes to compensate for disability to insert some of trans-membrane proteins and to fill “empty spots” [11]. Finally, lipid A is absolutely necessary for bacteria and the inhibition of its biosynthesis is lethal. Lipids A anchor LPS to the OM and lipid A’s general structure can vary between different species.

Bacterial LPS has conserved domains through a lot of Gram negative species which happens to be important for eukaryotes since it allows monocytes and macrophages to recognize LPS and therefore to start the inflammation process. It is noteworthy that, if all LPS consist of lipid A and core oligosaccharide, some LPS lack the O-antigen. In such case they are called “rough form” [26, 27]. A rough form is characterized by lower antibiotic resistance and a and lower viability but they are useful to study potential antimicrobial compounds which act on lipid A specifically, as far as all the complexity of the interactions with O-antigens is taken out of the picture. At the same time LPS-binding proteins are able to recognize both rough and smooth LPS, and even just lipid A [69].

Lipid A usually contains 6 acyl chains of different lengths which are esterified with the disaccharide backbone. It should be noted that unsaturated fatty acids are rarely present in lipid A. Acyl chains can be classified in two groups: primary – directly esterified with the sugar, and secondary – bonded with ester bond to the primary chains. Up to four primary chains can be attached to the head group. The head group of lipid A is a β(1→ 6)-linked glucosamine disaccharide backbone (Figure 12).

Generally the disaccharide is phosphorylated at positions 1 and 4' of saccharides, but phosphate groups can be further substituted with groups such as ethanolamine, ethanolamine phosphate, ethanolamine dipho/sphate, GlcN, 4-amino-4-deoxy-L-arabino-pyranose, or D-arabino-furanose. Such substitution plays a role in bacterial antibiotic resistance [26, 27]. Phosphate groups play an important role in maintaining the asymmetry of the outer membrane. Salt bridges are formed in between these groups of neighboring lipids A, with participation of divalent ions, such as calcium or magnesium. From another side, numerous fatty acids keep lipid A inside the membrane in stable state. These fatty acids strongly vary in between different bacterial species: for example, *Helicobacter pylori* has chains of 18:0 and 16:0, when *Halomonas pantelleriensis* four 12:0(2-OH) carrying one 12:0 and one 10:0 fatty acids [70]. These differences are also important for characterizing endotoxicity. Some studies show that number and length of fatty acids can change activity of lipid A up to a hundred times [71]. Not only fatty acids or phosphate groups can vary, but glucosamine disaccharide can also be replaced. For *Brucella*, *Legionella*, *Rhizobia* and *Ochrobactrum* it can be replaced by diaminoglucose disaccharide.

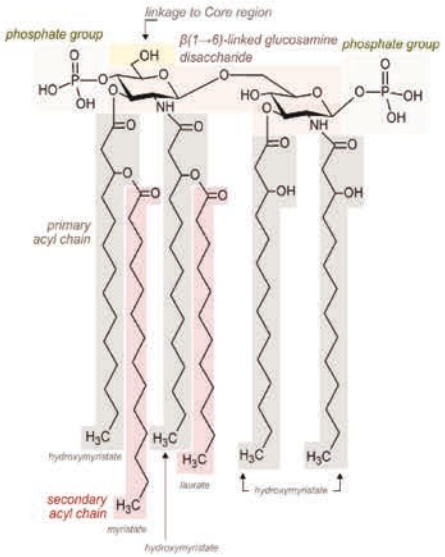

Figure 12. Structure of E. coli lipid A. Primary acyl chains (light grey) are directly linked to the sugar moieties, secondary acyl chains (light red) are esterified with the hydroxyl groups of primary acyl chains. All primary acyl chains of E.coli lipid are hydroxymyristates, one of the two secondary acyl chains is myristate while the other one being laurate .

The core oligosaccharide and its structure can vary a lot, however the inner core is better conserved and, as it was mentioned above, is made of Kdo and Hep. The inner core is directly linked to one of the sugar moieties of lipid A. The Kdo residue linked to the O-6' position of lipid A through an α-ketosidic linkage is named Kdo-I, and it can be glycosylated by one or two other Kdo residues (Kdo-II, and Kdo-III). Kdo-I is also glycosylated at the O-4 position by Hep, designated as Hep-I, which can be decorated by phosphate, diphosphate or phosphoethanolamine, by one or two other Hep or by another sugar making the inner-core structure. The bond between the lipid A and this first Kdo residue is normally very acid-labile with moderate pH (<4.4) easily hydrolyzing it and releasing the core from the lipid A. The outer core typically consists of common hexose sugars such as glucose, galactose, N-acetyl galactosamine and N-acetyl glucosamine and is generally more subject to variations than the inner core. Sugars in outer core are in pyranose form and generally have α-anomeric configuration. Number of monosaccharides in the core can be up to fifteen and they can be connected both linearly or branched way [28, 29].

The O-polysaccharides have a vast structural diversity and are truly important for bacterial environmental adaptation. O-polysaccharides are important for virulence and colonization and are one of the targets of the immune system of the host. Not only the types of used monosaccharides can vary, but also their lengths which ranges from zero (in rough LPS) to

10 saccharides. Different rare and common sugars can be building blocks for the O-antigens. This variability is extreme. For instance, 186 serogroups of the only *E.coli* are described. The dynamic diversity of O-antigens observed within species is due to various mechanisms. New O-antigens are derived from others by mutation, lateral transfer of O-antigen coding genes, insertion or deletion of O-antigen genes mediated by insertion sequence (IS) elements, transferring O-antigen clusters, or O-antigen genes, by plasmids as well as by serotype-converting bacteriophages [72].

ii. Gram-positive envelope

For Gram-positive bacteria the structure of the cell envelope is much simpler: one lipid membrane and one thick peptidoglycan wall. Some Gram-positive bacteria also have a capsule, which plays a role in phage resistance and immune evasion [73]. Capsule polysaccharides are strongly implicated in virulence of bacterial pathogens. Capsules are also able to mask the binding of opsonic C3 fragments to the complement receptor, thus decreasing opsonization and phagocytosis by leukocytes [74]. These and other properties of capsule polysaccharides make them be interesting for vaccinal development, which explains why immunization with polyvalent pneumococcal polysaccharide is effective as a vaccine [75].

A thick wall helps these bacteria with keeping their shape, protects them from the environment, and helps them to manage with turgor pressure. Cell wall and cell membrane are connected with lipotechoid acids, which are polymers anchored into membrane head groups and which go through layers of peptidoglycans. Other types of polymers in the cell wall are techoic acids which are covalently bound directly to peptidoglycans. These polymers represent more than 60% of the mass of the cell wall and that also makes them to be an important part of the envelope structure. Peptidoglycan layer in Gram-positive bacteria is around 30-100 nm thick, on the contrary to Gram negative bacteria which have only few nanometers of peptidoglycans in the periplasm. The peptidoglycan wall is composed of alternating units of disaccharide N-acetyl glucosamine – N-acetyl muramic acid (NAM – NAG) cross-linked by a pentapeptide side chain (stem). The pentapeptide is usually the L-alanyl-γ-D-glutamyl-diaminopimelyl (or L-lysyl)-D-alanyl-D-alanine, but in Gram-positive bacteria an inter-bridge structure of five amino acid residues varies between the species. Glycan strands can differ in length in a range generally comprised of 5 to 100

disaccharide units, although some studies show chains with up to 5000 units [76]. Moreover, bacteria can introduce various modifications of peptidoglycan subunits, such as *N*-deacetylation, removal of C2-acetyl groups from GlcNAc and/or MurNAc sugars, or *O*-acetylation of the MurNAc C6 hydroxyl to protect themselves from antimicrobial drugs [77]. On top of the intrinsic complexity of the Gram-positive cell wall, it also contains a wide variety of proteins, which contributes in its binding to the cell envelope. Since Gram-positive bacteria do not have periplasm, these extracellular proteins perform all the necessary functions out of the cell. The membrane by itself is a symmetric bilayer of phospholipids, similar as it was believed for the inner membrane of Gram negative bacteria [1, 12]. Gram-positive organisms are surrounded by bilayer membranes that can vary substantially in composition but which typically include large amounts of PE, PG, and CL. Interestingly, the presence of LPG seems to reduce susceptibility to antimicrobial peptides (AMPs), aminoglycosides, bacitracin, daptomycin and some beta-lactams, and the expression of MprF, the protein which synthesizes LPG, increases in resistant strains [79], [80]. The Gram-positive bacteria contain branched fatty acids with major distribution of anteiso C15:0 and C17:0 chains [78].

Supported lipid structures

Deposition of lipid bilayers on planar solid surfaces is nowadays one of the main ways to study experimentally membranes and their interactions with proteins or drugs with high precision, which remains challenging in living cells. The widespread use of techniques devoted to use lipid vesicles does not yet answer the need of some experimental techniques such as AFM or quartz-cristal microbalance, which rely on the use of a surface deposited structure. The so-called solid-supported lipid bilayers are especially attractive for both biotechnological applications involving functionalization and patterning of a surface as well as for modeling various biological processes since they provide a controlled environment, and an improved physical stability while preserving the key properties of the membrane, such as their lateral mobility [81], [82] or the ability to host functional proteins [83]–[85]. This is possible due to the structure of biological membranes under the form of a bilayer of lipids. Indeed, while the lower leaflet is coupled with the substrate, the upper one has good lipid mobility in case of lipid fluid phase. In SLBs, the friction between the monolayers determines the diffusion of the upper monolayer [86], [87]. These membrane platforms are used for environmental monitoring, drug discovery and drug testing as well as to investigate properties of biomembranes such as the influence or function of membrane proteins or peptides, phase separation and domain formation [88], transmembrane signaling or morphological changes inside cells [89].

I. Deposition methods

Since the structure of the SAM or SLB is potentially depending on the method used for the deposition, it is of interest to give an overview of the most common methods.

One of the most widespread methods uses small unilamellar vesicles (SUVs). The SUVs that are generally formed by sonication of bigger and heterogeneous solution of lipid vesicles are later incubated with the solid surface to let them adsorb. Vesicle fusion and rupture, which is enhanced by the presence of the surface can occur, leading to the planar supported lipid bilayer. If the kinetics of the process depends on the mechanical rupture

strength of the bilayer, and subsequently on its lipid content, it is largely influenced by surface heterogeneity [87].

For hydrophobic surfaces, the formation of self-assembled monolayers can be reached through the so-called solvent-controlled precipitation method or solvent exchange-induced physisorption, where lipids are solvated usually in ethanol and this solution is gradually diluted with water. The slow increase of the water content drives the lipids to coat the hydrophobic surface with their tails interacting favorably with it, while not creating a floating bilayer [90]. The method can also be used for hydrophilic surfaces to form SLBs. The sole disadvantage of that method being residual quantities of alcohol remaining in the final system [87].

The oldest technique for film deposition, which is still widely used, is the Langmuir-Blodgett (LB) technique, where monolayers (or multiple layers) are transferred from air-water interface to the solid substrate (Figure 13). Various modifications were proposed and applied to this technique, such as applying rotational flow on the liquid surface – contrary to the initial vibration-free requirements [91].

Another similar deposition technique is the Langmuir-Schaefer (LS) technique where the orientation of the substrate to the solvent differs from Langmuir-Blodgett, being dipped horizontally, instead of vertically. Another interesting property of the LS technique is the possibility to combine it with tethering, hence forming the so-called tethered bilayer lipid membranes (tBLMs) [92]. Combining these two techniques can allow to create complex asymmetric membranes, which can be useful, for instance, to model outer membrane of Gram negative bacteria. In his work, Clifton *et al* [93] were able to create such model membrane with using first Langmuir–Blodgett deposition on silica to create inner monolayer (DPPC) and later Langmuir-Schaefer deposition of LPS or lipid A monolayer was performed onto silicon crystal containing the LB-deposited DPPC monolayer [93].

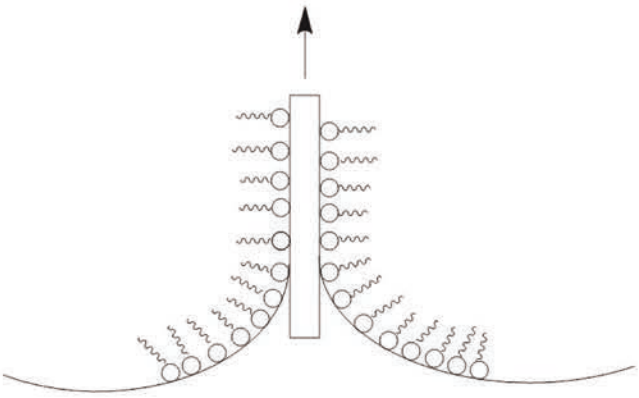

Figure 13. Schematic representation of Langmuir-Blodgett technique, where lipids are transferred onto a vertically placed into water solid surface.

tBLMs have grown in popularity for various applications, such as studying interactions with model lipid membranes of antimicrobial peptides and other drugs or studying membrane-proteins interactions [94]. These systems are characterized by a very high stability and availability to various experimental techniques, such as AFM or surface plasmon resonance among others. For tBLM systems, instead of using directly lipid-substrate interactions to stabilize the lipid structure, a layer of molecules such as anchorlipids, is used. On the top of this layer, the studied system is assembled [95].

II. Substrates used for deposited lipid structures

The choice of substrates for supporting phospholipid membranes is not straightforward and depends of the precise task, application and the technique used for measurements. For instance, for AFM measurements mica tends to be a good substrate, since it can be atomically flat, for the fluorescence microscopy glass is preferred as a material due to its optical transparency. It is necessary sometimes for one of the substrate layers to be a conductive material, for instance if one is conducting quartz crystal microbalance (QCM) or surface plasmon resonance (SPR) analyses [96], [97].

At the same time, it is expected that the deposited lipid patch will preserve the natural properties of the biomembranes such as a high lipid mobility, a good transversal flexibility, and other biomechanical properties, and present little to no defects along its surface. The preservation of these properties is highly affected by the choice of the substrate [83], [97]. For instance, the smoothness of the substrate is of importance, as it does not only drives to more favorable and homogeneous interactions with the membrane, but it also improves the

quality of surface-sensitive measurements. Gold substrate, for instance, has the tendency to be way rougher than mica or silica [88] which made it to be often disregarded without a proper coating [97]. It was also found that rougher substrates may create artifacts, such as nanoscale lipid domains, which are not present on smoother surfaces, such as mica or silicon [96].

Ultimately, the most driving criterion to select a substrate is its surface energy. Especially, one will want to select a sufficiently hydrophilic substrate to form stable SLBs. In that respect, oxidized surfaces like SiO_2 (silica) and TiO_2 have been often investigated for SLBs formation [98]–[100]. However, the list of supports on which SLBs were formed extends to a long list of candidates including graphene oxides (GOs) [101], [102] and a variety of glasses, especially fused silica or borosilicate glass [83] as well as different thin-films including gold, silver or platinum that can be used on top of a variety of materials [83], [103]. At the same time hydrophobic substrates – *e.g.* pristine graphene (GR) [102], [104]–[106], reduced graphene oxide (rGO), or polytetrafluoroethylene (Teflon) [107], [108] – are used to stabilize self-assembled monolayers (SAMs). In aqueous environment, SAMs usually display their fatty acid chains directed to the substrate and can subsequently serve to sustain an additional lipid bilayer onto the SAM without disrupting it [109]–[113]. It is important to underline that SAMs are characterized by higher melting temperature than lipid vesicles [114]. Hence, graphene oxide is a very interesting material to study since its hydrophilicity can be "tuned" depending on the obtained oxidation level (OL) of the material. GO fills the gap between purely hydrophilic and hydrophobic substrates [99], [115].

III. Membrane-substrate interactions

The hydrophilic and hydrophobic interactions which have a central role in the stability of SLBs are also involved in the formation of an interfacial water layer – frequently refer to as the hydration layer – between the substrate and the lipid structure. Lipid head groups of SLBs generally do not lay in direct contact with the surface of a hydrophilic material but on a thin water layer from a couple of atoms thick to ~25 Å [87], [116], [117]. Such a large range of thicknesses for this hydration layer is coming from multiple factors including the type of substrate [118], the temperature [111], the lipid content of the membrane [119], and the method of the measurement. One should note that the many definitions of that thickness

[116] add some additional difficulties to the direct comparison of the different works (see subsection III of section Influence of substrate hydrophilicity on structural properties of deposited lipid structures for more details).

Recently, Vishnyakov *et al.* [2] proposed an explanation to the disparity of measurements of the thickness of the hydration layer, which is based on the coexistence of two states, called α and β in his work, which are characterized by different interfacial layer thicknesses. The α state corresponds to the most stable conformation where the lipid bilayer is in close-contact with the substrate, and the β states due to higher disjoining pressure – *i.e.* the pressure resulting from the interaction between the substrate, the solvent, and the membrane which maintains the lipids at a given distance from the surface – are associated to larger hydration layer (up to a few nanometers) where the system looks like a “floating” bilayer. In the case of DMPC lipids on silica, the close-contact state was shown to result in hydration layers 3-4 Å thin. This small water content can be described as the remnant hydration layers of both the surface oxide groups and the lipid head groups. The work further hypothesize that far-contact states correspond to a group of metastable states with respect to the single α state (Figure 14).

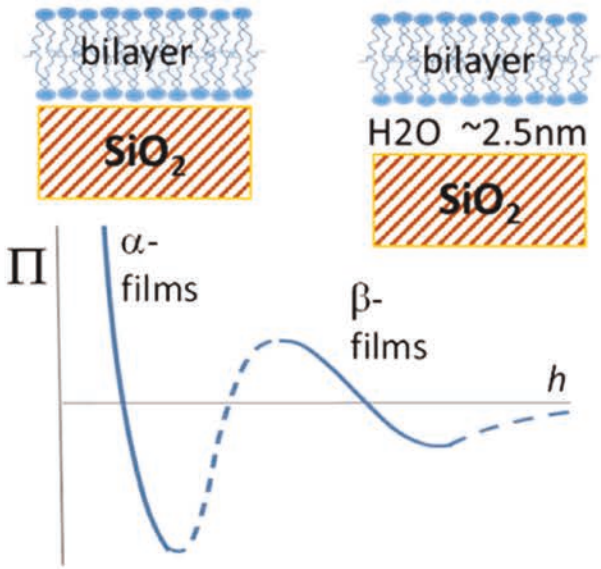

Figure 14. Schematic representation of α and β states, where on the vertical axis is disjoining pressure and on the horizontal axis is distance between the substrate and the bilayer (increasing from left to right). Reprinted (adapted) with permission from . Copyright 2023 American Chemical Society.

These two states are separated by an energy barrier (Figure 14) due to the repulsive hydration forces which occur at the water interface. A SLB can thus be trapped in the metastable β states if this barrier is high enough. Whether the SLB is able to cross that barrier or stays in the metastable floating state depends on both the time under which the measurements are made, the depth of the potential wells of the α and β states (which reflect the competition between lipid/substrate and lipid/lipid interactions), if they exist, and probably on the deposition method which is used. The presence of these different states is probably the reason why many experiments reported large hydration layers which could be associated to systems trapped in metastable states. In Table 3 we report an extended bibliography work[5], where we compile the results from different computations and experiments performed on various systems.

Table 3. Overview of relevant publications measuring the thickness of the interfacial layer of water between a hydrophilic substrate and a lipid bilayer. Most of lipids are the zwitterionic phosphatidylcholines (PC) and that most of the substrates are silica.

Year	First author	Substrate	Lipids	Thickness, Å	Error, Å	Method
1990	Bayerl [120]	Glass	DMPC	17	5	^{1}H NMR
1991	Johnson [121]	Quartz	DMPC	30	10	Neutron reflectivity

[5] This table is part of one publication made during the course of this PhD. Reprinted (adapted) with permission from [1]. Copyright 2023 American Chemical Society

1996	Koenig [122]	SiO2	DPPC	14.4	0.5	Neutron reflectivity
		SiO2	DSPC	16	1	Neutron reflectivity
1999	Charitat [123]	SiO2	DSPC	7	1	Neutron reflectivity
		SiO2	DPPC	8	1	Neutron reflectivity
1999	Fromherz [124]	SiO2	POPC	11	2	FLIC
2000	Fragneto [125]	SiO2	1:9 DPPS:DPPC	5	1	Neutron reflectivity
		SiO2	DPPC	5	1	Neutron reflectivity
		SiO2	(Di-C_n-PC)$_{n \in [16;20]}$	6	1	Neutron reflectivity
2003	Kiessling [126]	SiO2	POPC	17	10	FLIC
2004	Gutberlet [127]	SiO2	DMPC	5.8	N/A	Neutron reflectivity
		SiO2	DMPC	6.2	N/A	Neutron reflectivity
2005	Ajo-Franklin [128]	SiO2	Egg PC	13	2	FLIC
2005	Crane [129]	SiO2	POPC	13	8	FLIC
		SiO2	POPC	15	7	FLIC
		SiO2	POPC	19	5	FLIC
		SiO2	POPC	23	6	FLIC
2005	Doshi [130]	SiO2	POPC	14.6	0.5	Neutron reflectivity
2005	Miller [131]	Quartz	1:9 DLPC:DSPC	4	N/A	X-ray and Neutron reflectivity
		Quartz	DOPC	4	N/A	X-ray and Neutron reflectivity
2007	Stidder [132]	SiO2	DPPE	6	1	Neutron reflectivity
2008	Roark [5]	SiO2	POPC	14.6	N/A	AA MD simulations
2009	Watkins [133]	Quartz	DPPC	4.2	N/A	X-ray reflectivity
2010	Zwang [116]	SiO2	DOPC	10.2	0.4	DPI and QCM-D
2014	Lind [134]	SiO2	DPPC	14	N/A	Neutron reflectivity
2016	Duro [135]	SiO2	POPC	4.5	0.1	AA MD simulations
2017	Vishnyakov [2]	SiO2	DMPC	4.8	2	AA MD simulations

It is clearly visible, that distribution of reported hydration layer thickness (Figure 15) could be an indirect indication, that two types of contact states exist. The most commonly obtained values are either in the range 4-6 Å or in the range 14-16 Å.

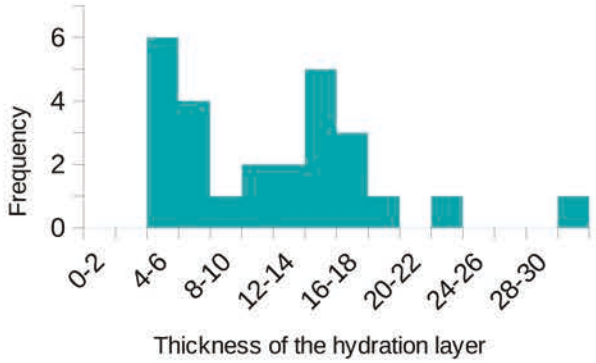

Figure 15. Histogram of the thicknesses of the hydration layer for SLBs on hydrophilic substrates reported in the literature.

In case of tethered systems, the use of anchors is made to form a bridge between the substrate and the lipid structure. Hence, tBLMs see the lower leaflet covalently bonded to the spacer group formed by these anchors. This group is not only binding to the membrane, but it also creates sufficient aqueous space to reduce hydrophobic influence of the substrate.

Many molecules have been used as an anchor, such as lipids which head group is strongly interacting with the substrate, carbohydrates, polyelectrolyte layers, polymer chains and peptides [114], [136]. These systems can thus allow to use hydrophobic substrates to study lipid bilayer, as it can be necessary for particular measurement techniques or to palliate the roughness of the substrate, as it can be useful, for instance, for gold (Figure 16) [88].

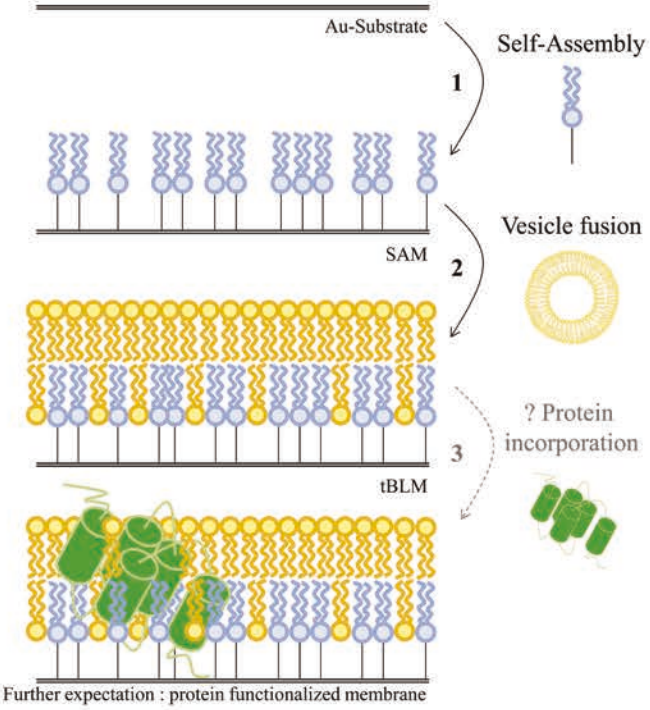

Figure 16. Schematic representation of formation of tBLMs: telechelics assamble on the gold substrate and then the rest of bilayer is completed by vesicle fusion. Copied from with permission of the publisher.

Membranes deposited with tethering exhibit high fluidity in the upper monolayer, comparable to the vesicle membranes, however lower monolayer has reduced mobility with decrease in diffusion constant by ~2.3-3.5 times [137]. It is noteworthy that density of tethers on the substrate (which can be tuned) also has an influence on membrane properties. For example, Park *et al* report that higher density of tethers promotes translocation of AH peptide in their system due to the interactions between the peptide and tether chains [138]. Electrochemical properties of anchors also play their role, such as interfacial capacitance [136].

There are two other possibilities similar to anchoring which are worth mentioning (Figure 17), including the creation of hybrid bilayers (HBMs), where monolayer of phospholipids is adsorbed on SAM of alkathiols (hydrophobic) attached with covalent bonds to the surface [139], or the creation of polymer-cushioned membranes, where membrane is separated by soft polymers from the substrate which reduce frictional coupling between the substrate and membrane or membrane-incorporated proteins [114]. Aforementioned methods have a distinct difference from tBLMs as they do not incorporate directly into the lipid structure of the bilayer or the monolayer, which could help reducing the potential effects of the

deposition on the membrane properties. The choice of the deposition method is finally driven by the general goal of the experiments, especially if interactions with drugs are studied or membrane proteins are involved as, in the first case, substrate-drug interactions might drastically influence the mechanism of interaction of the drugs with the membranes, and, on the other hand, especially with transmembrane proteins, a significant part might be directly exposed to the surface [87].

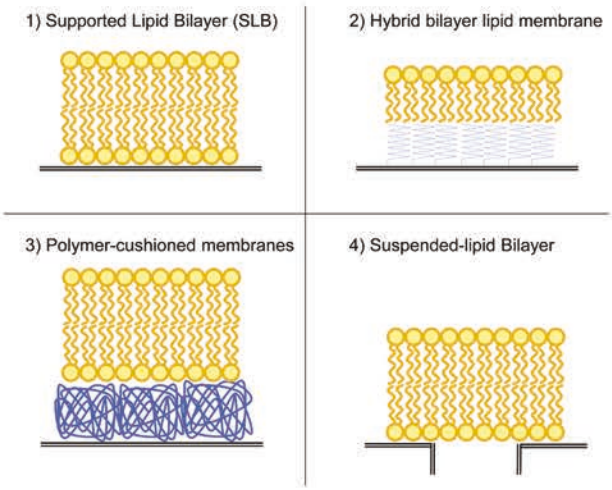

Figure 17. Schematic representations of 1) SLBs 2) HBMs 3) Polymer-cushioned membranes (described above) and 4) Suspensed-lipid bilayer (not mentioned in the main text). Copied from with permission of the publisher.

Hybrid membranes can be combined with other techniques to create truly complex systems. A good example is the model of Gram negative envelope created by Clifton *et al* [140], where DPPC inverted bilayer (head groups inside) was deposited to a SAM of ω-thiolipids on gold surface using LB technique. This HBM was supposed to mimic upper leaflet of IM and the lower leaflet of OM of a Gram negative bacteria. To build the complete asymmetric OM, LS technique was further applied using a Langmuir film of LPS (tails up to the air interface). This allowed to combine lower and upper leaflets of the OM into one complete bilayer. Finally, the OM and IM model membranes were separated [140].

IV. Conclusions

It is clear that the choice of substrate, deposition method, and lipid content all play a critical role in the final in the interactions between substrate and deposited lipid structures. Further on, the choice for those parameters is not only guided by the necessity to obtain the most

stable structure which preserves most its original biological functions but also by the type analyses that should be performed.

Although advanced techniques such as tBLMs or HBMs try to tackle the limitations of SLBs, the latter category remains widely used due to the ease of creation and the rather good preservation of the biological functions.

MD simulations are a tool of choice to further model lipid-substrate interactions to help designing experiments which improve further the preservation of the membrane functions while optimizing its stability. However, there is still, to the extent of our knowledge, a lack of tools able to predict the optimal choice of parameters for a given system [1], [2], [104], [117], [141], [142].

Antibacterial drugs

An initial definition of antibiotics was created by S. Waksman, who discovered streptomycin in collaboration with A. Schatz and E. Bugie, and was awarded the Nobel prize for his work. He called antibiotic a substance produced by microorganisms to inhibit the growth or destroy other microorganisms. Now, with discovery of synthetic antibiotics the definition expanded to them as well. Other terminologies can be found. For instance, antimicrobials are usually referred as all chemicals which kill or inhibit growth of microorganisms, where antibiotics are those which work within the body, antiseptics are those applied on living tissue to prevent infections and disinfectants are those which are used on non-living objects (*e.g.* on surfaces, materials, *etc.*) [143].

The ideal antibiotic should follow other rules than just being effective against bacteria such as being 1. selective – *i.e.* causing minimal damage to host cells, 2. water soluble – *i.e.* being easily transported through body fluids, 3. of low toxicity – *i.e.* causing minimal side effects, 4. stable – and that includes both shelf stability and bio-stability, 4. low cost – to promote affordability to a wide population, and 5. as less as possible a promoter of resistance development [143].

Different types of classifications exist for antibiotics: by chemical structure, by microbial coverage, by effect on growth and surviving (bacteriostatic or bactericidal), by mechanism of actions. The later can be separated in six classes [143], [144]:

1. Inhibiting cell wall synthesis
2. Cell membrane disruption
3. Inhibiting synthesis of important metabolites
4. Inhibiting DNA synthesis
5. Inhibiting RNA synthesis
6. Inhibiting protein synthesis

Those classes can be extended or slightly modified by different authors [144], [145], with development of new drugs. For instance, antibiotics with other than mentioned above

mechanisms of action appear such as interfering with non-coding RNA (ribocil), inhibiting cell division proteins (PC190723), targeting Clp proteases, which regulate quality of protein folding in bacterial cells (acyldepsipeptides) and many others [146].

World Health Organization (WHO) classifies antibiotics not only by chemical type but also accordingly to risks of resistance (AwaRe classification [147]) and the recent update was made in 2021.

In order to better understand which antibiotics are acting at the membrane level, we conducted an extensive work of bibliography at the beginning of the PhD. Table 4 is a short overview of common antibiotics structurally based by the aforementioned classification with short explanations of their mechanisms of action and known resistant mechanisms.

Table 4. [see the two next pages] General classification of antibiotics based on AWaRe WHO classification. Access status indicates the antibiotic of choice available at all times, watch – recommended for specific limited indications and reserve – last resort antibiotics. In bold, the categories of antibiotics which are active at the lipid membrane level and are categorized as last-resort antibiotics. The bibliographical references in the table are denoted by letters from (aa) to (bo) in exponent refer respectively to [143], [148]–[187].

Class of antibiotics	Mode of action	Resistance mechanisms
Aminocyclitols (Spectinomycin)	• Binding to 16S rRNA helix 34 of the 30S subunit of the bacterial ribosome, where it blocks translocation[na]	• Efflux transporters[ab] • Chromosomal mutations in the ribosomal 16S rRNA genes[ac] • Mutation in the gene for ribosomal protein S5[ad] • Modification of the drug by aminoglycoside-modifying enzymes[ae],[af]
Aminoglycosides (Amikacin, gentamycin)	• Inhibit protein synthesis by binding to the A-site on the 16S ribosomal RNA of the 30S ribosome[ag] • Blocking elongation or by directly inhibiting initiation[ag]	• Aminoglycoside-modifying enzymes (AMEs)[ag] • 16S rRNA methyltransferases (RMTs), which block drug from binding their target[ah] • Efflux (Mex) XY-OprM system and their orthologs[ag]
Aminoglycosides (Arbekacin, bekanamycin, dibekacin, isepamicin, kanamycin, micromonomicin, neomycin, netilmicin, ribostamycin, sisomicin, streptoduocin, streptomycin, tobramycin)		
Aminoglycosides (Plazomicin)		
Amphenicols (Chloramphenicol, thiamphenicol)	• Binding to the 50S subunit of the ribosome[ai]	• Acetylationof the drug with chloramphenicol acetyl transferase (CAT), except florfenicol[ai] • Efflux by CmlA proteins[aj] • ABC extrusion system[aj] • Inactivation by phosphotransferases[ak] • Mutations of the target site and permeability barriers[ak]
Beta-lactam/beta-lactamase inhibitors (Amoxicilin/Clavulanic acid*, ampicilin, sultamicin, sulbactam*)	• Interrupt bacterial cell-wall formation by binding to penicillin-binding proteins (PBPs), which are involved in peptidoglycan crosslinking[al]	• Lack of classical porins or preference for positive charge[al] • Mutations in PBPs[am] • Transferable enzymes that travel on mobile elements among species – beta-lactamases[an] • Mutations in beta-lactamase promoters[ao] • Mutations of the active site of beta-lactamases[ap]
Beta-lactam/beta-lactamase inhibitors (Piperacillin/tazobactam*)		
Penicillines (Amoxicillin, ampicillin, Benzathine-benzylpenicillin, benzylpenicillin, cloxacillin, Phenoxymethylpenicillin, Procaine-benzylpenicillin, azidocillin, bacampicillin, clometocillin, dicloxacillin, epicillin, fluxacillin, hetacillin, mecillinam, metampicillin, meticillin, nafcillin, oxacillin, penamecillin, pivampicillin, pivmecillinam, propicillin, talampicillin)		
Penicillines (Carbenicillin, carindacillin, temocillin, ticarcillin, aspoxicillin, azlocillin, mezlocillin, pheneticillin, piperacillin, sulbenicillin)		
Monobactams		
Carbapenems (Biapenem, doripenem, ertapenem, imipenem/cilastatin, meropenem,panipenem, tebipenem)	• Acylation of PBPs[aq] • Not inactivated by many beta-lactamases[ar]	• Mutations in PBPs and producing carbapenem-resistant PBPs[aq] • Carbapenemases production (type of beta-lactamases)[aq] • Substitutions in, or decreased expression of, nonefflux porins[aq] • Efflux pumps of RND, MFS, ABC, MATE superfamilies[aq]
Carbapenems (Imipenem/cilastatin/relebactam, Meropenem/vaborbactam)		
Penems (Faropenem)		
I generation cephalosporins	• Inhibit crosslinking of peptidoglycan[as] • For ceftaroline also binding to PBP 2a (expressed by multiresistant S. aureus)[at]	
II generation cephalosporins		
III generation cephalosporins		
III generation cephalosporins (Ceftazidime/avibactam)		
IV generation cephalosporins		
Vgeneration cephalosporines		
Other cephalosporins (Cefiderocol)	• Inhibit crosslinking of peptidoglycan[as] • Active uptake into bacteria (avoid porin changes mechanism of resistance)[au]	
Fluoroquinolones Quinolones	• Reversible trapping of gyrase-DNA and topoisomerase IV-DNA complexes[av]	• Overexpression of energy-dependent efflux pumps[aq] • Mutations in QRDR (quinolone resistance-determining region) in DNA gyraze coding part[aw] • Plasmid-borne gene *qnr* – protects DNA gyraze from inhibition[ax]
Glycopeptides (Teicoplanin, vancomycin) Glycopeptides (Dalbavancin, oritavancin, telavancin)	• Inhibition of cell wall synthesis through binding to the d-alanyl-d-alanine terminus of the lipid II bacterial cell-wall precursor, preventing cross-linking of the peptidoglycan layer[ar] • Self-association to increase affinity[ar]	• For Gram-negative, it is impossible to enter through outer membrane (OM)[ay] • For Gram-positive, altering the structure of peptidoglycan precursors to decrease binding affinity[az]
Glycylcyclines (Tigecycline)	• Binding bacterial 30S ribosome – inhibition of protein synthesis[ba] • The 7S ribosomal protein is part of the binding site. A highly conserved region of 16S rRNA may also be part of the binding site[ba]	• Efflux (Tet A-E, K, L, P genes)[ai],[ba]. Glycylcyclines are often resistant to it[ai],[ba]. • Ribosome protection (Tet M, O, Q) by dislodging tetracycline bound to ribosome[ai],[ba]. Glycylcyclines are resistant against Tet M[ai],[ba]
Tetracyclines (Doxycycline, tetracycline)		
Tetracyclines (Chlortetracycline, clomocycline, demeclocycline, lymecycline, metacycline, minocycline		

oral form, oxytetracycline, penimepicycline, rolitetracycline, sarecyclin) Tetracyclines (Omadacycline, minocycline intravenous form, eravacycline)	• Some tetracyclines: disturbing membrane organization and localization of the peripheral membrane proteins MinD, MinC, and MreB[av]	• Inactivation (TetX enzyme)[aw] • Efflux of tigecycline through AcrAB pump overexpression with mutations in AcrR and RamA[aw]
Imidazoles	• Flavohemoglobin coordination and NO dioxygenase (NOD) function inhibition[ax]	• Loss of oxygen-insensitive NADPH nitroreductase activity[ay] • Nim genes, which encode for reductases that convert the nitro group on the antibiotic into a non-bactericidal amine[az]
Lincosamides (Clindamycin) Lincosamides (Lincomycin) Macrolides Streptogramins (Pristinamycin) Streptogramins (Dalfopristin/quinipristin)	• Inhibiting protein synthesis by binding to 23S r RNA of the 50S subunit[ba],[bb]. • Combination of streptogramins A and B types has huge synergistic effect[bc].	• Methylation of adenine in conserved part of 23S rRNA (*erm* gene)[ad]. • Inactivation by erythromycin esterases[ad] • Phosphorylation or adenylation of lincosamides by LinB enzyme[ae] • Enzyme streptogramin B lyase which linearizes the cyclic antibiotic[aa].
Lipopeptides (Daptomycin)	• **Binding to membrane and forming transmembrane channel[bd]** • **Causing rapid depolarization of bacterial membrane[bb]**	• **Reduced levels of phosphatidylglycerol decrease the net negative charge of the membrane[bc]** • **Activation of Lia system – increased expression of wall remodeling-associated genes[bd]**
Nitrofuran derivatives	• DNA lesions • Oxidative stress • Inhibition of RNA and protein biosynthesis[be]	• Mutations in nitroreducing enzymes[be] • Mutated version of the extended spectrum β-lactamase CTX-M-14[bf]
Oxazolidinones	• Protein synthesis inhibition with targeting the binding of N-formylmethionyl-tRNA to the ribosome[bg] • Binding to 23S RNA of 50S subunit[ad]	• Gram-negative bacteria use efflux pumps[ad] • Gram-positive bacteria use mutations in 23S rRNA gene[bh]
Phenol derivatives (Clofoctol)	• Alteration of permeability of the envelope – damaging cytoplasmic membrane[bi]	• Not known • Only works for Gram- positive[bj]
Phosphonics (Fosfomycin oral form) Phosphonics (Fosfomycin intravenous)	• Pyruvyl transferase inhibition which disrupts cell wall synthesis[aa]	• Prevention of uptake into the bacterial cells by mutating transporter for glycerol-3-phosphate[ai] • Inactivation by FosA, FosB, FosX by addition of glutathione and cysteine (FosA, FosB) or transfer of water molecule to the C1 of the oxirane (FosX)[ak]
Pleuromutilin (Lefamulin)	• Protein synthesis inhibition by binding to domain V of 50S subunit[bk]	• Mutations in 23S rRNA, *rplC*, and *rplD* genes encoding the large ribosomal proteins L3 and L4 (in vitro) – causing indirect conformational changes to prevent binding[bk] • Acquisition of *vga*(A) encoded or related ATP-binding cassette (ABC)-F transporters – efflux transporters and interference of translation at peptidyl transferase center (PTC)[bk] • Acquisition of *cfr* encoding the Cfr methyltransferase - methylating the nucleotide A2503 of 23S rRNA[bk] • Mutations of target cite (*rrn* gene)[bk]
Polymyxins	• **Interaction with lipopolysaccharide (LPS) molecules via their cationic l-α-γ-diaminobutyric acid (Dab) side chains and hydrophobic interactions of the residues at position 6 and 7[bl]** • **Forming clystalline structures with involment of divalent cations of OM[bl]**	• **Modifications in LPS structures (ex. adding L-Ara4N, PEtn, galactosamine) – decreasing negative charge[bl],[bm]** • **Complete loss of LPS[bm]**
Rifamycins	• Binding to RNA polymerase to inhibit RNA synthesis[bn]	• Alteration of the target protein RNA polymerase via mutation of *rpoB*[bn] • ADP ribosylation of the rifampicin[bo] • Efflux[bn] • Duplication *rpoB* to "dillute" effectiveness[bn]
Steroid antibacterials (Fusidic acid)	• Interfering with elongation factor EF-G – blocking the next cycle of protein synthesis[ai]	• Point mutations in *fusA* – gene coding EF-G protein[bn]
Sulfonamides	• Inhibiting folic acid biosynthesis in bacteria by competing with PABA for binding dihydropteroate synthase (DHPS)[ai]	• Mutations in active cite of DHPS[ai] • Increasing synthesis of PABA[ai]
Trimethoprim derivatives (Brodimoprim, trimethoprim)	• Inhibition of ubiquitous chromosomal dihydrofolate reductase (DHFR)[bn]	• Mutations of DHFR[bn]

It is clearly noticeable that majority of modern antibiotics target proteins, DNA or RNA (Figure 18). These pathways make them sensitive to development of bacterial resistance. Following this observation, lipopeptides (for Gram-positive) and polymyxins (for Gram negative), which target cell membranes, are especially important. Cell membrane structure is highly conserved thus resistance does not occur as much as for protein-targeting antibiotics.

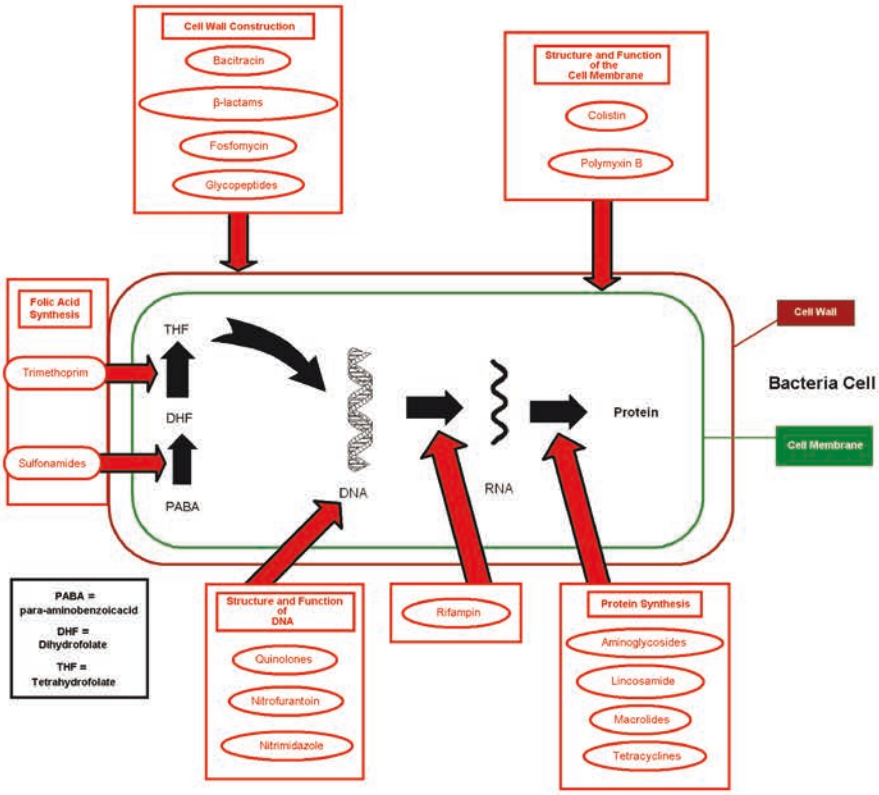

Figure 18: Scheme of mode of work for various antibiotics

From this literature search, it is evident that some efforts should be paid to understand drug interactions with bacterial membranes and develop this type of antibiotics which act primarily on bacterial membranes. Up to now, there is no universal mechanism of action for the membrane active drugs. In this work we focus on interactions of colistin (polymyxin E) with LPS of outer membrane of Gram negative bacteria, which is an important topic, taking into account the fact that resistance to polymyxins is growing [188].

Polymyxins are cyclic lipopeptides with 10 amino acids in their structure, where 7 of them are connected into a loop [185]. Non-proteogenic Dab residues give their positive charge to the molecule, which is really important for its function [185]. All polymyxins are classified

in 10 groups (A, B, C, D, E, F, M, P, S and T), however only polymyxins B and E (Figure 19) are widely studied, due to their active clinical use [185].

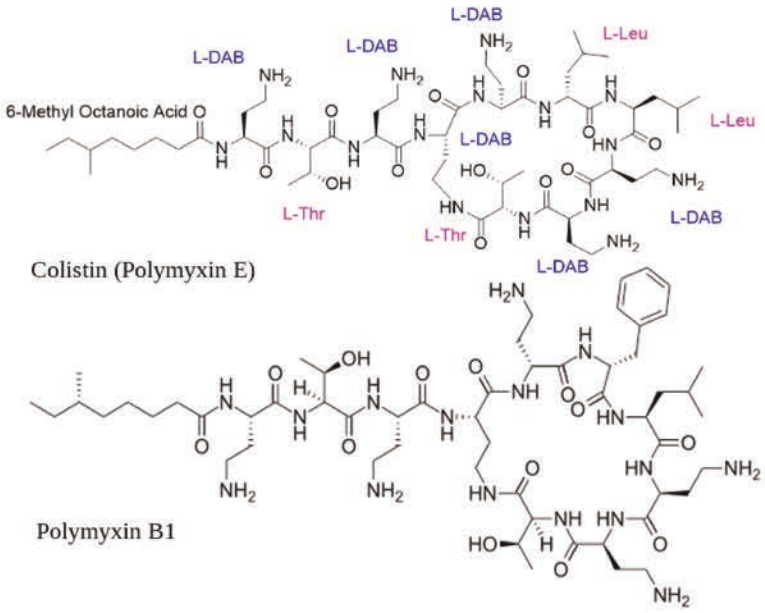

Figure 19. Structure of polymyxin B1 (bottom) and polymyxin E (top).

Polymyxins are believed to act through the electrostatic interactions of charged Dab residues with phosphate groups of lipid A of LPS, which displaces divalent calcium or magnesium ions, which act as bridges between phosphate groups of neighboring LPS molecules. This allows acyl chain and hydrophobic amino acids to insert into lipid tails region of outer membrane [11], [189]. Recent studies suggest that insertion of polymyxins into OM solidifies the patch around, as LPS is arranged into crystalline structure, and such structural changes strongly correlate with antimicrobial activity [184]. It is clear that cations displacement is not the only necessary step in antimicrobial activity, as polymyxin B nonapeptide (no fatty acid tail) has no antibiotic activity despite perturbing the OM leading to the suggestion that IM perturbation is necessary for killing [190]. Another proposed mechanism of action of polymyxins is mediating contact between outer and inner membranes, which would create phospholipid exchange and could create lethal for bacteria osmotic imbalance [191]. At the same time polymyxins inhibit alternative NADH dehydrogenase, thus disrupt bacterial respiratory chain [192].

With the fact that polymyxins act only if they are able to approach the outer membrane and insert themselves into it, it is not surprising that bacterial resistance mechanisms are based on structural changes in their OM. One of the main resistance mechanisms is adding to the phosphate groups of lipid A non-charged groups such as 4-amino-L-arabinose (L-Ara4N), phosphoethanolamine (PEtn) or galactosamine, as it abrogates initial electrostatic interaction of the drug with charged membrane [185], [193]. Another type of modification is changing the disaccharide backbone of lipid A where an *N*-linked acyl chain is added instead of an *O*-linked acyl chain. It can be possibly related to reduced flexibility of this linkage and increased membrane stability [194]. PEtn can be added not only to the lipid A part of LPS but also to the Kdo residue of the core, where it plays the same role of reducing net negative charge of the molecule [145]. The most drastic changes of OM performed by bacteria (specifically *Acinetobacter baumannii)* is total loss of LPS. In these resistant strains outer membrane was still present, even in total absence of LPS, however membrane integrity of it was compromised [195]. At the same time this mechanism of polymyxin resistance made bacteria sensitive to other antibiotics, such as teicoplanin (initially used for Gram-positive bacteria), azithromycin (macrolide class) and cefipime (cephalosporin IV gen.) [195]. The opposite strategy is applied by *Klebsiella pneumoniae*, which creates a polysaccharide capsule around its OM [196].

At the same time other mechanisms exist, such as efflux pumps. Thus *Neisseria meningitidis* has Mtr efflux pump and PorB porine [197], *Klebsiella pneumoniae* KpnGH efflux system [198], Vibrio cholerae with OmpU (not clear mechanism of action, possibly related to acting as a sensor to trigger a DegS-dependent σ^E-activating cascade) [199], [200], in *Yersinia enterocolitica* RosA/RosB efflux pump plays a role in resistance [201].

With an emerging danger of bacterial resistance it is important to clearly understand mechanisms of action of last-resort antibiotics, such as polymyxins, and to use this data to improve or create new antibacterial agents.

Molecular dynamics

Molecular dynamics (MD) is the study of molecular motion, deformation and interaction over time. Predicting or interpreting these changes is essential in fields such as chemistry, physics, biology, or engineering [202]. The beginning of MD simulations can be attributed to the work of Alder and Wainwright who published the method in 1959. They pointed that complexity of multi-atom system description is mainly mathematical and that powerful enough computers would be a privileged tool to deal with such tasks [203]. The importance of computer-aided modeling was underlined by the Nobel Prize in chemistry of 2013, when Martin Karplus, Michael Levitt and Arieh Warshel were awarded "for the development of multiscale models for complex chemical systems" [204].

Before the era of modern computer simulations, the dynamics of only few types of systems for which equilibrium properties could be computed exactly such as ideal gas, harmonic crystal, *etc.* where studied. However, real materials rarely fit into one of those categories, driving to different approximations, which reduce the quality of the model [205]. The N-body problems – which historically originates from astrophysics and was found to be central for studying microscopic systems – does not have general closed-form solutions for more than two bodies, driving the use of computer simulations as a paramount tool [206]. Numerical simulations made computers to become a laboratory place for the so-called *in silico* experiments. Where the real-life experiments are often set up so that more and more constraints are placed to isolate the variables that have to be measured and thus increase the precision on the measure, numerical experiments are generally fashioned upside-down, by increasing gradually the complexity and adding more and more variables that are supposedly affecting the studied phenomenon, in order to obtain increasingly realistic measurements. This approach makes *in-silico* experiments not only an exceptional tool for validating experiments or theories but also for making real discoveries and proposing new paths to explore [4, 5].

However, molecular dynamics has some limitations, particularly with the spatial and temporal scales that are accessible. All-atom molecular dynamics (AA MD) simulations are used to study systems at the scale of tens of nanometers, such as the famous model of bacterial cytoplasm, where crowding effect was taken into account for the first time to create a realistic description of biomolecular interactions [207]. Coarse-grained molecular dynamics (CG MD) simulations can handle larger systems, up to few micrometers in size (Figure 20) [7, 8]. At the same time some global projects were realized with CG MD, such as cell model by Stevens et al [210] and mitochondrion model by Pezeshkian *et al.* [211]. However, both AA MD and CG MD are limited in terms of time scale, with the longest AA MD simulations currently limited to the millisecond range and require the use of massive supercomputer specialized for MD purposes, which are among the most powerful machines available **[212]**. Considering that many biological processes, such as protein folding, occur on the timescale of hundreds of microseconds and above, MD may still not be powerful enough for certain scientific purposes, making room for other types of simulations based, for instance, on continuum mechanics models.

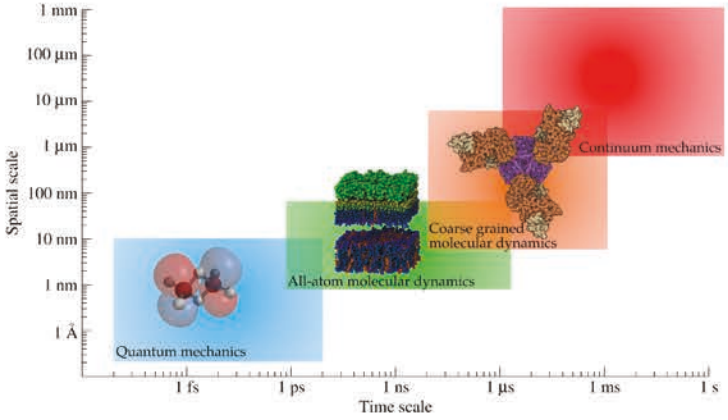

Figure 20: Characteristic scales associated with sizes of studied systems by such computational methods as quantum mechanical simulations (QM), AA MD , CG MD, and continuum mechanics.

Another important limitation of MD is the absence of electronic structure method to have a more realistic picture of the bonded interactions. This can make it challenging to study covalent bond-breaking and bond-making processes using classical MD alone [213]. However, it is worth noting the continuous efforts deployed to develop reactive force fields, such as ReaxFF [214]. QM structure and energy data train empirical force fields, moreover

electronic interactions driving chemical bonding are treated implicitly, allowing the method to simulate reaction chemistry [214].

I. Force fields, physical principles of MD

The basic idea of MD is straightforward: it requires a model system consisting of N particles for which Newton's equations of motion is applied. One may refine that description by mentioning that two main steps need to be undertaken in order to obtain measurements: 1. the system should reach thermodynamic equilibrium, 2. the dynamics should then be long enough so that the sampling of the configuration space will be satisfactory, as one should then proceed to make measurements of macroscopic variables by means of ensemble averages, which truthfulness will be ensured only by the sampling quality. Observables which we are able to measure with MD simulations should be described as a function of positions and momenta of the system, such as potential, temperature, root mean square deviation, *etc.* [205].

Molecular mechanics makes many simplifications. One of which is to consider the particles (atoms or beads) to be punctual. The interactions of each particle takes a formal description as a sum of 2-bodies, 3-bodies and 4-bodies interactions (Figure 21). A common example is the treatment of the inter-atomic bonds in AA MD that are modeled by spring-like potential. This simplistic description allows the atoms to interact realistically, the interaction being attractive if the spring is stretched over the equilibrium distance, and repulsive in the opposite case. The functional form of the potential energy as a sum of N-body contributions, along with the set of parameters defining each of those terms constitutes the force field [213]. These contributions are generally are by customarily divided as bonded interactions, which include bond stretching, angle bending, and torsion of dihedrals, and non-bonded interactions, which include repulsion resulting from Pauli exclusion principle, van der Waals and electrostatic interactions, and reads:

$$E = \sum_{bonds} E_{stretch} + \sum_{angles} E_{bend} + \sum_{dihedrals} E_{torsion} + \sum_{pairs} E_{non-bonded}.$$

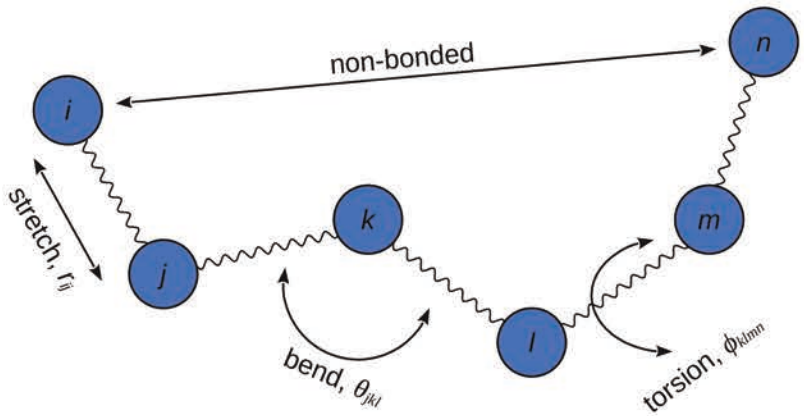

Figure 21: Scheme of the different interactions generally taken into account in a force field. The name of the interactions refers to the terms used in the manuscript. The common name of the name of the variable on which depend these interactions is written for the bonded interactions. Six atoms are represented and referred to as i, j, k, l, m, and n.

As mentioned above, the bond stretching term most generally takes the form of a harmonic oscillator such that $E_{stretch}=k_{stretch}(l-l_{eq})^2$, where $k_{stretch}$ is the force constant which describes the stiffness of the bond and where l is the length of the bond and l_{eq} is the length of the bond at equilibrium [213]. The harmonic form is suitable for the majority of systems, however, if one needs to be able to reproduce such values as the frequencies linked to the vibrational modes, the functional form must be improved by introducing some anharmonic terms. The harmonic and the latter anharmonic terms come from the Taylor expansion made to build the formal expression of the potential [215].

For the bending energy, the most common form is also harmonic, hence, the increase in the energy will be proportional to the square of the increase of the difference in the angle θ between the three atoms implied in this interaction and the angle θ_{eq} at equilibrium, such that: $E_{bend}=k_{bend}(\theta-\theta_{eq})^2$.

For the torsional term, the angle ϕ of the system, consisting of 4 consecutively bonded atoms referred to as *i*, *j*, *k*, and *l*, is an angle along *j*-*k* bond, and between *i*-*j* and *k*-*l* bonds. It is noticeable that this functional is 2-π periodic, so the energy varies as in a sine or cosine pattern or as a combination of them [213], such as it is described in the commonly used Ryckaert-Bellemans function which reads: $E_{rb}(\phi_{ijkl})=\sum_{n=0}^{5} C_n(\cos(\psi))^n$, $\psi=\phi-\pi$.

A final optional term of the potential energy which is often used is a sum over the so-called improper dihedrals. They are used to keep specific molecular geometries inside a given molecule, such as planar groups which would tend to adopt other conformations, or to avoid molecules flipping to their mirror images. For this type of dihedrals a harmonic potential is commonly applied to the angle ξ between planes generated by the atoms (*i*, *j*, *k*) and (*j*, *k*, *l*), where *i*, *j*, *k*, *l* refer to four consecutively bounded atoms in a given molecule. A common expression of that potential then reads: $E_{id}(\xi_{ijkl}) = \frac{1}{2} k_{\xi} (\xi_{ijkl} - \xi_0)^2$, where ξ_0 is the equilibrium value of this angle. This kind of terms are necessary for aromatic groups and many other structures, such as three atoms attached to the single "central" atom [216].

All terms mentioned above are bonded terms, as they describe interactions only between the atoms which have chemical bonds between them. On the other hand, non-bonded terms, describe interactions between all pairs of atoms, regardless of their chemical electronic bonds. Hereafter is a brief description of the most common functionals referring to them.

Van der Waals interactions describe the attraction between atoms and may be interpreted as a non-polar part of the non-bonded interactions, *i.e.* interactions which are not of electrostatic origin nor due to the displacement of the electronic cloud. Traditionally, the functionals describing it also include a repulsive term at very short distances, as a direct consequence of the Pauli exclusion principle. The general functional form, for two atoms *i* and *j*, reads: $E_{vdw}(r_{ij}) = E_{repulsion}(r_{ij}) - \frac{C_{ij}}{r_{ij}^6}$, where C_{ij} is a constant and r_{ij} is the distance between atoms *i* and *j* [215].

One of the most common potential used for describing van der Waals interactions is the Lennard-Jones potential (E_{LJ}). It is an inexpensive way to compute both repulsive and attractive terms, at the contrary to Buckingham potential – and as far as for large molecules calculating the non-bonded energy is the most time-consuming part [215] – that is why Lennard Jones (LJ) potential is the most widely used one. The expression of this potential is the following: $E_{LJ}(r_{ij}) = 4\varepsilon_{ij}\left(\left(\frac{\sigma_{ij}}{r_{ij}}\right)^{12} - \left(\frac{\sigma_{ij}}{r_{ij}}\right)^{6}\right)$, where σ_{ij} and ε_{ij} are parameters which characterize respectively the distance at which the potential is zero, and the depth of the potential well, *i.e.* the strength of the interaction between the two given atoms. When this

potential is implemented in a given force field, it is common that only the values of σ and ε are explicitly defined from quantum mechanical computations only for the interactions between pairs of atoms of the same type. Thus, the estimate for the van der Waals potential between atoms of different types is generally given using so-called combination rules which give an estimate of σ and ε from the defined parameters. The definition of this rule is made for the entire force field. For instance, in the case of CHARMM general force fields [217], the Lorentz-Berthelot combination rules are used, such that: $\begin{cases} \sigma_{ij} = \frac{\sigma_{ii} + \sigma_{jj}}{2} \\ \varepsilon_{ij} = \sqrt{\varepsilon_{ii}\,\varepsilon_{jj}} \end{cases}$, where i and j refer to two atoms of different types [216].

In most classical MD simulations, the force field is optimized to only one electronic state for each molecules in presence. This state is generally the ground state. In the case of the electrostatic interactions, the partial charges of each atom are computed in the ground state for each molecule. Those computations are either done in the absence of any environment or in the presence of the most common medium which is generally water. In the scope of biological systems where the molecules of interest often cross two media (water and lipids), this might lead to some inaccuracies. These partial charges are most commonly computed by fitting the calculations performed by electronic structures methods to the Coulomb potential E_{cl} which is used to describe electrostatic interactions as pair-type interactions, such that $E_{Cl}(r_{ij}) = \frac{q_i q_j}{\varepsilon r_{ij}}$, where q_i and q_j are the partial charges of atoms i and j respectively and ε being a dielectric constant.

II. Periodic boundary conditions

Periodic boundary conditions are used to avoid problems at the edges of the simulation box while allowing to simulate a system with a small number of atoms by making systems virtually infinite. It means that the simulation box – the virtual “container” of all the atoms of the system – is surrounded by translated copies of itself creating thus an infinitely periodic lattice.

The box can be of a different geometries: cubic, rhombic dodecahedron, or truncated octahedron being the most common. The rhombic dodecahedron is the smallest and most regular space-filling unit cell: each of the 12 image cells is at the same distance and the

volume is 71% of the volume of a cube having the same image distance. It is thus customary to use better space-filling geometries, the latter could be saving ~30% of CPU time using Gromacs package [218]. However, the choice of the geometry of the simulation box is generally driven by the type of system which is simulated.

Gromacs package also uses the minimum image convention, which means that for short-range non-bonded interactions, only the nearest image of the box will be used. This implies that cut-off radius can't exceed half of the shortest box vector. One should note that the box size is an important parameter while designing some system. One should always be sure that a molecule does not self interact by choosing accordingly a length of the box vectors should that exceeds the longest dimension of the molecule plus twice the cut-off radius [216].

III. Treatment of non-bonded interactions

i. van der Waals interactions – Hydrogen bonds, long-range treatment, and dispersion corrections

Interestingly, the definition of the van der Waals interactions raise difficulties for atoms involved in hydrogen bonds. Indeed, even though the main contribution to hydrogen bonds comes from electrostatic attraction, it was shown that shorter range – yet steeper – van der Waals interactions give better results. Hence, some force field introduce the use of a special pairs list, where all hydrogen bonds are assigned specific parameters, non-typical for regular interaction for these atom types. Alternatively, the use of a Lennard-Jones 10-12 has been reported (where 10-12 are the exponents of the attractive and repulsive terms respectively) [215].

To save computational resources, it is customary to introduce a cut-off distance r_C, such that $E_{LJ}(r_{ij})=0$ if $r_{ij} \geq r_C$. The value of r_C is taken so that the dispersion interactions will be small and generally range between 0.8 and 1.5 nm. This early method would define a plain, abrupt cut-off of the LJ potential[6]. However, most of the commonly used force fields (see Table 5) will also shift the potential so that $E_{LJ}(r_{ij}=r_C)=0$, to avoid abrupt changes of forces at $r_{ij}=r_C$. Another strategy which is often implemented is to smoothly switch the forces to zero between another value of $r_{ij}=r_{vdw\text{-}switch}$ *and* $r_{ij}=r_C$.

[6] We assume that the van der Waals are described by a LJ potential. The description of the plain cut-off applies also to other potentials, *e.g.* Buckingham potential. However, since we will describe smoother cut-offs which could be potential dependent, and that LJ potential is by far the most used for most of the available force fields, we made the choice to focus on that one.

Table 5: Example of parameter sets for the van der Waals interactions in the Gromacs packages [6] for a selection of commonly used force fields. Note that for each force field, more than one set of parameters could be valid. For instance, Martini 2 was originally implemented using a force switch, and making use of the group algorithm neighbor searching procedure, leading to a recommanded value of r_C=1.2 nm. For the Gromacs package, the type of cut-off is defined by vdw-modifier, $r_{vdw\text{-}switch}$ is referred to as rvdw-switch, r_C is denoted rvdw, the neighbor searching algorithm is defined by cutoff-scheme, and DispCorr permits to implement dispersion corrections to either the energy, the pressure, or both.

Gromacs package option	**Berger [219]**	**CHARMM 36**	**Martini2 [220]**	**Slipids [221]**	**Amber ff14SB [222]**
vdw-modifier	Potential-shift	Force-switch	Potential-shift	Potential-shift	Potential-shift
rvdw-switch	N/A	1.0	N/A	N/A	N/A
rvdw	1.0	1.2	1.1	1.4	0.8
cutoff-scheme	Verlet	Verlet	Verlet	Verlet	Verlet
DispCorr	Enerpres	no	no	Enerpres	Enerpres

In order to further reduce the computational cost, the use of cut-offs is associated to a neighbor searching algorithm. The simplest algorithm generates a pair list of atoms every *nstlist* step. This list contains, for each atom i, all the other M_i atoms which are susceptible, within *nstlist* time steps, to have a distance such that for any j atom of this list, we could possibly satisfy $r_{ij}<r_C$. Thus, for a system of N atoms, only the $\sum_{i=1}^{N} M_i$ distances shall be evaluated each step, instead of $N(N-1)$ otherwise[7]. In the past years, modern MD packages, including Gromacs, generally make use of the so-called Verlet list algorithm which is a version of the neighbor algorithm showing very good scalability.

At distances $r_{ij}\sim r_C$, the repulsion term will be negligible, however, the truncation of that potential leads to discrepancies on the system's energy and pressure. That correction is especially important on the pressure. For example, using a simple water box with a cut-off of 0.9 nm and a density of 1000 kg cm^{-3}, the correction on the energy is of 0.75 kJ mol^{-1} per molecule while the correction for such system, accounting for the use of SPC model of

[7] In reality, in the frame of this neighbor algorithm, other optimizations are made. For instance, instead of computing all the r_{ij} distances from that list and to compare them to the cut-off distance, to check whether they fall inside a sphere of radius r_C centered around atom i, the algorithm preselects only the atoms which fit in a cube of the same center and of dimension $2\ r_C$. This action will save some extra computation of the distance $r_{ij}=\sqrt{\Delta x^2+\Delta y^2+\Delta z^2}$ for all atoms which do not satisfy a simpler condition to compute being $\begin{cases}\Delta x<r_C\\ \Delta y<r_C\\ \Delta z<r_C\end{cases}$. On top, it is customary to exclude for the pairs list atoms which from the same molecules which are a few bonds away, for which non-bonded interactions are most likely to occur.

water, would be of -280 bar [218]! As denoted in Table 5, most of the modern AA force fields either recommend or are compatible with the use of such corrections as implemented in the Gromacs package.

ii. Electrostatic interactions – Reaction field, Ewald summation

Since the electrostatic potential decreases slowly in comparison to dispersion potential, applying cut-offs distances in the same fashion as for the van der Waals interactions would lead to drastic inaccuracies. To better picture the problem, let's consider using a cut-off at $r=r_C$, similarly to what was done in the previous section about the dispersion interactions. The general form of a decaying pair potential can be shortened to $E(r_{ij})=\frac{A}{r_{ij}^n}$, with A a constant of the system, and n, the power which sets the steepness of the decay. For such potential, in the case of a system of uniform density ρ, the tail of the potential that is the potential beyond r_C reads [223] :

$$E_{tail}(r_{ij};n)=2\pi N\rho\int_{r_c}^{\infty}\frac{Ar_{ij}^2}{r_{ij}^n}dr_{ij},$$

where N is the total number of atoms in the system, and from that expression, we see that $E_{tail}(r_{ij};n)$ is infinite for $n \leq 3$. Hence, potentials with $n \leq 3$ in a inhomogeneous system will be only conditionally convergent. On top of this drastic problem, convergence of the direct summation of each contribution to the Coulomb interaction is very slow.

Thus, it is customary to make use of methods based on the Ewald summation to compute this potential in the frame of MD simulations. This method relies on the fact that most MD simulations use periodic boundary conditions, creating a virtually infinite system [216]. The electrostatic potential of an infinitely periodic system of N atoms reads:

$$E_{Cl}(r_{ijn})=\frac{1}{8\pi\varepsilon}\sum_{n_x=-\infty}^{\infty}\sum_{n_y=-\infty}^{\infty}\sum_{n_z=-\infty}^{\infty}\sum_{i=1}^{N}\sum_{j=1,\,j\neq i\,\text{if}\,n_x=n_y=n_z=0}^{N}\frac{q_iq_j}{\left|r_{ij}+n_xL_x+n_yL_y+n_zL_z\right|},$$

where L_x, L_y, L_z are the lengths of the simulation box considered being a rectangular cuboid, and n_x, n_y, n_z are integers referring to the n^{th} periodic box along the given axis. Each punctual atom i is attributed a charge density distribution ρ_i such that:

$$\rho_i(\vec{r}) = q_i\,\delta(\vec{r} - \vec{r}_i),$$

where δ refers to a Dirac distribution. The Ewald summation method, introduced in 1921 [224] consists in computing the electrostatic potential for two contributions: a short-range and a long-range contribution. To do so, an arbitrary Gaussian distribution G is artificially added and subtracted to the charge distribution:

$$\begin{gathered}\rho_i(\vec{r}) = \rho_i^S(\vec{r}) + \rho_i^L(\vec{r}) \\ \rho_i^S(\vec{r}) = q_i\,\delta(\vec{r} - \vec{r}_i) - q_i G(\vec{r} - \vec{r}_i). \\ \rho_i^L(\vec{r}) = q_i G(\vec{r} - \vec{r}_i)\end{gathered}$$

Subsequently, the Poisson's equations for the short and long range contributions can be solved. Taking into account that punctual charge distribution can be taken as a limit case of a Gaussian distribution with a standard deviation equal to zero, it is thus possible to express the both contributions as a function of the error function and the complementary error function, respectively *erfc* and *erf*. Both contributions are still under the form of the summation introduced above. In the case of the short-range contribution, the terms for bigger values of the distance between atoms *i* and *j* are rapidly decreasing, ensuring thus, the rapid convergence of this summation.

However, the long-range contribution should be computed differently as the infinite sum over the *erf* functions does not converge rapidly. The idea proposed by Ewald for this term is to obtain a converging series in the reciprocal space. Since we work on a periodic lattice, we can express the charge density distribution by periodic function and apply the analogy of the Bloch's theorem. Hence, the Poison's equation can be advantageously solved in the reciprocal space. It is important to note, that simplification used implies that the system has a neutral charge – which explains the necessity to use counterions in MD simulations using Ewald summation. The rapid convergence of the long-range distribution in the reciprocal space is ensured by the presence of an exponentially decaying term of the form $e^{\frac{-\sigma^2|\vec{k}|^2}{2}}$, where σ is the standard deviation of the Gaussian distribution and $\vec{k}$ is a Bloch vector describing the periodicity of the system in the reciprocal space. Hence, the sum is rapidly converging, as the contributions for periodic images of the reciprocal for bigger values of $|\vec{k}|$ become rapidly small.

The complexity of this method for an optimal choice of σ can be driven to an algorithmic complexity of $\mathcal{O}(N^{3/2})$ which is still prohibitive for large systems. To optimize further this method, much work was done to lower the complexity of the long-range contribution as the direct sum on the short-range contribution alone has a low complexity of $\mathcal{O}(N)$. Particle mesh Ewald (PME) and smooth particle mesh Ewald[8] (sPME) were developed by Darden and co-workers [225] where the use of the efficient fast Fourier transform (FFT) algorithm is made to compute the Gaussian contributions of each particle on a grid that creates a discrete mesh over the simulation box. This implementation drives the complexity to drop to $\mathcal{O}(N \log N)$.

iii. Treating long-range non-bonded interactions of bonded atoms

Applying the non-bonded terms between close neighbors inside a given molecule is detrimental to the accuracy of the computations. Hence, non-bonded interactions between atoms *i*, *i+1*, *i+2*, and *i+3* (where *i+1* is directly bonded to *i*) for a same molecule are treated specifically. First, the atoms *i+1* and *i+2* are excluded from the non-bonded interactions. Secondly, the interactions between atom *i* and atom *i+3* are scaled by two weights, generally referred to as $fudge_{QQ}$ and $fudge_{LJ}$ applied respectively to the Coulomb and van der Waals interactions. To apply these modifications, a so-called exclusion list is created for the atoms *i+1* and *i+2*, and the 1-4 interaction list is defined for the interactions between atom *i* and the fourth closest atom(s), *i+3*.

IV. Potential energy surface

It is necessary to introduce the terminology that will be used throughout this manuscript, especially in the context of free energy computations. The force field associated with a system allows us to construct the complete potential energy surface (PES) for a given electronic state, which is typically the ground state in classical molecular dynamics (MD) simulations. Hence, each MD simulation frame represents one point on this hypersurface. When a system undergoes transformations between different energy minima on the PES, it follows a path of minimum energy, known as the minimum energy path (MEP). We will use the convention which tends to be employed in the scientific community by referring to the mathematical definition of this coordinate as the system reaction coordinate (RC) for that given transformation. On the other hand, since the analytical definition of that RC is

8 The latter is the version implemented in Gromacs packages

generally unknown, one often has to propose some analytical definition of that path which can arguably be considered close to the RC. This analytical expression is referred to as a collective variable (CV). A CV is thus defining an axis on which one can project the PES to have a better understanding of local energy minima, barriers, or saddle points during a given transformation.

As entropy and temperature play significant roles in natural transformations, our focus is generally on exploring regions of the free energy surface (FES) that are close to the minimum free energy path (MFEP). To accurately determine a point on the FES, extensive sampling of the phase space at that point is required. Further details regarding enhanced sampling methods in MD simulations will be discussed later in this chapter. However, it is worth noting that, to keep computational costs manageable, it is common practice to limit the dimensionality of these projections, typically using only one or two CVs, which provides only a partial view of the FES. Therefore, it is important to ensure that the set of CVs generates a base that is as complete as possible.

During the studied transformation – or reaction – reactants, products, and transition states are stationary points of the PES – *i.e.* points for which the PES as a zero gradient along one or more coordinates [213]. Mathematically speaking, any transition state on the PES is defined by $\partial^2 E/\partial^2 q<0$, for all the q geometric parameters (bond length, bond angle, *etc.*) which are components of the reaction coordinates, while for all other directions the value of the second derivative will be higher than zero. Points which have more than one coordinate where the second derivative is negative are called higher-order saddle points or hilltops [213].

The potential energy functional introduced earlier as a sum of N-bodies interactions depends *in fine* on the positions of the punctual representations of the atoms in the system. In other terms, we use only the nuclei coordinates as parameters to compute an estimate of the real PES function. This is a direct consequence of the Born-Oppenheimer approximation which shows that taking nuclei in the molecule as stationary with respect to the electrons is a good estimation [202]. The Born-Oppenheimer approximation is the assumption that the electronic motion and the nuclear motion in molecules can be separated [226]. The motion of nuclei is much slower than those of electrons due to a huge difference in mass of electrons and nuclei: a hydrogen nucleus is around 2000 times heavier than an electron, and

for the majority of systems the Born-Oppenheimer approximation creates only small errors [11, 15]. It should be noted, that many *ab initio methods* do not make that assumption [215].

The main methodology used to determine the set of parameters for a force field is by fitting the individual terms to the results of numerical quantum computations or experiments [17]. For instance, in the case of Slipids force field, experimental heats of vaporization and densities were used to fit the LJ parameters [227].

V. Ensembles, thermal and mechanical macroscopic quantities

MD simulations are powerful computational tools which permit to generate the data on which one will make measurements in order to investigate the behavior of complex systems at the atomic level. To connect MD simulations with macroscopic observables and obtain meaningful results, we should introduce the concept of statistical ensembles. Statistical ensembles provide a statistical framework to describe the collective behavior of many particles in terms of their probabilities and distributions.

i. Ergodicity, statistical ensembles, and measure in MD simulations

The ergodic principle is fundamental in MD simulations. It states that, given enough time, a dynamical system will explore all configuration space compatible with its energy, volume, and particle constraints. This principle is crucial because it allows us to connect the temporal evolution of a system in a simulation to the ensemble average properties of the system at equilibrium. This assumption is generally not verified for each and every system as it is very difficult to prove a system ergodic. The main conclusion from that assumption is that the frames of the simulations are as much a representation of the time evolution of the system as they are supposedly independent experiments. As a note, it is important to remember that memory effects are always present in the trajectories resulting from MD simulations. That means that each and every successive frames are correlated. Thus, when one will measure a macroscopic observable, it might be good either to use frames which are far enough from one another to avoid biasing the result or to use statistical methods to correct that correlation. It is anyway advisable to compute the integrated autocorrelation time (IACT) to get an estimate of the duration of that memory effect.

To obtain reliable and accurate results when doing a measure from MD simulations data, we should simulate a system for a sufficiently long time to ensure that it reached a

thermodynamic equilibrium. Then, one needs to run another sufficiently long simulation so that it explores all relevant configurations. The measurements should then take the form of an ensemble average, reflecting the statistical behavior of the system rather than the behavior of individual trajectories. The ensemble average is a statistical average taken over all possible configurations of a system within a given ensemble. It provides a way to calculate the average value of a property of interest, such as energy or position, considering the probabilities associated with each configuration. Mathematically, the ensemble average, denoted by ⟨A⟩, of a property A is given by:

$$\langle A \rangle = \sum P(i) A(i),$$

where *P(i)* represents the probability of configuration i occurring in the ensemble, and A(i) represents the value of property A for that particular configuration. The sum is taken over all possible configurations in the ensemble. In the case of an ergodic system, the time average of a property can be related to the ensemble average. The ergodic principle states that, over a sufficiently long time, the time average of a property is equal to its ensemble average. Mathematically, this is expressed as:

$$\lim_{T \to \infty} \left(\frac{1}{T} \right) \int_0^T A(t) dt,$$

where *T* is the total time of observation, A(t) represents the value of property A at time t, and the integral is taken over the time period [0, T]. Thus, this expression represents the time average of property A.

The fact that a measure in MD simulations is an ensemble average directly implies that the system should be simulated in a given statistical ensemble. The microcanonical ensemble, or NVE ensemble, is considered the natural ensemble for MD simulations. It describes an isolated system with a fixed number of particles (N), fixed volume (V), and fixed total energy (E). In the NVE ensemble, the system conserves its energy, allowing for accurate and straightforward integration of the equations of motion. This comes naturally with a pristine implementation of a MD software as the integration algorithm used are symplectic – *i.e.* they conserve the volume of the phase space – which implies that they also conserve the

energy of the system[9]. In reality, numerical approximation will always lead to some small energy drift, but that can be monitored and will always be very small. On top, the volume of the simulation box and the number of particles are initial parameters. That means that a pristine MD code will surely conserve those two properties. This is why the NVE ensemble is considered the natural ensemble in MD simulations. However, simulating systems in the NVE ensemble is not always practical. Lots of phenomena are temperature-dependent, and it is experimentally very difficult to work in the microcanonical ensemble – which would limit the direct comparison of MD-based measurements with *in vitro* or *in vivo* experiments.

ii. Temperature coupling, flying ice-cube effect, hot solvent/cold solute problem

To simulate systems at a desired temperature, the NVT ensemble, or canonical ensemble, is commonly used in MD simulations. In this ensemble, the system is in contact with a heat reservoir at a fixed temperature (T). The exchange of energy between the system and the reservoir ensures that the system reaches the desired temperature. Various algorithms are used to control the temperature, such as Berendsen, stochastic velocity rescaling (called v-rescale in Gromacs package), Andersen and Nosé-Hoover thermostats [228].

The simplest algorithm used for temperature coupling is the Berendsen algorithm [229]. In this case, the system at temperature T is coupled to a heat bath which is set at a given temperature T_0. This thermostat corrects the temperature of the system such that its deviation exponentially decays with time. This decay is set by a time constant τ_t in the following way:

$$\frac{dT}{dt} = \frac{T_0 - T}{\tau_t}.$$

However, Berendsen thermostat suppresses kinetic energy fluctuations, which drives the system not to sample the given statistical ensemble (*i.e.* canonical or isobaric-isothermal ensemble). The repeated velocity-rescaling procedure applied by this thermostat has other consequences. Indeed, it was shown [230] that this method violates the equipartition theorem which states that, for a system in thermal equilibrium, energy is shared equally for each degree of freedom. Because of that rescaling, high-frequency fundamental modes are

9 In reality the preservation of the volume of the phase space is a stronger property than just the energy conservation. It comes from the fact that any Hamiltonian system obeys the Liouville's theorem which states so. Later, in the manuscript, when we mention the use of temperature and / or pressure coupling, we may modify the equations of the dynamics and we are not anymore studying a Hamiltonian system.

drained to low-frequency modes, such as center of mass (COM) translation. Hence, especially for simulations where one does not remove the COM translations of (group(s)) of the system, the so-called flying ice-cube effect may occur. This non-physical artifact has one well-known visual consequence that takes the form of a seemingly frozen part of the solvent, flying over the simulation box[10]. Nonetheless, Berendsen thermostat is still widely used, although it is known to cause drastic problems [228]. At the present time, there are very few reasons to keep using it: 1. if, for some reason, the force field developers explicitly mention that its use is required, but that should still drive the users to exert extra care to make any conclusions on their simulations, or 2. in order to approach thermodynamic equilibrium during the equilibration procedure of a simulation, on which no properties are going to be computed[11].

It is noteworthy that the stochastic velocity-rescaling thermostat [232] – otherwise referred to as Bussi-Donadio-Parrinello thermostat – is an extension of Berendsen thermostat that does not exhibit the aforementioned artifact. That is because this algorithm preserves the fluctuations of the canonical ensemble, thanks to the introduction of a stochastic term. This term allows to not select the exact value of the target kinetic energy, but a value taken from the target distribution of the kinetic energy with an average taken as the target temperature. This algorithm is commonly used for production run as it is both simple to implement, and preserves the statistical ensemble of the system.

It is worth mentioning that nonphysical behaviors in simulations attributed to the presence of a thermostat are not limited to the flying ice-cube effect. It was shown that temperature coupling could influence the flux of water through nanotubes [233], the use of a single thermostat in the case of inhomogeneous solute solvent systems could lead to gradients of temperatures – even for other algorithms than Berendsen thermostat – leading to the so-called hot-solvent / cold-solute problem **[234]–[236]**.

10 It should be noted that the absence of such flying cube in the system does not mean that no artifacts are present. The violation of the equipartition theorem can trigger the development of gradients of temperature across the system, and the accumulation of kinetic energy either into the translational or the rotational degrees of freedom.

11 This use is now very common, for instance, CHARMM-GUI website [231], which is routinely used to prepare simulation systems, provide a set of equilibration steps which most often make use of Berendsen algorithm.

iii. Pressure coupling

Similarly as with systems with constant temperature, the choice of the pressure coupling algorithm is crucial when simulating systems under constant pressure conditions. The isobaric-isothermal ensemble (NpT) and its variations – namely isobaric-isothermal-constant lateral surface area of membranes (NpAT) and isobaric-isothermal-constant lateral surface tension of membranes (NpγT) [237] – are very often used as they mimic conditions with are very often used experimentally. In MD simulations, pressure coupling algorithms allow for the adjustment of the system's volume to maintain a desired pressure. The aforementioned NpAT and NpγT variations allow for controlling additional variables like surface tension or area fluctuations. These ensembles are particularly relevant when simulating systems with interfaces, such as liquid-liquid interfaces or lipid membranes. Berendsen algorithm has been commonly used for pressure coupling for a long period, although algorithms preserving the correct statistical ensemble are now the golden standard. As such, we can cite Parrinello-Rahman barostat [238], or an analogous algorithm to stochastic velocity rescale called stochastic cell rescaling [239].

VI. Energy minimization

Exploring PES and locating stationary points are important for geometrical optimization of the studied molecules. This step is generally called energy minimization. It also allows the system to get rid of steric clashes - *i.e.* improper relative positions of different molecules. While building a system, it is customary to use automatized process to add the solvent. Solvent molecules at the interface with solutes can be too close or in unfavorable regions, *e.g.* inside the hydrophobic core of a membrane, inside some unfavorable regions of a protein, or simply too close to the atoms of other molecules. Energy minimization procedure will be used to manage with these issues and get a sufficiently stable structure to further proceed with MD simulations.

Energy minimization algorithms requires two inputs: 1. the definition of energy surface, *i.e.* a force field, and 2. the initial coordinates of each and every atoms in the system, *i.e.* a structure file. These inputs will be used by the minimization algorithm to determine the fastest direction towards local minimum of the PES and the distance to the minimum in that direction [240]. In computational chemistry, we make an assumption that the gradient can be calculated analytically. Also, in practice we consider the optimization converged when the

gradient the potential energy change between two iterations becomes sufficiently small or if the maximum forces between two atoms is lower than some predefined tolerance. This approach obviously has limitations for functions with a very flat energy surface in the studied region, because they can meet the convergence criteria without being in proximity of a stationary point [215].

The steepest descent method – which is the most frequently used one – computes a displacement in order to minimize the maximal force acting on any atom. Thus, the set of new positions of all the N atoms of the system and referred to as $\vec{r}$ is computed in the following way for the step k of the minimization process:

$$\overrightarrow{r_{k+1}} = \vec{r_k} - \frac{\overrightarrow{F_k}}{max\left(\left|\overrightarrow{F_k}\right|\right)} h_k,$$

where $\overrightarrow{F_k} = -\vec{\nabla} E_k$, which permits to propagate the system in the opposite direction to the gradient of the potential E. The motion is scaled both, by the largest scalar force on any atom, and by the maximum displacement at the step k. This displacement depends on the initial maximum displacement h_0. For any step $k+1$, the displacement is defined as such:

$$\begin{cases} h_{k+1} = 1.2\, h_k & \text{if } E_{k+1} < E_k \\ h_{k+1} = 0.2\, h_k & \text{if } E_{k+1} \geq E_k \end{cases}.$$

The algorithm will then stop either if the maximal force is lower than some tolerance, or if a maximum number of steps was reached.

More refined methods are also often implement, such as the conjugate gradient method, or even some quasi-Newtonian method such as the limited-memory Broyden-Fletcher-Goldfarb-Shanno algorithm [218] which can be advantageously used, either along with a steepest descent procedure or as a standalone minimization procedure in case the initial attempts of energy minimization did not succeed.

VII. Numerical integration of the equations of motion

The heart of MD simulations consists in the integration of the classical equations of motion applied to each punctual atom to which is associated a force which is derived from the potential generated by the sum of N-body contributions described above and which is set by

the choice of the force field. We mention in section V that, since we pristine MD simulations work with Hamiltonian systems, these integrators should be symplectic. This fundamental property implies that upon any canonical transformation such as time-integration of the equations of motion, the volume of the phase space of a Hamiltonian system is conserved. Since a time-independant Hamiltonian system will conserve energy and other properties, the use of symplectic integrators will also conserve those system properties, which are fundamental to follow the dynamics of the system accurately.

Since one turns into numerical integration of the equations, that implies that the user should choose a finite time step such that we sample well enough the highest-frequency modes of the system. Some of the fastest vibrational modes are linked to C-H bonds, which have a period around τ~11 fs [241]. It can be shown that – given the order of the symplectic integrator – its stability can be assessed for a given value of τ. For a value of 10 fs, the maximum time-step for a Verlet integrator is of 2.25 fs [241]. This explains why it is customary to choose a value Δt=1 fs AA MD for which all bonds are treated explicitly and not as constraints.

To apply the chosen integrator numerically, one should discretize the Newton's equations – *e*.g. by means of a Taylor expansion, which is generally written for both coordinates and velocities for any given atom *i* such that:

$$\begin{cases} \vec{r}_i(t+\Delta t)=\vec{r}_i(t)+\vec{v}_i(t)\Delta t+\vec{F}_i(t)\frac{\Delta t^2}{2m_i}+\vec{\dot{F}}_i(t)\frac{\Delta t^3}{3!}+\mathcal{O}(\Delta t^4) \\ \vec{v}_i(t+\Delta t)=\vec{v}_i(t)+\vec{F}_i(t)\frac{\Delta t}{m_i}+\vec{\dot{v}}_i(t)\frac{\Delta t^2}{2}+\vec{\ddot{v}}_i(t)\frac{\Delta t^3}{3!}+\mathcal{O}(\Delta t^4) \end{cases},$$

where $\vec{F}_i$ is the force acting on the atom *i*. The Verlet family of symplectic integrators was thus developed to integrate these equations and the Verlet integrator is obtained by summing $\vec{r}_i(t+\Delta t)$ and $\vec{r}_i(t-\Delta t)$ and reads:

$$\vec{r}_i(t+\Delta t)=2\vec{r}_i(t)-\vec{r}_i(t-\Delta t)+\vec{F}_i(t)\frac{\Delta t^2}{2m_i}+\mathcal{O}(\Delta t^4).$$

Thus, the velocities are computed simply as follows:

$$\vec{v}_i(t) = \frac{\vec{r}_i(t+\Delta t) - \vec{r}_i(t-\Delta t)}{2\Delta t} + \mathcal{O}(\Delta t^2),$$

which drives the velocities to be only of order 2. That later issue drives to summing errors rather fast and might not be appropriate for long runs of MD simulations. At the moment, two numerical symplectic integrators are solving this issue and are the most often used for MD simulations, namely velocity-Verlet and leap frog integrators.

VIII. Free energy calculations

Free energy is a state function in thermodynamics that plays a central role in understanding the behavior of physical and chemical systems. At its core, free energy represents the maximum amount of work that can be extracted from a system while keeping its temperature and volume (or pressure, depending on the ensemble) constant. We propose here to briefly explain the importance of free energy measurement in MD simulations, driving to a first overview at the thermodynamic scale. The statistical physics origin of MD simulations also rises in this very topic. We show in this section why pristine MD simulations are not appropriate to make such measurements. Finally, we describe the method we used the most during the present work to compute the free energy profile for given processes, *i.e.* the umbrella sampling procedure.

i. Thermodynamics, work, kinetics, and experiments

In thermodynamics, there are different definitions of free energy, each tailored to specific ensembles and related conditions. The two most commonly used definitions are the Gibbs free energy (G) and the Helmholtz free energy (A). The Gibbs free energy is applicable to systems at constant pressure, while the Helmholtz free energy applies to systems at constant volume. Mathematically[12], the Gibbs free energy is defined as $G = H - TS$, where H represents the enthalpy, T is the temperature, and S is the entropy. On the other hand, the Helmholtz free energy is given by $A = U - TS$, where U is the internal energy of the system.

These different formulations of free energy provide valuable insights into the thermodynamic favorability of a process. If the free energy infinitesimal change for a system – which is formally the differential form, respectively dG and dA – is negative, it indicates that the related infinitesimal process is thermodynamically favorable, meaning it

12 For the sake of simplicity, we stay in the frame of closed-systems, *i.e.* for a constant number of particles N in the system.

can occur spontaneously. Conversely, a positive free energy change suggests that the process is energetically unfavorable and requires an input of energy to proceed. By understanding the free energy landscape, one can predict and analyze various phenomena, ranging from chemical reactions and phase transitions to the stability of biological macromolecules.

Understanding the variation of free energy is crucial in MD simulations as it provides insights into the available work of a system which is mediated by thermal energy. To better see how thermal energy drives a given process, one can relate to the Arrhenius law, which links the speed of a reaction to the probability of a chemical process crossing an activation barrier. This probability depends, obviously, on the height of the barrier – which can be proven[13] to be $\Delta G^{\ddagger}$, *i.e.* the difference of free energy between the barrier and the initial state of the reaction – but the exponential term is also inversely proportional on the temperature of the system, which governs the Brownian motion and determines the speed at which the system explores the configuration space.

In MD simulations, the work done in different ensembles, such as the canonical ensemble (*NVT*) and the isobaric-isothermal ensemble (*NpT*), can be formally related to the free energy by examining the differential form of the free energies in each case. By analyzing the differential expressions of Gibbs free energy (*dG*) and Helmholtz free energy (*dA*) in these ensembles, one can establish a formal link between the variations in free energy and the work done by the system. The differential Gibbs and Helmoltz free energy (*dG*) are related to the reversible work (δW_{rev}) performed by the system. The reasoning is written here only in the case of Gibbs free energy as it is very similar for Helmoltz free energy:

$$\begin{cases} dG = dH - TdS - SdT \\ dG = dU + pdV + Vdp - TdS - SdT \\ dG = \delta Q + \delta W + pdV + Vdp - TdS - SdT \\ dG = TdS + \delta W_{other} - pdV + pdV - TdS + SdT \\ dG = \delta W_{rev} + SdT \text{ if process is reversible } (2^{nd} \text{ law of thermodynamics}) \\ dG = \delta W_{rev} \text{ if } T = const \end{cases},$$

13 In the frame of the transition state theory (TST), the Eyring equation was formally introduced, based on developments from statistical physics.

The reversible work (W_{rev}) corresponds to the maximum work that can be extracted from the system, and it represents the reversible component of the total work done by the system. In contrast, the irreversible work arises due to dissipative processes and is not accounted for in the differential free energy expressions. It is important to note that the reversible work is the component directly related to the changes in free energy, as it represents the work that can be recovered without any energy losses.

Furthermore, the aforementioned Arrhenius equation shows that accessing to the free energy variations of certain processes could be a step to a better understanding of the kinetics of a process in a second step. Conversely, other processes, such as ligand permeation, require to access the free energy profile for the process in order to access to an estimate of the kinetic of the process, such as the permeability coefficient [242].

Finally, free energy variations not only offer fundamental insights into the thermodynamic favorability of a process but also find their origin in experimental observations. Experiments are typically conducted in the canonical ensemble and even more often in the isobaric-isothermal ensemble, making the observables associated with free energy variations natural measures of the available work of the system.

ii. Reaction coordinates and collective variables

To obtain meaningful free energy profiles of a given process, this one should be evaluated along the minimum free energy path (MFEP) on the free energy surface (FES). This path is formally described by a basis formed by a set of orthogonal vectors referred to as reaction coordinates (RCs).

When computing the free energy profile of a process, one must identify and estimate this set of reaction coordinates. However, directly sampling all the degrees of freedom of a system is generally not accessible either because of the high dimension of subsequent RCs, or most often, because we lack the knowledge to appropriately describe these RCs formally. Collective variables are functions that capture the essential features of a system and provide a low-dimensional representation of the reaction coordinates. Formally that has two consequences that one tries to minimize during their design: 1. the basis they generate is incomplete, but to make the CVs meaninful, the projection of the MFEP on the CVs should account for most of it, and 2. the basis might not be generated by orthogonal vectors, which

leads to double-counting issues, but the choice of the CVs is generally made such that orthogonality is mainly preserved. These variables are typically chosen based on their relevance to the process under investigation. They can include geometric parameters, distances between atoms or groups, angles, torsional angles, or any other suitable descriptors that capture the important changes occurring during the process. Employing accurate CVs can allow to effectively navigate the high-dimensional configuration space and to focus on the essential changes that define the reaction coordinates. The choice of appropriate collective variables is crucial for obtaining accurate and informative free energy profiles [243]–[247].

iii. Measuring free energy with MD simulations

In MD simulations, the measure of the potential energy of the system is inherent to the simulation as it is computed at every frame while propagating the system through time by integrating the equations of motion. The potential energy represents the energy associated with a specific conformation – or microstate – of the system.

In a macroscopic thermodynamic state, there are numerous microstates or conformations that correspond to different arrangements of the system's atoms and molecules. Accessing the free energy of a system that transitions between different states requires formally sampling each microstate associated with a given macroscopic state. This is because in statistical physics, to obtain meaningful measurements, one must perform an ensemble average, which involves sampling all accessible conformations.

MD simulations allow for the exploration of different conformations by generating trajectories that capture the system's evolution over time. However, it is important to recognize that MD simulations, in their pristine form, may not adequately sample the entire conformational space or sufficiently explore high-energy regions and energy barriers. The limitations of sampling arise due to the finite length of simulations and the inherent stochasticity of molecular dynamics.

To better understand the origin of the sampling difficulties that arise to measure the free energy using pristine MD simulations, it is best to leave the thermodynamic point of view and to further refer to statistical physics. In this frame, in the case of the canonical ensemble,

the probability P_i that the system lies in the microstate i is such that $P_i \propto e^{\frac{-E_i}{k_{BT}}}$, which means that it decreases exponentially with the energy of the system in the given microstate. This observation further explains why natural MD simulations will undersample regions of high energy. It also explains that the system will potentially never cross high energy barriers during the course of a simulation, driving to potentially unexplored portions of the RC.

iv. Umbrella sampling

To tackle the aforementioned problems, many so-called enhanced sampling methods were designed in order to access FE profiles following a system path on the FES using MD simulations, including, but not limited to metadynamics, replica-exchange, alchemical free energy computations, accelerated weight histogram. The general idea is often to modify the probability the system has to explore a given region of the FE landscape.

One of the most used method at the time is called umbrella sampling [248], [249]. The method divides the system in many slabs along the chosen CV which are referred to as umbrella windows. The name of this method is linked the use of biasing potentials which act along the CV and which generally take the shape of an inverted umbrella. The most common of those biasing potentials w being a simple harmonic potential, such that $w^i = k^i_{bias}\left(CV - CV^i_0\right)^2$, where CV^i_0 is the central value of window i. Hence, in each slab, the system is biased to stay in the surrounding of CV^i_0, allowing to obtain a proper sampling in this region of the conformational space.

In the frame of the canonical ensemble, one would compute the Helmholtz free energy[14] as described in statistical physics such that $A = -k_BT \ln Z$, where Z is the partition coefficient which reads $Z = \int e^{-\beta E|r|} dr$, where E is the potential energy of the system. To evaluate the free energy along a given RC, which we will refer to as ξ, one can express the probability distribution of the system along that RC:

$$Z(\xi) = \frac{\int \delta\left(\xi(r) - \xi\right) e^{-\beta E} dr}{\int e^{-\beta E} dr},$$

14 In the case of the isobaric-isothermal ensemble, one would consider computing the Gibbs free energy. The expression of the partition coefficient would thus be affected, but the general reasoning will be same.

with δ referring to the Dirac distribution. Hence, the free energy along ξ can be expressed as $A(\xi) = -k_B T \ln(Z(\xi))$, and is often referred to as the potential of mean force (PMF). The ergodic principle is once more assumed to access to *Z(ξ)* in the frame of MD simulations, yielding

$$Z(\xi) = \lim_{t \to \infty} \frac{1}{t} \int_0^t \rho(\xi(t'))\, dt',$$

where ρ is the count of occurrence of ξ in a given interval. In this case, *Z(ξ)* is nothing more than the probability distribution to find the system in the vicinity of a given value of the RC.

After a sampling procedure, the unbiased free energy profile can be accessed since we know the analytical form of the biasing potentials that where applied on each windows. To do so, it is common to use the weighted histogram analysis method (WHAM) [250].

v. Safety checks

Many parameters control the quality of the free energy profile estimated by means of US. At first, the preparation of the system is of great importance. In order to generate the initial conformations for the set of umbrella windows, many strategies can be adopted. The most common one is by means of a procedure often referred to as steered molecular dynamics (SMD). The idea is to gradually move the center of a biasing potential along the CV that is implemented for the US procedure. This slow motion of the potential will induce the system to be *pulled* in a range of values of the CV for which one wants to compute the free energy profile. In this regard, it is critical to choose the rate of pulling with care as a too fast pulling will drive the system far from equilibrium. That can induce the system to not having the time to relax in the further simulations used for the US procedure.

As we mentioned above, the choice of the CV which is describing the RC is of utter importance as it can be very complicated to notice the effects linked to a poor CV on the profile. Mainly, two consequences that should be mentioned are integrated barriers and averaged wells. These problems happen when the MFEP is partly orthogonal to the chosen CV, or when multiple wells are located closely to one another. In the first case, if the MFEP is orthogonal to the CV around a saddle point, the system will have higher probability to explore regions of low energy which are located orthogonally to the transition state. Hence, when the free energy of the related windows will be computed, the integration of the all

contributions will delete the presence of the energy barrier along the CV. In the second case, if there is a minima located orthogonally to the CV, a long sampling might drive the system to explore it as well as the system will explore the region close to the MFEP. Hence, the final value of the free energy will be a weighted average of the many minima orthogonal to the CV, driving to a wrong estimate of the free energy profile.

The first step to check for the quality of a given free energy profile is to check the convergence of the free energy values with time. For that, we plot the profile for many chunks of the trajectory, *i.e.* 0-n ns; n+2n ns; … ; i n-(i+1) n ns; … From this plot, the relative difference in free energy should get smaller when the system is at equilibrium[15]. This is one necessary safety check as, since we are doing an ensemble average, the system should be at thermodynamic equilibrium. From this plot, it is also possible to notice some signs showing a poor CV. For instance, if the system is seemingly converging and suddenly drops to another value. Such behavior could be the sign the system crossed a barrier orthogonal to the CV and that the FE values that are obtained in a second time are an average of the values in the two minima that are explored, orthogonally to the CV.

Secondly, it is important to estimate the errors and to keep any comment within them. The most common method to estimate the errors is by means of bootstrapping analysis [251]. One should note that bootstrapping can lead to underestimating the real errors on the FE [251].

Finally, if the quality of the CV is uncertain, one could perform the FE calculation using conformations generated with 2 SMD procedures: one in the *forward* direction from a given initial state to the final state and a second in the *backward* direction. This is a common way to evaluate the quality of the CV. If the two profiles show a hysteresis, that means that the system take two different paths on the FES which are not the MFEP [244].

IX. Physical limitations and conclusions

Through this chapter, we briefly went through the methods underlying MD simulations. This overview draws a clear picture of the wide range of application of this method: from the study of ligand-ligand interactions, to the study of membrane-protein interactions or to

15 The system is generally out of equilibrium at the beginning because of the SMD procedure that is generally used to generate the initial configurations for the umbrella windows.

the dynamics of small organelles, and, in a near future to the coarse-grained model of the whole cell!

However, and it is necessary to strengthen it, there are many boundaries and limits to MD simulations. At first, MD simulations were not designed to tackle reactivity, and even though some attempts are in progress, most of force fields optimized only for the ground states of each and every molecules.

Secondly, MD simulations are intrinsically of statistical nature. Thus, quantitative measurements are to be under the form of ensemble averages. This implies that the user should make sure to sample a given statistical ensemble by checking the quality of the pressure and temperature coupling algorithms which are used, but also that the system should be at thermodynamic equilibrium when one wants to make any measurements. It is possible to make use of the trajectories to obtain a qualitative idea of some process – but then extra caution should be applied, and, it is advisable to make use of several replicas of the simulation to obtain some statistics on observations linked to the dynamics.

However, once the user exert proper care to build, run, and analyze simulations, MD simulations are a tool of choice to have access to spatio-temporal scales which are above the limits of most experimental techniques. These simulations are now routinely used, along with experiments, to create or validate new physical models of many phenomena. In the course of this manuscript, we will apply MD simulations especially to bacterial membrane models and to their interactions with surfaces and antibacterial drugs.

Part II –

Results and

discussion

Influence of substrate hydrophilicity on structural properties of deposited lipid structures

The importance of membranes in nature, as an host to many biological functions or as a natural barrier between cellular compartment, drove to the development of model systems to mimic their structures. Various applications followed those models, starting with the idea to create a *lab on the chip*, designed to model a portion of a biological system and to run measurements – such as quartz-crystal microbalance (QCM), surface plasmon resonance, or atomic force microscopy (AFM) analyses [97] – which require a stable deposited lipid structure. It is with this general aim that we wanted to get a better understanding of the underlying interactions between lipid membranes and substrates, as they are a tools of choice to explore drug-membrane interactions. Although this method is widely used [88], [99], [100], it is of great importance to characterize the substrates which could balance best between leaving the lipid structure unharmed, so that all its biological functions will be preserved, and stabilizing that structure well and for a long time, so that experiments will give accurate results. In this chapter, we decided to focus on the influence of the material on the interactions with simple mono-component structures, although, in the end, our aim is to simulate the deposition of a model of the outer membrane of Gram negative bacteria, *i.e.* an asymmetric bilayer made of LPS in the upper leaflet, and a majority of phosphatidylethanolamine in the lower leaflet.

The focus of this work is to understand the influence of hydrophilicity of the substrate on the structure of supported lipid bilayers (SLBs). For this purpose, we selected a several types of substrates with a wide range of hydrophilicity: pristine graphene (GR), graphene oxide (GO) with several types of oxidation and silica. This choice of substrates comes from the popularity of oxidized surfaces for SLB formation [98]–[102]. At the same time hydrophobic surfaces, such as GR, are used for studying self-assembled monolayers (SAMs) [102], [104]–[106]. In this regards GO is an interesting choice, as it can come in various oxidation and one can “tune” its hydrophilicity. In this work, we tested oxidation levels

(OL) of 5 and 17%. OL is defined as the ratio between the number of oxygen atoms of epoxy and hydroxyl groups and the number of carbon atoms on the surface. We also addressed the effect of the ratio between between epoxy and hydroxyl groups (E:H) at a fixed OL of 17% to check how each functional group affects SLB stability. The results presented in this chapter were recently published [252].

I. Strategies to model supported lipid bilayers

To be able to study the influence of water interfacial layer we created several types of systems:

a. A lipid bicelle limited by semi-cylindrical caps in XZ plane which forms an infinite bilayer in Y direction (Figure 22 A, B).
b. An infinite lipid bilayer adsorbed directly onto the substrate without water molecules in between (dry interface) (Figure 22. C, D).
c. An infinite lipid bilayer adsorbed onto the given substrate with a thin layer of water molecules (wet interface), (Figure 22 E, F).

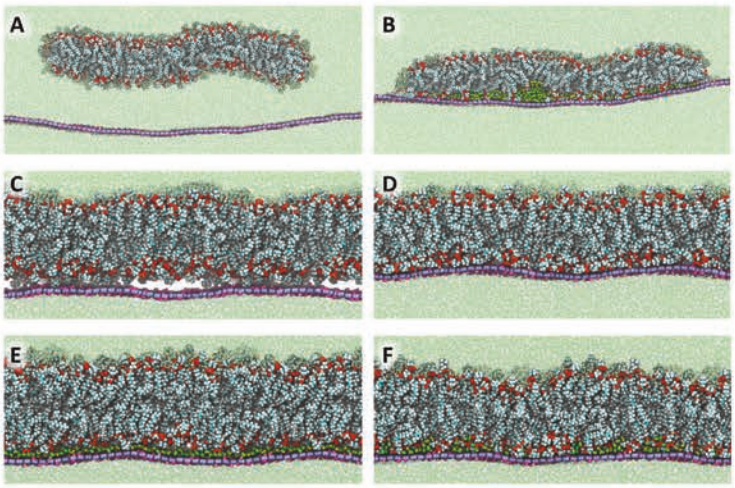

Figure 22. Snapshots of the simulated DOPC systems deposited on GO with 17% OL. A, B: the bicelle setup (a); C, D: the bilayer setup with dry interface (b); E, F: the bilayer setup with wet interface (c). Left column (A, C, E) shows initial states of the systems, while the right column (B, D, F) corresponds to the final adsorbed state. In GO, carbons are blue, oxygens are purple, and hydrogens are pink. Bulk water is shown as light-green balls and sticks. Interfacial water is shown in space fill representation with green oxygens and yellow hydrogens.

The bilayer setup does not allow water to diffuse between bulk solvent and the lipid-surface interface, leaving the number of water molecules unchanged during the time of our simulations. This creates an important limitation for this system. Interlayer of water trapped in between the infinite bilayer and the infinite substrate might drive the system to a metastable state. Of course, the system can get involved in a very slow process of equilibration via spontaneous passive diffusion of water [9], but it is not relevant in the present study due to the time range of diffusion process not accessible by means of AA MD. However, it is a widely used model which allows a direct comparison with many existing studies [7], [8], [104], [253] and, at the same time, with the bicelle setup we introduce in the present work. The bicelle setup allows interfacial water molecules to freely exchange with bulk water molecules, at the expense of a larger system with no control on the final thickness of the hydration layer, and potential inhomogeneities.

Table 6 summarizes the different systems which were simulated during this work, and details the different OL and surface hydrations which were used for each system.

Table 6: The list of the modeled systems used in this study.

System	Surface (OL, groups ratio)	Interface	Setup
Reference	No surface	Wet	Bilayer
S1	GR	Wet	Bicelle
S2	GO (5%; 1:1)	Wet	Bicelle
S3	GO (5%; 1:1)	Dry	Bilayer
S4	GO (17%; 1:1)	Wet	Bicelle
S5	GO (17%; 1:1)	Wet	Bilayer
S6	GO (17%; 1:1)	Dry	Bilayer
S7	GO (17%; 1:2)	Dry	Bilayer
S8	GO (17%; 2:1)	Dry	Bilayer
S9	Silica	Wet	Bicelle

II. Methods

The structures of GO were created by first constructing a sheet of planar pristine graphene and then distributing protonated epoxy and hydroxyl groups randomly on both sides of the graphene plane following the widely used Lerf-Klinowski model [254]. We respected the

tendency that hydroxyl groups cannot be in neighboring positions when they are located on the same side of the plane and prevented placement of epoxy and hydroxyl groups on the same side of plane on nearest neighbor carbon atoms to avoid energetically unfavorable states which can cause defects of GO structure in real life [252]. As the plane was considered periodic, we did not add carboxyl groups typical for the edges of the nanoparticles of GO.

The silicon dioxide substrate was modeled as an infinite perfect layer which surface contains silanol groups (Si-OH) only (model named silica_Q2_9_4OH_0) [255]. We did not consider the protonation-deprotonation equilibrium of the silanol groups and did not include any ionized siloxide (SiO−Na+) groups, even though non-ionized silica is typical for far more acidic environment due to the fact that, at the moment of the study, INTERFACE force field was not implemented directly to any publicly available modeler and we were limited to use the structure kindly provided by Dr. Hendrik Heinz [255].

All simulations were performed using Gromacs packages (version 2016.3, 2018.2 and 2019.2) [256]. The Stockholm lipids (Slipids) force field was selected for DOPC molecules, as Slipids was compared with various experimental data such as X-ray and NMR and was shown to give a good agreement, which makes the force field to be suitable for simulating biomembranes in a tensionless ensemble. It was used in combination with AMBER99sb force field for water [257] using TIP3P model. The parameters for GR and GO developed and tested by H. Tang *et al* [258], [259], are based on OPLS-AA force field and this combination demanded an adaptation to be used with AMBER types of functions. OPLS-AA uses value of 0.5 for *fudgeQQ* parameter (the multiplication factor for electrostatic 1-4 interactions) and AMBER is using 0.8333, so non-bonded interactions between GO atoms were adjusted with *pairs* section. Like that, this adjustment does not influence other molecules in the system. For silica, the INTERFACE force field [255] was used since it reproduces properties of oxides with high accuracy and combines well with AMBER force field, as it uses similar parameters for 1-4 interactions and its potential energy function is basically the same.

All simulations were performed in the NpT ensemble at a pressure of 1 atm and a temperature of 320 K maintained by velocity-rescale thermostats [260] applied respectively to the substrate (either GR, GO, or silica), to the lipid membrane, and to the water, and

involving a time constant for coupling of 0.1 ps, with semi-isotropic pressure coupling using Berendsen barostat. Since the system embeds a periodic solid substrate along X and Y dimensions, no pressure coupling was applied along these dimensions. No bonds were converted to rigid constraints. An integration step of 1 fs was used for all setups. Long range electrostatics was computed with the PME method [261].

To create the bicelle setup we let an infinite DOPC bilayer equilibrating for 200 ns to reshape after adding water along the X axis to form the bicelle caps. The newly created bicelle was equilibrated for 100 ns and only after that the system was used for the deposition procedure. The bicelle was initially placed around 5 nm from the surface. 3 flat-bottom potentials with a force constant of 500 kJ mol^{-1} nm^{-2} and a flat area spanning over 2 nm from the center of mass (COM) of the substrate – or from the COM of the surface of the substrate in the case of silica – were applied to three adjacent regions of the bicelle along the X axis to avoid its deformation. The potentials were removed when the distance from the substrate to the head groups of the lipid monolayer facing the substrate was lower than 1 nm. This allows water to redistribute and the bicelle to deposit naturally. The production run was started once the bicelle was totally deposited and no major water redistribution was present.

For the setup 2 (S5), a thin layer of water was added between the infinitely periodic bilayer and substrate resulting in around 7 water molecules per head group. This state associated with a partial hydration of the polar groups of the membrane, sometimes referred to as a dehydrated state, was used to create an interfacial layer of 4-8 Å thick, leaving the SLB in a close-contact conformation with the substrate for which water molecules are trapped, if they do not undergo a slow passive diffusion through the membrane. This number of waters per lipid was selected as the minimal number of waters to hydrate phosphate groups of a free bilayer [262], [263]. Moreover Stachura and co-workers [264] show that for DOPC lipids simulated with Slipids, 6.8 hydrogen bonds with water are found on average in fully hydrated states. Yin and Zhao [265] found that there are 6 water molecules in the first hydration layer. Even if many studies show that head groups of DOPC exhibit commonly values ranging 9-16 waters in their first hydration shell [266]–[270], we wanted to study the minimal adequate number of waters to compare with absolutely dry interfaces and bicelles. Interestingly, Vishnyakov and co-workers [2] show that in the conformation of the SLB in

close-contact with the support, the hydration is partial and does not cover the whole lipid surface.

III. Structural changes of SLBs

i. Distance from the support and thickness of SLB

Deposition changes structural properties of lipid bilayers, even if it is a well made surface. We studied those changes to give a better understanding on which substrate keeps the bilayer in the most natural structural state. For every substrate except GR and for every MD setup, we obtained equilibrium systems in close-contact state (Table 7), which once again underlines how energetically favorable this state is. Distances were computed for the last 100 ns of the simulation to ensure taking into account only equilibrated structures and error was computed as a standard deviation of the distance value. For all systems error did not exceed 10%.

Table 7: Distance from the COM of the substrate to the one of the phosphate group of the proximal lipid leaflet. The error was computed as a standard deviation.

System	Surface (LO, group ratio)	Distance (Å)	Error (Å)
S2 (bicelle)	GO (5%; 1:1), wet	5.4	0.4
S4 (bicelle)	GO (17%; 1:1), wet	4.2	0.1
S5 (bilayer)	GO (17%; 1:1), wet	5	0.2
S9 (bicelle)	Silica, wet	5.8	0.4

The hydration layers obtained for these systems remained not thicker than 4 Å. All lipid bilayers formed at 4-6 Å from the substrate and were stabilized with well-defined thicknesses ranging from 2.8 to 3.8 nm (Table 8).

Table 8. Thicknesses of lipid bilayers and bicelles obtained from FATSLiM program [271].

System	Surface (LO, groups ratio)	Thickness (nm)	Error (nm)
S0 (bilayer)	Reference	3.88	0.04
S2 (bicelle)	GO (5%; 1:1), wet	2.8	0.1
S3 (bilayer)	GO (5%; 1:1), dry	3.66	0.04
S4 (bicelle)	GO (17%; 1:1), wet	3.29	0.03
S5 (bilayer)	GO (17%; 1:1), wet	3.79	0.04

S6 (bilayer)	GO (17%; 1:1), dry	3.68	0.03
S7 (bilayer)	GO (17%; 1:2), dry	3.51	0.02
S8 (bilayer)	GO (17%; 2:1), dry	3.56	0.02
S9 (bicelle)	Silica, wet	3.62	0.03

In this study we also observed shrinking of the bilayer thickness. According to Table 8, we obtained relative thicknesses of 93% for silica, 84% for GO 17% and 72 % for GO 5%; we showed that the bilayer thickness can also be a fingerprint of the close-contact state since this one appears to be very sensitive to the surface hydrophilicity. Interestingly, this effect was also shown experimentally while using quantitative differential interference contrast microscopy. Regan *et al.* [3] have shown that the bilayer thickness of DOPC on glass with different treatments is reduced from its initial state (a second bilayer on top of the SLB). The observed thicknesses relative to the bilayer were found to range from 89 to 92.7%.

However, one should remember that data obtained from MD simulations are not directly comparable with experimentally determined thicknesses. In MD simulations, the density profile of each chemical or functional group can be measured whereas the raw data from experiments such as neutron reflectivity are intrinsically convoluted. Thus, in order to access information on the thickness of the different layers, experimental data should be fitted using a model defining the number of selected groups as well as initial parameters including a first guess of the thickness of each layer. Each slice is generally modeled by a switching function, where a switching function is a function which has values only 0 and 1 and . Even if it is less and less the case, those fitting models long assumed that there is no overlapping between the different groups [131]. All in all, these switching functions cannot give a directly comparable estimate of the thickness [4]. Moreover, the definition of the measure of the thickness is not uniform in the literature, which can give results differing up to a nanometer. We report here several of the widely accepted definitions of the bilayer thickness (see Figure 23):

1. $d_{p\text{-}p}$ – the thickness is defined as a distance between phosphate groups of different monolayers. In practice, this observable is computed from mass density profiles.
2. $d_{surface}$ – the thickness computation takes into account the local fluctuations of the membrane by considering neighboring lipids. This is utterly important for highly curved membranes. This approach allows to compute the distance between two

surfaces: upper and lower leaflet. The distance between two surfaces is computed by projecting the vertices of a given surface onto the other (head groups positions are used as vertices for the triangulation of the surface) – see the recent example by Bhatia *et al*. [272].

3. d_B – in that case the thickness is defined between the intersections of the head group profile with water for both monolayers as mentioned by Golovina *et* al. [269].
4. d_{FWHM} – the thickness is defined between the outer values at half maximum of the heights of head group distributions [141].

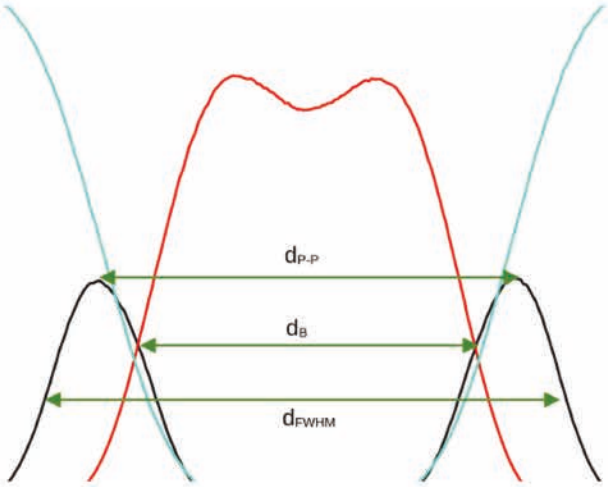

Figure 23: Schematic representation of different methods to compute thicknesses of membranes.

In the present work on GO with various OL, we observed an increase of the thickness of deposited bicelles while the hydrophilicity of the surface increases. This could be explained by the fact that bicelles systems had the opportunity to redistribute such a way that as many hydrophilic head groups as possible can get in contact with more hydrophilic substrate. At the same time, an opposite tendency appears in the case of the bilayer setup. Bilayers deposited without interfacial water with 17 % OL are thinner than with 5 % OL for epoxy / hydroxyl ratios 1:2 and 2:1, but thicker with the standard ratio 1:1. One should note that Regan *et al.* [3] obtained a decrease of the relative bilayer thickness with decreasing hydrophilicity for DOPC on glass. Stachura *et al.* [264] addressed the structure of non-deposited stacks of lipid bilayers for different hydration levels. They showed that the progressive dehydration of the systems drives to an increase in their thicknesses. In the present work, however, we observe that the system S6 – with dry interface – is thinner by 1.1 Å than the system S5 – with wet interface.

ii. Influence of interfacial water

Straightforwardly, the number of interfacial water molecules between the head groups of the lower layer and the substrate increased accordingly with the hydrophilicity of the surface. In the case of GR/GO systems, the surface hydrophilicity can be characterized by following the variation of the OL. We found that no interfacial water is present in the monolayer deposited on the GR (S1), only 2.5 waters per lipid are present for the bicelle on GO 5% OL (S2), 13 for the bicelle on GO 17% OL (S4), and 14 in the case of the silica (S9). The influence of the hydration layer on the close-contact state can be revealed by looking at the differences between wet and dry setups. For instance, for S6 and S5 systems, namely bilayers which are deposited on GO with 17 % OL either with no interfacial water (dry interface) or with a minimal amount (dehydrated system with ~7 water molecules per lipid in the lower monolayer), we observed that the peak of the distal head groups of the dehydrated SLB is shifted by 4 Å more from the support than the one of the SLB with a dry interface (Figure 24). Meanwhile, the head groups of the lower leaflet are equilibrated around the same distance to the support (3.0-3.5 Å). Even though the distances between substrates and bilayers in those two systems are the same, the variation of the hydration level already has some consequences on the bilayer properties such as its thickness. For these dry and dehydrated systems, we obtained thicknesses of 3.79 and 3.68 nm, respectively. For GO 5% in the dry setup (S3), a similar bilayer thickness was obtained (3.66 nm).

These results altogether highlight the main role played by GO substrate interactions. The presence and the thickness of the interfacial hydration layer are not sufficient to promote such large variations (1 nm) observed for the bilayer thickness.

iii. General structural changes

The density profile of systems mentioned above are presented in Figure 25. The variation of hydrophilicity modifies the way lipids organize themselves, as clearly visible from the profile.

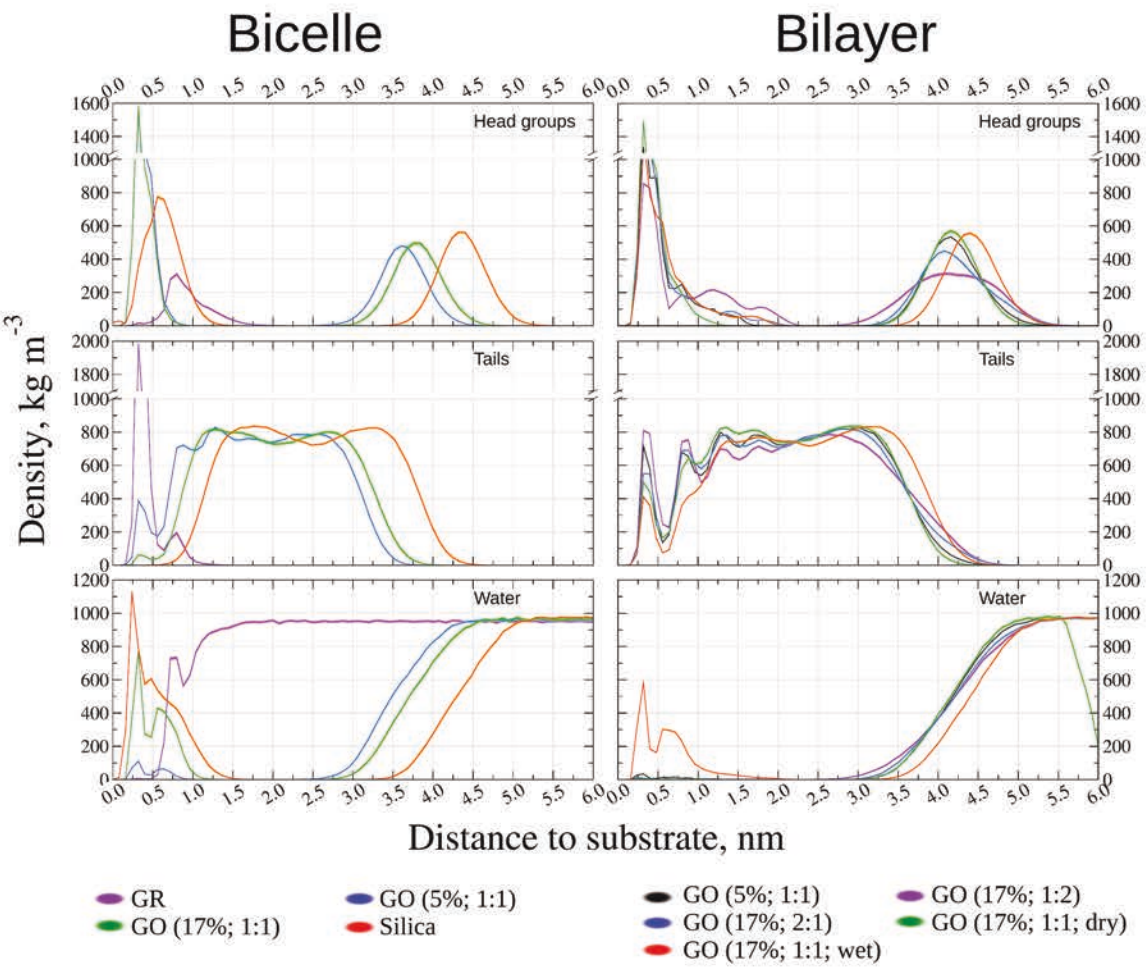

Figure 24: Density distributions of head groups, tails and water averaged over the last 50 ns of the trajectory for the different studied systems. The error bars are represented in a lighter shade of the color of the system and were computed using a Bayesian method considering the time autocorrelations.

The density profiles (Figure 24 left panel) obtained for GO showed that the proximal head group profile is quite similar for the two OL investigated here. However, the density of the proximal head group is higher than it is for the reference bilayer or for silica. The associated peak is also much thinner for GO than for the reference system. This feature reveals the tendency for lipids to strongly adapt in the vicinity of the surface. For GO, the distal part, although displaying the same broadening, was found to move toward the substrate with decreasing OL. In that respect, the bilayer on silica was found the most preserved system for which even the proximal head group profile is widening in a similar way as it is for the distal head group. For GO and silica, the tails profiles look quite similar and roughly resemble that of the reference bilayer. However, they shift toward the substrate while the substrate becomes less and less hydrophilic (silica > GO 17% OL > GO 5% OL > GR). Moreover, an additional peak appeared in the tails' profiles close to the surface. The

corresponding density is higher in the case of GO 5%. This shows that two types of conformations of the tails occurred during the simulations for less hydrophilic systems. The first one is roughly similar to the case of a natural bilayer while the second one is imposed by GO / GR surfaces. It is though at the expense of a system-wide lipid reorganization, involving an important change both in the APL and in the membrane thickness, that a distribution of the lipid tails closer to the one of a free solvated lipid bilayer is obtained for GO at 5% and in a less extend for GO 17%. This statement can be checked by comparing bicelle and bilayer setups which allow or prevent the lipid reorganization. Indeed, if in all the density profiles of the SLBs deposited on GO there exist a peak of the tails in the region 3.5-4.0 Å from the substrate, the density of those groups is systematically lower in the case of the bicelle.

In the case of GO, the proportion of epoxy / hydroxyl on the surface might change the quality of the deposited systems since the surface energy should be affected as it is known that those two groups exhibit drastically different electrostatic interactions [273]. It is thus important to address this topic in the close-contact configuration where those differences in short-range interactions prevail. We investigated the GO system at 17 % OL for three epoxy / hydroxyl ratios: 1:1 (Figure 25, right panel, green), 1:2 (Figure 25, right panel, purple), and 2:1 (Figure 25, right panel, blue). The ratio 2:1 (E:H) shows a slightly broaden distribution of the distal head groups and a slightly reduced thickness of the membrane. Surprisingly, we observe a more important effect with the ratio 1:2 where the membrane quality is way more affected, and the shape of the distal head groups is widely broadened leaving on the density profile a peak presenting a large shoulder.

iv. Lipid tails, their order and orientation

The study of the tails, their order and orientation are thus of high importance to characterize the interactions of the GO substrate with the membrane. We analyzed first the deuterium order parameters of all studied systems separately for lower and upper monolayers (Figure 25). It is clearly visible that in the case of GR all lipid tails are completely disordered and mostly lay flat on the surface (the order parameter is negative). In the case of GO 5% there is a striking difference between lower and upper monolayers. In the lower monolayer the ordering of the tails is decreased dramatically. The parts below the double bond (positions 9-10) lay almost flat on the GO surface while proximal parts are more inclined to the surface

but are still dramatically less ordered than in the reference bilayer. In the case of GO 17% there is almost no difference between the ordering of lower and upper monolayer while both are somewhat less ordered than the reference. For silica both monolayers are even more ordered, and the upper monolayer almost reaches the values of the reference bilayer. In general, there is an obvious trend of increasing the ordering of both monolayers from GR to GO 5%, GO 17%, and silica. This trend is especially visible for the lower monolayer which responds to the decrease of the surface hydrophobicity. For all studied systems, the lower monolayer is less ordered than the upper one due to the disturbance brought by the support.

The fact that the upper monolayer, which is at best weakly interacting with the support, never reaches the ordering of the reference system suggests that there is a significant amount of inter-monolayer coupling. Disturbed lower monolayer influences the upper one by means of the interconnected lipid tails in the central part of the membrane. Thus, selection of the least disturbing substrate is truly important to make the model be as close as possible to natural membrane systems.

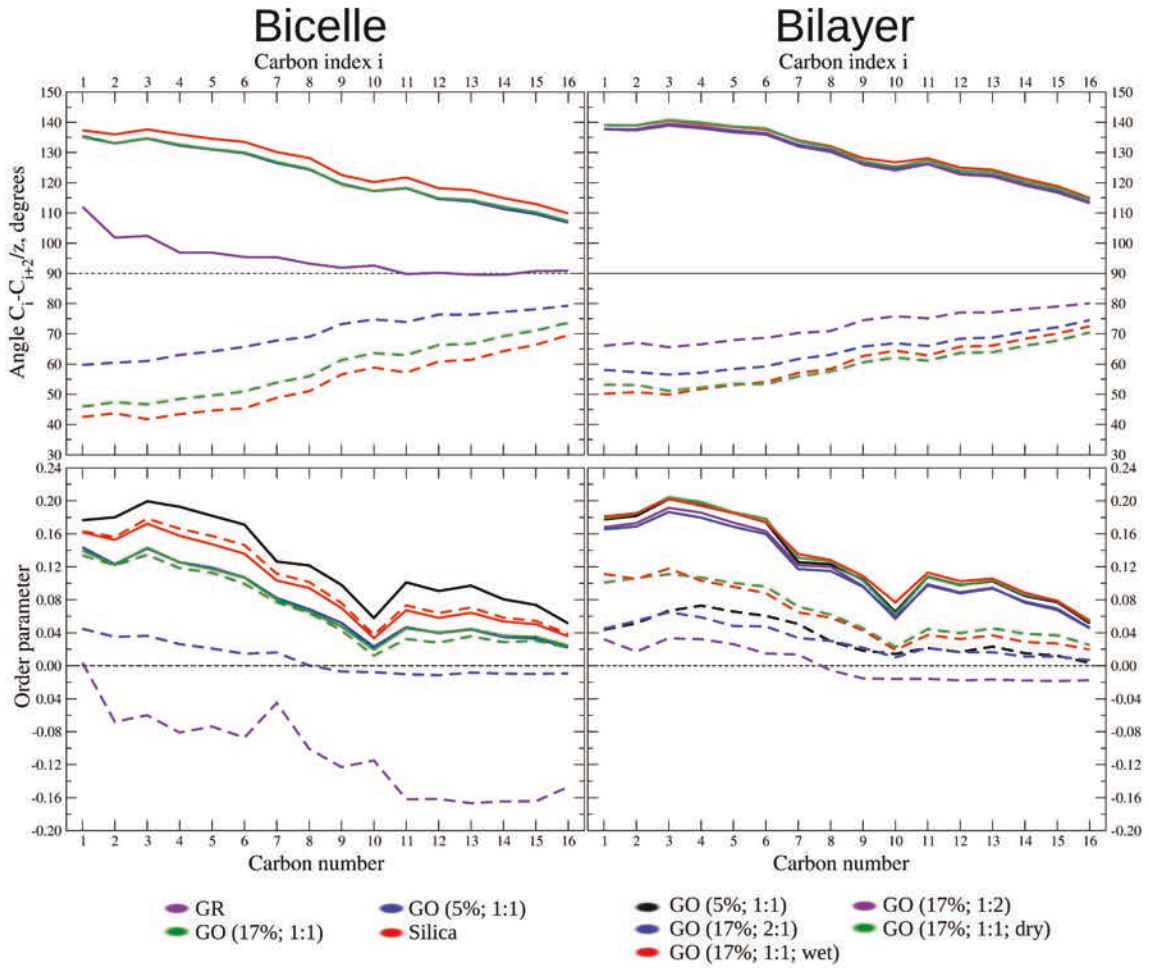

Figure 25: Deuterium order parameter and angle formed between the normal to the membrane and the vector formed by the carbons C_i-C_{i+2}. Dashed lines are for the outer leaflet and plain lines are for the inner leaflet.

To get a more straightforward view of the inclination of the aliphatic tail towards the substrates, we made the computation of the angle formed between the normal to the membrane and the vector formed by the carbons C_i-C_{i+2} that we also report in the Figure 26. This observable was made so that the angle will be comprised between 0 and 90° – 90° corresponding thus to an orientation coplanar with the substrate – if the carbon C_i is lower than the carbon C_{i+2} along the z axis and between 90 and 180° otherwise. It is thus clearly visible that the proximal leaflet is more aligned to the substrate than the distal one, in all cases. Once again, we notice that, in the case of the bicelle setup, the more the system is hydrophilic, the less the lipid tails are parallel to the substrate.

v. Interactions between the head groups and the substrate

The orientation of the P-N vector is also a known observable which permits to characterize the interactions that endure a given aminophospholipid monolayer [2], [5]. We report the probability distribution of the P-N angles to the normal of the membrane for each monolayer and each systems computed using the bicelle setup (Figure 26). The distributions are drastically different. The one of the upper leaflet is a wide distribution showing the mobility of the head groups of a free monolayer. In the lower leaflet, at the exception of the system on silica, the distribution is centered around 90° showing the strong influence of the substrate on the head groups. For silica, as it is visible on Figure 27, the choline groups are mainly closer to the surface than the phosphate groups.

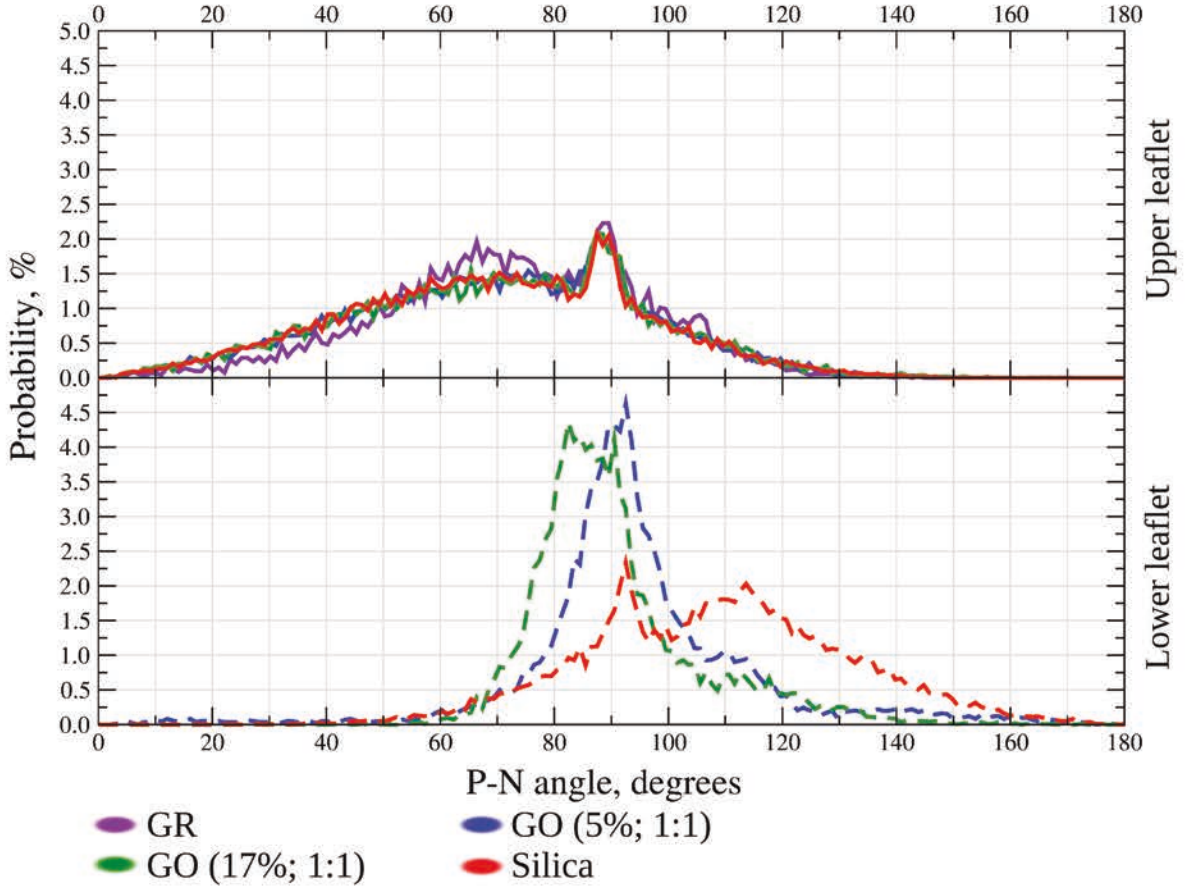

Figure 26: Probability distribution of the P-N angles to the normal of the membrane for each monolayer for the systems computed using the bicelle setup.

On Figure 27, snapshots of the contact layer obtained with the bicelle setups on different substrate ranged by order of hydrophilicity are plotted. It clearly shows the continuous transition from a supported monolayer formed on a hydrophobic substrate to the close-

contact state obtained on hydrophilic substrates. It should be noted that the density peaks of the tails observed close to the surface in Figure 24 represent in fact the tails laying down and parallel to the substrate.

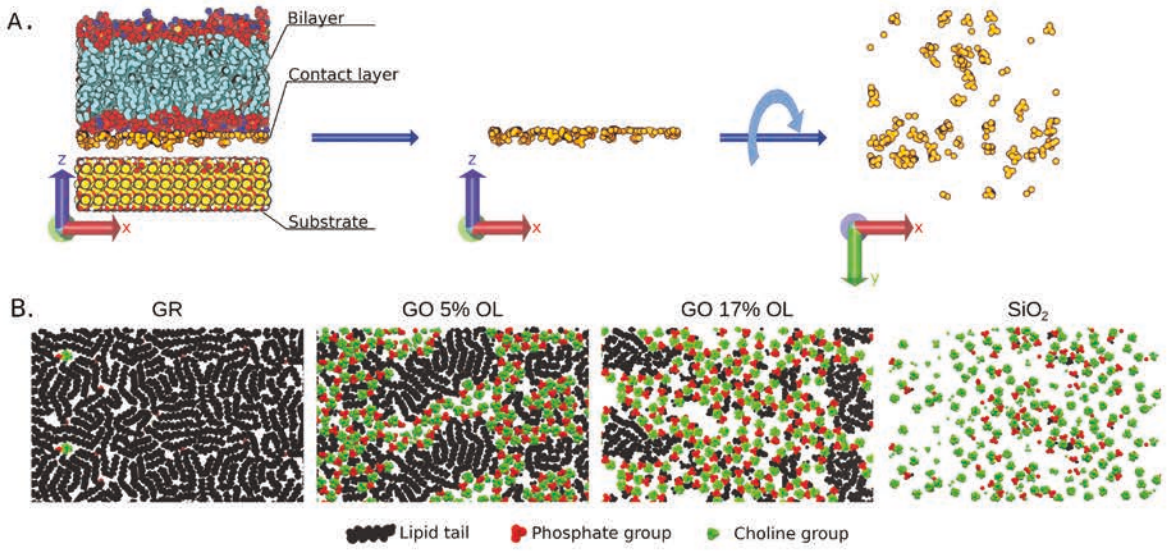

Figure 27: Panel A. is a schematic representation of the subset of atoms which are shown on the panel B. Panel B. shows snapshots in the XY plane of the last frame of our simulations for the different systems simulated with the bicelle setup. The snapshot shows a cut of the bicelle representing only the atoms closer than 6 Å from the substrate.

IV. Electrostatic interactions, influence of different surface groups

The effects of lipid / substrate electrostatic interactions and inhomogeneous distribution of the epoxy / hydroxyl groups on the close-contact state were also addressed by calculating the electrostatic potential created by the substrates (Figure 28). As expected, the local electric potential created by GO (5 and 17 %) and 3 different epoxy / hydroxyl ratios displays strong inhomogeneities at short range distance from the surface. At 0.5 nm from the surface, *i.e.* a distance comparable to the contact distance between the substrate and the bilayer found in this study, the potential ranges from -0.86V to 0.86V. It thus spans over a twice bigger range than the difference of potential of single component PC membranes (around 0.8V [274]). However, the characteristic drop of the electrostatic interactions with the distance shrinks the difference of potential to the order of 0.5 V at about 10 Å from the surface. This can drive to the conclusion that the upper monolayer and even the tails of the lower monolayer are not strongly influenced by electrostatic interactions with an oxidized substrate. It also brings to the light that depending on the distance from the membrane to the

surface, electrostatics will or will not come at play with the head groups of the lower monolayer, especially in the metastable states which could occur far from the surface.

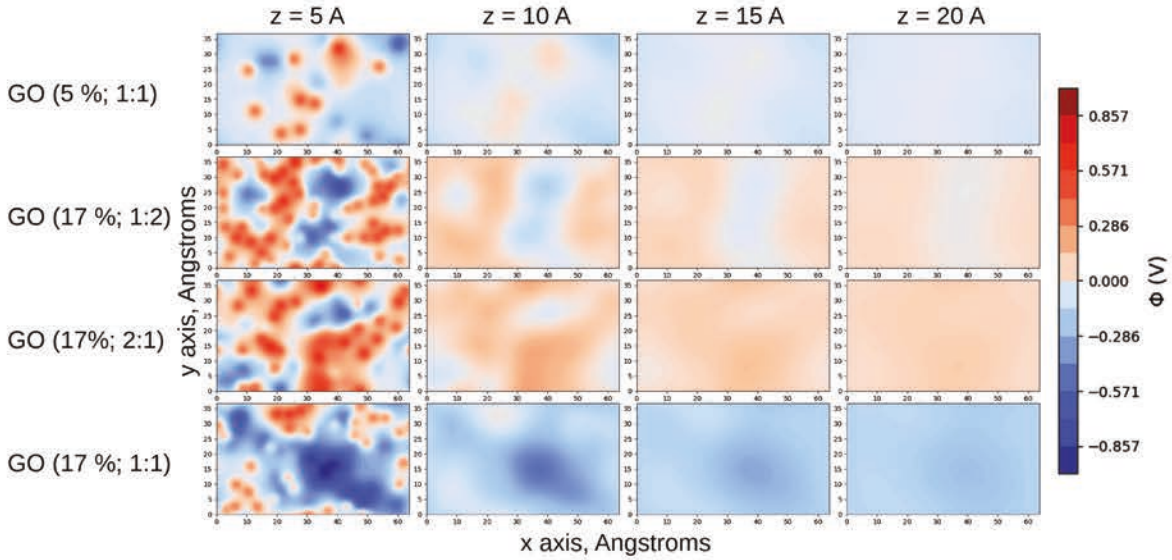

Figure 28: Electrostatic potential maps of the GO substrates used in the present work.

V. Conclusions

In this work, we investigated SLBs of DOPC onto surfaces with different oxidation levels for GO – thus various hydrophilicity – and silica. We modeled the deposition using not only infinite bilayers, but also semi-infinite bicelles, which allow fast redistribution of the interfacial water molecules and lipids between the two leaflets. Such properties as thickness of bilayer, tails orientation and thickness of hydration layer differ for different substrates. This nonhomogeneous structure creates a particular shape of the lower monolayer, where tails still try to approach parts with lower density of functional groups and head groups near hydrophilic parts. Strong difference in between hydrophobic and hydrophilic regions on GO are present in the variation of electrostatic potential close to the substrate. This shows that close-contact state is characterized by strong electrostatic interactions with the substrate. This also extends the idea that electrostatic interactions matter in the cases of charged lipids or charged surfaces [275]. We only observed the close-contact stable state for which the thickness of the interfacial hydration layer is comprised in the range 4-8 Å. These results do not exclude the existence of potentially metastable β states for DOPC on GO but imply that the barrier which separates α and β states is probably lower than the thermal energy or that the pulling on the bicelles overcomes this barrier.

In the forthcoming study, we will estimate this energy barrier within a potential of mean force methodology. This would allow to add quantitative characteristics to the whole process of deposition and moreover this method can allow to simulate adequately various lipid membranes, including those modeling outer membrane (OM) of Gram negative bacteria, containing lipopolysaccharides (LPS). However, it is worth mentioning, that highly hydrophilic supports still reshape the inner layer of deposited membranes, even if such changes would be minimal comparably to more hydrophobic supports (Figure 24). To avoid these changes in structures, other approaches for models of OM are considered, such as a floating bilayer on the top of the deposited SAM [140]. It is important to avoid structural deformation to study biological functions of such complex membranes properly and to be able to study interactions with potential antimicrobial peptides (AMP) in vitro.

This work points that the close-contact state is a stable conformation which might appear in reality. The question remains to know the proportion of the membrane on this state on a given lipid patch.

Free energy of deposition of lipid membranes on solid substrates

In order to verify the observations from our previous work [1] and from the work by Vishnyakov *et al.* [2], we wanted to design a protocol to measure the free energy profile of membrane deposition on a surface. To the extent of our knowledge, this work has never been carried out previously and would be a strong insight into the fine interactions between membrane and solid substrates that would allow us to better understand 1. whether both α and β states, first introduced by Vishnyakov *et al. [2]*, exist, and 2. the extend to which surfaces may influence supported membranes. This work is of high importance to design lab-on-the-chip experiments which will optimize the balance between a stable deposited layer and an unperturbed layer – so that the measure of biological properties will be unbiased. It would also complement the work by [3].

In this section, we describe a series of important steps that were undertaken on the way to create a working protocol to measure the free energy of adsorption. Although it is uncommon to focus on negative results, this work is of true importance and will permit to better understand which further steps should be undertaken in order to create a better protocol in the future.

I. Modeling silica with CHARMM-GUI

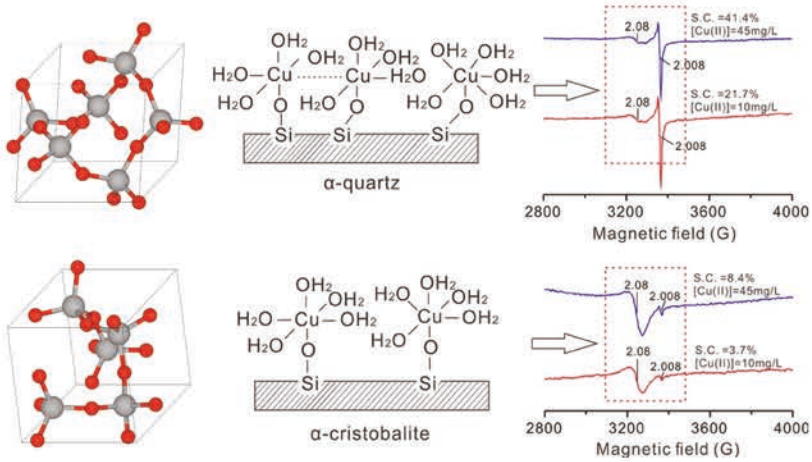

Figure 29: Schematic representation of the quartz and cristolabite structures of silica [2], [68], [114], [255], [277], [299], [300]. Differences in their structures imply different surface properties, for instance, quartz has a higher silanol density than cristobalite.

CHARMM-GUI implemented the so-called Nanomaterial Modeler module which is a graphical user interface on the portal guiding through the steps of creation of all-atoms nanomaterial structures. In the case of silica, the two main structures which are (meta)stable at room temperature and used in the industry are present – namingly α-cristobalite and α-quartz (Figure 29). They present different surface microstructures and ion adsorption properties [277]. Overall, the choice was to use the α-quartz since it is the most abundant.

II. A semi-periodic system in all-atoms simulations

To study membrane substrate interactions, several properties are of importance: 1. the membrane area might change when the distance to the substrate is very small [1], [276], 2. the interfacial water should be able to escape while the distance from the membrane to silica is affected by the steered MD process [1], [2], [278].

In the previous work, we introduced an original setup making use of bicelle – *i.e.* of a semi-periodic membrane. The advantage of such setup is that the system lets water to flow between bulk and interfacial areas. In the meantime, there are several drawbacks:

1. The system must be larger than with a similar fully periodic membrane. Indeed, the analysis of the deposition should exclude the caps of the bicelle, where the lipids are partially flipped. This kind of orientation may exist on real systems, however, in a MD setup, those lipids would be statistically over-represented if they are not excluded.

2. The system must be rather long on the axis which is capped. As a consequence, the membrane might undulate more and the subsequent analysis are more complicated.

To avoid such issues, it was decided to build a system with a fully periodic membrane whose area per lipid could still vary. In this regard, we designed a semi-periodic silica surface (Figure 31). This system fulfills all the properties which are needed: 1. the membrane area can change, since the dimension of the box along the x axis, along which the silica is not periodic, is now allowed to vary, as far as we apply an anisotropic pressure coupling, and 2. the interfacial water can freely exchange with the bulk water through the gap along that axis.

The first task to build that system was to choose the size of the gap along the x-axis. Four systems were prepared with initial distances of 1.0, 1.5, 2.0, and 2.5 nm.

The choice was made to first generate the system in all-atoms, to be sure that the electrostatic interactions, which are known to be fundamental in the process of membrane-substrate interactions, will accurately be taken into account. To increase the realism, the surface of α-quartz, which was created with the Nanomaterial Modeler module from CHARMM-GUI, was modeled with a ionization degree of 13.3 %, which is what one may expect at neutral pH (Figure 30) [255].

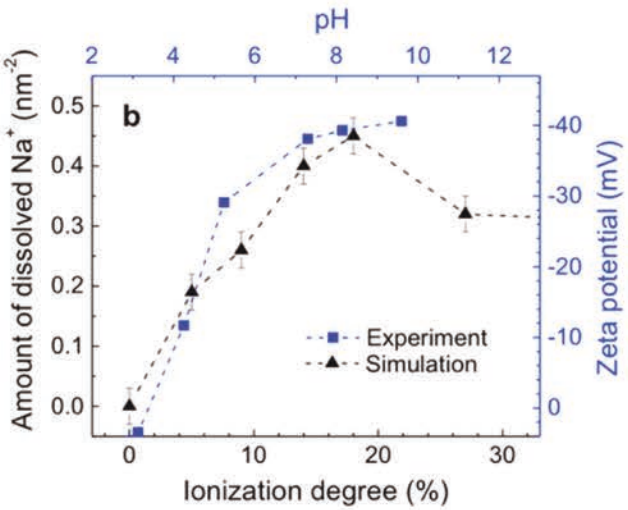

Figure 30: Amount of dissolved sodium ions depending of the pH. Reprinted with permission from Emami *et al.* Copyright *2023* American Chemical Society.

To be sure that the membrane will not be disrupted or drastically affected by the absence of periodicity in the silica, the size of the system was chosen so that space between the periodic images for the largest accounted distance (2.5 nm) generates a hole in the substrate which represents less than 30 % of the surface of the substrate. Thus, we built a silica of dimensions 8.7x10.2 nm.

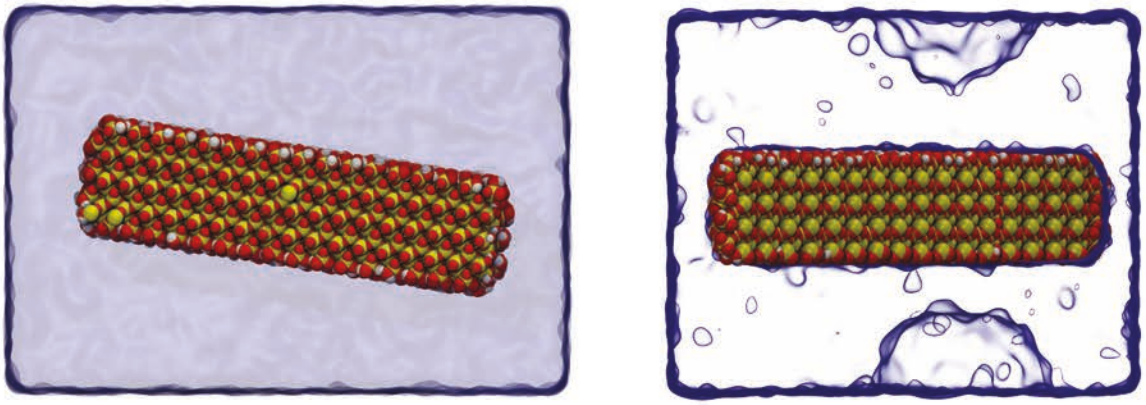

Figure 31: Screenshot from molecular dynamics simulations showing A. the rotation with respect to the initial horizontal orientation of the semi-periodic model of silica and B. the cavitation taking place in the solvent. The solvent is represented by means of blue surfaces, silicon atoms are represented as gold spheres, oxygen atoms as red spheres, and hydrogen atoms as white spheres

A B

Since there is no periodicity along the x-axis, we expected to see some rotation of the silica around the y axis (Figure 31). To avoid this effect, we first applied position restraints acting along the three dimensions on all heavy atoms with an initial force constant of 1000 kcal / mol / nm². The presence of the constraints was inducing artifacts in the simulation box in the form of cavitation (Figure 31) which did not disappear, either after reducing the force constant, appending the simulation to up to 200 ns, annealing up to 360 K for 100 ns, or applying restraints by means of Gromacs pull code. This issue, combined with the poor performance linked to the periodicity of the molecule drove us to conclude that this setup is not appropriate for the simulation of membrane adsorption on solid surfaces. Using periodic-molecule options requires a slower PBC algorithm and does not allow to use MPI parallelization with the newest versions of Gromacs packages available at that time. Additionally, using OpenMP is less efficient for these systems. The only workaround was to run every simulations on nodes embedding GPU – which was driving to performances 10 x better than on CPU-only nodes. However, the performance was still in the range 10-15 ns / day.

III. A periodic system with a pore in the membrane in all-atoms

To avoid the issues encountered with the semi-periodic silica, we decided to use a fully periodic silica patch along with a periodic membrane bilayer. Although this strategy is not perfect, as it hampers the ability of the membrane to adjust its area per lipid while interacting with the surface, it was already used in different studies [1], [2], [279]–[281] and it could be a first insight into the free energy of membrane adsorption.

In such systems, two possibilities would allow interfacial water molecules to redistribute during the steered MD, when the membrane is pulled toward the surface. The first possibility proposed by Roark *et al.* [278] uses a semi-porous silica designed so that water molecules could flow through a pore. Their model had a silica slab with a real pore with the diameter of around 2 nm. In order to avoid creating a realistic porous silica slab, which would require to create a complicated script to compute the distribution of the groups on a curved surface correctly and which goes beyond the scope of this work, we decided to try creating a “virtual pore”. The idea was to create a subset of atoms of a different type, which do not interact with water atoms but have the same bonded and non-bonded interactions with any other atoms (Figure 32). Even though Gromacs allows in the “free energy” section of the mdp file to interpolate between two topologies, this applies only to a whole molecules so that we cannot set the fudge coefficient $f_{QQ}=0$ only to that selection of atoms from the silica virtual pore. Thus, it was possible to remove only the van der Waals interactions between silica and water, and the coulomb interactions forbade water molecules to go through the substrate.

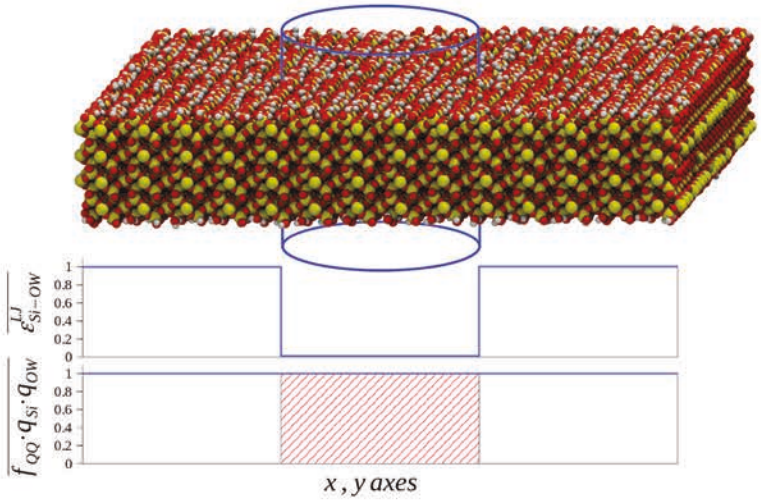

Figure 32: A. Schematic representation of the virtual pore in the silica. B. Projection of the value of resp. van der Waals interaction and to the scaling coefficient applied to electrostatic interactions on both x and y axes. Note that it is impossible with Gromacs to apply a different coefficient on the electrostatic potential for different parts of one molecule

Since it was not possible to create a simple and realistic model of porous silica, the choice was made to maintain a 1 nm-radius pore in the membrane using Plumed [10] plug-in that is later used to implement the collective variable (CV) (Figure 33):

```
# Loading all the index groups
membrane:               GROUP NDX_FILE=plumed.ndx NDX_GROUP=Lipid UNIQUE
tails:                  GROUP NDX_FILE=plumed.ndx NDX_GROUP=Tails UNIQUE
# Computing the COG of the membrane
membrane_com:           CENTER ATOMS=membrane NOPBC
# Defining the minimal distance between the center of the simulation box and the lipid tails.
dist_tails:         XYDISTANCES GROUPA=membrane_com GROUPB=tails
ALT_MIN={BETA=15.0} LOWMEM
# Biasing the system to maintain the membrane pore
restpore:           RESTRAINT ...
                        ARG=dist_tails.altmin
                        AT=1.0
```

The area of the opened pore is kept to less than 5 % of the surface of the membrane, to ensure that further free energy (FE) calculations will not be drastically affected. One should also keep in mind that the surface of the membrane affected by the pore is much larger than the water channel itself, as the partial lipid flip flop involved in that structure could also affect the interactions with the surface.

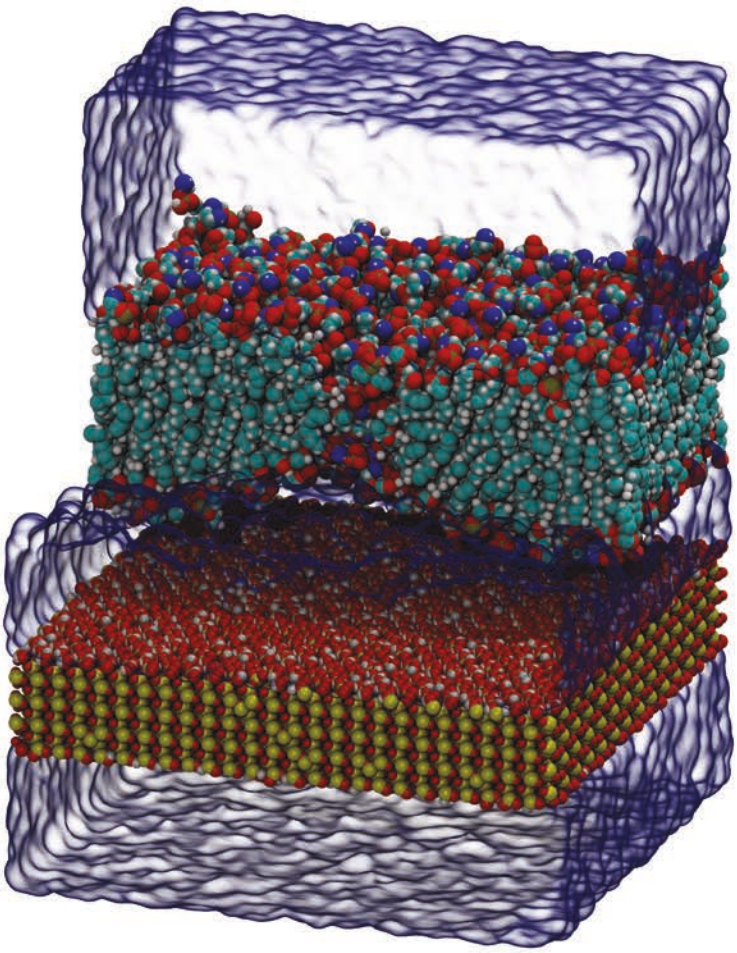

Figure 33: Representation of the setup built to compute the free energy of membrane deposition on solid surface, making use of a pore maintained in the membrane using Plumed plug-in.

i. Deposition is a solvent-driven process

The first CV that we developed relied on the assumption that the deposition of the membrane is driven by the removal of extra interfacial water molecules. To obtain a CV independent from the size of the system, we decided to use the number of interfacial water per lipid in the monolayer facing the surface.

To access this number, it is straightforward to use the predefined *multicolvar* – *i.e.* a collective variable depending on a number of other coordinates – called DENSITY. This function allows to calculate the number of atoms of a given group.

Plumed implements different methods which allow to restrict that function to some geometrical shapes – *e.g.* cylinder, sphere – allowing to restrict that computation in some regions of the simulation box. In that case, the region of interest could be defined as a cavity

limited on z by the COGs of the substrate and that of the membrane and taking on x/y the size of the box.

However, Plumed does not provide, to our knowledge, any way to implement such geometrical restriction straightforwardly, but it does provide the method to define a cavity. As shown on the Figure 34 , the cavity should be defined by means of 4 atoms. Since the steered MD (SMD) process will drive the membrane to move closer to the surface, it is important to define the cavity in such a way that it really takes into account the COG of the membrane. Plumed allows only two way to use an atom which coordinates are not fixed:

- either by taking an atom from the system – but there is no atom in the system whose COG will always coincide with the one of the membrane,
- or by defining a virtual atom as the center of geometry of a group.

It is not possible to define a third atom with the components of another atom or virtual atoms, to obtain for instance, a virtual atom which coordinates read:

$$\boldsymbol{v}=\begin{pmatrix} 0 \\ 0 \\ z_{membrane\,COG} \end{pmatrix}.$$

That limitation drives us to make use of a virtual atom defined as the COG of the membrane. A schematic representation of the cavity is reported in Figure 34. To build the cavity, one needs to understand how it is defined. Plumed defines it out of 4 atoms. The first 3 atoms are used to generate the 3 unit vectors which will define the 3 dimensions of the rectangular cuboid that will define the cavity. The first of these unit vectors, *u*, points from the first reference atom to the second. The second, *v*, is then the normal to the plane containing atoms 1,2 and 3 and the the third, *w*, is the unit vector orthogonal to these first two vectors. Finally the vector connecting atom 1 to atom 4 is used to define the extent of the box in each of the *u*, *v* and *w* directions. Since we can define only one atom in the membrane due its motion (center), this atom should be the 4th atom, which is used only once. Then, the coordinates of the 3 other atoms are expressed in scaled components to take into account the box dimension and express the coordinates of the system for each dimension in the range [-0.5;0.5]. One should note that the z position of these 3 atoms is system

dependent. In our case z=0.25 is lying in the middle of silica. Here is are the coordinates we should thus use:

$$a_1=\begin{pmatrix}-0.5\\-0.5\\0.25\end{pmatrix};a_2=\begin{pmatrix}0.5\\-0.5\\0.25\end{pmatrix};a_3=\begin{pmatrix}-0.5\\-0.5\\0.50\end{pmatrix}.$$

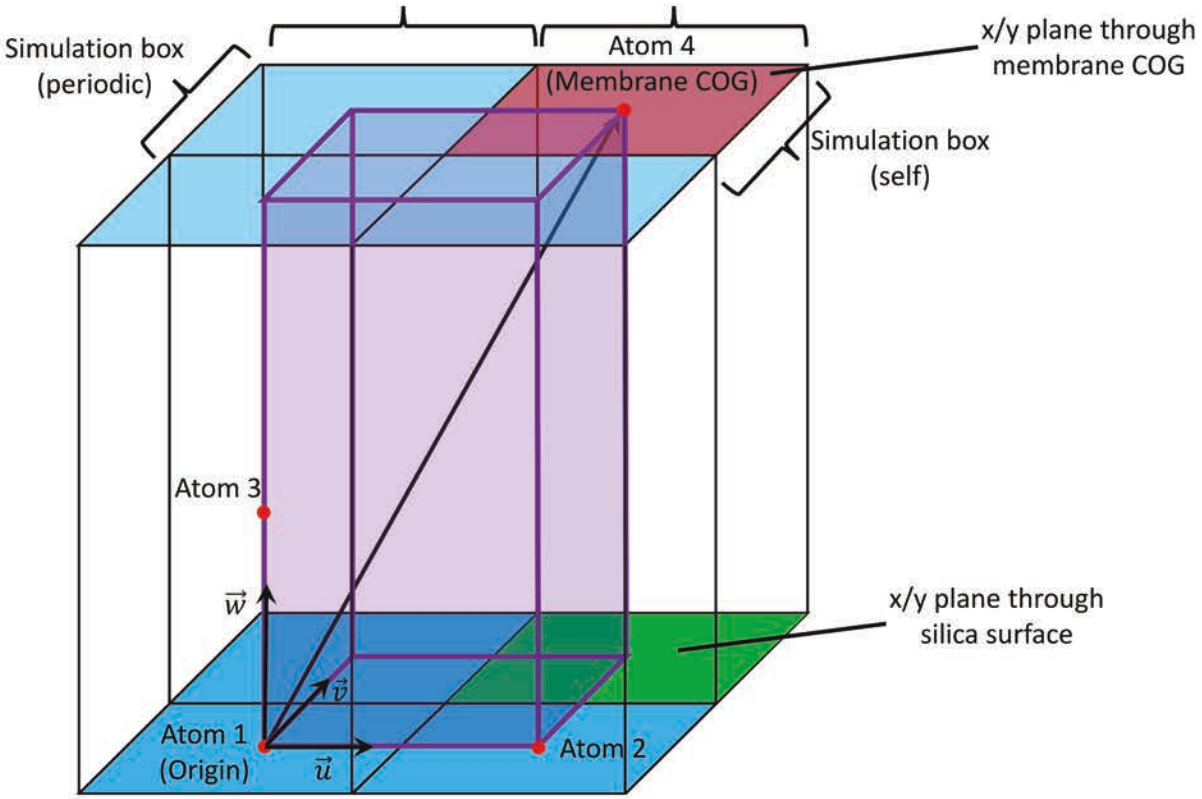

Figure 34: Schematic representation of the cavity built using Plumed. The cavity is made by defining it across 3 periodic images from the simulation box and the simulation box itself. This is needed, due to the use of the scaled components for the definition of the vectors generating the cavity. The cavity is represented in mauve, the 4 atoms generating the cavity are red dots, and the vectors generated by those virtual atoms are represented and named $\vec{u},\vec{v},\vec{w},$ following the convention in Plumed documentation.

Unfortunately, this definition drives to a divergence in the count of water molecules in the box. That could be due to a wrong definition of that cavity relatively to the PBC of the system. Indeed, if the x and y dimension of the box change, it is possible that some atoms will be inside the box multiple times. We tried to take some small margin by shifting the origin of the the coordinates defining the cavity, but this issue kept appearing. However, if only a cavity of size a forth of the box is defined by shifting the origin in (0,0,0), we obtained a correctly defined cavity:

$$a_1=\begin{pmatrix}0.0\\0.0\\0.25\end{pmatrix};a_2=\begin{pmatrix}0.5\\0.0\\0.25\end{pmatrix};a_3=\begin{pmatrix}0.0\\0.0\\0.50\end{pmatrix}.$$

In that case, only a fourth of the water molecules present in the interfacial area were selected, as compared with a selection using MDAnalysis. One may think that it is possible to simply generate 4 cavities and sum them to define the CV. However, the unique definition of an atom located at the COG of the membrane hampers this possibility. This drives this CV not to be an option with the current version of Plumed.

Here is the implementation of the CV:

```
## Selections from the index file
  water:          GROUP NDX_FILE=plumed.ndx NDX_GROUP=Water UNIQUE
  membrane:       GROUP NDX_FILE=plumed.ndx NDX_GROUP=membrane UNIQUE
  tails:          GROUP NDX_FILE=plumed.ndx NDX_GROUP=Tails UNIQUE
  si_surf:        GROUP NDX_FILE=plumed.ndx NDX_GROUP=si_surf UNIQUE
  phosphates:     GROUP NDX_FILE=plumed.ndx NDX_GROUP=phosphates UNIQUE

# Definition of the COG of the different groups
  membrane_cog:   COM ATOMS=membrane NOPBC # nopbc
  si_surf_cog:    COM ATOMS=si_surf NOPBC

# Definition of the 4 local referentials. The silica COG is [61.91050636, 59.46251586, 40.26026869] initially (MDAnalysis). Initial box is [2.35594  11.87835  16.34846] nm. COG Silica is about 0.24626.
  ref1_atom1:     FIXEDATOM AT=0.0,0.0,0.25 SCALED_COMPONENTS
  ref1_atom2:     FIXEDATOM AT=0.5,0.0,0.25 SCALED_COMPONENTS
  ref1_atom3:     FIXEDATOM AT=0.0,0.0,0.50 SCALED_COMPONENTS

# Compute the density between the COGs of the silica and membrane
  dens_water:     DENSITY SPECIES=water
  CAVITY  DATA=dens_water  ATOMS=ref1_atom1,ref1_atom2,ref1_atom3,membrane_cog  SIGMA=0.1 LABEL=cav1

# Compute the number of water molecules to check with the reality
  n_water:        CUSTOM ...
          ARG=cav1
          VAR=c1
          FUNC=c1/3
          PERIODIC=NO
  ... CUSTOM

# Define the CV: Number of water / lipid (245 lipid / ML) – for tmonitoring, this is done in a second CUSTOM
  hydra:          CUSTOM ...
          ARG=n_water
```

```
            VAR=n
            FUNC=n/245
            PERIODIC=NO
  ... CUSTOM

# Defining the CV
  pulling:          MOVINGRESTRAINT ...
            ARG=hydra
            STEP0=0              AT0=100.0          KAPPA0=1000.0
            STEP1=5000           AT1=100.0          KAPPA1=1000.0
            STEP2=505000         AT2=0.00           KAPPA2=1000.0
  ... MOVINGRESTRAINT
```

ii. Deposition is driven by the distance from membrane to substrate

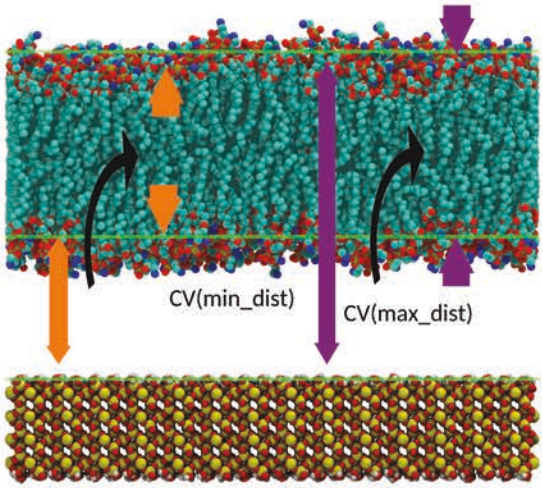

Figure 35: Schematic representation of the CV definition. The choice of the maximum distance is motivated by the study which focuses on the deposition of membrane at the exclusion of any adsorption mechanism. Thus, by choosing the minimal distance represented by the orange double arrow, one may stretch the membrane during the SMD procedure, which will drive the membrane in a further out-of-equilibrium than by pulling the system along the maximum distance depicted by the purple double arrow which would have as a consequence to stretch the membrane which will react to this stress faster than to the stretching stress.,

It is a common assumption to characterize membrane deposition by the distance from the silica surface – which could be characterize by the average position of the first layer of silicon atoms – and the average position of the phosphate from the lower monolayer, which is facing the silica (Figure 35). However, in order to build a CV which will be use to pull the system by means of a SMD procedure, one may want to avoid using this as a CV. Indeed, the SMD procedure will inevitably drive the system out of equilibrium. In the case of that aforementioned CV, it will stretch the membrane which will be far from equilibrium and might partially dissociate. To avoid these issues, the CV was defined as the maximal

distance between the average position of the phosphate from the upper monolayer and the surface of silica (Figure 35). That allows to drive the system out of equilibrium by compressing the membrane – since the water at the interface will not have the time to redistribute though the pore, it will act even more as a wall than normally equilibrated bulk water. The advantage is that the compressibility of the membrane will be limited which will not possibly drive the system that much out of equilibrium in case of an aggressive steering.

Obviously these considerations should be taken at the light of the pretty poor performance of those simulations linked – once again – to the use of the *periodic-molecule* parameter for Gromacs simulations. Being able to use only OpenMP and GPU – and obtaining all in all a poor scalability for a mid-size all-atoms system in the range of 250 000 atoms required from us to optimize every procedure if we wanted to obtain satisfactory performance. For the SMD procedure, 2 fs time step was used, v-rescale temperature coupling was applied for three separate groups, namely to the membrane, silica and solvent. Berendsen pressure coupling was used as it is the most appropriate algorithm for systems so far from equilibrium. At the moment the system was designed, the best performance were between 10 and 15 ns/day for the SMD and umbrella sampling (US) procedures. To allow the membrane and water to relax and to sample sufficiently at any given window of the US procedure, it was expected that 200-400 ns would be sufficient. In fact, some simulations were done to have a look at the rate at which water at the interface was equilibrating, prior to running the US procedure. For that, after a steering procedure and running several windows, the evolution of the number of water molecules at the interface with time was computed. Figure 36 shows that water redistributes upon the applied bias within 100-200 ns. We concluded that a further sampling of 100-200 ns/window would lead to a well-sampled FE profile. With the computational speed and the available resources it seemed as a reasonable assumption: realistic and yet enough to let water reach stable density.

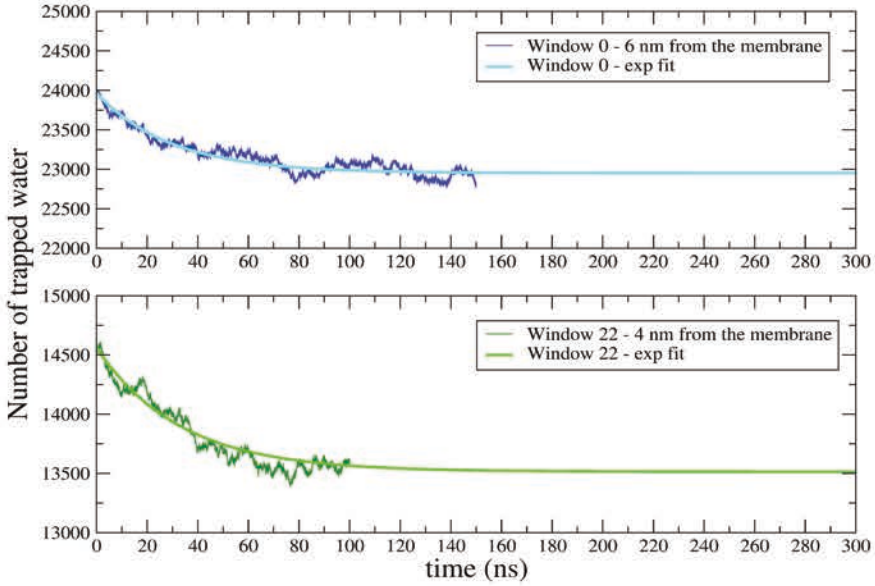

Figure 36: Evolution of the number of trapped water molecules at the interface between the membrane and the substrate with the simulation time for two positions of the center of the biasing potential following a SMD procedure

To avoid the waiting of a month-long single SMD simulation, we decided to opt for a fast pulling rate for short distance. This allowed to generate sequentially a bunch of 3-5 windows that were subsequently running in parallel for 100 ns before using the last frame of the last window to start another SMD procedure. Also, this way allowed to limit membrane deformations while pulling, as after equilibration of the last window system had the possibility to let the trapped interfacial water to redistribute. Due to the rate of pulling (~40 ns/nm) which is faster than the speed for water to reach equilibrium, part of that water accumulates at the level of the lower leaflet of the membrane. If we select windows were this “pocket” drives the membrane to be too far from equilibrium, the time to let the system relax and reach equilibrium would grow dramatically. Since the compressibility of water is known to be pretty small, we expected the membrane to endure intense stress during the SMD procedure and the beginning of the US procedure. To overcome this problem, the first 100ns were ran with a steeper biasing potential (κ=30000 kcal/mol/nm) to hold membrane on place while trapped water is diffusing through the pore and the membrane is relaxing. These first 100ns are not taken into account in our analyses. Afterwards, a much weaker harmonic potential (κ=1000 kcal/mol/nm) is used. Although this method allowed to gain a considerable amount of time, obtaining a first profile with 20-25 windows still requires a considerable amount of time, independently of the available computational resources due to

the issue to set up a nice parallelization scheme. Hence, obtaining one single profile sums more than 5 months of computations.

The implementation of the CV was made in Plumed and can be summed up as follows:

```
# Loading all the index groups for the substrate surface and the membrane phosphates
  membrane:          GROUP NDX_FILE=plumed.ndx NDX_GROUP=Lipid UNIQUE
  tails:             GROUP NDX_FILE=plumed.ndx NDX_GROUP=Tails UNIQUE
  silica:            GROUP NDX_FILE=plumed.ndx NDX_GROUP=silica UNIQUE
  phosphate0:        GROUP NDX_FILE=plumed.ndx NDX_GROUP=phosphate0 UNIQUE
  phosphate1:        GROUP NDX_FILE=plumed.ndx NDX_GROUP=phosphate1 UNIQUE
  phosphate2:        GROUP NDX_FILE=plumed.ndx NDX_GROUP=phosphate2 UNIQUE
  phosphate3:        GROUP NDX_FILE=plumed.ndx NDX_GROUP=phosphate3 UNIQUE
  phosphate4:        GROUP NDX_FILE=plumed.ndx NDX_GROUP=phosphate4 UNIQUE
  phosphate5:        GROUP NDX_FILE=plumed.ndx NDX_GROUP=phosphate5 UNIQUE
  phosphate6:        GROUP NDX_FILE=plumed.ndx NDX_GROUP=phosphate6 UNIQUE
  phosphate7:        GROUP NDX_FILE=plumed.ndx NDX_GROUP=phosphate7 UNIQUE
  phosphate8:        GROUP NDX_FILE=plumed.ndx NDX_GROUP=phosphate8 UNIQUE
  phosphate9:        GROUP NDX_FILE=plumed.ndx NDX_GROUP=phosphate9 UNIQUE
  phosphate10:       GROUP NDX_FILE=plumed.ndx NDX_GROUP=phosphate10 UNIQUE
  phosphate11:       GROUP NDX_FILE=plumed.ndx NDX_GROUP=phosphate11 UNIQUE
  phosphate12:       GROUP NDX_FILE=plumed.ndx NDX_GROUP=phosphate12 UNIQUE
  phosphate13:       GROUP NDX_FILE=plumed.ndx NDX_GROUP=phosphate13 UNIQUE
  phosphate14:       GROUP NDX_FILE=plumed.ndx NDX_GROUP=phosphate14 UNIQUE
  phosphate15:       GROUP NDX_FILE=plumed.ndx NDX_GROUP=phosphate15 UNIQUE
  phosphate16:       GROUP NDX_FILE=plumed.ndx NDX_GROUP=phosphate16 UNIQUE
  phosphate17:       GROUP NDX_FILE=plumed.ndx NDX_GROUP=phosphate17 UNIQUE

# Computing the COG of each group
  membrane_com:      CENTER ATOMS=membrane NOPBC
  silica_cog:        COM ATOMS=silica NOPBC
  phosphate0_cog:    COM ATOMS=phosphate0 NOPBC
  phosphate1_cog:    COM ATOMS=phosphate1 NOPBC
  phosphate2_cog:    COM ATOMS=phosphate2 NOPBC
  phosphate3_cog:    COM ATOMS=phosphate3 NOPBC
  phosphate4_cog:    COM ATOMS=phosphate4 NOPBC
  phosphate5_cog:    COM ATOMS=phosphate5 NOPBC
  phosphate6_cog:    COM ATOMS=phosphate6 NOPBC
  phosphate7_cog:    COM ATOMS=phosphate7 NOPBC
  phosphate8_cog:    COM ATOMS=phosphate8 NOPBC
  phosphate9_cog:    COM ATOMS=phosphate9 NOPBC
  phosphate10_cog:   COM ATOMS=phosphate10 NOPBC
  phosphate11_cog:   COM ATOMS=phosphate11 NOPBC
  phosphate12_cog:   COM ATOMS=phosphate12 NOPBC
  phosphate13_cog:   COM ATOMS=phosphate13 NOPBC
  phosphate14_cog:   COM ATOMS=phosphate14 NOPBC
```

```
phosphate15_cog:        COM ATOMS=phosphate15 NOPBC
phosphate16_cog:        COM ATOMS=phosphate16 NOPBC
phosphate17_cog:        COM ATOMS=phosphate17 NOPBC

# Computing the distances
interf_dist:            ZDISTANCES GROUPA=silica_cog GROUPB=phosphate0_cog,
phosphate1_cog, phosphate2_cog, phosphate3_cog, phosphate4_cog, phosphate5_cog,
phosphate6_cog, phosphate7_cog, phosphate8_cog, phosphate9_cog, phosphate10_cog,
phosphate11_cog, phosphate12_cog, phosphate13_cog, phosphate14_cog, phosphate15_cog,
phosphate16_cog, phosphate17_cog MAX={BETA=0.02} NOPBC LOWMEM

# Defining the CV
restdist:               RESTRAINT ...
        ARG=interf_dist.max
        AT=6.0
        KAPPA=1000.0
... RESTRAINT
```

In this Plumed implementation of the CV, we use a grid of phosphate groups which divides the membrane surface in 18 groups. There are two reasons to use this extra complexity. The first being that the selection of subgroups permits easily to select those phosphates which are not involved in the pore. Secondly, the extra averaging also smooths the membrane surface and helps avoiding extra fluctuations which we do not wish to consider in our model.

The US procedure is using rather standard parameters. The windows are spaced every 1 Å , for the production run a value of the force constant for the biasing potential κ=1000 kcal mol^{-1} nm^{-1} permitted to obtain a sufficient overlap even while using a bin size of 0.1 Å (Figure 37).

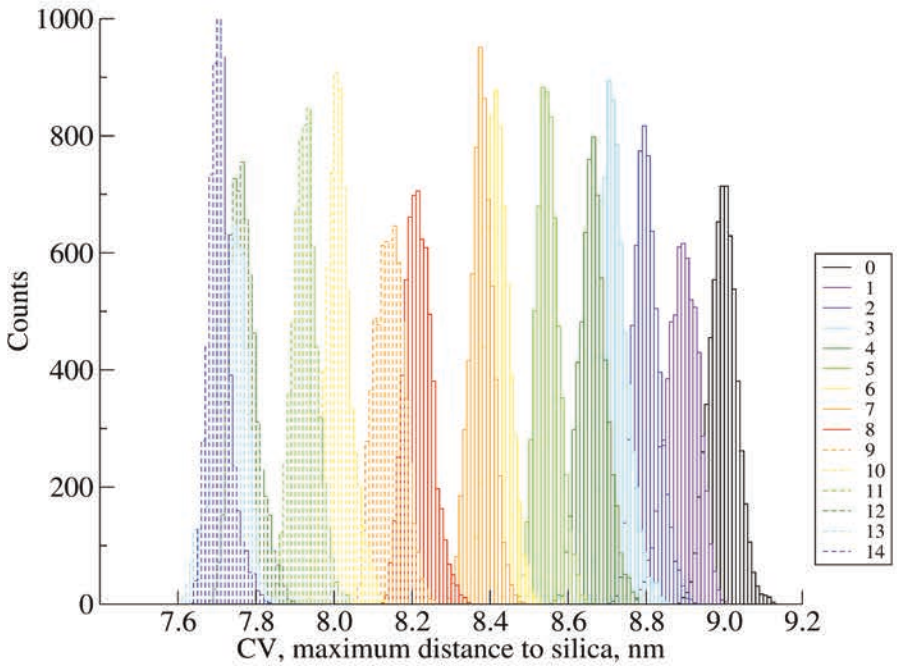

Figure 37: Histograms for the first 15 windows involved in the US procedure for the first 150 ns. One can see that the overlap is already substantial between adjacent windows and that the lowest cardinal in any bin is always statistically representative which ensures to obtain a smooth FE profile.

Although the system was sampled for more than 250 ns for the whole set of windows and up to 350 ns for the first 23 windows, the FE profile did not reach convergence. Figure 38 shows the convergence plot by bunch of 30 ns and presents visibly strong variations. It is clear that any trends presented in this graph is not trustworthy for general conclusions, as variations are far too big and it is hard to see the general tendency for this profile without complete convergence. Similar conclusions are drawn on the free energy profiles computed from the subset of windows ran for 350 ns. Interestingly, the water exchange between bulk and interfacial water is almost null, but the profile was not converged. That could be the sign that the CV that was chosen is not appropriately describing the deposition mechanism. Indeed, we know that membranes endure some major changes while interacting with surfaces, starting by an increase of the area per lipid, some drastic changes of the order parameter and followed by partial or complete reorganizations of the lipid at the surface of the substrate [1], [104], [276], [282]. It is worth mentioning that the most important modifications at the membrane level should not be able to happen due to the setup using a fixed area per lipid, thus it is very possible that the SMD procedure just drove the system too far out of equilibrium to be able to relax it in the range of 300 ns.

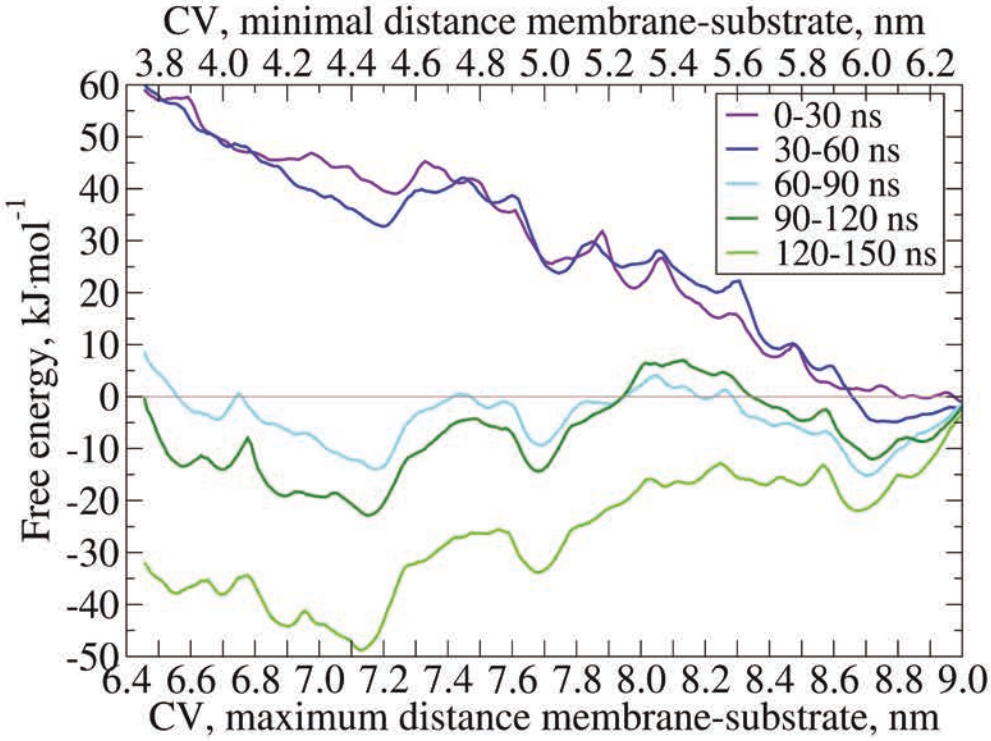

Figure 38: Convergence plot showing the free energy profile of deposition of POPE on silica for the first 26 windows sampled for 250 ns.

IV. A rough model in coarse gained simulations

Since the initial attempts did not succeed with all-atoms MD simulations, particularly due to the drastic amount of time needed to sample correctly the system, was decided to start to build up a naive system in CG MD, that would be later refined, to give a better understanding of the major contributions to the interactions between substrate and membrane. First we decided to use a very rough model of silica published by Perrin *et al.* [283]. This model consists of 1 type of neutral bead which represents a silanol group, this model does not take into account the bulk silica, as their computations show no differences for their computations for multiple-layer silica model.

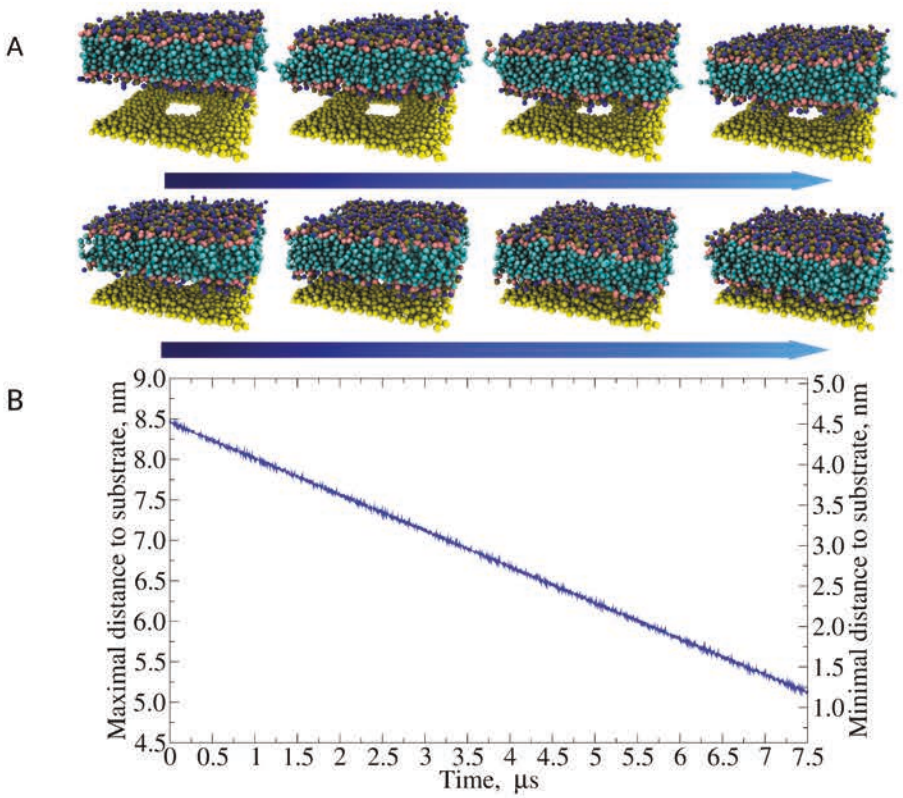

Figure 39: A. Screenshots from the simulation showing the SMD procedure for the deposition of a CG model of POPE on the simple CG model of silica. All atoms are represented as spheres except water which is not shown for the sake of clarity. B. The evolution of the maximal and minimal distance of the system is shown along with the simulation time during the SMD procedure where the center of the biasing potential is move linearly with time and for which the potential biases the maximal distance between the membrane and the silica surface.

Figure 39 A. shows the process of membrane deposition driven by SMD procedure which we used to generate the windows for the subsequent US procedure. The CV used to run the SMD procedure was the same as for the all-atom attempt. We checked that the reaction of the system to the moving restraint is linear and follows well the CV as one can see on Figure 39 B. The free energy profile – which converged pretty fast due to the oversimplification of the system – takes into account 17 windows which were ran for 1 μs each. However, that profile shows (Figure 40) clearly that the present model is not appropriate to show accurate interactions between membrane and surface as no local minima are present contrary to what happens in reality and that the membrane only encounters an energy barrier in the viscinity of the substrate. One can still use this information to notice that 1. the van der Waals interactions play some important role from a distance of 2 nm between the membrane and the surface, 2. that the interactions compensating these repulsive interactions should be strong enough to compensate that energy barrier. Since experiments show that the membranes tend to equilibrate at distances in the range 0.6 – 2.5 nm, it is clear that the

presence of charged silanols, absent from this model, play a fundamental role: the electrostatic interactions due to the partial charges of the silanol groups, and to the net charge of the deprotonated silanols, are the main contribution to the membrane equilibration.

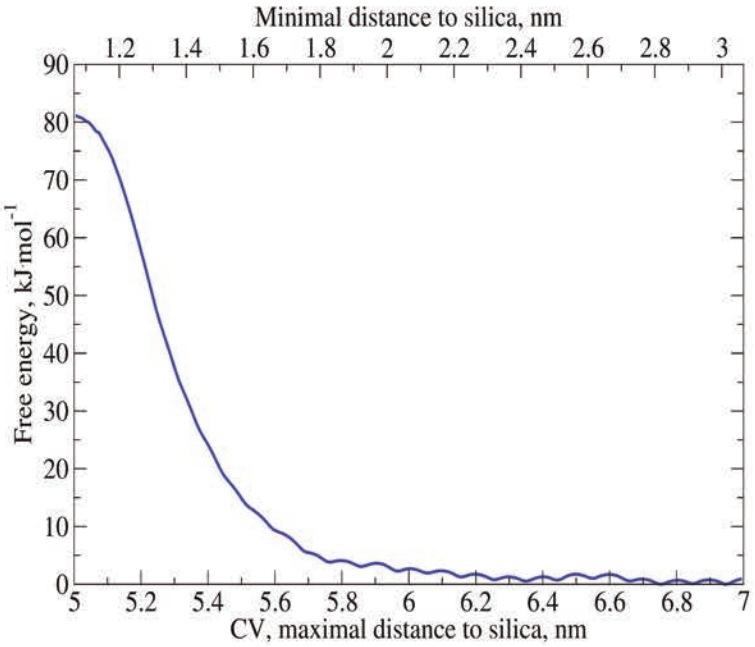

Figure 40: Free energy profile of deposition of POPE membrane on the simple model of silica.

V. A refined model in coarse grained simulations

To add some more complexity to the CG model, we decided to use a second model, making use of two beads to model the silica; one bead for the inner material and one bead modeling the silanols. This model was chosen to answer the two following questions:

- Are the electrostatic interactions with silanols playing the most important role?
- Can heterogeneous CG model bring more realistic description of the deposition process?

This model is taken from the work by David *et al.* [284]. They use this model to study interactions between the silica and poly(cis-1,4-butadiene) polymer to simulate rubber-silica nanocomposites.

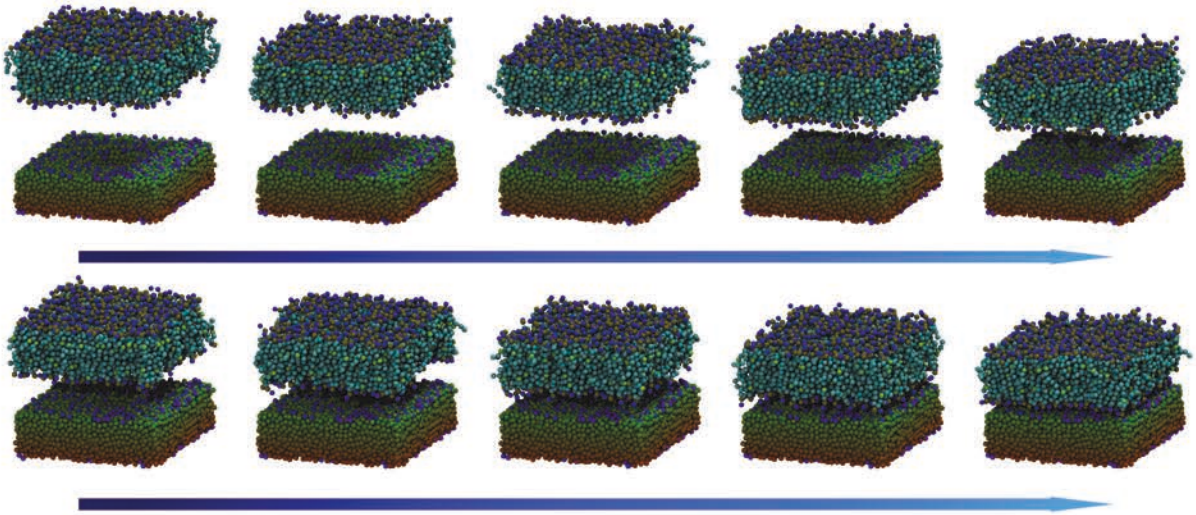

Figure 41: Snapshot from the simulation showing the SMD procedure. Beads are represented as spheres. Note that Q4 beads from core silica are represented with a gradient of colors form green to red to help seeing the pore at the center. Q3 beads are in mauve. The color code for the membrane is the same as before but the beads showing the double bonds in the lipid tails which are set in green to avoid confusions with Q3. The arrows refer to the the time evolution of the trajectory from which these snapshots were taken.

To answer the second question, the pristine model from that work was applied directly. There, the electrostatic interactions are not assigned to silica as they are encoded in the van der Waals term due to the way the Iterative Boltzmann inversion (IBI) procedure was applied. That means that no partial charges are applied to the two bead types forming silica. The second model which was used is a simple model where the silanols beads (called Q3) are assigned a positive partial charge (0.8) and the silica beads (Q4) are assigned a very weakly negative charge (-0.041) to keep the system neutral. As far as it was just an initial test for proving the concept, charges were assigned indicatively and no charge-fitting procedures were used.

Figure 41 shows a depiction of the SMD procedure that was used to prepare the windows for the US procedure in the case of the pristine model of silica. Again, the same CV was used for running the SMD procedure and the same windows were used for the US procedure but simply changed the partial charges for the second model. The reaction of the system to the applied moving restraint was plotted on Figure 42 to check that the system reacts linearly to the motion of the biasing potential.

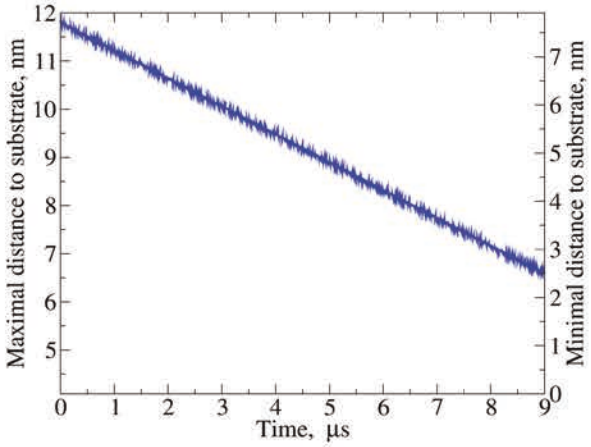

Figure 42: Reaction of the system to the moving restraint applied during the SMD procedure.

Figure 43 shows the FE energy profiles for those two setups. One will notice that the general trend is very similar to that of the rough silica model from the previous section, showing only one huge potential barrier. There is also no big difference between the model with partial charges and the other one – which does not allow us to conclude. Indeed, it seems surprising that adding electrostatic interactions doesn't change the shape of the FE profile. Yet it can come out from the oversimplified description of silica and just leaves us out of the full description of complexity of electrostatics between the membrane and charged substrate.

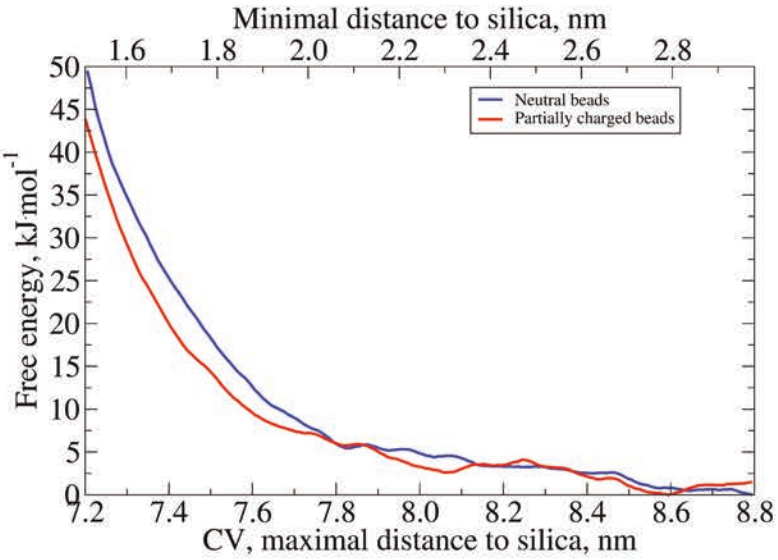

Figure 43: Free energy profile using a 2-beads model for silica. In blue the original model is used, in red, partial charges are assigned to the two beads Q3 and Q4 representing resp. the silanol groups and the core silica.

VI. Conclusions

This development work which has yet to be further complemented (see section Conclusions and Perspective), has shown that it is possible to design a collective variable which allows to apply a steered MD procedure driving a lipid bilayer from bulk solvent to the immediate vicinity of a solid substrate.

Many setups have been built to evaluate the best way to drive such simulations with both AA and CG MD simulations. Even though it would be best to obtain a setup where at least one of the axes along the membrane surface could be coupled in pressure, we showed that, with the current abilities of MD packages such as Gromacs, this task might be hard to accomplish due to the periodic surface-surface interactions of a non-periodic substrate, for instance.

Moreover, as the systems involved in this free energy calculations are relaxing with long characteristic times – we have shown that water, for instance would equilibrate in the range of 100-300 ns, and we know that lipid membranes in all-atoms can reach an equilibrium in the range of 200-500 ns – such enhanced sampling techniques as US procedure could be applied only if the computational performance are high. As we mentioned, the use of the *periodic-molecule* option in Gromacs, does not allow to make use of MPI parallelization, driving to very poor performance. Hence, further simplification should be made to design a system where the free energy computation can be made which such method. Alternatively, some less costly method, such as the accelerated weight histogram could potentially be applied for such system [285].

Antimicrobial drugs facing the outer membrane of Gram negative bacteria

The outer membrane of Gram negative bacteria is recognized for its impermeability to hydrophilic drugs and its high rigidity comparably to that of the inner membrane **[11]–[13]**. The presence of divalent cations – magnesium and calcium – has been proven to be essential to maintain the stability of the outer membrane of Gram negative bacteria [14], [15]. These ions are mainly situated in the vicinity of the LPS phosphate groups and are known to cross-link LPS molecules, which greatly participate to the membrane stability and low fluidity along with the many hydrogen bonds between each LPS [16]–[19]. Hence, the OM is highly sensitive to the concentration of divalent ions. A lower concentration can increase the fluidity of the membrane, subsequently increasing its permeability to drugs, however, a higher concentration is known to "freeze" the OM, which could locally disrupt the membrane and allow the permeation of large proteins or DNA [11].

Different molecules, including ethylenediaminetetraacetic acid (EDTA), and cationic antimicrobial peptides (AMPs) or peptide antibiotics, are believed to permeabilize the OM by acting on these divalent ions [20]. Particularly, two polymyxins, polymyxin B and E (colistin), which are lipopeptides are currently used as last resort antibiotics against Gram negative bacteria. Their pathway is still subject to discussion [21], [22], however, it is believed that their efficiency is linked to their interactions with the divalent ions present in the core and lipid A regions of LPS. It was hypothesized that polymyxins can weaken the LPS-LPS interactions by removing the bridge formed by the divalent cations leading either to the OM (complete or partial) disruption or to its permeabilization [15]. The presence of polymyxin B^1 (PMB1) was shown to increase the water content in the sugar region of the OM, which could be a consequence to the lowered LPS-LPS interactions [15]. Jiang *et al.* [23] have shown that the presence of PMB1 affects the density of ions in the LPS inner and outer core.

If the pathway of colistin has been studied extensively, and that extensive *in silico* studies were led [24], there is, to our knowledge, no quantitative observation of its effects with divalent ions at a molecular resolution. In this part, we first propose a new collective variable which affects only the divalent ions in the vicinity of an adsorbed peptide, in order to quantify the facilitation of their displacement caused by this peptide. For that purpose, we compute the difference of the variation of the free energy of this displacement ΔG_{dis} between two systems: one containing colistin and one in the absence of colistin, using a rough model of the LPS (RAMP) implemented in Martini force field [25] which shows a mutated LPS presenting the entire core (*i.e.* inner and outer portions of the core) but no O-antigens. This model gives much more realism than using a deep rough LPS (REMP model for instance) or the only lipid A, as it is known that such mutations of LPS *in vitro* have drastic consequences on the membrane permeability [11]. Moreover the model membrane that we use is that of an asymmetric bilayer where the inner leaflet is composed of POPE, and not a symmetric LPS membrane which would also not correspond to the reality. This initial part allow us to quantify the content in divalent ions in the vicinity of colistin, which would be difficult without enhanced sampling methods, due to the rigidity of the membrane and the presence of many charged groups which ultimately lead to the presence of many potential metastable states. We then used the knowledge of the preferred distribution of ions around colistin to study the influence on the structure of the membrane in the presence of colistin with an optimal divalent ion content in its surrounding.

It is known that polymyxin concentration has an important impact on its action, as it is the case with most drugs [15]. We investigated the effect of the presence of a localized increased amount of colistin, both on the free energy of ion displacement, and on the consequence on the membrane structure.

In a second part, we built four model membranes in all-atoms, using CHARMM36 force field recent implementations [286]. Since we are interested in electrostatic interactions with divalent ions, it seemed necessary to make use of a more accurate description of these interactions than with Martini force field. Since the current versions of CHARMM36 force field embed the so-called non-bonded fix (NBFIX) modifications, which scales down the non-bonded interactions to more realistic values, the choice of this force field seemed rather justified. Although we know that electronic continuum corrections (ECC) could add even

more realism to the depiction of electrostatic interactions between LPS and divalent ions, we chose to start with a widely used model, to be able to compare directly our results with previously published data. The ECC is basically proposing to scale charges of the atoms or beads to be able to take into account the screening of the Coulomb interactions by electron cloud and this approach would allow to obtain higher precision of the force field without direct taking into account of polarizability effect [287]. The model membranes are asymmetric LPS:POPE membranes, where the outer leaflet is composed exclusively of LPS. We used four models which are attributed to *Salmonella enterica* strains. The first two models, referred to as P1 and P2 use a native form of lipid A with two different protonation states for the phosphate groups in the glucosamide dimer of lipid A, as this state is still a matter of debate [286]. On top of these two initial LPS, two mutated versions, associated to resistance mechanisms to colistin and polymyxin B were considered [288]. The mutations are namely the attachment to the first phosphate group of an additional 4-amino-4-deoxy-L-arabinose, L-Ara4N, from which a model membrane referred to as Ara4N was created, and the replacement of a phosphate group by a phosphoethanolamine group, from which a model membrane referred to as PEtn was created.

In this second part, we were interested in the structural modifications of the membrane upon localized density changes in divalent ions. These changes were driven along the same CV as described in the previous part. Here, all the simulations were led in the absence of peptide, in order to focus on the only effect of ion displacements on the membrane structure.

Finally, we selected a set of peptides which were shown in the literature to affect OM stability. We aim in this last section at understanding if such peptides can exhibit similar effects on the membrane as colistin. This work aim at transposing effects of lipopeptides such as colistin to alpha-helical AMPs which sequence is much easier to tune and optimize.

I. Does colistin enhance the displacement of calcium ions?

i. A collective variable to describe local ion displacement in a membrane

The OM being extremely rigid, the use of MD simulations to follow any processes related to this membrane are generally computationally costly, if ever accessible. Efforts were driven, in the past years, to assess the free energy profile of (partial) translocation of potent drugs in models of the OM [23], [24], [288], [289]. However, the use of enhanced-sampling methods

such as umbrella sampling along with a simple CV (evolution of the position of the COG of the ligand along the normal to the membrane), drives to question the effective quality of these predictions. Even though, in the case of lipid extraction, the use of Martini force field along with specific CVs has shown some relative success [290], one should note that the simulation time for each windows was of 10 µs, which represents a consequent investment in terms of computational resources. Even if the extraction of a LPS and the insertion of a drug, such as a polymyxin, are different processes, it is expected that most the problem comes from the same source, being the low fluidity of LPS molecules, which is at least one order of magnitude lower than that of phospholipids. On the basis of these conclusions about free energy convergence, we reported in Table 9 some representative values of the parameters used for US procedure aiming at estimating the free energy profile of translocation of diverse molecules of biological interest, including polymyxins. We can see that the sampling time per window in the two systems we found that use CG MD simulations is by far lower than the estimated times needed to obtain a poor convergence in the aforementioned study. In the case of AA MD simulations, it is customary to use sampling times in the order of 100 ns or more per window for following such kinds of complex processes as translocation of peptides in simpler phospholipid model membranes, for adjacent windows distant by 1 Å from one another. It is noteworthy that, even with times up to 500-600 ns per window, free energy calculations of processes such as lipid flip-flopping show difficulties to be sampled.

Table 9: Representative parameters used for US procedure of the partial or total translocation process of a molecule of biological interest through models of the OM.

Year; first author [reference]	Force field	Number of windows	Distance between two adjacent windows (Å)	Force constant of the biasing potential (kJ/mol/nm)	Sampling time per window (ns)
2020; Sharma *et al.* [291]	CHARMM36	140	1	1000	100
2021; Jiang *et al.* [23]	Martini 2	10	2	1000	300
2022; Jiang *et al.* [288]	CHARMM36	35	2	500	50
2022; Sharma *et al.* [289]	CHARMM36	35	2	1000	100
2022; Fu *et al.* [22]	Martini 2	36	2	1000	300-1000[16]

It is clear that US procedure is, at the moment of that work, not the best choice to follow the process of translocation of a given hydrophilic ligand through LPS-containing model membranes, as it lays beyond the reasonable computational time. Hence, in order to quantify the ability of colistin to interact with the calcium ions[17], we did not sample this reaction coordinate. However, we propose an original CV, ξ_{dis}, that follows the displacement of divalent ions in a local area of the membrane. This CV, that we implemented using Plumed plug-in [10], defines a cylinder spanning across the membrane, in which the number of calcium ions is computed. This last quantity is the collective variable that we follow to study the displacement of the divalent ions in a local place of the membrane. When the ions are removed from that cylinder, they could diffuse freely in the whole system, so we do not apply any bias to drive the ions to go either to the rest of the lipid membrane or to the bulk water.

Even though the divalent ions are strongly stabilized by the phosphates present in LPS, they could diffuse much faster than bigger molecules such as AMPs or lipopeptides. Hence, the characteristic time of relaxation of the system is considerably reduced, allowing to sample efficiently the processes at stake within acceptable simulation time.

ii. Free energy profiles

To assess the propensity of ions to be displaced by colistin, we computed the free energy profile of calcium ion displacement $G_{dis}^{N_{pep}}(\xi_{dis})$ in a cylinder of radius 1.2 nm centered in the simulation box, for a number of peptides, N_{pep}, of 0, 1, 3, or 5 colistins. The simulations with one or many peptides were made by applying a soft restrains to the peptide(s) (κ=100 kJ/mol/nm) so that colistins will stay inside the defined cylinder. The bias induced by such restrain is expected to be small as colistin does not diffuses fast once adsorbed on the LPS (see sections hereafter for comments on that matter). This restriction was made to ensure that the displacement of ions is centered in the zone were colistin is present, to sample its effect.

16 That range is provided in the article without further details mentioning which systems were simulated for which time. The only analysis of the convergence shown in the supplementary information is that of the RMSD of the polymyxin that is translocating the membrane, for the first 5 windows only (where the barrier is the smallest). This only assessment of the convergence does not show the convergence of the free energy profile, and this only information shows simulation times of 300 ns.

17 All the divalent ions in our systems are calcium ions.

Figure 44 B. and C. show the free energy profiles for these 4 systems. The error bars were reported only for the free energy profiles Figure 44 A. and were not reported for the difference of free energy mentioned hereafter as they are small relatively to the values of free energy. They were computed by means of 200 Bayesian bootstrapping runs by assigning random weights. The profiles were computed from the last 500 ns of the production runs using WHAM algorithm. The difference of free energy of calcium displacement $\Delta G_{dis}^{N_{pep}}(\xi_{dis})$, shown in Figure 44 D., reads $\Delta G_{dis}^{N_{pep}}(\xi_{dis}) = G_{dis}^{N_{pep}}(\xi_{dis}) - G_{dis}^{0}(\xi_{dis})$.

It is noteworthy to mention that the free energy differences between each profile is significant, with differences above 50 kJ/mol. Hence, even if the errors reported in Figure 44 A. would be drastically underestimated, it is clear that the observed trends in free energy are markedly different. Surprisingly, the addition of colistin in the system appears to not lower the free energy barrier to displace the ions farther away, but, on the contrary, seems to generally steepen the free energy well around an equilibrium value.

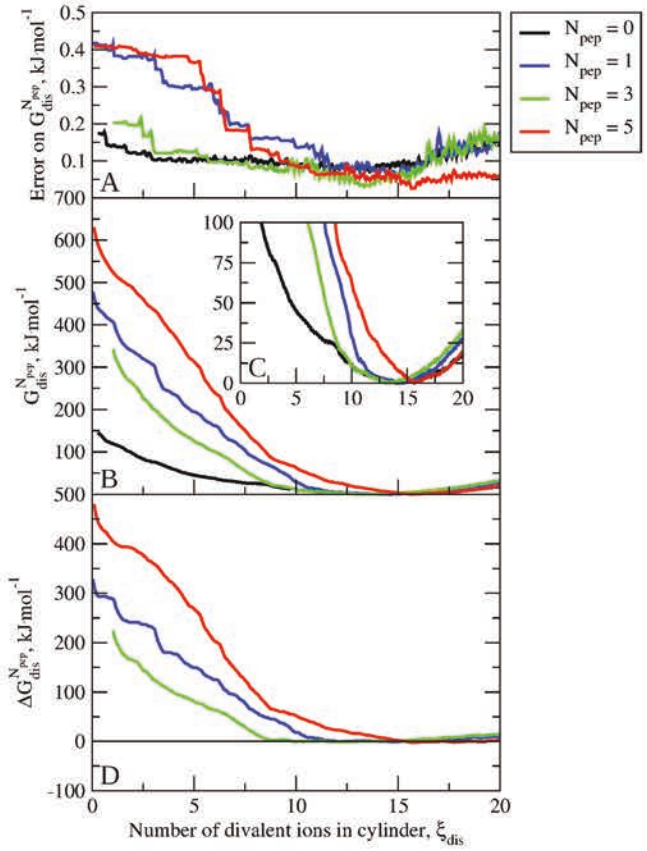

Figure 44: Results from the free energy calculations showing, in A. the error computed over 200 Bayesian bootstrapping runs, in B. the free energy profiles of calcium displacement from a local cylinder centered in the membrane, in C, a subset of B. showing the energy variations in the range 0-100 kJ/mol, and in D. the variation of free energy of calcium displacement for 1, 3, and 5 peptides in the simulation box.

To check for convergence of the US procedure, the convergence plots are reported in Figure 45. For $N_{pep}=\{0,3\}$, the total time of the sampling was respectively of 2.8 or 3.0 µs per window, while, for $N_{pep}=\{1,5\}$, the total sampling time was of 2 µs per window. The convergence plot consists in the computation of the free energy for portions of 200 ns for the last microsecond of run. On can see that the variations of free energy over the last 3 portions do not exceed the fluctuations which is one clear sign of convergence.

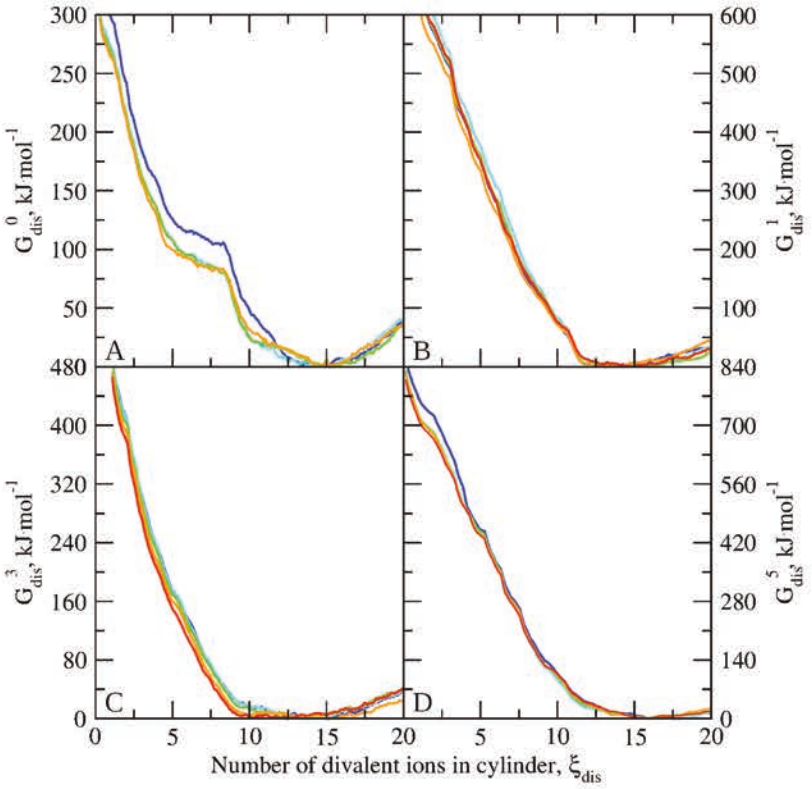

Figure 45: Convergence plots of the free energy of calcium displacement from a cylinder. The subplots A, B,C, and D correspond respectively to systems with 0, 1, 3, and 5 colistins. Each plot is made for a portion of 200 ns of the trajectory, during the last microsecond of sampling for each window. Dark blue correspond to the first portion, cyan to the second, green to the third, orange to the fourth, and red to the fifth. Sampling the system with 0 colistins is shown only until 2.8 µs as it is the maximum time for 5 windows out of 80. The other windows of this system were sampled for 3 µs.

It is hence needed to understand the origin of this counter-intuitive behavior for which several explanations could be attributed. The next section consists in deciphering whether these observations are meaningful in the frame of the study of colistin and other polymyxins pathways, or if it comes from a ill-defined setup, or reaches the limits of coarse-grained definition.

iii. Density profile of calcium ions

To better understand the reason why the presence of adsorbed colistin steepens the free energy well around the equilibrium value of calcium ions, we first investigated the density profile of these ions for the different systems, respectively inside and outside of the cylinder (Figure 46). At first, it is clear that the general shape of the density in the part of the membrane outside from the cylinder, that we will refer to as bulk membrane hereafter, is generally conserved even for the extreme values of the CV which are far from the equilibrium value. Indeed, one can see a first peak in the density profile (Figure 46, dashed

lines), which exhibit a shoulder on its right (towards higher values along the Z axis). This first peak is followed by a lower more convoluted second peak closer to the top of the core.

The profiles in continuous lines in Figure 46 represent the calcium density inside the cylinder where the biasing potential is applied. For most of systems, we still can see that the distribution of ions is generally comprised in two areas, which correspond roughly to the two peaks mentioned above, at the exception of systems for $\xi_{dis}=9;\ N_{pep}=1$ and $\xi_{dis}=1$. Hence, one can conclude that the general distribution of calcium ions along the Z axis is not affected by the biasing potential or by the presence of adsorbed colistins and that the action of the SMD procedure is most likely a stochastic process.

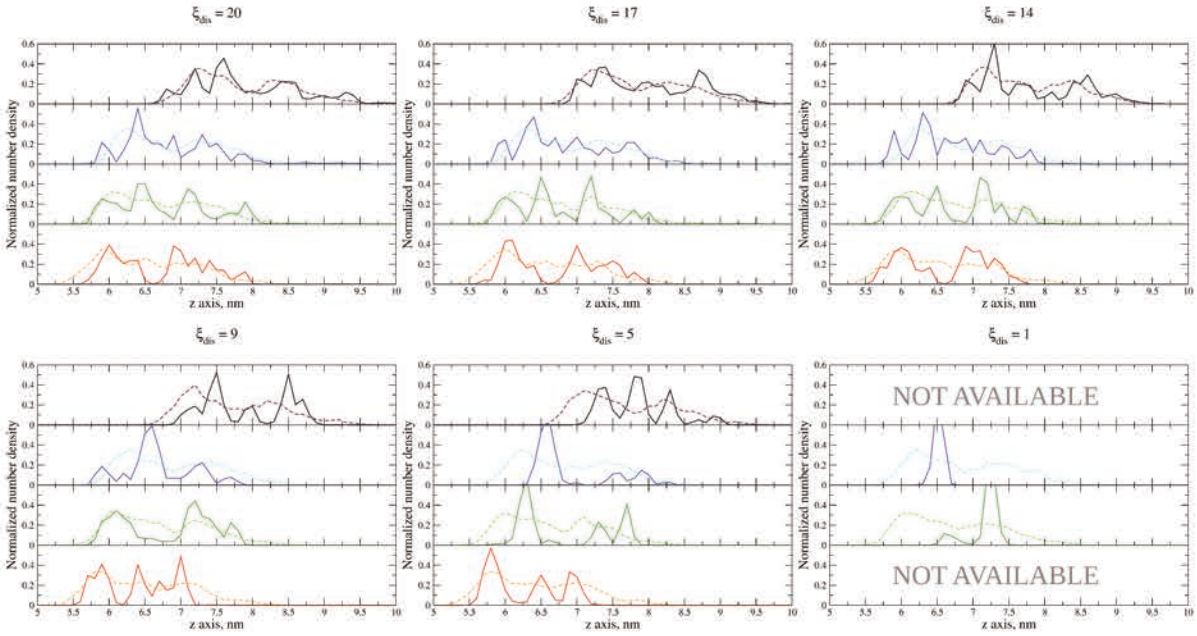

Figure 46: Plots of the normalized number density, along the Z axis of the simulation box, of calcium ions for different values of the CV ranging from 20 to 1 ion. Each line of the different subfigures correspond to a given number of colistin(s) in the system, from top to bottom, respectively 0, 1, 3, and 5 colistins. The continuous lines correspond to the averaged normalized number density of calcium ions in the cylinder, while the dashed lines correspond to that out of the cylinder. Some of the selection are empty due to the fluctuations of the number of ions in the cylinder which can drive to empty selections, which were not handled by the analysis script written for this analysis. Hence, we do not report the values for 0 and 5 colistins when the CV is centered around 1. These density profiles are computed over the last microsecond of the umbrella sampling window for which the biasing potential is centered around the indicated value of the CV.

It is noteworthy that the exchange of ions through the cylinder is happening entirely with the bulk membrane. Indeed, after following the calcium ions that leave or enter the cylinder, we noticed that none of these ions come from or go to the bulk water during the set of simulations ran using Martini force field.

iv. XY density map

Since the density profiles of calcium across the membrane do not explain why we observe that free energy of calcium removal is steeper in the case of the presence of colistin than the opposite, we decided to observe the density of different characteristic groups along the X and Y axes, for different values of the CV.

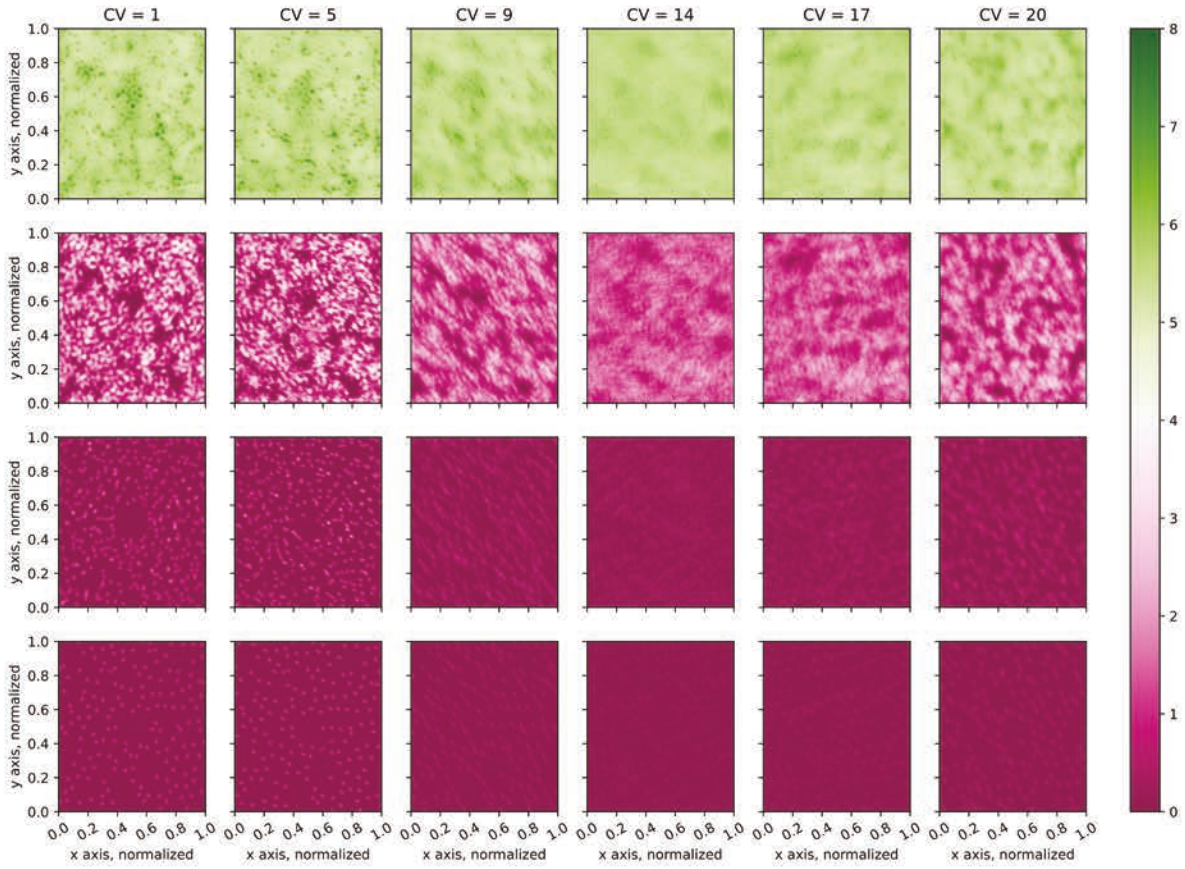

Figure 47: XY density profiles for the system with $N_{pep} = 0$. The first line is the density of water, the second line is the density of LPS core, the third line of the calcium ions, and the fourth of LPS phosphates. The number densities are in nm^{-3}.

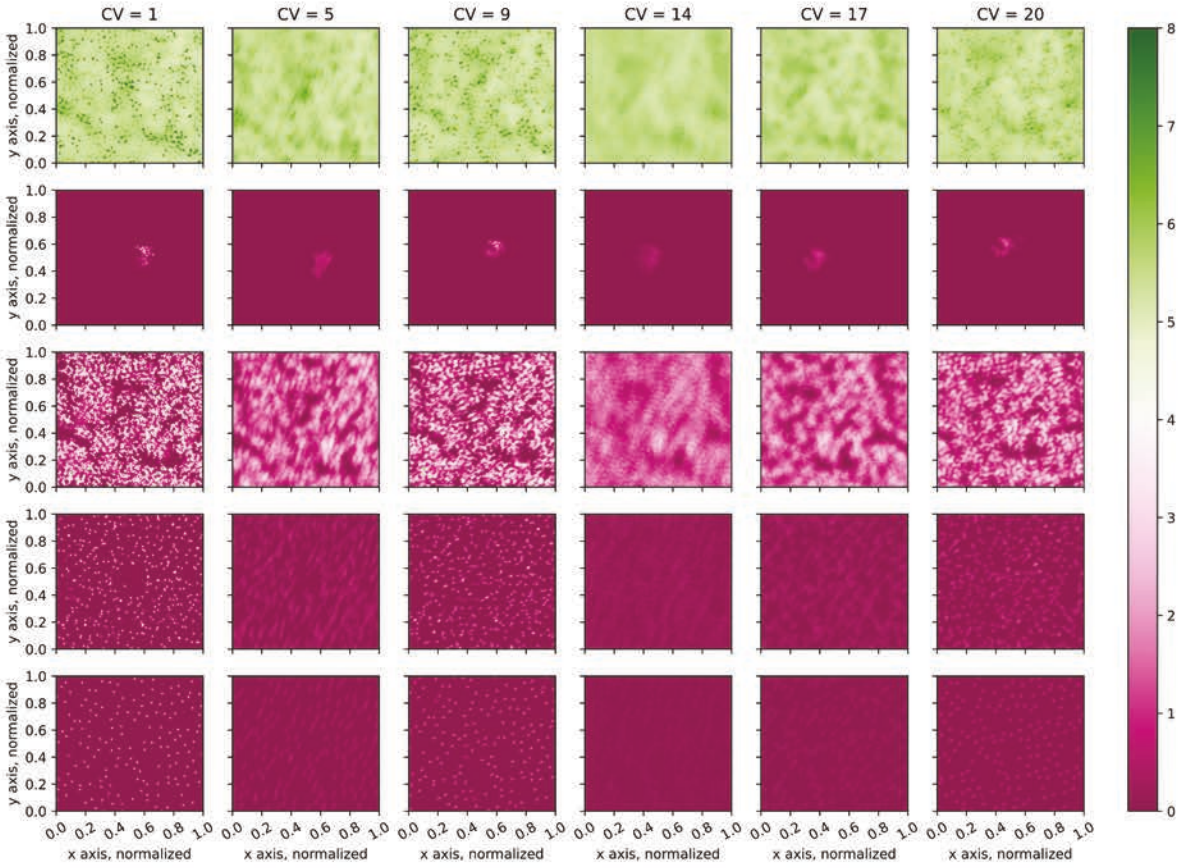

Figure 48: XY density profiles for the system with N_{pep} = 1. The first line is the density of water, the second line is the density of colistin, the third is the density of LPS core, the fourth line of the calcium ions, and the fifth of LPS phosphates. The number densities are in nm^{-3}.

We report the XY density maps for the system with $N_{pep} = 0$ (Figure 47) and $N_{pep} = 1$ (Figure 48) only as the general behaviors do not differ markedly with greater concentrations in colistin. Around the equilibrium value of calcium ions in the cylinder (~14 ions, see Figure 44), the average density shows that the system keeps some fluidity. The individual positions of the water molecules present in the core, of the colistin, of the sugars from the core, of the calcium ions, and of the phosphate groups is not well defined in the related density maps. However, there is a clear tendency towards such reduction of the mobility of the system both upon increase or decrease of the value of the CV from the expected value, although this behavior is not consistent for some values of the CV. Indeed, for $\xi_{dis}=1$ we observe a complete freezing of each of the groups in contact with the membrane. It appears that this phenomenon is only visible for values far enough to the equilibrium value of ions in the cylinder, *i.e.* for values under XX or above YY. It is of high importance to understand if this effect is an artifact linked to the use of Martini force field, a consequence of the CV that

we are using, or the observation of a phase change of the LPS as described in the literature [11], [21].

v. Mobility of LPS

To characterize the mobility of LPS as a function of the CV, we computed the root mean square fluctuation (RMSF) of the phosphate groups of LPS for different values of the CV, either for molecules lying inside, or outside of the cylinder.

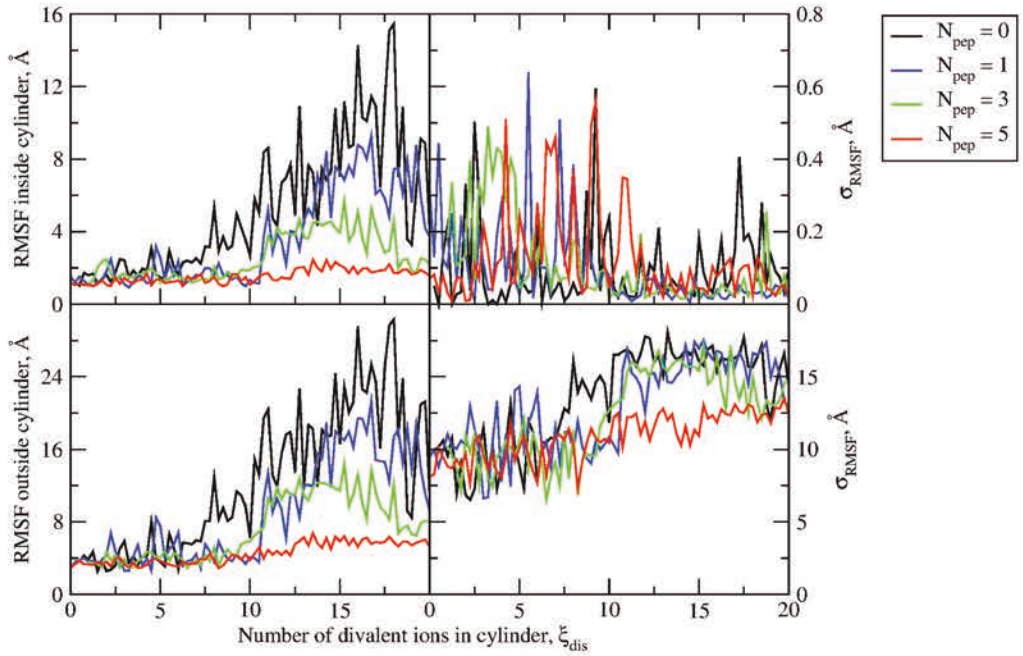

Figure 49: Calculation of the RMSF of the phosphate groups of LPS respectively inside and outside the cylinder defined for the CV. The plots on the right panels represent the standard deviation σ_{RMSF} of the RMSF.

Figure 49 shows the RMSF computed both inside and outside of the cylinder. It is first interesting to note that the trends in the both regions are similar for all the concentrations in colistin, although the fluctuations are much higher in the bulk membrane, which could be a statistical effect. Accordingly, the standard deviation over the RMSF is also higher for the calculations outside of the cylinder. The RMSF of the phosphate groups denotes the "freezing" of the membrane observed while analyzing the XY density maps. Indeed, the RMSF value reaches its highest value around the equilibrium value of the number of calcium ions. It decreases rapidly in the range $\xi_{dis}=15$ to $\xi_{dis}=10$, where it seemingly

reaches a very low plateau. Interestingly, the increase of colistin concentration correlates with an important decrease of the RMSF.

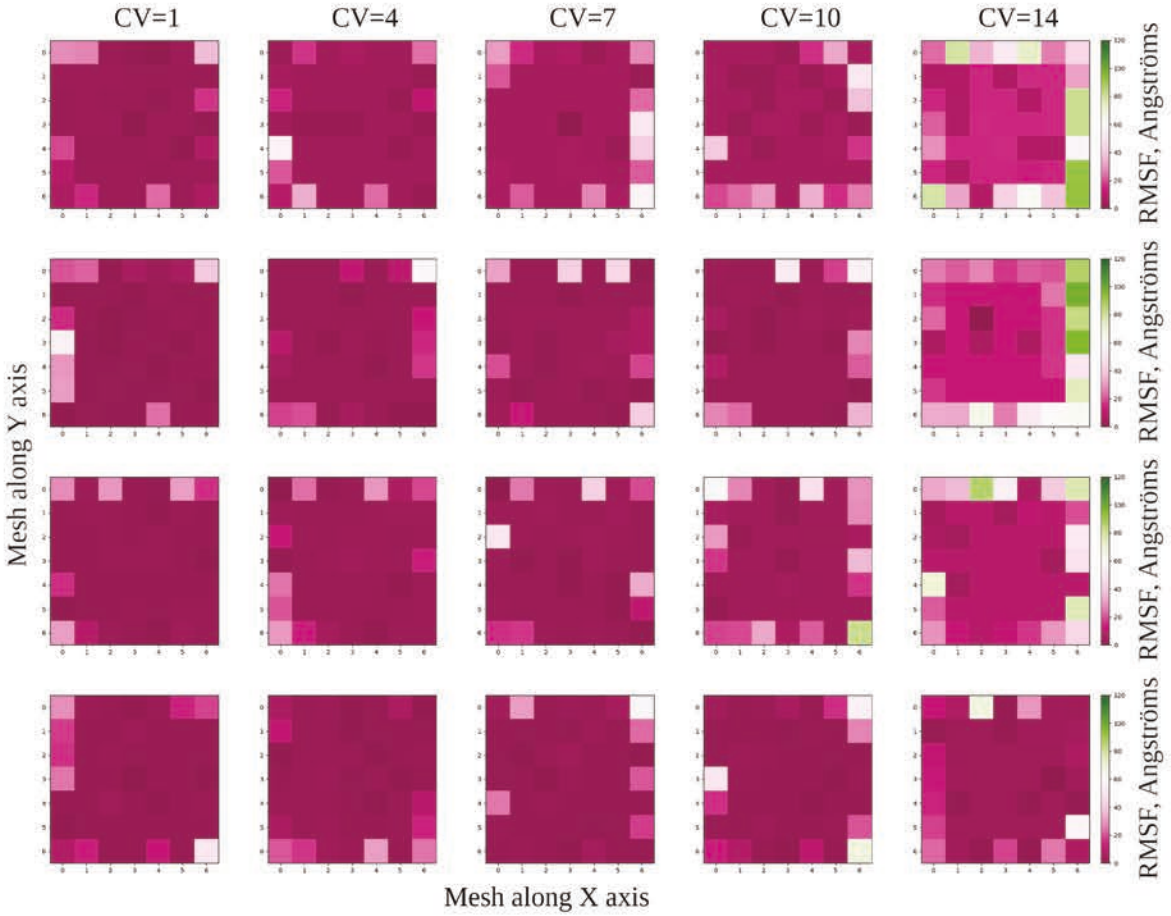

Figure 50: Map of the RMSF along the XY axes. The simulation box was meshed by six bins along each X and Y axis to compute the average value on this map. First line is for the system with no colistin present, second line is for the system with 1 colistin, third one – for 3 colistins and the fourth one is for the system with 5 colistins.

To check whether this freezing that affects the membrane under a given threshold value along the CV is coming from the local defect created in the membrane by the removal of the calcium ions, we computed the map of the RMSF for different values of the CV (Figure 50). This figure shows that lowering of the RMSF values starts at the center of the simulation box, around the position of the cylinder and gradually propagate to the whole surface of the membrane. On top, this effect is visibly stronger for higher concentration in colistin which supports the aforementioned idea that colistin promotes this effect in our systems. While free energy profiles show that the local change in calcium concentration is generally hindered, the potential phase change of the membrane could be enhanced by the presence of colistin, driving to the increase in free energy profile in systems containing peptides.

Manioglu *et al.* [21] recently commented on the necessity of divalent ions to form crystalline structure around polymyxin and on the positive relation between this transition and the concentration in divalent ions. Our present result could thus support the idea that colistin favorizes the nucleation process of such change by affecting the local distribution of calcium ions.

II. Comparison of the coarse-grained models with of all-atom simulations

However, to further investigate whether the changes in membrane fluidity and potentially local phase changes coming from perturbations of the density of divalent ions is not an artifact due to the inherent limitations of coarse-grained force fields or due to the rough parametrization of the divalent ions in Martini force field, it is important to address this topic using all-atom force field.

Not only it is important to validate the previous systems by using an all-atom force field that better describes the membrane dynamics and provides an optimized set of parameters for the non-bonded parameters [292], especially with divalent ions, such as CHARMM36, but it is also necessary to explore variations on the LPS topology to ensure that the observations made in the previous sections are not artifacts. Indeed, Rice and coworkers [292] have shown recently that phosphate charge and calcium parametrization is critically important for obtaining structural properties of LPS-containing membranes close to experimental ones. One of the important conclusions of this study is that calcium parametrization with NBFIX (correction of Lennard-Jones parameters which scale the non-bonded interactions) makes better agreement with experimental values, which is why we used it too. Moreover NMR protonation state prediction assigns -1 charge in physiological pH and using -2 net charge is shown to overestimate affinity of calcium ions to phosphate groups [292].

We present in Figure 51 B. the free energy profiles for four all-atom asymmetric model membranes of the OM containing LPS on the outer leaflet and POPE in the inner leaflet. At the exception of model P2, the free energy is computed only from the equilibrium value to lower values of the CV. We studied the effect of the protonation state of the LPS phosphates by using two models, which attribute respectively a net charge of -1 or -2 to the LPS phosphate groups, for P1 and P2 models. The decrease of the net charge obviously decreases drastically the density of calcium ions in the membranes – however, the general trend is similar to that of P2 model leading to an analogous steepness of the free energy well.

We also computed the free energy profiles for the so-called Ara4N and PEtn mutations of LPS attributed to resistance mechanisms to polymyxins. The resistance mechanisms add some functional group on one of the phosphate, reducing the number of calcium ions in the membrane. Hence, the free energy shows a minimum which is also shifted towards lower values of the CV, comparably with P2 model.

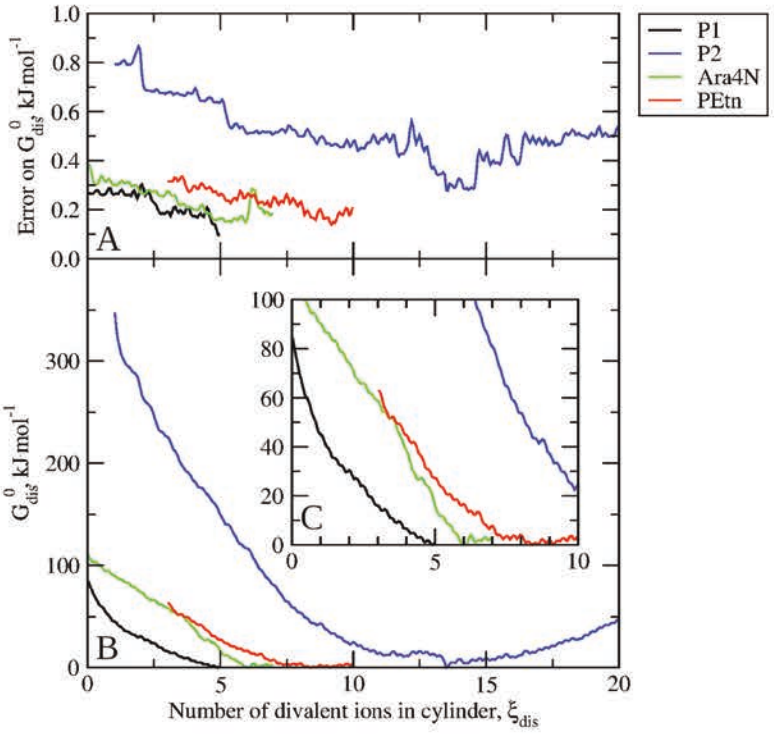

Figure 51: Results from the free energy calculations showing, in A. the error computed over 200 Bayesian bootstrapping runs, in B. the free energy profiles of calcium displacement from a local cylinder centered in the membrane, in C, a subset of B. showing the energy variations in the range 0-100 kJ/mol, and only up to values of the CV up to 10 calcium in the cylinder.

To understand whether the OM in all-atom models is also subject to changes in mobility while creating a local change in the calcium ion density, we first computed the 2D density maps for water, calcium ions, and LPS phosphates (Figure 52, Figure 53, Figure 54, Figure 55). From these maps, it is not as clear as it is for CG simulations whether the change in calcium density modifies the fluidity of the membrane. However, we notice at first that the maps are rather similar for the different LPS models, and that no visible water molecules are trapped in the LPS core in such a way that it alters their diffusion.

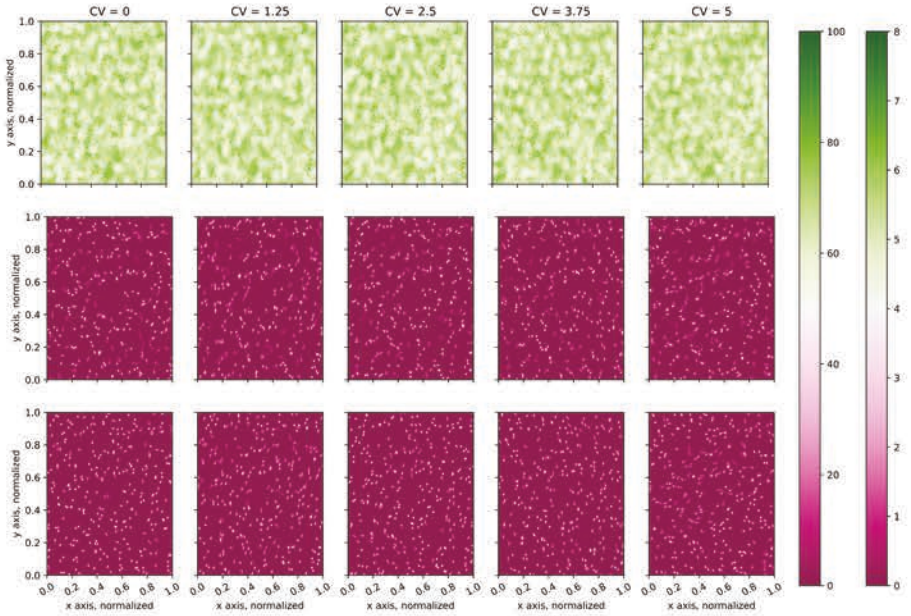

Figure 52: XY density profiles for P1. The first line is the density of water, the second line is the density of calcium ions, and the third is the density of LPS phosphates. The number densities are in nm^{-3}. The first heatmap scale, on the left, corresponds to water densities, the second, on the right, to ions and phosphates.

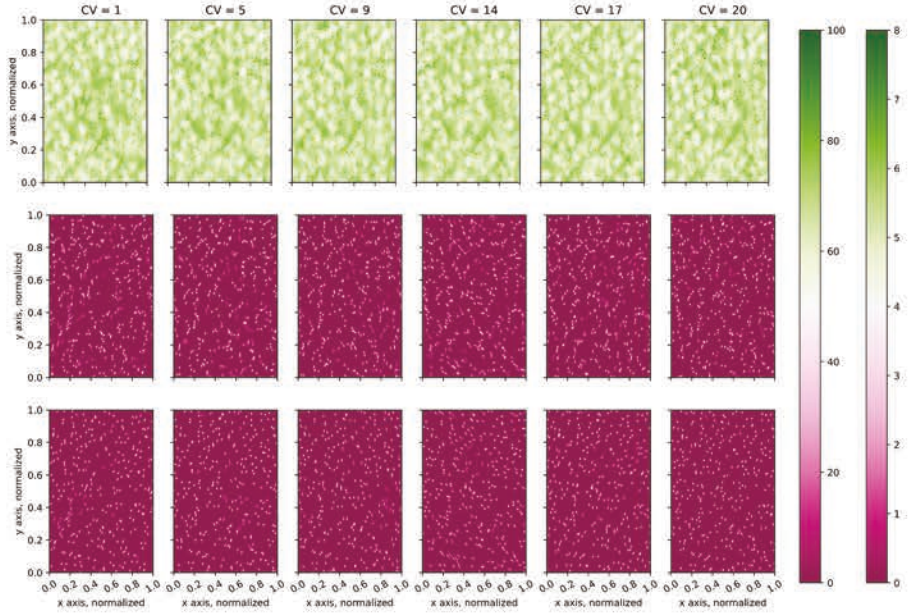

Figure 53: XY density profiles for P2. The first line is the density of water, the second line is the density of calcium ions, and the third is the density of LPS phosphates. The number densities are in nm^{-3}. The first heatmap scale, on the left, correspond to water densities, the second, on the right, to ions and phosphates.

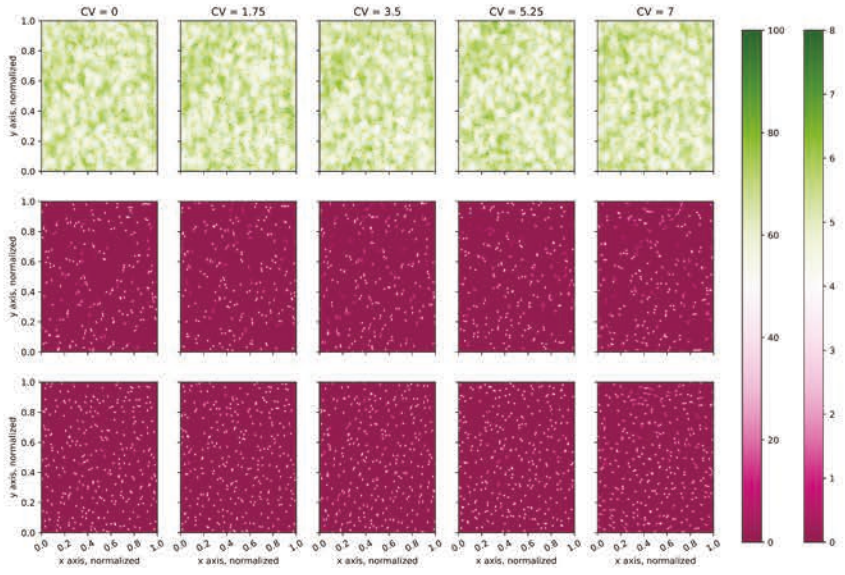

Figure 54: XY density profiles for Ara-4N. The first line is the density of water, the second line is the density of calcium ions, and the third is the density of LPS phosphates. The number densities are in nm^{-3}. The first heatmap scale, on the left, correspond to water densities, the second, on the right, to ions and phosphates.

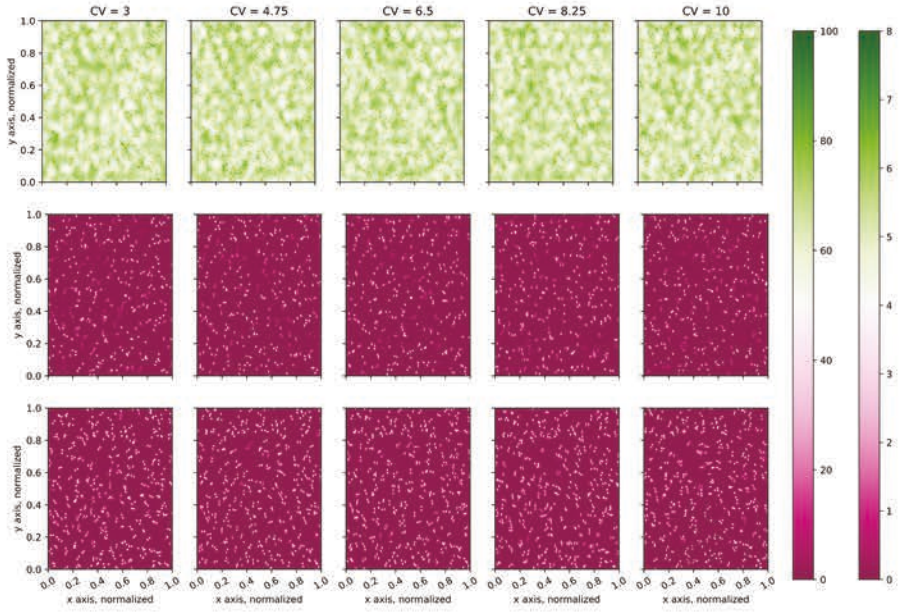

Figure 55: XY density profiles for PEtn. The first line is the density of water, the second line is the density of calcium ions, and the third is the density of LPS phosphates. The number densities are in nm^{-3}. The first heatmap scale, on the left, correspond to water densities, the second, on the right, to ions and phosphates.

We thus computed the average value of the RMSF of phosphates inside and outside the cylinder to have a better understanding of the dynamics of the constituents of the membrane. It appears that both average values are comparable to the smallest values observed in CG MD, here ranging from 1.1 to 1.4 ± 0.2 Å. Hence, the fluctuations over these values are also considerably lower. We notice a slight tendency of increase of the RMSF in the cylinder while removing the ions, but further analyses show a poor correlation with a R^2 of ~0.5-0.6. The variations in RMSF between the smallest and highest values of the regression along the CV do not exceed 0.5 Å. Hence, all the all-atom systems based on CHARMM36 force field appears to be much more stable to local disturbance of the divalent ion density in the membrane, which is surprising.

III. Conclusions

We have introduced a new collective variable which aim at sampling the effect of the creation of a local inhomogeneity in the distribution of ions in a lipid membrane. We applied this CV to compute the free energy associated to the variation of the number of calcium ions in a local cylinder situated in the middle of a simulation box. We observe, using Martini force field, that the addition of colistin steepens the energy well around the equilibrium value of calcium ions. Interestingly, we noticed that varying the value of this CV induces the system to rapidly gain order and lose fluidity. This effect is even emphasized by the presence of colistin. It is possible that we observe a similar transition to the phase transition observed experimentally for bacterial OM while modifying the concentration of divalent ions.

Further calculations using CHARMM36 force field show a qualitative agreement with the free energy calculated using Martini force field. Especially, it is worth mentioning that the free energy profile for the system P2 is the closest to the equivalent simulations ran with Martini force field. However, in the absence of colistin or other peptide, we do not observe such drastic changes in the fluidity of the LPS-containing membrane. Further calculations using AA force field in the presence of peptides should be led to address this observation.

Conclusions and Perspective

In the frame of this work, we first draw a better picture of the interactions between lipid membranes and substrates. The first study of the present work showed that hydrophilicity of a substrate is one of the principal parameters which defines the structure of a deposited lipid structure. We observed that deposited lipid structures continuously reorganize between two extremes – a SAM and a floating SLB – depending on the hydrophilicity of the surface. We have shown as well that SLBs can be stable in such a close-contact state which was observed in many experiments. In the case of close-contact state on a hydrophilic substrate, the lower and upper leaflets can show drastically different conformations, with the upper monolayer showing density profiles extremely close to free-floating bilayer. In the case of a DOPC membrane on silica – the most hydrophilic substrate that we modeled – the density profile of the lower monolayer is very close to that of an unperturbed membrane, even if we can note that few phosphate groups appear in the close vicinity of the substrate, at the same level than the choline. If we make a choice towards less hydrophilic substrate, the effect will be more pronounced. This is further followed by tails having enough affinity with the substrate to flip and lay horizontally close to the surface. These effects are correlated with a decrease of the membrane thickness and of the order parameter of the lower leaflet. All in all, for a pure DOPC membrane, silica seems to stabilize efficiently the lipid bilayer while driving to rather small structural modification.

However, in order to assess the effect on realistic model of the outer membrane (OM) of Gram negative bacteria, further simulations should be led. At first, it would be important to investigate the effect of the substrate on a pure POPE membrane, as PE represents most of the lipid content of the lower leaflet of OM. Nonetheless, to obtain a full picture of the interactions between substrates and model membranes, it is ultimately necessary to simulate an asymmetric LPS:POPE membrane to better understand if the structure of LPS are affected by the substrate. Since we have shown that electrostatic interactions play a non-negligeable role on the deposited system, such refined model makes even more sense as LPS are known to keep their structure partly due to the presence of calcium ions.

Following these conclusions, we further designed systems to quantify the interactions membrane-substrate. We aimed at designing a setup and a collective variable which will allow us to compute the free energy of membrane deposition. We explored a wide set of designs with the aim to allow the interfacial water to redistribute freely while the membrane gets closer to the substrate. We also tested different designs aiming at allowing the membrane to adapt its area per lipid. We wanted to avoid using a bicelle as it was made during the previous study, as the computational time required is rather high and that such design implies extra complexities during the analyses. We concluded that this latter task was hardly possible with the techniques at the time of that work. However, we proposed a design allowing water to redistribute by creating and maintaining a pore in the bilayer. We showed that water can redistribute in the range of 100-150 ns while applying some stress to the system by means of an SMD procedure. We further proposed two collective variables that could effectively follow the deposition process. The first one, which follows the number of water molecules per lipid at the interface between substrate and membrane is complicated to implement. However, we believe that such task could be achieved by hardcoding it directly in Gromacs. On the other hand, we implemented a CV which follows a measure of the distance between membrane phosphates and substrate surface groups. However, the SMD procedure was driving the system far from equilibrium, due to a too low flux of water through the pore and limits linked to both the available computational resources which did not allow us to simulate bigger systems where we could work with a larger pore, and to technical limitations linked to the periodicity of the substrate, which was driving to poor performance on our simulations, did not allow us to obtain a converged free energy profile.

Finally, studying free energy of calcium ions displacement with Martini force field with and without presence of colistin demonstrates that colistin presence strongly helps transition to crystalline or analogous structure of the OM, characterized by its low mobility, thus making calcium displacement being more energy consuming in its presence. Such “freezing” around colistins is very similar to structural changes observed experimentally. At the same time, all-atom simulations for different types of LPS do not show any phase transition in the absence of colistin.

If our results show some structural differences between model membranes based on Martini force field and those based on CHARMM36 force field, it is important to underline that the

free energy profiles follow the same shape. Particularly, our results underline the proximity between Martini model of the OM and all-atom models LPS with deprotonated phosphates. Although this is still a matter of discussion, it seems that deprotonated phosphates are not typical for typical values of the pH in the environment of many bacteria – especially when hosted in human body. Our study does not show clear tendencies of the influence of colistin aggregation on ions mobility. However, one should note that the simulations that we designed were not aiming at describing the complete pathway of colistin. Indeed, to gain more realism, one should follow colistin insertion / translocation through the LPS core at the same as sampling extra degrees of freedom, such as ion mobility. However, at the time of that work, the calculation of translocation profiles in normal fluid membrane using AA force fields is still a very complicated task, due to sampling issues alongside to difficulties to define accurate CV.

This work sets directions for further studies in two complementary topics. First, the tests of different designs and CVs to compute the free energy of membrane deposition on a substrate drove us to a more pragmatic approach which we describe in section I. Finally, after the work by Lundbord *et al.* [293], it is clear that our study of the interaction between colistin and outer membrane can be extended. Section II gives elements on that topic, along with other perspective on the development of new AMPs dedicated to permeabilize the outer membrane of Gram negative bacteria.

I. A rough model of graphene oxide with a pore in all-atoms simulations

The attempts with coarse-grained models had the advantage to validate the general methodology as the CV is shown to be able to drive the unperturbed membrane toward the surface without inducing any visible bias. However, to have an insight on the interactions between membrane and substrate and on the presence of α and β states – it seems that a complete modeling of a new silica topology has to be considered. This work itself is an entire project and would greatly exceed the scope of this work, but it would clearly serve the community and be used in many fields, especially in the modeling of silicon-based nanoparticles. However, until such major advances would be performed, we noticed a more pragmatical approach consisting in using GO surface to address the topic of membrane-substrate interactions.

In order to obtain a simpler setup, we started to drastically simplify the GO by removing any bonded interactions and keeping the surface restrained by freezing all its atoms. The non-bonded interactions between each and every atom from the GO surface also were set to zero using the *energygrp-excl* mdp option. The aforementioned steps were made to alleviate the computational time required to run the simulations. This also allows the system to be computed without the option *periodic-molecules* from Gromacs and thus to use MPI parallelization. However, these choices bind to use only MPI parallelization: the use of OpenMP and GPU architectures are not possible with frozen atoms. They also require the neighbor searching algorithm to be an explicit pair list without buffering (no Verlet algorithm) which was removed in Gromacs version 2020. Consequently, we started to run those simulations with Gromacs 2019. Finally, the system are computed with semi-isotropic pressure coupling where the pressure coupling is acting only along the z axis. That is necessary since we do not set GO as a periodic molecule.

To allow water to flow through the surface a pore is made in the GO surface in such a way that the surface remains globally neutral. Before removing the bonded interactions, an energy minimization of the solvated structure was ran so that the surface groups (hydroxyl an epoxyl) will be close to some natural conformation.

This system seems to a good balance between computational resources and system realism, and the calculations of free energy should be performed to finally obtain some quantitative insights in the presence of close-contact and far-contact states of deposited membranes.

II. Free energy of translocation of colistin in the outer membrane of Gram negative bacteria

At the present time, there is a high demand for the development of innovative therapeutics that could permeate the OM of Gram negative bacteria, particularly antimicrobial peptides. In the meantime, it is still very complicated to predict the quality of *de novo* designed or optimized AMPs. *In silico* computations very often rely on the calculation of the free energy of translocation which bring important insight into peptide-membrane interactions. At the same time, such studies require a correct parametrization, appropriate collective variable, and most often, extensive computational resources.

We are at the moment using the results from the present work and extending it to access free energy profiles of translocations of antimicrobial peptides through the OM. For that work, we first selected peptides from the literature which were able to demonstrate ability to pass through, or disrupt partially or totally the LPS-containing membrane. Among such peptides we could cite I1W and I4W [294], Caerin [295], $MreB_{1-9}$ [296], NK-2 [297], and P1 [298]. These alpha-helical peptides were showing not only general antimicrobial activity against Gram negative bacteria, but also leakage essays and other more specific experiments were able to show that they can permeate OM membranes without help of porins and potentially disrupt them partially creating, in some cases, transient structures analogical to the pores observed on phospholipid membranes targeted by AMPs.

As a primary step to understand the behavior of these AMPs, we studied their adsorption (for all the aforementioned peptides except I4W and P1) using Martini 2 force field. All those peptides were equilibrated on the surface of OM model for 10 to 12 µs. This first study aimed at discriminating potential candidates for further investigations. Indeed, unbiased simulations can give an initial guess on the potential a peptide had to later on permeate the membrane and on the general structural properties of the peptide.

While simulated time was not enough to observe partial translocation we still were able to see some interesting properties. During these 10-12 µs, $MreB_{1-9}$ and NK-2 reached rapidly a plateau value, with the same kinetics and depth of insertion as colistin. On the other hand, Caerin floating on the very top of the sugars for almost 7 µs before reaching a plateau until the end of the simulation ~4 Å lower.

Another difference in between the AMPs is their mobility on the LPS surface. Colistin, NK-2, and $MreB_{1-9}$ were sufficiently immobilized on the surface with MSD values plateauing not higher than 0.3 nm^{-2}. On the contrary, I1W and Caerin did not reach any constant value of the MSD plateau during those 12 microseconds.

Caerin, which did not insert well, had an orientation constantly parallel to the membrane all along the simulation. $MreB_{1-9}$ was exposing its N-terminus toward the surface with angles in the range 90-120° at the beginning of the adsorption process. I1W, which fluctuated the most along the Z-axis was sampling larger spectrum of orientation, but facing consistently N-terminus again, with angles ranging from 90° to almost 140°. On the other hand, NK-2

was exposing more its C-terminus while adsorbing on the LPS leaflet with orientations in the range 50° to 110°. Colistin behavior is not directly comparable as its structure differs to the one of a peptide. Its orientation distribution was clearly convoluted between two behavior. Colistin was alternating phases during which it was lying parallel to the membrane surface, and some when its orientation was widely fluctuating, but with its tail facing consistently downwards, and an average angle of 55°.

This preliminary study could help to understand what are the key parameters for peptides to disrupt the OM. However, the adsorption process alone does not allow to have a clear understanding of these AMPs behavior. Hence, we plan to perform a translocation free energy calculation optimized for the presence of LPS. Indeed, not only the LPS-containing membrane is extremely rigid, making it slow to sample a wide part of the configurational space, but alpha-helical peptides are sensitive to the SMD procedure. Indeed, the “pulling” of the peptide through the membrane along the chosen CV (which is generally oversimplified), could drive the peptide far from equilibrium, potentially stuck in the LPS lipid A which drive a very stiff energetic barrier. Following the article by Lundbord *et al.* [293] we started to implement a similar approach which makes use of a 2D accelerated weight histogram (AWH) method. The advantage of the AWH method in that case is not even the main one, though we know that the method is converging fastly with regard to US procedure. The main interest is that, if the first coordinate used is describing only the translocation process, the second is an alchemical coordinate which was proven to assist a better and more efficient sampling of the configurational space in a very stiff medium. This approach could help to get a better picture of the conformations of the peptides of interest in the vicinity of the lipid A, and hence to run further computations dedicated to understand the effects of those peptides on divalent ions at different depth of insertion in the OM.

Bibliography

[1] M. Savenko, T. Rivel, S. Yesylevskyy, and C. Ramseyer, "Influence of Substrate Hydrophilicity on Structural Properties of Supported Lipid Systems on Graphene, Graphene Oxides, and Silica," *J. Phys. Chem. B*, vol. 125, no. 29, pp. 8060–8074, Jul. 2021, doi: 10.1021/acs.jpcb.1c04615.

[2] A. Vishnyakov, T. Li, and A. V. Neimark, "Adhesion of Phospholipid Bilayers to Hydroxylated Silica: Existence of Nanometer-Thick Water Interlayers," *Langmuir*, vol. 33, no. 45, pp. 13148–13156, Nov. 2017, doi: 10.1021/acs.langmuir.7b03582.

[3] D. Regan, J. Williams, P. Borri, and W. Langbein, "Lipid Bilayer Thickness Measured by Quantitative DIC Reveals Phase Transitions and Effects of Substrate Hydrophilicity," *Langmuir*, vol. 35, no. 43, pp. 13805–13814, Oct. 2019, doi: 10.1021/acs.langmuir.9b02538.

[4] M. Schneemilch and N. Quirke, "Free energy of adhesion of lipid bilayers on titania surfaces," *J. Chem. Phys.*, vol. 151, no. 13, p. 134707, Oct. 2019, doi: 10.1063/1.5120810.

[5] M. Roark and S. E. Feller, "Structure and Dynamics of a Fluid Phase Bilayer on a Solid Support as Observed by a Molecular Dynamics Computer Simulation," *Langmuir*, vol. 24, no. 21, pp. 12469–12473, Nov. 2008, doi: 10.1021/la802079h.

[6] M. J. Abraham *et al.*, "GROMACS: High performance molecular simulations through multi-level parallelism from laptops to supercomputers," *SoftwareX*, vol. 1–2, pp. 19–25, Sep. 2015, doi: 10.1016/j.softx.2015.06.001.

[7] A. Lamberg and T. Taniguchi, "Coarse-Grained Computational Studies of Supported Bilayers: Current Problems and Their Root Causes," *J. Phys. Chem. B*, vol. 118, no. 36, pp. 10643–10652, Sep. 2014, doi: 10.1021/jp5053419.

[8] S. V. Bennun, A. N. Dickey, C. Xing, and R. Faller, "Simulations of biomembranes and water: Important technical aspects," *Fluid Phase Equilibria*, vol. 261, no. 1–2, pp. 18–25, Dec. 2007, doi: 10.1016/j.fluid.2007.07.056.

[9] C. Xing and R. Faller, "Interactions of Lipid Bilayers with Supports: A Coarse-Grained Molecular Simulation Study," *J. Phys. Chem. B*, vol. 112, no. 23, pp. 7086–7094, Jun. 2008, doi: 10.1021/jp077305l.

[10] The PLUMED consortium, "Promoting transparency and reproducibility in enhanced molecular simulations," *Nat. Methods*, vol. 16, no. 8, pp. 670–673, Aug. 2019, doi: 10.1038/s41592-019-0506-8.

[11] H. Nikaido, "Molecular Basis of Bacterial Outer Membrane Permeability Revisited," *Microbiol. Mol. Biol. Rev.*, vol. 67, no. 4, pp. 593–656, Dec. 2003, doi: 10.1128/MMBR.67.4.593-656.2003.

[12] S. Khalid, C. Schroeder, P. J. Bond, and A. L. Duncan, "What have molecular simulations contributed to understanding of Gram-negative bacterial cell envelopes?: This article is part of the Bacterial Cell Envelopes collection.," *Microbiology*, vol. 168, no. 3, Mar. 2022, doi: 10.1099/mic.0.001165.

[13] M. W. Martynowycz *et al.*, "*Salmonella* Membrane Structural Remodeling Increases Resistance to Antimicrobial Peptide LL-37," *ACS Infect. Dis.*, vol. 5, no. 7, pp. 1214–1222, Jul. 2019, doi: 10.1021/acsinfecdis.9b00066.

[14] M. Schindler and M. J. Osborn, "Interaction of divalent cations and polymyxin B with lipopolysaccharide," *Biochemistry*, vol. 18, no. 20, pp. 4425–4430, Oct. 1979, doi: 10.1021/bi00587a024.

[15] N. A. Berglund, T. J. Piggot, D. Jefferies, R. B. Sessions, P. J. Bond, and S. Khalid, "Interaction of the Antimicrobial Peptide Polymyxin B1 with Both Membranes of E. coli: A Molecular Dynamics Study," *PLOS Comput. Biol.*, vol. 11, no. 4, p. e1004180, Apr. 2015, doi: 10.1371/journal.pcbi.1004180.

[16] E. L. Wu *et al.*, "Molecular Dynamics and NMR Spectroscopy Studies of E. coli Lipopolysaccharide Structure and Dynamics," *Biophys. J.*, vol. 105, no. 6, pp. 1444–1455, Sep. 2013, doi: 10.1016/j.bpj.2013.08.002.

[17] T. Velkov, K. D. Roberts, R. L. Nation, P. E. Thompson, and J. Li, "Pharmacology of polymyxins: new insights into an 'old' class of antibiotics," *Future Microbiol.*, vol. 8, no. 6, pp. 711–724, Jun. 2013, doi: 10.2217/FMB.13.39.

[18] A. Rice and J. Wereszczynski, "Atomistic Scale Effects of Lipopolysaccharide Modifications on Bacterial Outer Membrane Defenses," *Biophys. J.*, vol. 114, no. 6, pp. 1389–1399, Mar. 2018, doi: 10.1016/j.bpj.2018.02.006.

[19] L. D. Ginez *et al.*, "Changes in fluidity of the *E. coli* outer membrane in response to temperature, divalent cations and polymyxin-B show two different mechanisms of membrane fluidity adaptation," *FEBS J.*, vol. 289, no. 12, pp. 3550–3567, Jun. 2022, doi: 10.1111/febs.16358.

[20] N. H. Lam, Z. Ma, and B.-Y. Ha, "Electrostatic modification of the lipopolysaccharide layer: competing effects of divalent cations and polycationic or polyanionic molecules," *Soft Matter*, vol. 10, no. 38, pp. 7528–7544, 2014, doi: 10.1039/C4SM01262C.

[21] S. Manioglu *et al.*, "Antibiotic polymyxin arranges lipopolysaccharide into crystalline structures to solidify the bacterial membrane," *Nat. Commun.*, vol. 13, no. 1, p. 6195, Oct. 2022, doi: 10.1038/s41467-022-33838-0.

[22] L. Fu, X. Li, S. Zhang, Y. Dong, W. Fang, and L. Gao, "Polymyxins induce lipid scrambling and disrupt the homeostasis of Gram-negative bacteria membrane," *Biophys. J.*, vol. 121, no. 18, pp. 3486–3498, Sep. 2022, doi: 10.1016/j.bpj.2022.08.007.

[23] X. Jiang *et al.*, "Coarse-grained simulations uncover Gram-negative bacterial defense against polymyxins by the outer membrane," *Comput. Struct. Biotechnol. J.*, vol. 19, pp. 3885–3891, 2021, doi: 10.1016/j.csbj.2021.06.051.

[24] C. González-Fernández, E. Bringas, C. Oostenbrink, and I. Ortiz, "In silico investigation and surmounting of Lipopolysaccharide barrier in Gram-Negative Bacteria: How far has molecular dynamics Come?," *Comput. Struct. Biotechnol. J.*, vol. 20, pp. 5886–5901, 2022, doi: 10.1016/j.csbj.2022.10.039.

[25] P.-C. Hsu *et al.*, "CHARMM-GUI Martini Maker for modeling and simulation of complex bacterial membranes with lipopolysaccharides," *J. Comput. Chem.*, vol. 38, no. 27, pp. 2354–2363, 2017, doi: 10.1002/jcc.24895.

[26] S. J. Singer and G. L. Nicolson, "The Fluid Mosaic Model of the Structure of Cell Membranes: Cell membranes are viewed as two-dimensional solutions of oriented globular proteins and lipids.," *Science*, vol. 175, no. 4023, pp. 720–731, Feb. 1972, doi: 10.1126/science.175.4023.720.

[27] A. Kleinzeller, "William Hewson's studies of red blood corpuscles and the evolving concept of a cell membrane," *Am. J. Physiol.-Cell Physiol.*, vol. 271, no. 1, pp. C1–C8, Jul. 1996, doi: 10.1152/ajpcell.1996.271.1.C1.

[28] W. Stillwell, *An introduction to biological membranes: composition, structure and function*, Second edition. Amsterdam ; Boston: Academic Press is an imprint of Elsevier, 2016.

[29] A. Kleinzeller, "Chapter 1 Charles Ernest Overton's Concept of a Cell Membrane," in *Current Topics in Membranes*, vol. 48, Elsevier, 1999, pp. 1–22. doi: 10.1016/S0070-2161(08)61039-4.

[30] E. Gorter and F. Grendel, "ON BIMOLECULAR LAYERS OF LIPOIDS ON THE CHROMOCYTES OF THE BLOOD," *J. Exp. Med.*, vol. 41, no. 4, pp. 439–443, Apr. 1925, doi: 10.1084/jem.41.4.439.

[31] J. Lombard, "Once upon a time the cell membranes: 175 years of cell boundary research," *Biol. Direct*, vol. 9, no. 1, p. 32, Dec. 2014, doi: 10.1186/s13062-014-0032-7.

[32] M. J. Karnovsky, A. M. Kleinfeld, R. L. Hoover, and R. D. Klausner, "The concept of lipid domains in membranes.," *J. Cell Biol.*, vol. 94, no. 1, pp. 1–6, Jul. 1982, doi: 10.1083/jcb.94.1.1.

[33] K. Simons and E. Ikonen, "Functional rafts in cell membranes," *Nature*, vol. 387, no. 6633, pp. 569–572, Jun. 1997, doi: 10.1038/42408.

[34] I. Levental, K. R. Levental, and F. A. Heberle, "Lipid Rafts: Controversies Resolved, Mysteries Remain," *Trends Cell Biol.*, vol. 30, no. 5, pp. 341–353, May 2020, doi: 10.1016/j.tcb.2020.01.009.

[35] E. Fahy *et al.*, "A comprehensive classification system for lipids," *J. Lipid Res.*, vol. 46, no. 5, pp. 839–861, May 2005, doi: 10.1194/jlr.E400004-JLR200.

[36] B. Alberts, Ed., *Molecular biology of the cell*, 4th ed. New York: Garland Science, 2002.

[37] H. Fernández-Morán, T. Oda, P. V. Blair, and D. E. Green, "A MACROMOLECULAR REPEATING UNIT OF MITOCHONDRIAL STRUCTURE AND FUNCTION," *J. Cell Biol.*, vol. 22, no. 1, pp. 63–100, Jul. 1964, doi: 10.1083/jcb.22.1.63.

[38] I. Virtanen, V. P. Lehto, and P. Aula, "LECTINS AS PROBES FOR MEMBRANE ASYMMETRY AND COMPARTMENTALIZATION OF SACCHARIDE MOIETIES IN CELLS," in *Proceedings of the Third Lectin Meeting: Copenhagen, June 1980*, T. C. Bøg-Hansen, Ed., De Gruyter, 1981, pp. 215–220. doi: 10.1515/9783111618845-026.

[39] L. McEvoy, P. Williamson, and R. A. Schlegel, "Membrane phospholipid asymmetry as a determinant of erythrocyte recognition by macrophages.," *Proc. Natl. Acad. Sci.*, vol. 83, no. 10, pp. 3311–3315, May 1986, doi: 10.1073/pnas.83.10.3311.

[40] V. A. Fadok, D. L. Bratton, S. C. Frasch, M. L. Warner, and P. M. Henson, "The role of phosphatidylserine in recognition of apoptotic cells by phagocytes," *Cell Death Differ.*, vol. 5, no. 7, pp. 551–562, Jul. 1998, doi: 10.1038/sj.cdd.4400404.

[41] L. D. Frye and M. Edidin, "The rapid intermixing of cell surface antigens after formation of mouse human heterokaryons," *J. Cell Sci.*, vol. 7, no. 2, pp. 319–335, Sep. 1970, doi: 10.1242/jcs.7.2.319.

[42] T. Söllner *et al.*, "SNAP receptors implicated in vesicle targeting and fusion," *Nature*, vol. 362, no. 6418, pp. 318–324, Mar. 1993, doi: 10.1038/362318a0.

[43] M. S. Bretscher, "Asymmetrical Lipid Bilayer Structure for Biological Membranes," *Nature. New Biol.*, vol. 236, no. 61, pp. 11–12, Mar. 1972, doi: 10.1038/newbio236011a0.

[44] T. J. Silhavy, D. Kahne, and S. Walker, "The Bacterial Cell Envelope," *Cold Spring Harb. Perspect. Biol.*, vol. 2, no. 5, p. a000414, May 2010, doi: 10.1101/cshperspect.a000414.

[45] C. Kleanthous and J. P. Armitage, "The bacterial cell envelope," *Philos. Trans. R. Soc. B Biol. Sci.*, vol. 370, no. 1679, p. 20150019, Oct. 2015, doi: 10.1098/rstb.2015.0019.

[46] J. W. Bartholomew and T. Mittwer, "THE GRAM STAIN," *Bacteriol. Rev.*, vol. 16, no. 1, pp. 1–29, Mar. 1952.

[47] "Gram Stain Protocols," ASM.org. Accessed: Dec. 14, 2021. [Online]. Available: https://asm.org/Protocols/Gram-Stain-Protocols

[48] H. Strahl and J. Errington, "Bacterial Membranes: Structure, Domains, and Function," *Annu. Rev. Microbiol.*, vol. 71, no. 1, pp. 519–538, Sep. 2017, doi: 10.1146/annurev-micro-102215-095630.

[49] Y. Sakayori, M. Muramatsu, S. Hanada, Y. Kamagata, S. Kawamoto, and J. Shima, "Characterization of Enterococcus faecium mutants resistant to mundticin KS, a class IIa bacteriocin," *Microbiology*, vol. 149, no. 10, pp. 2901–2908, 2003, doi: 10.1099/mic.0.26435-0.

[50] M. Hayami, A. Okabe, R. Kariyama, M. Abe, and Y. Kanemasa, "Lipid Composition of Staphylococcus aureus and Its Derived L-forms," *Microbiol. Immunol.*, vol. 23, no. 6, pp. 435–442, 1979, doi: 10.1111/j.1348-0421.1979.tb00483.x.

[51] K. Yasuhiro, Y. Tieko, and H. Hideo, "Alteration of the phospholipid composition of Staphylo-coccus aureus cultured in medium containing NaCl," *Biochim. Biophys. Acta BBA - Lipids Lipid Metab.*, vol. 280, no. 3, pp. 444–450, Nov. 1972, doi: 10.1016/0005-2760(72)90251-2.

[52] S. A. Young, A. P. Desbois, P. J. Coote, and T. K. Smith, "Characterisation of Staphylococcus aureus lipids by nanoelectrospray ionisation tandem mass spectrometry (nESI-MS/MS)," *bioRxiv*, p. 593483, Mar. 2019, doi: 10.1101/593483.

[53] R. M. Epand and R. F. Epand, "Bacterial membrane lipids in the action of antimicrobial agents," *J. Pept. Sci.*, vol. 17, no. 5, pp. 298–305, May 2011, doi: 10.1002/psc.1319.

[54] S. Lu *et al.*, "Cell Morphology Variations of Klebsiella pneumoniae Induced by Acetate Stress Using Biomimetic Vesicle Assay," *Appl. Biochem. Biotechnol.*, vol. 171, no. 3, pp. 731–743, Oct. 2013, doi: 10.1007/s12010-013-0368-y.

[55] Y. Luo, M. A. Javed, H. Deneer, and X. Chen, “Nutrient depletion-induced production of tri-acylated glycerophospholipids in Acinetobacter radioresistens,” *Sci. Rep.*, vol. 8, no. 1, pp. 1–11, May 2018, doi: 10.1038/s41598-018-25869-9.

[56] P. Lopalco, J. Stahl, C. Annese, B. Averhoff, and A. Corcelli, “Identification of unique cardiolipin and monolysocardiolipin species in Acinetobacter baumannii,” *Sci. Rep.*, vol. 7, no. 1, pp. 1–12, Jun. 2017, doi: 10.1038/s41598-017-03214-w.

[57] I. C. Hancock and P. M. Meadow, “The extractable lipids of Pseudomonas aeruginosa,” *Biochim. Biophys. Acta BBA - Lipids Lipid Metab.*, vol. 187, no. 3, pp. 366–379, Oct. 1969, doi: 10.1016/0005-2760(69)90010-1.

[58] Y. Uratani and A. Aiyama, “Effect of Phospholipid-Composition on Activity of Sodium-Dependent Leucine Transport-System in Pseudomonas-Aeruginosa,” *J. Biol. Chem.*, vol. 261, no. 12, pp. 5450–5454, Apr. 1986.

[59] S. T. Albelo and C. E. Domenech, “Carbons from choline present in the phospholipids of Pseudomonas aeruginosa,” *FEMS Microbiol. Lett.*, vol. 156, no. 2, pp. 271–274, Nov. 1997, doi: 10.1111/j.1574-6968.1997.tb12739.x.

[60] “Characterization of Membrane Lipidome Changes in Pseudomonas aeruginosa during Biofilm Growth on Glass Wool,” *PLOS ONE*, vol. 9, no. 9, p. e108478, Sep. 2014, doi: 10.1371/journal.pone.0108478.

[61] J. W. Costerton, J. M. Ingram, and K. J. Cheng, “Structure and function of the cell envelope of gram-negative bacteria,” *Bacteriol. Rev.*, vol. 38, no. 1, pp. 87–110, Mar. 1974.

[62] J. A. Robinson, “Folded Synthetic Peptides and Other Molecules Targeting Outer Membrane Protein Complexes in Gram-Negative Bacteria,” *Front. Chem.*, vol. 7, 2019, doi: 10.3389/fchem.2019.00045.

[63] H. Dong *et al.*, “Structural insights into cardiolipin transfer from the Inner membrane to the outer membrane by PbgA in Gram-negative bacteria,” *Sci. Rep.*, vol. 6, no. 1, pp. 1–10, Aug. 2016, doi: 10.1038/srep30815.

[64] M. Bogdanov *et al.*, “Phospholipid distribution in the cytoplasmic membrane of Gram-negative bacteria is highly asymmetric, dynamic, and cell shape-dependent,” *Sci. Adv.*, Jun. 2020, doi: 10.1126/sciadv.aaz6333.

[65] C. De Duve and R. Wattiaux, “Functions of lysosomes,” *Annu. Rev. Physiol.*, vol. 28, pp. 435–492, 1966, doi: 10.1146/annurev.ph.28.030166.002251.

[66] S. I. Miller and N. R. Salama, “The gram-negative bacterial periplasm: Size matters,” *PLOS Biol.*, vol. 16, no. 1, p. e2004935, Jan. 2018, doi: 10.1371/journal.pbio.2004935.

[67] C. Erridge, E. Bennett-Guerrero, and I. R. Poxton, “Structure and function of lipopolysaccharides,” *Microbes Infect.*, vol. 4, no. 8, pp. 837–851, Jul. 2002, doi: 10.1016/S1286-4579(02)01604-0.

[68] A. Steimle, I. B. Autenrieth, and J.-S. Frick, “Structure and function: Lipid A modifications in commensals and pathogens,” *Int. J. Med. Microbiol.*, vol. 306, no. 5, pp. 290–301, Aug. 2016, doi: 10.1016/j.ijmm.2016.03.001.

[69] P. S. Tobias, K. Soldau, and R. J. Ulevitch, “Identification of a lipid A binding site in the acute phase reactant lipopolysaccharide binding protein,” *J. Biol. Chem.*, vol. 264, no. 18, pp. 10867–10871, Jun. 1989.

[70] M. Caroff and A. Novikov, “LPS Structure, Function, and Heterogeneity,” in *Endotoxin Detection and Control in Pharma, Limulus, and Mammalian Systems*, K. L. Williams, Ed., Cham: Springer International Publishing, 2019, pp. 53–93. doi: 10.1007/978-3-030-17148-3_3.

[71] E. Th. Rietschel *et al.*, “The chemical structure of bacterial endotoxin in relation to bioactivity,” *Immunobiology*, vol. 187, no. 3, pp. 169–190, Apr. 1993, doi: 10.1016/S0171-2985(11)80338-4.

[72] I. Lerouge and J. Vanderleyden, “O-antigen structural variation: mechanisms and possible roles in animal/plant–microbe interactions,” *FEMS Microbiol. Rev.*, vol. 26, no. 1, pp. 17–47, Mar. 2002, doi: 10.1111/j.1574-6976.2002.tb00597.x.

[73] K. O’Riordan and J. C. Lee, “Staphylococcus aureus capsular polysaccharides,” *Clin. Microbiol. Rev.*, vol. 17, no. 1, pp. 218–234, Jan. 2004, doi: 10.1128/CMR.17.1.218-234.2004.

[74] K. M. Cunnion, H.-M. Zhang, and M. M. Frank, "Availability of complement bound to Staphylococcus aureus to interact with membrane complement receptors influences efficiency of phagocytosis," *Infect. Immun.*, vol. 71, no. 2, pp. 656–662, Feb. 2003, doi: 10.1128/IAI.71.2.656-662.2003.

[75] E. D. Shapiro *et al.*, "The protective efficacy of polyvalent pneumococcal polysaccharide vaccine," *N. Engl. J. Med.*, vol. 325, no. 21, pp. 1453–1460, Nov. 1991, doi: 10.1056/NEJM199111213252101.

[76] E. J. Hayhurst, L. Kailas, J. K. Hobbs, and S. J. Foster, "Cell wall peptidoglycan architecture in Bacillus subtilis," *Proc. Natl. Acad. Sci. U. S. A.*, vol. 105, no. 38, pp. 14603–14608, Sep. 2008, doi: 10.1073/pnas.0804138105.

[77] K. M. Davis and J. N. Weiser, "Modifications to the Peptidoglycan Backbone Help Bacteria To Establish Infection," *Infect. Immun.*, vol. 79, no. 2, pp. 562–570, Feb. 2011, doi: 10.1128/IAI.00651-10.

[78] N. Malanovic and K. Lohner, "Gram-positive bacterial cell envelopes: The impact on the activity of antimicrobial peptides," *Biochim. Biophys. Acta BBA - Biomembr.*, vol. 1858, no. 5, pp. 936–946, May 2016, doi: 10.1016/j.bbamem.2015.11.004.

[79] M. Rajagopal and S. Walker, "Envelope Structures of Gram-Positive Bacteria," *Curr. Top. Microbiol. Immunol.*, vol. 404, pp. 1–44, 2017, doi: 10.1007/82_2015_5021.

[80] H. Nishi, H. Komatsuzawa, T. Fujiwara, N. McCallum, and M. Sugai, "Reduced Content of Lysyl-Phosphatidylglycerol in the Cytoplasmic Membrane Affects Susceptibility to Moenomycin, as Well as Vancomycin, Gentamicin, and Antimicrobial Peptides, in Staphylococcus aureus," *Antimicrob. Agents Chemother.*, vol. 48, no. 12, pp. 4800–4807, Dec. 2004, doi: 10.1128/AAC.48.12.4800-4807.2004.

[81] A. Mashaghi, M. Swann, J. Popplewell, M. Textor, and E. Reimhult, "Optical Anisotropy of Supported Lipid Structures Probed by Waveguide Spectroscopy and Its Application to Study of Supported Lipid Bilayer Formation Kinetics," *Anal. Chem.*, vol. 80, no. 10, pp. 3666–3676, May 2008, doi: 10.1021/ac800027s.

[82] K. Furukawa and H. Hibino, "Self-spreading of Supported Lipid Bilayer on SiO_2 Surface Bearing Graphene Oxide," *Chem. Lett.*, vol. 41, no. 10, pp. 1259–1261, Oct. 2012, doi: 10.1246/cl.2012.1259.

[83] E. T. Castellana and P. S. Cremer, "Solid supported lipid bilayers: From biophysical studies to sensor design," *Surf. Sci. Rep.*, vol. 61, no. 10, pp. 429–444, Nov. 2006, doi: 10.1016/j.surfrep.2006.06.001.

[84] J. Salafsky, J. T. Groves, and S. G. Boxer, "Architecture and Function of Membrane Proteins in Planar Supported Bilayers: A Study with Photosynthetic Reaction Centers," *Biochemistry*, vol. 35, no. 47, pp. 14773–14781, Jan. 1996, doi: 10.1021/bi961432i.

[85] K. D. Mossman, G. Campi, J. T. Groves, and M. L. Dustin, "Altered TCR Signaling from Geometrically Repatterned Immunological Synapses," *Science*, vol. 310, no. 5751, pp. 1191–1193, Nov. 2005, doi: 10.1126/science.1119238.

[86] R. Merkel, E. Sackmann, and E. Evans, "Molecular friction and epitactic coupling between monolayers in supported bilayers," *J. Phys.*, vol. 50, no. 12, pp. 1535–1555, 1989, doi: 10.1051/jphys:0198900500120153500.

[87] C. R. Safinya and J. O. Rädler, Eds., *Handbook of lipid membranes: molecular, functional, and materials aspects*, First edition. Boca Raton, FL: CRC Press, 2021.

[88] J. Kurniawan, J. F. Ventrici de Souza, A. T. Dang, G. Liu, and T. L. Kuhl, "Preparation and Characterization of Solid-Supported Lipid Bilayers Formed by Langmuir–Blodgett Deposition: A Tutorial," *Langmuir*, vol. 34, no. 51, pp. 15622–15639, Dec. 2018, doi: 10.1021/acs.langmuir.8b03504.

[89] R. N. Orth, M. Wu, D. A. Holowka, H. G. Craighead, and B. A. Baird, "Mast Cell Activation on Patterned Lipid Bilayers of Subcellular Dimensions," *Langmuir*, vol. 19, no. 5, pp. 1599–1605, Mar. 2003, doi: 10.1021/la026314c.

[90] A. O. Hohner, M. P. C. David, and J. O. Rädler, "Controlled solvent-exchange deposition of phospholipid membranes onto solid surfaces," *Biointerphases*, vol. 5, no. 1, pp. 1–8, Mar. 2010, doi: 10.1116/1.3319326.

[91] O. N. Oliveira, L. Caseli, and K. Ariga, "The Past and the Future of Langmuir and Langmuir–Blodgett Films," *Chem. Rev.*, vol. 122, no. 6, pp. 6459–6513, Mar. 2022, doi: 10.1021/acs.chemrev.1c00754.

[92] C. G. Cranfield, A. P. Le Brun, A. Garcia, B. A. Cornell, and S. A. Holt, "Langmuir-Schaefer Deposition to Create an Asymmetrical Lipopolysaccharide Sparsely Tethered Lipid Bilayer," in *Membrane Lipids*, vol. 2402, C. G. Cranfield, Ed., in Methods in Molecular Biology, vol. 2402. , New York, NY: Springer US, 2022, pp. 21–30. doi: 10.1007/978-1-0716-1843-1_3.

[93] L. A. Clifton *et al.*, "Asymmetric phospholipid: lipopolysaccharide bilayers; a Gram-negative bacterial outer membrane mimic," *J. R. Soc. Interface*, vol. 10, no. 89, p. 20130810, Dec. 2013, doi: 10.1098/rsif.2013.0810.

[94] T. Penkauskas and G. Preta, "Biological applications of tethered bilayer lipid membranes," *Biochimie*, vol. 157, pp. 131–141, Feb. 2019, doi: 10.1016/j.biochi.2018.11.011.

[95] J. Andersson, J. J. Knobloch, M. V. Perkins, S. A. Holt, and I. Köper, "Synthesis and Characterization of Novel Anchorlipids for Tethered Bilayer Lipid Membranes," *Langmuir*, vol. 33, no. 18, pp. 4444–4451, May 2017, doi: 10.1021/acs.langmuir.7b00778.

[96] J. A. Goodchild, D. L. Walsh, and S. D. Connell, "Nanoscale Substrate Roughness Hinders Domain Formation in Supported Lipid Bilayers," *Langmuir*, vol. 35, no. 47, pp. 15352–15363, Nov. 2019, doi: 10.1021/acs.langmuir.9b01990.

[97] I. Czolkos, A. Jesorka, and O. Orwar, "Molecular phospholipid films on solid supports," *Soft Matter*, vol. 7, no. 10, pp. 4562–4576, May 2011, doi: 10.1039/C0SM01212B.

[98] R. Tero, T. Ujihara, H. Watanabe, and T. Urisu, "Supported planar lipid bilayers on TiO2 and SiO2 surfaces: Effects of surface atomic structures and chemical species," *Abstr. Pap. Am. Chem. Soc.*, vol. 233, Mar. 2007.

[99] R. Tero, H. Watanabe, and T. Urisu, "Supported phospholipid bilayer formation on hydrophilicity-controlled silicon dioxide surfaces," *Phys. Chem. Chem. Phys.*, vol. 8, no. 33, pp. 3885–3894, Aug. 2006, doi: 10.1039/B606052H.

[100] I. Reviakine and A. Brisson, "Formation of Supported Phospholipid Bilayers from Unilamellar Vesicles Investigated by Atomic Force Microscopy," *Langmuir*, vol. 16, no. 4, pp. 1806–1815, Feb. 2000, doi: 10.1021/la9903043.

[101] R. Frost, G. E. Jönsson, D. Chakarov, S. Svedhem, and B. Kasemo, "Graphene Oxide and Lipid Membranes: Interactions and Nanocomposite Structures," *Nano Lett.*, vol. 12, no. 7, pp. 3356–3362, Jul. 2012, doi: 10.1021/nl203107k.

[102] N. Willems *et al.*, "Biomimetic Phospholipid Membrane Organization on Graphene and Graphene Oxide Surfaces: A Molecular Dynamics Simulation Study," *Acs Nano*, vol. 11, no. 2, pp. 1613–1625, Feb. 2017, doi: 10.1021/acsnano.6b07352.

[103] N.-J. Cho, C. W. Frank, B. Kasemo, and F. Höök, "Quartz crystal microbalance with dissipation monitoring of supported lipid bilayers on various substrates," *Nat. Protoc.*, vol. 5, no. 6, pp. 1096–1106, Jun. 2010, doi: 10.1038/nprot.2010.65.

[104] T. Rivel, S. O. Yesylevskyy, and C. Ramseyer, "Structures of single, double and triple layers of lipids adsorbed on graphene: Insights from all-atom molecular dynamics simulations," *Carbon*, vol. 118, pp. 358–369, Jul. 2017, doi: 10.1016/j.carbon.2017.03.072.

[105] P. K. Ang *et al.*, "A bioelectronic platform using a graphene-lipid bilayer interface," *ACS Nano*, vol. 4, no. 12, pp. 7387–7394, Dec. 2010, doi: 10.1021/nn1022582.

[106] K. Krishnamoorthy, M. Veerapandian, L.-H. Zhang, K. Yun, and S. J. Kim, "Antibacterial Efficiency of Graphene Nanosheets against Pathogenic Bacteria via Lipid Peroxidation," *J. Phys. Chem. C*, vol. 116, no. 32, pp. 17280–17287, Aug. 2012, doi: 10.1021/jp3047054.

[107] S. R. Tabaei, W. B. Ng, S.-J. Cho, and N.-J. Cho, "Controlling the Formation of Phospholipid Monolayer, Bilayer, and Intact Vesicle Layer on Graphene," *ACS Appl. Mater. Interfaces*, vol. 8, no. 18, pp. 11875–11880, May 2016, doi: 10.1021/acsami.6b02837.

[108] S. J. Wilk *et al.*, "Teflon™-coated silicon apertures for supported lipid bilayer membranes," *Appl. Phys. Lett.*, vol. 85, no. 15, pp. 3307–3309, Oct. 2004, doi: 10.1063/1.1805712.

[109] M. Hirtz, A. Oikonomou, T. Georgiou, H. Fuchs, and A. Vijayaraghavan, "Multiplexed biomimetic lipid membranes on graphene by dip-pen nanolithography," *Nat. Commun.*, vol. 4, no. 1, p. 2591, Oct. 2013, doi: 10.1038/ncomms3591.

[110] E. Kalb, S. Frey, and L. K. Tamm, "Formation of supported planar bilayers by fusion of vesicles to supported phospholipid monolayers," *Biochim. Biophys. Acta BBA - Biomembr.*, vol. 1103, no. 2, pp. 307–316, Jan. 1992, doi: 10.1016/0005-2736(92)90101-Q.

[111] T. Phung, Y. Zhang, J. Dunlop, and J. Dalziel, "Bilayer lipid membranes supported on Teflon filters: A functional environment for ion channels," *Biosens. Bioelectron.*, vol. 26, no. 7, pp. 3127–3135, Mar. 2011, doi: 10.1016/j.bios.2010.12.013.

[112] J. Daillant *et al.*, "Structure and fluctuations of a single floating lipid bilayer," *Proc. Natl. Acad. Sci.*, vol. 102, no. 33, pp. 11639–11644, Aug. 2005, doi: 10.1073/pnas.0504588102.

[113] T. Charitat, S. Lecuyer, and G. Fragneto, "Fluctuations and destabilization of single phospholipid bilayers," *Biointerphases*, vol. 3, no. 2, pp. FB3–FB15, Jun. 2008, doi: 10.1116/1.2936938.

[114] S. Rebaud, O. Maniti, and A. P. Girard-Egrot, "Tethered bilayer lipid membranes (tBLMs): Interest and applications for biological membrane investigations," *Biochimie*, vol. 107, pp. 135–142, Dec. 2014, doi: 10.1016/j.biochi.2014.06.021.

[115] R. Tero, "Substrate Effects on the Formation Process, Structure and Physicochemical Properties of Supported Lipid Bilayers," *Materials*, vol. 5, no. 12, pp. 2658–2680, Dec. 2012, doi: 10.3390/ma5122658.

[116] T. J. Zwang, W. R. Fletcher, T. J. Lane, and Malkiat. S. Johal, "Quantification of the Layer of Hydration of a Supported Lipid Bilayer," *Langmuir*, vol. 26, no. 7, pp. 4598–4601, Apr. 2010, doi: 10.1021/la100275v.

[117] F. Benedetti, L. Fu, F. Thalmann, T. Charitat, A. Rubin, and C. Loison, "Coarse-Grain Simulations of Solid Supported Lipid Bilayers with Varying Hydration Levels," *J. Phys. Chem. B*, vol. 124, no. 38, pp. 8287–8298, Sep. 2020, doi: 10.1021/acs.jpcb.0c03913.

[118] T. N. Sut, J. A. Jackman, and N.-J. Cho, "Understanding How Membrane Surface Charge Influences Lipid Bicelle Adsorption onto Oxide Surfaces," *Langmuir*, p. acs.langmuir.9b00570, Jun. 2019, doi: 10.1021/acs.langmuir.9b00570.

[119] R. Lipowsky, "The conformation of membranes," *Nature*, vol. 349, no. 6309, pp. 475–481, Feb. 1991, doi: 10.1038/349475a0.

[120] T. M. Bayerl and M. Bloom, "Physical properties of single phospholipid bilayers adsorbed to micro glass beads. A new vesicular model system studied by 2H-nuclear magnetic resonance," *Biophys. J.*, vol. 58, no. 2, pp. 357–362, Aug. 1990, doi: 10.1016/S0006-3495(90)82382-1.

[121] S. J. Johnson *et al.*, "Structure of an adsorbed dimyristoylphosphatidylcholine bilayer measured with specular reflection of neutrons," *Biophys. J.*, vol. 59, no. 2, pp. 289–294, Feb. 1991, doi: 10.1016/S0006-3495(91)82222-6.

[122] B. W. Koenig *et al.*, "Neutron Reflectivity and Atomic Force Microscopy Studies of a Lipid Bilayer in Water Adsorbed to the Surface of a Silicon Single Crystal," *Langmuir*, vol. 12, no. 5, pp. 1343–1350, Jan. 1996, doi: 10.1021/la950580r.

[123] T. Charitat, E. Bellet-Amalric, G. Fragneto, and F. Graner, "Adsorbed and free lipid bilayers at the solid-liquid interface," *Eur. Phys. J. B*, vol. 8, no. 4, pp. 583–593, Apr. 1999, doi: 10.1007/s100510050725.

[124] P. Fromherz, V. Kiessling, K. Kottig, and G. Zeck, "Membrane transistor with giant lipid vesicle touching a silicon chip," *Appl. Phys. Mater. Sci. Process.*, vol. 69, no. 5, pp. 571–576, Nov. 1999, doi: 10.1007/s003390051476.

[125] G. Fragneto, F. Graner, T. Charitat, P. Dubos, and E. Bellet-Amalric, "Interaction of the Third Helix of Antennapedia Homeodomain with a Deposited Phospholipid Bilayer: A Neutron Reflectivity Structural Study," *Langmuir*, vol. 16, no. 10, pp. 4581–4588, May 2000, doi: 10.1021/la991119s.

[126] V. Kiessling and L. K. Tamm, “Measuring Distances in Supported Bilayers by Fluorescence Interference-Contrast Microscopy: Polymer Supports and SNARE Proteins,” *Biophys. J.*, vol. 84, no. 1, pp. 408–418, Jan. 2003, doi: 10.1016/S0006-3495(03)74861-9.

[127] T. Gutberlet, R. Steitz, G. Fragneto, and B. Klösgen, “Phospholipid bilayer formation at a bare Si surface: a time-resolved neutron reflectivity study,” *J. Phys. Condens. Matter*, vol. 16, no. 26, pp. S2469–S2476, Jul. 2004, doi: 10.1088/0953-8984/16/26/020.

[128] C. M. Ajo-Franklin, C. Yoshina-Ishii, and S. G. Boxer, “Probing the Structure of Supported Membranes and Tethered Oligonucleotides by Fluorescence Interference Contrast Microscopy,” *Langmuir*, vol. 21, no. 11, pp. 4976–4983, May 2005, doi: 10.1021/la0468388.

[129] J. M. Crane, V. Kiessling, and L. K. Tamm, “Measuring Lipid Asymmetry in Planar Supported Bilayers by Fluorescence Interference Contrast Microscopy,” *Langmuir*, vol. 21, no. 4, pp. 1377–1388, Feb. 2005, doi: 10.1021/la047654w.

[130] D. A. Doshi *et al.*, “Neutron Reflectivity Study of Lipid Membranes Assembled on Ordered Nanocomposite and Nanoporous Silica Thin Films,” *Langmuir*, vol. 21, no. 7, pp. 2865–2870, Mar. 2005, doi: 10.1021/la0471240.

[131] C. E. Miller, J. Majewski, T. Gog, and T. L. Kuhl, “Characterization of Biological Thin Films at the Solid-Liquid Interface by X-Ray Reflectivity,” *Phys. Rev. Lett.*, vol. 94, no. 23, p. 238104, Jun. 2005, doi: 10.1103/PhysRevLett.94.238104.

[132] B. Stidder, G. Fragneto, and S. J. Roser, “Structure and stability of DPPE planar bilayers,” *Soft Matter*, vol. 3, no. 2, pp. 214–222, 2007, doi: 10.1039/B612538G.

[133] E. B. Watkins, C. E. Miller, D. J. Mulder, T. L. Kuhl, and J. Majewski, “Structure and Orientational Texture of Self-Organizing Lipid Bilayers,” *Phys. Rev. Lett.*, vol. 102, no. 23, p. 238101, Jun. 2009, doi: 10.1103/PhysRevLett.102.238101.

[134] T. K. Lind, M. Cárdenas, and H. P. Wacklin, “Formation of Supported Lipid Bilayers by Vesicle Fusion: Effect of Deposition Temperature,” *Langmuir*, vol. 30, no. 25, pp. 7259–7263, Jul. 2014, doi: 10.1021/la500897x.

[135] N. Duro, M. Gjika, A. Siddiqui, H. L. Scott, and S. Varma, “POPC Bilayers Supported on Nanoporous Substrates: Specific Effects of Silica-Type Surface Hydroxylation and Charge Density,” *Langmuir*, vol. 32, no. 26, pp. 6766–6774, Jul. 2016, doi: 10.1021/acs.langmuir.6b01155.

[136] J. Jackman, W. Knoll, and N.-J. Cho, “Biotechnology Applications of Tethered Lipid Bilayer Membranes,” *Materials*, vol. 5, no. 12, pp. 2637–2657, Dec. 2012, doi: 10.3390/ma5122637.

[137] S. Shenoy, R. Moldovan, S. Rauhala, D. Vanderah, and M. Loesche, “Lipid Diffusion in Tethered Bilayer Lipid Membranes (tBLMs),” *Biophys. J.*, vol. 98, no. 3, p. 667a, Jan. 2010, doi: 10.1016/j.bpj.2009.12.4269.

[138] S. Park *et al.*, “Probing the influence of tether density on tethered bilayer lipid membrane (tBLM)-peptide interactions,” *Appl. Mater. Today*, vol. 18, p. 100527, Mar. 2020, doi: 10.1016/j.apmt.2019.100527.

[139] A. Hosseini, C. J. Barile, A. Devadoss, T. A. Eberspacher, R. A. Decreau, and J. P. Collman, “Hybrid Bilayer Membrane: A Platform To Study the Role of Proton Flux on the Efficiency of Oxygen Reduction by a Molecular Electrocatalyst,” *J. Am. Chem. Soc.*, vol. 133, no. 29, pp. 11100–11102, Jul. 2011, doi: 10.1021/ja204418j.

[140] L. A. Clifton *et al.*, “An Accurate In Vitro Model of the E. coli Envelope,” *Angew. Chem. Int. Ed.*, vol. 54, no. 41, pp. 11952–11955, 2015, doi: 10.1002/anie.201504287.

[141] M. I. Hoopes, M. Deserno, M. L. Longo, and R. Faller, “Coarse-grained modeling of interactions of lipid bilayers with supports,” *J. Chem. Phys.*, vol. 129, no. 17, p. 175102, Nov. 2008, doi: 10.1063/1.3008060.

[142] S. Wang and R. G. Larson, “Coarse-grained molecular dynamics simulation of tethered lipid assemblies,” *Soft Matter*, vol. 9, no. 2, pp. 480–486, 2013, doi: 10.1039/C2SM26850G.

[143] M. K. Bhattacharjee, *Chemistry of antibiotics and related drugs*, 2nd ed. Cham: Springer, 2022.

[144] A. O'Rourke *et al.*, "Mechanism-of-Action Classification of Antibiotics by Global Transcriptome Profiling," *Antimicrob. Agents Chemother.*, vol. 64, no. 3, pp. e01207-19, Feb. 2020, doi: 10.1128/AAC.01207-19.

[145] A. O. Olaitan, S. Morand, and J.-M. Rolain, "Mechanisms of polymyxin resistance: acquired and intrinsic resistance in bacteria," *Front. Microbiol.*, vol. 5, p. 643, Nov. 2014, doi: 10.3389/fmicb.2014.00643.

[146] P. Sass, Ed., *Antibiotics: methods and protocols*, Second edition. New York, NY: Humana Pres, 2023.

[147] "2021 AWaRe classification." Accessed: Jun. 08, 2023. [Online]. Available: https://www.who.int/publications-detail-redirect/2021-aware-classification

[148] S. Kanchugal P and M. Selmer, "Structural Recognition of Spectinomycin by Resistance Enzyme ANT(9) from Enterococcus faecalis," *Antimicrob. Agents Chemother.*, vol. 64, no. 6, pp. e00371-20, May 2020, doi: 10.1128/AAC.00371-20.

[149] S. Ramón-García, C. Martín, E. De Rossi, and J. A. Aínsa, "Contribution of the Rv2333c efflux pump (the Stp protein) from Mycobacterium tuberculosis to intrinsic antibiotic resistance in Mycobacterium bovis BCG," *J. Antimicrob. Chemother.*, vol. 59, no. 3, pp. 544–547, Mar. 2007, doi: 10.1093/jac/dkl510.

[150] P. Anderson, "Sensitivity and Resistance to Spectinomycin in *Escherichia coli*," *J. Bacteriol.*, vol. 100, no. 2, pp. 939–947, Nov. 1969, doi: 10.1128/jb.100.2.939-947.1969.

[151] G. Funatsu, K. Nierhaus, and B. Wittmann-Liebold, "Ribosomal proteins," *J. Mol. Biol.*, vol. 64, no. 1, pp. 201–209, Feb. 1972, doi: 10.1016/0022-2836(72)90329-4.

[152] J. Davies and G. D. Wright, "Bacterial resistance to aminoglycoside antibiotics," *Trends Microbiol.*, vol. 5, no. 6, pp. 234–240, Jun. 1997, doi: 10.1016/S0966-842X(97)01033-0.

[153] K. J. Shaw, P. N. Rather, R. S. Hare, and G. H. Miller, "Molecular genetics of aminoglycoside resistance genes and familial relationships of the aminoglycoside-modifying enzymes," *Microbiol. Rev.*, vol. 57, no. 1, pp. 138–163, Mar. 1993, doi: 10.1128/mr.57.1.138-163.1993.

[154] K. M. Krause, A. W. Serio, T. R. Kane, and L. E. Connolly, "Aminoglycosides: An Overview," *Cold Spring Harb. Perspect. Med.*, vol. 6, no. 6, p. a027029, Jun. 2016, doi: 10.1101/cshperspect.a027029.

[155] J. Wachino and Y. Arakawa, "Exogenously acquired 16S rRNA methyltransferases found in aminoglycoside-resistant pathogenic Gram-negative bacteria: An update," *Drug Resist. Updat.*, vol. 15, no. 3, pp. 133–148, Jun. 2012, doi: 10.1016/j.drup.2012.05.001.

[156] M. Fernández, S. Conde, J. De La Torre, C. Molina-Santiago, J.-L. Ramos, and E. Duque, "Mechanisms of Resistance to Chloramphenicol in Pseudomonas putida KT2440," *Antimicrob. Agents Chemother.*, vol. 56, no. 2, pp. 1001–1009, Feb. 2012, doi: 10.1128/AAC.05398-11.

[157] S. Schwarz, C. Kehrenberg, B. Doublet, and A. Cloeckaert, "Molecular basis of bacterial resistance to chloramphenicol and florfenicol," *FEMS Microbiol. Rev.*, vol. 28, no. 5, pp. 519–542, Nov. 2004, doi: 10.1016/j.femsre.2004.04.001.

[158] K. Bush and P. A. Bradford, "β-Lactams and β-Lactamase Inhibitors: An Overview," *Cold Spring Harb. Perspect. Med.*, vol. 6, no. 8, p. a025247, Aug. 2016, doi: 10.1101/cshperspect.a025247.

[159] J. F. Fisher and S. Mobashery, "β-Lactam Resistance Mechanisms: Gram-Positive Bacteria and *Mycobacterium tuberculosis*," *Cold Spring Harb. Perspect. Med.*, vol. 6, no. 5, p. a025221, May 2016, doi: 10.1101/cshperspect.a025221.

[160] K. Bush, "Proliferation and significance of clinically relevant β-lactamases: β-lactamase overview," *Ann. N. Y. Acad. Sci.*, vol. 1277, no. 1, pp. 84–90, Jan. 2013, doi: 10.1111/nyas.12023.

[161] K. M. Papp-Wallace, A. Endimiani, M. A. Taracila, and R. A. Bonomo, "Carbapenems: Past, Present, and Future," *Antimicrob. Agents Chemother.*, vol. 55, no. 11, pp. 4943–4960, Nov. 2011, doi: 10.1128/AAC.00296-11.

[162] Y. Katayama, H.-Z. Zhang, and H. F. Chambers, "PBP 2a Mutations Producing Very-High-Level Resistance to Beta-Lactams," *Antimicrob. Agents Chemother.*, vol. 48, no. 2, pp. 453–459, Feb. 2004, doi: 10.1128/AAC.48.2.453-459.2004.

[163] J. C. Gallagher and C. MacDougall, *Antibiotics simplified*, 5th ed. Burlington: Jones & Bartlett Learning, 2022.

[164] D. C. Hooper, "Mechanisms of Action and Resistance of Older and Newer Fluoroquinolones," *Clin. Infect. Dis.*, vol. 31, no. Supplement_2, pp. S24–S28, Aug. 2000, doi: 10.1086/314056.

[165] G. A. Jacoby, J. Strahilevitz, and D. C. Hooper, "Plasmid-Mediated Quinolone Resistance," *Microbiol. Spectr.*, vol. 2, no. 5, p. 2.5.33, Sep. 2014, doi: 10.1128/microbiolspec.PLAS-0006-2013.

[166] D. Zeng *et al.*, "Approved Glycopeptide Antibacterial Drugs: Mechanism of Action and Resistance," *Cold Spring Harb. Perspect. Med.*, vol. 6, no. 12, p. a026989, Dec. 2016, doi: 10.1101/cshperspect.a026989.

[167] G. G. Zhanel *et al.*, "The Glycylcyclines: A Comparative Review with the Tetracyclines," *Drugs*, vol. 64, no. 1, pp. 63–88, 2004, doi: 10.2165/00003495-200464010-00005.

[168] M. Wenzel *et al.*, "A flat embedding method for transmission electron microscopy reveals an unknown mechanism of tetracycline," *Commun. Biol.*, vol. 4, no. 1, p. 306, Mar. 2021, doi: 10.1038/s42003-021-01809-8.

[169] Z.-K. Sheng *et al.*, "Mechanisms of Tigecycline Resistance among Klebsiella pneumoniae Clinical Isolates," *Antimicrob. Agents Chemother.*, vol. 58, no. 11, pp. 6982–6985, Nov. 2014, doi: 10.1128/AAC.03808-14.

[170] R. A. Helmick *et al.*, "Imidazole Antibiotics Inhibit the Nitric Oxide Dioxygenase Function of Microbial Flavohemoglobin," *Antimicrob. Agents Chemother.*, vol. 49, no. 5, pp. 1837–1843, May 2005, doi: 10.1128/AAC.49.5.1837-1843.2005.

[171] A. Goodwin, D. Kersulyte, G. Sisson, S. J. O. Veldhuyzen Van Zanten, D. E. Berg, and P. S. Hoffman, "Metronidazole resistance in Helicobacter pylori is due to null mutations in a gene (rdxA) that encodes an oxygen-insensitive NADPH nitroreductase," *Mol. Microbiol.*, vol. 28, no. 2, pp. 383–393, Apr. 1998, doi: 10.1046/j.1365-2958.1998.00806.x.

[172] H.-K. S. Leiros, S. Kozielski-Stuhrmann, U. Kapp, L. Terradot, G. A. Leonard, and S. M. McSweeney, "Structural Basis of 5-Nitroimidazole Antibiotic Resistance," *J. Biol. Chem.*, vol. 279, no. 53, pp. 55840–55849, Dec. 2004, doi: 10.1074/jbc.M408044200.

[173] T. Tenson, M. Lovmar, and M. Ehrenberg, "The Mechanism of Action of Macrolides, Lincosamides and Streptogramin B Reveals the Nascent Peptide Exit Path in the Ribosome," *J. Mol. Biol.*, vol. 330, no. 5, pp. 1005–1014, Jul. 2003, doi: 10.1016/S0022-2836(03)00662-4.

[174] S. K. Straus and R. E. W. Hancock, "Mode of action of the new antibiotic for Gram-positive pathogens daptomycin: Comparison with cationic antimicrobial peptides and lipopeptides," *Biochim. Biophys. Acta BBA - Biomembr.*, vol. 1758, no. 9, pp. 1215–1223, Sep. 2006, doi: 10.1016/j.bbamem.2006.02.009.

[175] A.-B. Hachmann, E. Sevim, A. Gaballa, D. L. Popham, H. Antelmann, and J. D. Helmann, "Reduction in Membrane Phosphatidylglycerol Content Leads to Daptomycin Resistance in Bacillus subtilis," *Antimicrob. Agents Chemother.*, vol. 55, no. 9, pp. 4326–4337, Sep. 2011, doi: 10.1128/AAC.01819-10.

[176] A. Tymoszewska, M. Szylińska, and T. Aleksandrzak-Piekarczyk, "The LiaFSR-LiaX System Mediates Resistance of Enterococcus faecium to Peptide Antibiotics and to Aureocin A53- and Enterocin L50-Like Bacteriocins," *Microbiol. Spectr.*, vol. 11, no. 3, pp. e00343-23, Jun. 2023, doi: 10.1128/spectrum.00343-23.

[177] V. V. H. Le and J. Rakonjac, "Nitrofurans: Revival of an 'old' drug class in the fight against antibiotic resistance," *PLOS Pathog.*, vol. 17, no. 7, p. e1009663, Jul. 2021, doi: 10.1371/journal.ppat.1009663.

[178] Y. Edowik, T. Caspari, and H. M. Williams, "The Amino Acid Changes T55A, A273P and R277C in the Beta-Lactamase CTX-M-14 Render E. coli Resistant to the Antibiotic Nitrofurantoin, a First-Line Treatment of Urinary Tract Infections," *Microorganisms*, vol. 8, no. 12, p. 1983, Dec. 2020, doi: 10.3390/microorganisms8121983.

[179] D. Shinabarger, "Mechanism of action of the oxazolidinone antibacterial agents," *Expert Opin. Investig. Drugs*, vol. 8, no. 8, pp. 1195–1202, Aug. 1999, doi: 10.1517/13543784.8.8.1195.

[180] S. Besier, A. Ludwig, J. Zander, V. Brade, and T. A. Wichelhaus, "Linezolid Resistance in *Staphylococcus aureus* : Gene Dosage Effect, Stability, Fitness Costs, and Cross-Resistances," *Antimicrob. Agents Chemother.*, vol. 52, no. 4, pp. 1570–1572, Apr. 2008, doi: 10.1128/AAC.01098-07.

[181] F. Yablonsky, "Alteration of Membrane Permeability in Bacillus subtilis by Clofoctol," *Microbiology*, vol. 129, no. 4, pp. 1089–1095, Apr. 1983, doi: 10.1099/00221287-129-4-1089.

[182] C. Bailly and G. Vergoten, "A new horizon for the old antibacterial drug clofoctol," *Drug Discov. Today*, vol. 26, no. 5, pp. 1302–1310, May 2021, doi: 10.1016/j.drudis.2021.02.004.

[183] S. Paukner and R. Riedl, "Pleuromutilins: Potent Drugs for Resistant Bugs—Mode of Action and Resistance," *Cold Spring Harb. Perspect. Med.*, vol. 7, no. 1, p. a027110, Jan. 2017, doi: 10.1101/cshperspect.a027110.

[184] S. Manioglu *et al.*, "Antibiotic polymyxin arranges lipopolysaccharide into crystalline structures to solidify the bacterial membrane," *Nat. Commun.*, vol. 13, no. 1, p. 6195, Oct. 2022, doi: 10.1038/s41467-022-33838-0.

[185] J. Li, R. L. Nation, and K. S. Kaye, Eds., *Polymyxin antibiotics: from laboratory bench to bedside*. in Advances in experimental medicine and biology, no. volume 1145. Cham, Switzerland: Springer, 2019.

[186] K. R. Hardie and S. J. Fenn, "JMM profile: rifampicin: a broad-spectrum antibiotic: This article is part of the JMM Profiles collection," *J. Med. Microbiol.*, vol. 71, no. 8, Aug. 2022, doi: 10.1099/jmm.0.001566.

[187] B. B. Bonev and N. M. Brown, Eds., *Bacterial Resistance to Antibiotics – From Molecules to Man*, 1st ed. Wiley, 2019. doi: 10.1002/9781119593522.

[188] P. Kesharwani, S. Chopra, and A. Dasgupta, Eds., *Drug discovery targeting drug-resistant bacteria*. London ; San Diego, CA: Academic Press, 2020.

[189] T. Velkov, P. E. Thompson, R. L. Nation, and J. Li, "Structure−Activity Relationships of Polymyxin Antibiotics," *J. Med. Chem.*, vol. 53, no. 5, pp. 1898–1916, Mar. 2010, doi: 10.1021/jm900999h.

[190] L. Zhang, P. Dhillon, H. Yan, S. Farmer, and R. E. W. Hancock, "Interactions of Bacterial Cationic Peptide Antibiotics with Outer and Cytoplasmic Membranes of *Pseudomonas aeruginosa*," *Antimicrob. Agents Chemother.*, vol. 44, no. 12, pp. 3317–3321, Dec. 2000, doi: 10.1128/AAC.44.12.3317-3321.2000.

[191] A. Clausell, M. Garcia-Subirats, M. Pujol, M. A. Busquets, F. Rabanal, and Y. Cajal, "Gram-Negative Outer and Inner Membrane Models: Insertion of Cyclic Cationic Lipopeptides," *J. Phys. Chem. B*, vol. 111, no. 3, pp. 551–563, Jan. 2007, doi: 10.1021/jp064757+.

[192] T. Mogi *et al.*, "Polymyxin B Identified as an Inhibitor of Alternative NADH Dehydrogenase and Malate: Quinone Oxidoreductase from the Gram-positive Bacterium Mycobacterium smegmatis," *J. Biochem. (Tokyo)*, vol. 146, no. 4, pp. 491–499, Oct. 2009, doi: 10.1093/jb/mvp096.

[193] B. W. Simpson and M. S. Trent, "Pushing the envelope: LPS modifications and their consequences," *Nat. Rev. Microbiol.*, vol. 17, no. 7, pp. 403–416, Jul. 2019, doi: 10.1038/s41579-019-0201-x.

[194] A. van Mourik *et al.*, "Altered Linkage of Hydroxyacyl Chains in Lipid A of Campylobacter jejuni Reduces TLR4 Activation and Antimicrobial Resistance," *J. Biol. Chem.*, vol. 285, no. 21, pp. 15828–15836, May 2010, doi: 10.1074/jbc.M110.102061.

[195] J. H. Moffatt *et al.*, "Colistin Resistance in Acinetobacter baumannii Is Mediated by Complete Loss of Lipopolysaccharide Production," *Antimicrob. Agents Chemother.*, vol. 54, no. 12, pp. 4971–4977, Dec. 2010, doi: 10.1128/AAC.00834-10.

[196] E. Llobet, J. M. Tomás, and J. A. Bengoechea, "Capsule polysaccharide is a bacterial decoy for antimicrobial peptides," *Microbiology*, vol. 154, no. 12, pp. 3877–3886, 2008, doi: 10.1099/mic.0.2008/022301-0.

[197] Y.-L. Tzeng *et al.*, "Cationic Antimicrobial Peptide Resistance in *Neisseria meningitidis*," *J. Bacteriol.*, vol. 187, no. 15, pp. 5387–5396, Aug. 2005, doi: 10.1128/JB.187.15.5387-5396.2005.

[198] V. B. Srinivasan, B. B. Singh, N. Priyadarshi, N. K. Chauhan, and G. Rajamohan, "Role of Novel Multidrug Efflux Pump Involved in Drug Resistance in Klebsiella pneumoniae," *PLoS ONE*, vol. 9, no. 5, p. e96288, May 2014, doi: 10.1371/journal.pone.0096288.

[199] J. Mathur and M. K. Waldor, "The *Vibrio cholerae* ToxR-Regulated Porin OmpU Confers Resistance to Antimicrobial Peptides," *Infect. Immun.*, vol. 72, no. 6, pp. 3577–3583, Jun. 2004, doi: 10.1128/IAI.72.6.3577-3583.2004.

[200] J. Mathur, B. M. Davis, and M. K. Waldor, "Antimicrobial peptides activate the Vibrio cholerae ? ^{E} regulon through an OmpU-dependent signalling pathway," *Mol. Microbiol.*, vol. 63, no. 3, Feb. 2007, doi: 10.1111/j.1365-2958.2006.05544.x.

[201] J. A. Bengoechea and M. Skurnik, "Temperature-regulated efflux pump/potassium antiporter system mediates resistance to cationic antimicrobial peptides in Yersinia," *Mol. Microbiol.*, vol. 37, no. 1, pp. 67–80, Jul. 2000, doi: 10.1046/j.1365-2958.2000.01956.x.

[202] B. Leimkuhler and C. Matthews, *Molecular Dynamics: With Deterministic and Stochastic Numerical Methods*. in Interdisciplinary Applied Mathematics. Springer International Publishing, 2015. doi: 10.1007/978-3-319-16375-8.

[203] B. J. Alder and T. E. Wainwright, "Studies in Molecular Dynamics. I. General Method," *J. Chem. Phys.*, vol. 31, no. 2, pp. 459–466, Aug. 1959, doi: 10.1063/1.1730376.

[204] "The Nobel Prize in Chemistry 2013," NobelPrize.org. Accessed: Mar. 02, 2020. [Online]. Available: https://www.nobelprize.org/prizes/chemistry/2013/summary/

[205] B. S. Daan Frenkel, *Understanding Molecular Simulation: From Algorithms to Applications*, Second. in Computational science series: from theory to applications, no. 1. Elsevier, 2002. doi: 10.1016/B978-0-12-267351-1.X5000-7.

[206] D. C. Rapaport, *The Art of Molecular Dynamics Simulation*, 2nd ed. Cambridge, UK ; New York, NY: Cambridge University Press, 2004.

[207] I. Yu *et al.*, "Biomolecular interactions modulate macromolecular structure and dynamics in atomistic model of a bacterial cytoplasm," *eLife*, vol. 5, p. e19274, Nov. 2016, doi: 10.7554/eLife.19274.

[208] H. I. Ingólfsson *et al.*, "The power of coarse graining in biomolecular simulations," *Wiley Interdiscip. Rev. Comput. Mol. Sci.*, vol. 4, no. 3, pp. 225–248, May 2014, doi: 10.1002/wcms.1169.

[209] N. Singh and W. Li, "Recent Advances in Coarse-Grained Models for Biomolecules and Their Applications," *Int. J. Mol. Sci.*, vol. 20, no. 15, Aug. 2019, doi: 10.3390/ijms20153774.

[210] J. A. Stevens *et al.*, "Molecular dynamics simulation of an entire cell," *Front. Chem.*, vol. 11, p. 1106495, Jan. 2023, doi: 10.3389/fchem.2023.1106495.

[211] W. Pezeshkian, M. König, T. A. Wassenaar, and S. J. Marrink, "Backmapping triangulated surfaces to coarse-grained membrane models," *Nat. Commun.*, vol. 11, no. 1, p. 2296, May 2020, doi: 10.1038/s41467-020-16094-y.

[212] D. E. Shaw *et al.*, "Atomic-level characterization of the structural dynamics of proteins," *Science*, vol. 330, no. 6002, pp. 341–346, Oct. 2010, doi: 10.1126/science.1187409.

[213] E. G. Lewars, *Computational Chemistry: Introduction to the Theory and Applications of Molecular and Quantum Mechanics*, 3rd ed. Springer International Publishing, 2016. doi: 10.1007/978-3-319-30916-3.

[214] T. P. Senftle *et al.*, "The ReaxFF reactive force-field: development, applications and future directions," *Npj Comput. Mater.*, vol. 2, no. 1, p. 15011, Mar. 2016, doi: 10.1038/npjcompumats.2015.11.

[215] F. Jensen, *Introduction to Computational Chemistry*, 2nd Edition. Chichester, England ; Hoboken, NJ: Wiley-Blackwell, 2011.

[216] Lindahl, Abraham, Hess, and van der Spoel, "GROMACS 2021 Manual," Jan. 2021, doi: 10.5281/zenodo.4457591.

[217] I. Soteras Gutiérrez *et al.*, "Parametrization of halogen bonds in the CHARMM general force field: Improved treatment of ligand–protein interactions," *Bioorg. Med. Chem.*, vol. 24, no. 20, pp. 4812–4825, Oct. 2016, doi: 10.1016/j.bmc.2016.06.034.

[218] M. Abraham *et al.*, "GROMACS 2023.1 Manual," Apr. 2023, doi: 10.5281/ZENODO.7852189.

[219] O. Berger, O. Edholm, and F. Jähnig, "Molecular dynamics simulations of a fluid bilayer of dipalmitoylphosphatidylcholine at full hydration, constant pressure, and constant temperature," *Biophys. J.*, vol. 72, no. 5, pp. 2002–2013, May 1997, doi: 10.1016/S0006-3495(97)78845-3.

[220] S. J. Marrink, H. J. Risselada, S. Yefimov, D. P. Tieleman, and A. H. De Vries, "The MARTINI Force Field: Coarse Grained Model for Biomolecular Simulations," *J. Phys. Chem. B*, vol. 111, no. 27, pp. 7812–7824, Jul. 2007, doi: 10.1021/jp071097f.

[221] F. Grote and A. P. Lyubartsev, "Optimization of Slipids Force Field Parameters Describing Headgroups of Phospholipids," *J. Phys. Chem. B*, vol. 124, no. 40, pp. 8784–8793, Oct. 2020, doi: 10.1021/acs.jpcb.0c06386.

[222] J. A. Maier, C. Martinez, K. Kasavajhala, L. Wickstrom, K. E. Hauser, and C. Simmerling, "ff14SB: Improving the Accuracy of Protein Side Chain and Backbone Parameters from ff99SB," *J. Chem. Theory Comput.*, vol. 11, no. 8, pp. 3696–3713, Aug. 2015, doi: 10.1021/acs.jctc.5b00255.

[223] D. Frenkel and B. Smit, "Long-Range Interactions," in *Understanding Molecular Simulation*, Elsevier, 2002, pp. 291–320. doi: 10.1016/B978-012267351-1/50014-6.

[224] A. Y. Toukmaji and J. A. Board, "Ewald summation techniques in perspective: a survey," *Comput. Phys. Commun.*, vol. 95, no. 2–3, pp. 73–92, Jun. 1996, doi: 10.1016/0010-4655(96)00016-1.

[225] U. Essmann, L. Perera, M. L. Berkowitz, T. Darden, H. Lee, and L. G. Pedersen, "A smooth particle mesh Ewald method," *J. Chem. Phys.*, vol. 103, no. 19, pp. 8577–8593, Nov. 1995, doi: 10.1063/1.470117.

[226] M. Born and R. Oppenheimer, "Zur Quantentheorie der Molekeln," *Ann. Phys.*, vol. 389, no. 20, pp. 457–484, 1927, doi: 10.1002/andp.19273892002.

[227] J. P. M. Jämbeck and A. P. Lyubartsev, "Derivation and Systematic Validation of a Refined All-Atom Force Field for Phosphatidylcholine Lipids," *J. Phys. Chem. B*, vol. 116, no. 10, pp. 3164–3179, Mar. 2012, doi: 10.1021/jp212503e.

[228] E. Braun, S. M. Moosavi, and B. Smit, "Anomalous Effects of Velocity Rescaling Algorithms: The Flying Ice Cube Effect Revisited," *J. Chem. Theory Comput.*, vol. 14, no. 10, pp. 5262–5272, Oct. 2018, doi: 10.1021/acs.jctc.8b00446.

[229] H. J. C. Berendsen, J. P. M. Postma, W. F. Van Gunsteren, A. DiNola, and J. R. Haak, "Molecular dynamics with coupling to an external bath," *J. Chem. Phys.*, vol. 81, no. 8, pp. 3684–3690, Oct. 1984, doi: 10.1063/1.448118.

[230] S. C. Harvey, R. K.-Z. Tan, and T. E. Cheatham, "The flying ice cube: Velocity rescaling in molecular dynamics leads to violation of energy equipartition," *J. Comput. Chem.*, vol. 19, no. 7, pp. 726–740, May 1998, doi: 10.1002/(SICI)1096-987X(199805)19:7<726::AID-JCC4>3.0.CO;2-S.

[231] S. Jo, T. Kim, V. G. Iyer, and W. Im, "CHARMM-GUI: A web-based graphical user interface for CHARMM," *J. Comput. Chem.*, vol. 29, no. 11, pp. 1859–1865, Aug. 2008, doi: 10.1002/jcc.20945.

[232] G. Bussi, D. Donadio, and M. Parrinello, "Canonical sampling through velocity rescaling," *J. Chem. Phys.*, vol. 126, no. 1, p. 014101, Jan. 2007, doi: 10.1063/1.2408420.

[233] J. Wong-ekkabut, M. S. Miettinen, C. Dias, and M. Karttunen, "Static charges cannot drive a continuous flow of water molecules through a carbon nanotube," *Nat. Nanotechnol.*, vol. 5, no. 8, pp. 555–557, Aug. 2010, doi: 10.1038/nnano.2010.152.

[234] M. Lingenheil, R. Denschlag, R. Reichold, and P. Tavan, "The 'Hot-Solvent/Cold-Solute' Problem Revisited," *J. Chem. Theory Comput.*, vol. 4, no. 8, pp. 1293–1306, Aug. 2008, doi: 10.1021/ct8000365.

[235] H. Watanabe, "Failure of Deterministic and Stochastic Thermostats to Control Temperature of Molecular Systems," *J. Phys. Soc. Jpn.*, vol. 86, no. 7, p. 075004, Jul. 2017, doi: 10.7566/JPSJ.86.075004.

[236] R. Halonen, I. Neefjes, and B. Reischl, "Further cautionary tales on thermostatting in molecular dynamics: Energy equipartitioning and non-equilibrium processes in gas-phase simulations," *J. Chem. Phys.*, vol. 158, no. 19, p. 194301, May 2023, doi: 10.1063/5.0148013.

[237] M. Ikeguchi, "Partial rigid-body dynamics in NPT, NPAT and NP?T ensembles for proteins and membranes," *J. Comput. Chem.*, vol. 25, no. 4, pp. 529–541, Mar. 2004, doi: 10.1002/jcc.10402.

[238] M. Parrinello and A. Rahman, "Polymorphic transitions in single crystals: A new molecular dynamics method," *J. Appl. Phys.*, vol. 52, no. 12, pp. 7182–7190, Dec. 1981, doi: 10.1063/1.328693.

[239] M. Bernetti and G. Bussi, "Pressure control using stochastic cell rescaling," *J. Chem. Phys.*, vol. 153, no. 11, p. 114107, Sep. 2020, doi: 10.1063/5.0020514.

[240] D. H. J. Mackay, A. J. Cross, and A. T. Hagler, "The Role of Energy Minimization in Simulation Strategies of Biomolecular Systems," in *Prediction of Protein Structure and the Principles of Protein Conformation*, G. D. Fasman, Ed., Boston, MA: Springer US, 1989, pp. 317–358. doi: 10.1007/978-1-4613-1571-1_7.

[241] T. Schlick, *Molecular Modeling and Simulation: An Interdisciplinary Guide: An Interdisciplinary Guide*, vol. 21. in Interdisciplinary Applied Mathematics, vol. 21. New York, NY: Springer New York, 2010. doi: 10.1007/978-1-4419-6351-2.

[242] T. Rivel, C. Ramseyer, and S. Yesylevskyy, "The asymmetry of plasma membranes and their cholesterol content influence the uptake of cisplatin," *Sci. Rep.*, vol. 9, no. 1, Dec. 2019, doi: 10.1038/s41598-019-41903-w.

[243] N. Awasthi and J. S. Hub, "Simulations of Pore Formation in Lipid Membranes: Reaction Coordinates, Convergence, Hysteresis, and Finite-Size Effects," *J. Chem. Theory Comput.*, vol. 12, no. 7, pp. 3261–3269, Jul. 2016, doi: 10.1021/acs.jctc.6b00369.

[244] J. S. Hub and N. Awasthi, "Probing a Continuous Polar Defect: A Reaction Coordinate for Pore Formation in Lipid Membranes," *J. Chem. Theory Comput.*, vol. 13, no. 5, pp. 2352–2366, May 2017, doi: 10.1021/acs.jctc.7b00106.

[245] F. Pietrucci, "Strategies for the exploration of free energy landscapes: Unity in diversity and challenges ahead," *Rev. Phys.*, vol. 2, pp. 32–45, Nov. 2017, doi: 10.1016/j.revip.2017.05.001.

[246] R. T. McGibbon, B. E. Husic, and V. S. Pande, "Identification of simple reaction coordinates from complex dynamics," *J. Chem. Phys.*, vol. 146, no. 4, p. 044109, Jan. 2017, doi: 10.1063/1.4974306.

[247] G. Bussi and A. Laio, "Using metadynamics to explore complex free-energy landscapes," *Nat. Rev. Phys.*, vol. 2, no. 4, pp. 200–212, Mar. 2020, doi: 10.1038/s42254-020-0153-0.

[248] G. M. Torrie and J. P. Valleau, "Monte Carlo free energy estimates using non-Boltzmann sampling: Application to the sub-critical Lennard-Jones fluid," *Chem. Phys. Lett.*, vol. 28, no. 4, pp. 578–581, Oct. 1974, doi: 10.1016/0009-2614(74)80109-0.

[249] J. Kästner, "Umbrella sampling: Umbrella sampling," *Wiley Interdiscip. Rev. Comput. Mol. Sci.*, vol. 1, no. 6, pp. 932–942, Nov. 2011, doi: 10.1002/wcms.66.

[250] S. Kumar, J. M. Rosenberg, D. Bouzida, R. H. Swendsen, and P. A. Kollman, "THE weighted histogram analysis method for free-energy calculations on biomolecules. I. The method," *J. Comput. Chem.*, vol. 13, no. 8, pp. 1011–1021, Oct. 1992, doi: 10.1002/jcc.540130812.

[251] J. S. Hub, B. L. De Groot, and D. Van Der Spoel, "g_wham—A Free Weighted Histogram Analysis Implementation Including Robust Error and Autocorrelation Estimates," *J. Chem. Theory Comput.*, vol. 6, no. 12, pp. 3713–3720, Dec. 2010, doi: 10.1021/ct100494z.

[252] A. Bagri, C. Mattevi, M. Acik, Y. J. Chabal, M. Chhowalla, and V. B. Shenoy, "Structural evolution during the reduction of chemically derived graphene oxide," *Nat. Chem.*, vol. 2, no. 7, pp. 581–587, Jul. 2010, doi: 10.1038/nchem.686.

[253] A. Koutsioubas, "Combined Coarse-Grained Molecular Dynamics and Neutron Reflectivity Characterization of Supported Lipid Membranes," *J. Phys. Chem. B*, vol. 120, no. 44, pp. 11474–11483, Nov. 2016, doi: 10.1021/acs.jpcb.6b05433.

[254] H. He, J. Klinowski, M. Forster, and A. Lerf, "A new structural model for graphite oxide," *Chem. Phys. Lett.*, vol. 287, no. 1, pp. 53–56, Apr. 1998, doi: 10.1016/S0009-2614(98)00144-4.

[255] F. S. Emami *et al.*, "Force Field and a Surface Model Database for Silica to Simulate Interfacial Properties in Atomic Resolution," *Chem. Mater.*, vol. 26, no. 8, pp. 2647–2658, Apr. 2014, doi: 10.1021/cm500365c.

[256] M. J. Abraham *et al.*, "GROMACS: High performance molecular simulations through multi-level parallelism from laptops to supercomputers," *SoftwareX*, vol. 1–2, pp. 19–25, Sep. 2015, doi: 10.1016/j.softx.2015.06.001.

[257] J. P. M. Jämbeck and A. P. Lyubartsev, "An Extension and Further Validation of an All-Atomistic Force Field for Biological Membranes," *J. Chem. Theory Comput.*, vol. 8, no. 8, pp. 2938–2948, Aug. 2012, doi: 10.1021/ct300342n.

[258] H. Tang, D. Liu, Y. Zhao, X. Yang, J. Lu, and F. Cui, "Molecular Dynamics Study of the Aggregation Process of Graphene Oxide in Water," *J. Phys. Chem. C*, vol. 119, no. 47, pp. 26712–26718, Nov. 2015, doi: 10.1021/acs.jpcc.5b07345.

[259] H. Tang *et al.*, "New Insight into the Aggregation of Graphene Oxide Using Molecular Dynamics Simulations and Extended Derjaguin–Landau–Verwey–Overbeek Theory," *Environ. Sci. Technol.*, vol. 51, no. 17, pp. 9674–9682, Sep. 2017, doi: 10.1021/acs.est.7b01668.

[260] G. Bussi, D. Donadio, and M. Parrinello, "Canonical sampling through velocity rescaling," *J. Chem. Phys.*, vol. 126, no. 1, p. 014101, Jan. 2007, doi: 10.1063/1.2408420.

[261] T. Darden, D. York, and L. Pedersen, "Particle mesh Ewald: An N·log(N) method for Ewald sums in large systems," *J. Chem. Phys.*, vol. 98, no. 12, pp. 10089–10092, Jun. 1993, doi: 10.1063/1.464397.

[262] C. H. Hsieh and W. G. Wu, "Structure and dynamics of primary hydration shell of phosphatidylcholine bilayers at subzero temperatures," *Biophys. J.*, vol. 71, no. 6, pp. 3278–3287, Dec. 1996, doi: 10.1016/S0006-3495(96)79520-6.

[263] A. S. Rosa, J. P. Cejas, E. A. Disalvo, and M. A. Frías, "Correlation between the hydration of acyl chains and phosphate groups in lipid bilayers: Effect of phase state, head group, chain length, double bonds and carbonyl groups," *Biochim. Biophys. Acta BBA - Biomembr.*, vol. 1861, no. 6, pp. 1197–1203, Jun. 2019, doi: 10.1016/j.bbamem.2019.03.018.

[264] S. S. Stachura, C. J. Malajczuk, E. Kuprusevicius, and R. L. Mancera, "Influence of Bilayer Size and Number in Multi-Bilayer DOPC Simulations at Full and Low Hydration," *Langmuir*, vol. 35, no. 6, pp. 2399–2411, Feb. 2019, doi: 10.1021/acs.langmuir.8b03212.

[265] J. Yin and Y.-P. Zhao, "Hybrid QM/MM simulation of the hydration phenomena of dipalmitoylphosphatidylcholine headgroup," *J. Colloid Interface Sci.*, vol. 329, no. 2, pp. 410–415, Jan. 2009, doi: 10.1016/j.jcis.2008.09.070.

[266] R. J. Mashl, H. L. Scott, S. Subramaniam, and E. Jakobsson, "Molecular Simulation of Dioleoylphosphatidylcholine Lipid Bilayers at Differing Levels of Hydration," *Biophys. J.*, vol. 81, no. 6, pp. 3005–3015, Dec. 2001, doi: 10.1016/S0006-3495(01)75941-3.

[267] E. A. Disalvo *et al.*, "Structural and functional properties of hydration and confined water in membrane interfaces," *Biochim. Biophys. Acta BBA - Biomembr.*, vol. 1778, no. 12, pp. 2655–2670, Dec. 2008, doi: 10.1016/j.bbamem.2008.08.025.

[268] W. Zhao, D. E. Moilanen, E. E. Fenn, and M. D. Fayer, "Water at the Surfaces of Aligned Phospholipid Multibilayer Model Membranes Probed with Ultrafast Vibrational Spectroscopy," *J. Am. Chem. Soc.*, vol. 130, no. 42, pp. 13927–13937, Oct. 2008, doi: 10.1021/ja803252y.

[269] E. A. Golovina, A. V. Golovin, F. A. Hoekstra, and R. Faller, "Water Replacement Hypothesis in Atomic Detail—Factors Determining the Structure of Dehydrated Bilayer Stacks," *Biophys. J.*, vol. 97, no. 2, pp. 490–499, Jul. 2009, doi: 10.1016/j.bpj.2009.05.007.

[270] J. D. Nickels and J. Katsaras, "Water and Lipid Bilayers," in *Membrane Hydration*, vol. 71, E. A. Disalvo, Ed., in Subcellular Biochemistry, vol. 71. , Cham: Springer International Publishing, 2015, pp. 45–67. doi: 10.1007/978-3-319-19060-0_3.

[271] S. Buchoux, "FATSLiM: a fast and robust software to analyze MD simulations of membranes," *Bioinformatics*, vol. 33, no. 1, pp. 133–134, Jan. 2017, doi: 10.1093/bioinformatics/btw563.

[272] H. Bhatia, H. I. Ingólfsson, T. S. Carpenter, F. C. Lightstone, and P.-T. Bremer, "MemSurfer: A Tool for Robust Computation and Characterization of Curved Membranes," *J. Chem. Theory Comput.*, vol. 15, no. 11, pp. 6411–6421, Nov. 2019, doi: 10.1021/acs.jctc.9b00453.

[273] D. Stauffer *et al.*, "An atomic charge model for graphene oxide for exploring its bioadhesive properties in explicit water," *J. Chem. Phys.*, vol. 141, no. 4, p. 044705, Jul. 2014, doi: 10.1063/1.4890503.

[274] A. A. Gurtovenko and I. Vattulainen, “Calculation of the electrostatic potential of lipid bilayers from molecular dynamics simulations: Methodological issues,” *J. Chem. Phys.*, vol. 130, no. 21, p. 215107, Jun. 2009, doi: 10.1063/1.3148885.

[275] T. Cha, A. Guo, and X.-Y. Zhu, “Formation of Supported Phospholipid Bilayers on Molecular Surfaces: Role of Surface Charge Density and Electrostatic Interaction,” *Biophys. J.*, vol. 90, no. 4, pp. 1270–1274, Feb. 2006, doi: 10.1529/biophysj.105.061432.

[276] M. Schneemilch and N. Quirke, “Free energy of adhesion of lipid bilayers on silica surfaces,” *J. Chem. Phys.*, vol. 148, no. 19, p. 194704, May 2018, doi: 10.1063/1.5028557.

[277] C. Tang and L. Cai, “The effect of surface heterogeneity between α-quartz and α-cristobalite on adsorption behaviors toward Cu2+ solution,” *Colloids Surf. Physicochem. Eng. Asp.*, vol. 609, p. 125651, Jan. 2021, doi: 10.1016/j.colsurfa.2020.125651.

[278] M. Roark and S. E. Feller, “Structure and Dynamics of a Fluid Phase Bilayer on a Solid Support as Observed by a Molecular Dynamics Computer Simulation,” *Langmuir*, vol. 24, no. 21, pp. 12469–12473, Nov. 2008, doi: 10.1021/la802079h.

[279] A. Lamberg and T. Taniguchi, “Coarse-Grained Computational Studies of Supported Bilayers: Current Problems and Their Root Causes,” *J. Phys. Chem. B*, vol. 118, no. 36, pp. 10643–10652, Sep. 2014, doi: 10.1021/jp5053419.

[280] S. V. Bennun, A. N. Dickey, C. Xing, and R. Faller, “Simulations of biomembranes and water: Important technical aspects,” *Fluid Phase Equilibria*, vol. 261, no. 1–2, pp. 18–25, Dec. 2007, doi: 10.1016/j.fluid.2007.07.056.

[281] C. Xing and R. Faller, “Density imbalances and free energy of lipid transfer in supported lipid bilayers,” *J. Chem. Phys.*, vol. 131, no. 17, p. 175104, Nov. 2009, doi: 10.1063/1.3262315.

[282] S. S. Stachura, C. J. Malajczuk, E. Kuprusevicius, and R. L. Mancera, “Influence of Bilayer Size and Number in Multi-Bilayer DOPC Simulations at Full and Low Hydration,” *Langmuir*, vol. 35, no. 6, pp. 2399–2411, Feb. 2019, doi: 10.1021/acs.langmuir.8b03212.

[283] E. Perrin, M. Schoen, F.-X. Coudert, and A. Boutin, “Structure and Dynamics of Solvated Polymers near a Silica Surface: On the Different Roles Played by Solvent,” *J. Phys. Chem. B*, vol. 122, no. 16, pp. 4573–4582, Apr. 2018, doi: 10.1021/acs.jpcb.7b11753.

[284] A. David, M. Pasquini, U. Tartaglino, and G. Raos, “A Coarse-Grained Force Field for Silica–Polybutadiene Interfaces and Nanocomposites,” *Polymers*, vol. 12, no. 7, p. 1484, Jul. 2020, doi: 10.3390/polym12071484.

[285] V. Lindahl, J. Lidmar, and B. Hess, “Accelerated weight histogram method for exploring free energy landscapes,” *J. Chem. Phys.*, vol. 141, no. 4, p. 044110, Jul. 2014, doi: 10.1063/1.4890371.

[286] Y. Gao *et al.*, “CHARMM-GUI Supports Hydrogen Mass Repartitioning and Different Protonation States of Phosphates in Lipopolysaccharides,” *J. Chem. Inf. Model.*, vol. 61, no. 2, pp. 831–839, Feb. 2021, doi: 10.1021/acs.jcim.0c01360.

[287] E. Duboué-Dijon, M. Javanainen, P. Delcroix, P. Jungwirth, and H. Martinez-Seara, “A practical guide to biologically relevant molecular simulations with charge scaling for electronic polarization,” *J. Chem. Phys.*, vol. 153, no. 5, p. 050901, Aug. 2020, doi: 10.1063/5.0017775.

[288] X. Jiang *et al.*, “An Intelligent Strategy with All-Atom Molecular Dynamics Simulations for the Design of Lipopeptides against Multidrug-Resistant *Pseudomonas aeruginosa*,” *J. Med. Chem.*, vol. 65, no. 14, pp. 10001–10013, Jul. 2022, doi: 10.1021/acs.jmedchem.2c00657.

[289] P. Sharma and K. G. Ayappa, “A Molecular Dynamics Study of Antimicrobial Peptide Interactions with the Lipopolysaccharides of the Outer Bacterial Membrane,” *J. Membr. Biol.*, vol. 255, no. 6, pp. 665–675, Dec. 2022, doi: 10.1007/s00232-022-00258-6.

[290] J. Shearer, J. K. Marzinek, P. J. Bond, and S. Khalid, “Molecular dynamics simulations of bacterial outer membrane lipid extraction: Adequate sampling?,” *J. Chem. Phys.*, vol. 153, no. 4, p. 044122, Jul. 2020, doi: 10.1063/5.0017734.

[291] P. Sharma *et al.*, "Assessing Barriers for Antimicrobial Penetration in Complex Asymmetric Bacterial Membranes: A Case Study with Thymol," *Langmuir*, vol. 36, no. 30, pp. 8800–8814, Aug. 2020, doi: 10.1021/acs.langmuir.0c01124.

[292] A. Rice, M. T. Rooney, A. I. Greenwood, M. L. Cotten, and J. Wereszczynski, "Lipopolysaccharide Simulations Are Sensitive to Phosphate Charge and Ion Parameterization," *J. Chem. Theory Comput.*, vol. 16, no. 3, pp. 1806–1815, Mar. 2020, doi: 10.1021/acs.jctc.9b00868.

[293] M. Lundborg, C. Wennberg, J. Lidmar, B. Hess, E. Lindahl, and L. Norlén, "Skin permeability prediction with MD simulation sampling spatial and alchemical reaction coordinates," *Biophys. J.*, vol. 121, no. 20, pp. 3837–3849, Oct. 2022, doi: 10.1016/j.bpj.2022.09.009.

[294] D. Shang, Q. Zhang, W. Dong, H. Liang, and X. Bi, "The effects of LPS on the activity of Trp-containing antimicrobial peptides against Gram-negative bacteria and endotoxin neutralization," *Acta Biomater.*, vol. 33, pp. 153–165, Mar. 2016, doi: 10.1016/j.actbio.2016.01.019.

[295] A. Mularski, J. J. Wilksch, E. Hanssen, R. A. Strugnell, and F. Separovic, "Atomic force microscopy of bacteria reveals the mechanobiology of pore forming peptide action," *Biochim. Biophys. Acta BBA - Biomembr.*, vol. 1858, no. 6, pp. 1091–1098, Jun. 2016, doi: 10.1016/j.bbamem.2016.03.002.

[296] K. Saikia and N. Chaudhary, "Interaction of MreB-derived antimicrobial peptides with membranes," *Biochem. Biophys. Res. Commun.*, vol. 498, no. 1, pp. 58–63, Mar. 2018, doi: 10.1016/j.bbrc.2018.02.176.

[297] M. U. Hammer *et al.*, "Lipopolysaccharide interaction is decisive for the activity of the antimicrobial peptide NK-2 against *Escherichia coli* and *Proteus mirabilis*," *Biochem. J.*, vol. 427, no. 3, pp. 477–488, May 2010, doi: 10.1042/BJ20091607.

[298] J. C. Espeche *et al.*, "Unravelling the mechanism of action of 'de novo' designed peptide P1 with model membranes and gram-positive and gram-negative bacteria," *Arch. Biochem. Biophys.*, vol. 693, p. 108549, Oct. 2020, doi: 10.1016/j.abb.2020.108549.

[299] A. of original G. version: de:User:FEERERO Author of translated E. copy: en:User:J_Raghu The original uploader was J. R. at E. Wikipedia, *English: How various antibiotics work.* 2007. Accessed: Jun. 09, 2023. [Online]. Available: https://commons.wikimedia.org/wiki/File:Antibiotics_action.png

[300] J. McMurry, *Organic chemistry*, 8e ed. Belmont, CA: Brooks/Cole, Cengage Learning, 2012.

Titre : Études numériques de membranes lipidiques supportées ou bactériennes

Mots clés : simulation, dynamique moléculaire, biophysique, membrane lipidique, bactérie

Résumé :

L'utilisation de molécules ciblant la matrice lipidique des membranes bactériennes est l'une des pistes actuellement explorées pour faire face à la résistance croissante aux antibiotiques. Les bactéries à Gram négatif sont une cible importante, car la présence d'une membrane externe (OM) réduit les classes d'antibiotiques efficaces et confère des mécanismes de résistance spécifiques directement liés à la présence de lipopolysaccharides. Dans le cadre de ce travail, nous avons modélisé l'OM et diverses membranes phospholipidiques pour aborder deux sujets complémentaires.

D'une part, un large éventail d'expériences destinées à étudier l'action des médicaments sur les membranes nécessitent de les immobiliser, ce qui se fait souvent par dépôt sur des substrats hydrophiles. Cependant, les interactions substrat-membrane peuvent modifier les fonctions biologiques et les propriétés structurelles des membranes. Ainsi, nous avons appliqué des simulations de dynamique moléculaire pour prédire les modifications de structure des membranes lipidiques en fonction des propriétés du substrat. En particulier, nous avons montré que la structure des systèmes lipidiques déposés varie graduellement entre celle d'une monocouche auto-assemblée (SAM) et celle d'une bicouche lipidique supportée (SLB), en fonction de l'hydrophilicité du substrat. Par la suite, nous avons conçu une variable collective qui décrit le processus d'adsorption, afin d'estimer le profil d'énergie libre. Cette méthode peut être utilisée pour prédire les états énergétiquement favorables des bicouches lipidiques supportées pour une surface donnée.

D'autre part, nous nous sommes concentrés sur le mode d'action de la colistine, un lipopeptide de la famille des polymyxines actuellement utilisé en dernier recours, en partie à cause de sa forte toxicité, mais aussi pour endiguer l'apparition de souches résistantes. Les polymyxines sont connues pour cibler l'OM, potentiellement en déplaçant les ions divalents qui contribuent à sa stabilité. Nous avons conçu une nouvelle variable collective pour comprendre comment les inhomogénéités locales dans la densité des ions divalents affectent l'OM. Nous avons modélisé l'OM en utilisant à la fois des champs de force à gros grains et tout atome. Nous avons observé, à l'aide de simulations à gros grains, que la fluidité membranaire est fortement affectée par la création de cette inhomogénéité, et que la colistine favorise davantage ces modifications de la mobilité des LPS.

Title : Computational study of supported or bacterial lipid membranes.

Keywords : simulation, molecular dynamics, biophysics, lipid membrane, bacteria

Abstract :

The use of molecules targeting the lipid matrix of bacterial membranes is one of the avenues currently being explored to deal with growing antibiotic resistance. Gram negative bacteria are an important target, as the presence of an outer membrane (OM) reduces classes of effective antibiotics and confers specific resistance mechanisms directly linked to the presence of lipopolysaccharides. In the frame of this work, we model the OM and phospholipid membranes to address two complementary topics.

On the first hand, a wide range of experiments designed to study the action of drugs on membranes require to immobilize them, which is often done by deposition on hydrophilic substrates. However, substrate-membrane interactions can hamper the biological functions and structural properties of the membranes. Hence, we applied molecular dynamics simulations to predict the structure modifications of lipid membranes depending on the substrate properties. Particularly, we showed that deposited lipid structure can form self-assembled monolayers (SAM) or supported lipid bilayers (SLB), according to the hydrophilicity of the substrate. Subsequently, we designed a collective variable that describes the adsorption process, in order to estimate the free energy profile. This method can be used to predict energetically favorable states of supported lipid bilayers for a given surface.

On the second hand, we focused on the mode of action of colistin, a lipopeptide from the polymyxin family that is currently used as a last resort, partly because of its high toxicity, but also to stem the appearance of resistant strains. Polymyxins are known to target the OM, potentially by displacing the divalent ions which contribute to its stability. We designed a new collective variable to understand how local inhomogeneities in the density of divalent ions affect the OM. We modeled the OM using both coarse-grained and all-atom force fields to give a complementary insight in that topic. We observed, using coarse-grained simulations, that the membrane fluidity is strongly affected by the creation of this inhomogeneity, and that colistin further promotes these changes in LPS mobility.

UBFC UNIVERSITE BOURGOGNE FRANCHE-COMTE

Université Bourgogne Franche-Comté
32, avenue de l'Observatoire
25000 Besançon

ÉCOLE DOCTORALE Environnements - Santé Bourgogne | Franche-Comté